



# City Research Online

## City, University of London Institutional Repository

---

**Citation:** Azabi, Y. O. (2017). Spiral photonic crystal fibers. (Unpublished Doctoral thesis, City, Universtiy of London)

This is the accepted version of the paper.

This version of the publication may differ from the final published version.

---

**Permanent repository link:** <https://openaccess.city.ac.uk/id/eprint/19372/>

**Link to published version:**

**Copyright:** City Research Online aims to make research outputs of City, University of London available to a wider audience. Copyright and Moral Rights remain with the author(s) and/or copyright holders. URLs from City Research Online may be freely distributed and linked to.

**Reuse:** Copies of full items can be used for personal research or study, educational, or not-for-profit purposes without prior permission or charge. Provided that the authors, title and full bibliographic details are credited, a hyperlink and/or URL is given for the original metadata page and the content is not changed in any way.

# **Spiral Photonic Crystal Fibers**



**Yousaf Omar Yousaf Azabi**

School of Mathematics, Computer Science & Engineering  
City, University of London

*A thesis submitted to the City, University of London in partial fulfilment  
of the requirement for the degree of Doctor of Philosophy*

November 2017

I would like to dedicate this thesis to my loving parents . . .

## **Declaration**

I hereby declare that except where specific reference is made to the work of others, the contents of this dissertation are original and have not been submitted in whole or in part for consideration for any other degree or qualification in this, or any other university. This dissertation is my own work and contains nothing which is the outcome of work done in collaboration with others, except as specified in the text and Acknowledgements. This dissertation contains fewer than 65,000 words including appendices, bibliography, footnotes, tables and equations and has fewer than 150 figures.

Yousaf Omar Yousaf Azabi  
November 2017

## **Acknowledgements**

I would like to thank my family for their support, help and encouragement to finish this work.

I would like to acknowledge both of my supervisors Dr. Arti Agrawal and Prof. B.M.A. Rahman for their help and patience. They always inspired me and helped me throughout my research.

I would also thank Dr. Kejalakshmy Namassivayane and special thanks to all colleagues at the Photonic Modeling group. I would thank every body has helped me to achieve this success.

## Abstract

This thesis is concerned with the study of special types of photonic crystal fibers (spiral) and their optical properties. The work is carried out using simulation techniques to obtain the modal field profile and properties for the designs. The method used in solving the Maxwell's equations is the full vectorial finite element method with the implementation of penalty function and perfectly matched layer. The penalty function is used to eliminate nonphysical solutions. The perfectly matched layer is integrated to absorb rays of light traveling away from the core. These rays are absorbed by the layer and do not reflect back to negatively influence the results.

The spiral shapes are implemented in the distribution of the holes in the cladding region of the photonic crystal fiber to determine the photonic crystal fiber properties. Three different spirals have been introduced which are equiangular, Archimedean and Fermat's spiral. The study of the effective refractive index, effective area and dispersion with varying spiral parameters have been carried out and the results are analyzed to understand the effect of each parameter. The variation of similar parameters in the spirals leads to similar variation in the optical properties under consideration.

Furthermore, the equiangular spiral photonic crystal fibers (ES-PCF) have been investigated in two different dimensional scales. The scales are in comparison with the wavelength of operation in the first case when core size is larger than the operating wavelength. In this case the total dispersion of the fiber has slightly higher values than the material dispersion but similar curve and slope. On the other hand, when the core size is comparable with the wavelength of operation, the dispersion is varying significantly with varying the spiral parameters. The effective area can be made very small and therefore the nonlinearity of the fiber very large to facilitate non-linear applications such as super continuum generation.

The equiangular spiral photonic crystal fiber has been modified slightly where the position of holes in the third ring are shifted further from the center and their size is much bigger. This manipulation is proposed in an algorithm in this thesis to facilitate the fabrication of ES-PCF using an adaptive stack and draw technique. The design shows similar optical behavior to an ideal spiral and its dispersion has been tailored for supercontinuum generation.

# Table of contents

<b>Abstract</b>	<b>v</b>
<b>List of figures</b>	<b>x</b>
<b>List of tables</b>	<b>xviii</b>
<b>Abbreviations</b>	<b>xix</b>
<b>Symbols</b>	<b>xxi</b>
<b>1 Introduction to Optical Fibers</b>	<b>1</b>
1.1 Optical Fiber Technology . . . . .	2
1.1.1 Optical fibers . . . . .	3
1.1.2 Guiding mechanism . . . . .	5
1.1.3 Types of optical fibers and fabrication . . . . .	7
1.1.4 Modes in optical fiber and their properties . . . . .	9
1.2 Optical Properties of Fibers . . . . .	12
1.2.1 Attenuation . . . . .	13
1.2.2 Dispersion . . . . .	16
1.2.3 Non-linearity . . . . .	19
1.3 Photonic Crystal Fibers . . . . .	29
1.3.1 Brief history of photonic crystal fibers . . . . .	29
1.3.2 Types of photonic crystal fibers . . . . .	30
1.3.3 Hexagonal photonic crystal fiber . . . . .	35
1.3.4 Properties of photonic crystal fibers . . . . .	36
1.3.5 Fabrication of photonic crystal fibers . . . . .	41
1.4 Materials for Fiber Fabrication . . . . .	45
1.4.1 Soft-Glasses . . . . .	46
1.4.2 Polymers . . . . .	47

1.5	Summary . . . . .	48
<b>2</b>	<b>Methodology</b>	<b>49</b>
2.1	Introduction to Electromagnetism . . . . .	50
2.1.1	Maxwell's equations . . . . .	50
2.1.2	Boundary conditions . . . . .	51
2.1.3	Wave equation . . . . .	54
2.2	Numerical Methods . . . . .	56
2.2.1	Analytical methods . . . . .	56
2.2.2	Numerical methods . . . . .	57
2.3	Finite Element Method . . . . .	59
2.3.1	Formulation . . . . .	62
2.3.2	Vector formulation . . . . .	63
2.3.3	Domain discretization . . . . .	65
2.3.4	Element and global matrices . . . . .	69
2.3.5	Penalty function . . . . .	73
2.3.6	Perfectly matched layers . . . . .	74
2.4	Summary . . . . .	77
<b>3</b>	<b>Spiral Photonic Crystal Fibers</b>	<b>79</b>
3.1	Definition of Spiral . . . . .	80
3.2	Equiangular Spiral . . . . .	81
3.2.1	Equiangular spiral curve . . . . .	81
3.2.2	Characteristics of equiangular spiral . . . . .	82
3.2.3	ES-PCF . . . . .	82
3.3	Study of the ES-PCF Parameters . . . . .	87
3.3.1	Study of number of arms ( $N_{arms}$ ) . . . . .	88
3.3.2	Study of number of rings ( $N_{rings}$ ) . . . . .	90
3.3.3	Study of pitch size ( $\Lambda$ ) . . . . .	92
3.3.4	Study of the ratio ( $d/\Lambda$ ) . . . . .	93
3.3.5	Study of angle ( $\theta$ ) . . . . .	95
3.3.6	Study of wavelength ( $\lambda$ ) . . . . .	97
3.4	Archimedean Spiral (AS) . . . . .	99
3.4.1	AS curve . . . . .	100
3.4.2	AS-PCF . . . . .	100
3.5	Study of the AS-PCF Parameters . . . . .	102
3.5.1	Study of number of holes ( $N_{holes}$ ) . . . . .	102

3.5.2	Study of pitch size ( $\Lambda$ ) . . . . .	104
3.5.3	Study of hole size ( $d$ ) . . . . .	105
3.5.4	Study of turns spacing factor ( $b$ ) . . . . .	106
3.5.5	Study of angle ( $\theta$ ) . . . . .	107
3.6	Fermat's Spiral (FS) . . . . .	110
3.6.1	FS curve . . . . .	110
3.6.2	FS-PCF . . . . .	111
3.7	Study of the FS-PCF Parameters . . . . .	112
3.7.1	Study of number of holes ( $N_{holes}$ ) . . . . .	112
3.7.2	Study of pitch size ( $\Lambda$ ) . . . . .	114
3.7.3	Study of hole size ( $d$ ) . . . . .	115
3.8	Comparison of Spiral PCFs . . . . .	117
3.9	Results of Ideal ES-PCF . . . . .	122
3.9.1	Large pitch scenario ( $\Lambda = 4\mu m$ ) . . . . .	123
3.9.2	Small pitch scenario ( $\Lambda = 1\mu m$ ) . . . . .	128
3.10	Summary . . . . .	134
<b>4</b>	<b>Steiner ES-PCF Design</b>	<b>136</b>
4.1	Properties of Steiner ES-PCF . . . . .	137
4.1.1	Study of the effective refractive index . . . . .	139
4.1.2	Study of the dispersion . . . . .	142
4.1.3	Study of the non-linearity and effective area . . . . .	148
4.1.4	Comparison of Steiner ES-PCF with other PCF . . . . .	156
4.2	Supercontinuum Generation . . . . .	159
4.2.1	Parameters optimization . . . . .	159
4.2.2	Results of optimum design . . . . .	163
4.2.3	Result of supercontinuum generation . . . . .	167
4.3	Towards Steiner ES-PCF Fabrication . . . . .	168
4.3.1	Steiner chain . . . . .	168
4.3.2	Algorithm of fabrication . . . . .	170
4.3.3	Adapted stack and draw . . . . .	173
4.4	Comparison between Ideal and Steiner ES-PCF . . . . .	174
4.4.1	Comparison of ideal and Steiner ES-PCF ( $\Lambda = 3\mu m$ ) . . . . .	175
4.4.2	Comparison of ideal and Steiner ES-PCF ( $\Lambda = 1\mu m$ ) . . . . .	177
4.5	Summary . . . . .	179

---

<b>5 Conclusion and Suggestions for Future Work</b>	<b>181</b>
5.1 Conclusion . . . . .	181
5.2 Future Work . . . . .	183
<b>Author Publications</b>	<b>185</b>
<b>References</b>	<b>187</b>

**THE FOLLOWING PARTS OF THIS THESIS HAVE BEEN REDACTED  
FOR COPYRIGHT REASONS:**

Photograph (ref no. 230).....pg.80

# List of figures

1.1	Typical optical fiber structure . . . . .	3
1.2	Refractive index profile of fused silica material . . . . .	4
1.3	Dispersion of fused silica material . . . . .	4
1.4	Snell's law of refraction . . . . .	5
1.5	Sketch of TIR in optical fiber . . . . .	6
1.6	Intrinsic silica material losses . . . . .	8
1.7	Typical dimensions of SMF and MMF . . . . .	9
1.8	Mode field profiles for low $LP_{lm}$ . . . . .	10
1.9	Normalized frequency ( $V$ ) vs normalized propagation constant ( $b$ ) curves for LP modes in step index fiber . . . . .	12
1.10	Optical fiber attenuation . . . . .	14
1.11	Fiber macrobending . . . . .	15
1.12	Fiber microbending . . . . .	15
1.13	Schematic of effect of dispersion on the signal . . . . .	17
1.14	Dispersion of typical single mode optical fibers . . . . .	18
1.15	Chirped pulse . . . . .	23
1.16	Solitons - Linear and non-linear effects on pulses (a) is input pulse, (b) a pulse propagate in dispersive media where leading edge of the pulse is compressed and trailing edge is expanded, and (c) a pulse propagates under Kerr non-linear effect and pulse is compressed in the trailing edge and expanded in the leading edge of the pulse. . . . .	24
1.17	Four-wave mixing . . . . .	25
1.18	Stimulated Raman scattering . . . . .	26
1.19	Stimulated Brillouin scattering . . . . .	27

1.20	Different designs of PCF (a) fiber with a pure silica core surrounded by air-holes in the cladding, (b) air-guiding fiber in which light is confined to a hollow core by band-gap effect, (c) core is made of pure silica while the holes in the cladding are filled with a high index liquid, and (d) hollow cylindrical multilayer fiber with an all solid cladding (Bragg fiber). . . . .	31
1.21	Hollow-core photonic band-gap fiber . . . . .	32
1.22	Cross section of Kagome fiber . . . . .	33
1.23	Cross sections of different HC-NCF designs with; (a) touching capillaries in the cladding, (b) non-touching capillaries in the cladding, (c) double nested capillaries in the cladding, and (d) ice-cream cone shape capillary in the cladding . . . . .	33
1.24	High-index guiding photonic crystal fiber . . . . .	34
1.25	A schematic of hexagonal photonic crystal fiber transverse section . . . . .	35
1.26	Fabrication process of PCF . . . . .	43
2.1	Interface between two media . . . . .	52
2.2	Basic finite element in 1,2 and 3D . . . . .	66
2.3	Mesh comparison of triangle and rectangle element . . . . .	67
2.4	First- second- and third-order triangle elements . . . . .	67
2.5	Pascal triangle and number of terms for a complete polynomial . . . . .	67
2.6	A schematic diagram of simulation window of a conventional fiber structure with PML boundaries . . . . .	76
3.1	Spirals in Nature . . . . .	80
3.2	Equiangular spiral . . . . .	82
3.3	A schematic of H-PCF cross section in transverse direction . . . . .	83
3.4	A schematic of ES-PCF cross section in transverse direction . . . . .	84
3.6	Change in (a) $n_{eff}$ , $A_{eff}$ and (b) loss with varying $N_{arms}$ , and (c-f) the corresponding field plots of 5, 6, 7 and 8 arms structures, respectively. Structure parameters are $N_{rings} = 3$ , $\Lambda = 3\mu m$ , $d/\Lambda = 0.35$ and $\theta = 30^\circ$ . . . . .	89
3.7	Change in (a) $n_{eff}$ , $A_{eff}$ and (b) loss with varying $N_{rings}$ , and (c-e) the corresponding field plots of 2, 3, 5 and 7 rings structures. Structure Parameters are $N_{arms} = 6$ , $\Lambda = 2\mu m$ , $d/\Lambda = 0.35$ and $\theta = 30^\circ$ . . . . .	91

3.8	Change in (a) $n_{eff}$ , $A_{eff}$ and (b) normalized $A_{eff}$ with varying $\Lambda$ , and (c-f) the corresponding field plots of pitch size 1, 3, 5 and $8\mu m$ for $d/\Lambda = 0.6$ . Structure Parameters are $N_{arms} = 6$ , $N_{rings} = 3$ , $d/\Lambda = 0.35$ and $0.6$ , and $\theta = 30^\circ$ . . . . .	93
3.9	Change in (a) $n_{eff}$ , $A_{eff}$ and (b) loss with varying $d/\Lambda$ , and (c-e) the correspondence field plots for $d/\Lambda = 0.15$ , $0.3$ and $0.6$ . Structure parameters are $N_{arms} = 6$ , $N_{rings} = 3$ , $\Lambda = 5\mu m$ and $\theta = 30^\circ$ . . . . .	94
3.10	Change in (a) $n_{eff}$ , $A_{eff}$ and (b) loss with varying $\theta$ , and (c-f) the corresponding field plots for $\theta = 28, 30, 32$ and $42^\circ$ . Structure parameters are $N_{arms} = 6$ , $N_{rings} = 3$ , $\Lambda = 3\mu m$ and $d/\Lambda = 0.35$ . . . . .	96
3.11	Schematics of different ES-PCF holes distribution with $N_{arms} = 6$ , $N_{rings} = 3$ , $\Lambda = 3\mu m$ , $d/\Lambda = 0.35$ and $\theta$ varied. Starting from top left corner and moving to the right, the values of $\theta$ are $28^\circ, 30^\circ, 32^\circ, 34^\circ, 35^\circ, 37^\circ, 40^\circ$ and $42^\circ$ . . . . .	97
3.12	Change in (a) $n_{eff}$ , loss and (b) normalized $A_{eff}$ with varying $\lambda$ , and (c-f) the corresponding field plots at $\lambda = 0.6$ and $1.5\mu m$ for $d/\Lambda = 0.3$ and $0.5$ , respectively. Structure parameters are $N_{arms} = 6$ , $N_{rings} = 3$ , $\theta = 30^\circ$ , $\Lambda = 5\mu m$ , and $d/\Lambda = 0.3$ . . . . .	98
3.13	Dispersion of ES-PCF $N_{arms} = 6$ , $N_{rings} = 3$ , $\theta = 30^\circ$ , $\Lambda = 3\mu m$ and $d/\Lambda = 0.3$ and $0.5$ . . . . .	99
3.14	Archimedean Spiral . . . . .	100
3.15	Schematics of different AS-PCF hole distribution with $N_{rings} = 18$ (middle row) and $40$ (upper and lower rows) for different $\theta$ values. Starting from top left corner and moving to the right, the values of $\theta$ are $36, 45, 60, 31, 67, 105, 31, 67$ , and $110^\circ$ . . . . .	101
3.16	Change in (a) $n_{eff}$ , $A_{eff}$ and (b) loss with varying $N_{holes}$ , and (c-e) the corresponding field plots for $N_{holes} = 18, 24$ and $30$ . Structure parameters are $\Lambda = 3\mu m$ , $d = 1\mu m$ , $\theta = 65^\circ$ and $b = 0.3$ . . . . .	103
3.17	Change in (a) $n_{eff}$ , $A_{eff}$ and (b) loss with varying $\Lambda$ , and (c-e) the corresponding field plots for $\Lambda = 4, 5$ and $6\mu m$ . Structure parameters are $N_{holes} = 18$ , $d = 1\mu m$ , $\theta = 65^\circ$ and $b = 0.3$ . . . . .	104
3.18	Change in (a) $n_{eff}$ , $A_{eff}$ and (b) loss with varying $d$ , and (c-e) the corresponding field plots for $d = 0.8, 1.1$ and $1.4\mu m$ . Structure parameters are $N_{holes} = 18$ , $\Lambda = 3\mu m$ , $\theta = 65^\circ$ and $b = 0.3$ . . . . .	105
3.19	Change in (a) $n_{eff}$ , $A_{eff}$ and (b) loss with varying $b$ , and (c-e) the corresponding field plots for $b = 0.2, 0.35$ and $0.5$ . Structure parameters are $N_{holes} = 18$ , $\Lambda = 3\mu m$ , $d = 1\mu m$ and $\theta = 65^\circ$ . . . . .	107

3.20	Change in (a) $n_{eff}$ , $A_{eff}$ and (b) loss with varying $\theta$ , and (c-e) the corresponding field plots for $\theta = 64, 66$ and $68^\circ$ . Structure parameters are $N_{holes} = 18$ , $\Lambda = 3\mu m$ , $d = 1\mu m$ and $b = 0.3$ . . . . .	108
3.21	A schematic of a cross section of the transverses direction of an ES-PCF with varying hole size. Structure parameters are $N_{arms} = 16$ , $N_{rings} = 8$ , $\theta = 33.75^\circ$ , $\Lambda = 5\mu m$ , $d_{min} = 1\mu m$ , $d_{max} = 2.2\mu m$ and $p = 1.5$ . . . . .	109
3.22	Fermat's Spiral . . . . .	111
3.23	Hole distribution of Fermat's spiral . . . . .	112
3.24	Change in (a) $n_{eff}$ , $A_{eff}$ and (b) birefringence with varying $N_{holes}$ , $\Lambda = 1.5\mu m$ and $d = 0.75\mu m$ with one missing hole in the center, and (c-e) the corresponding field plots for $N_{holes} = 10$ and $40$ for x and y polarized $H_{11}^y$ fields. . . . .	113
3.25	Change in (a) $n_{eff}$ , $A_{eff}$ and (b) birefringence with varying $\Lambda$ , $N_{holes} = 50$ and $d = 6\mu m$ with one missing hole in the center, and (c-e) the corresponding field plots for $\Lambda = 3.8$ and $4.3\mu m$ for $H^x$ and $H^y$ fields. . . . .	115
3.26	Change in (a) $n_{eff}$ , $A_{eff}$ and (b) birefringence with varying $d$ , $N_{holes} = 50$ and $\Lambda = 4\mu m$ with one missing hole in the center, and (c-e) the corresponding field plots for $d = 2.6$ and $3.2\mu m$ for $H^x$ and $H^y$ fields. . . . .	116
3.27	Schematics of cross sections of four structures: ES-PCF has $N_{arms} = 6$ , $N_{rings} = 3$ , $d/\Lambda = 0.6$ and $\theta = 30^\circ$ ; AS-PCF has $N_{holes} = 18$ , $d/\Lambda = 0.6$ , $b = 0.3$ and $\theta = 65^\circ$ ; and two FS-PCF has $N_{holes} = 18$ , $\theta = 30^\circ$ and $d/\Lambda = 0.6$ and $1.2$ . All structures has $\Lambda = 2\mu m$ . . . . .	118
3.28	Comparison of the change in $n_{eff}$ with wavelength. The structures parameters are: ES-PCF has $N_{arms} = 6$ , $N_{rings} = 3$ , $d/\Lambda = 0.6$ and $\theta = 30^\circ$ ; AS-PCF has $N_{holes} = 18$ , $d/\Lambda = 0.6$ , $b = 0.3$ and $\theta = 65^\circ$ ; FS-PCF has $N_{holes} = 18$ , $\theta = 30^\circ$ and $d/\Lambda = 0.6$ and $1.2$ . All structures have $\Lambda = 2\mu m$ . . . . .	119
3.29	Comparison of the change in Birefringence with wavelength. The structures parameters are: AS-PCF has $N_{holes} = 18$ , $d/\Lambda = 0.6$ , $b = 0.3$ and $\theta = 65^\circ$ ; FS-PCF has $N_{holes} = 18$ , $\theta = 30^\circ$ and $d/\Lambda = 0.6$ and $1.2$ . All structures have $\Lambda = 2\mu m$ . . . . .	120
3.30	Comparison of the change in $A_{eff}$ with wavelength. The structures parameters are: ES-PCF has $N_{arms} = 6$ , $N_{rings} = 3$ , $d/\Lambda = 0.6$ and $\theta = 30^\circ$ ; AS-PCF has $N_{holes} = 18$ , $d/\Lambda = 0.6$ , $b = 0.3$ and $\theta = 65^\circ$ ; FS-PCF has $N_{holes} = 18$ , $\theta = 30^\circ$ and $d/\Lambda = 0.6$ and $1.2$ . All structures have $\Lambda = 2\mu m$ . . . . .	120

3.31	Comparison of the change in $\gamma$ with wavelength. The structures parameters are: ES-PCF has $N_{arms} = 6$ , $N_{rings} = 3$ , $d/\Lambda = 0.6$ and $\theta = 30^\circ$ ; AS-PCF has $N_{holes} = 18$ , $d/\Lambda = 0.6$ , $b = 0.3$ and $\theta = 65^\circ$ ; FS-PCF has $N_{holes} = 18$ , $\theta = 30^\circ$ and $d/\Lambda = 0.6$ and 1.2. All structures have $\Lambda = 2\mu m$ . . . . .	121
3.32	Comparison of the change in loss with wavelength. The structures parameters are: ES-PCF has $N_{arms} = 6$ , $N_{rings} = 3$ , $d/\Lambda = 0.6$ and $\theta = 30^\circ$ ; AS-PCF has $N_{holes} = 18$ , $d/\Lambda = 0.6$ , $b = 0.3$ and $\theta = 65^\circ$ ; FS-PCF has $N_{holes} = 18$ , $\theta = 30^\circ$ and $d/\Lambda = 0.6$ and 1.2. All structures have $\Lambda = 2\mu m$ . . . . .	122
3.33	Air-hole arrangements in ES-PCF (7 arms & $\theta = 30^\circ$ ) . . . . .	123
3.34	Study the effect of varying $N_{rings}$ on $n_{eff}$ for ES-PCF with 7 arms, $d/\Lambda = 0.42$ , $\Lambda = 4\mu m$ and $\theta = 30^\circ$ . . . . .	124
3.35	Study the effect of varying $N_{rings}$ on $A_{eff}$ for ES-PCF with 7 arms, $d/\Lambda = 0.42$ , $\Lambda = 4\mu m$ and $\theta = 30^\circ$ . . . . .	124
3.36	Study the effect of varying the ratio $d/\Lambda$ on $A_{eff}$ for ES-PCF with 7 arms, 4 rings, $\Lambda = 4\mu m$ and $\theta = 30^\circ$ . . . . .	125
3.37	Study the effect of varying the ratio $d/\Lambda$ on $n_{eff}$ for ES-PCF with 7 arms, 4 rings, $\Lambda = 4\mu m$ and $\theta = 30^\circ$ . . . . .	125
3.38	Study the effect of varying the number of arms on $n_{eff}$ for ES-PCF with 4 rings, ratio of 0.4 and 0.38, $\Lambda = 4\mu m$ and $\theta = 30^\circ$ . . . . .	126
3.39	Study the effect of varying the number of arms on $A_{eff}$ for ES-PCF with 4 rings, ratio of 0.4 and 0.38, $\Lambda = 4\mu m$ and $\theta = 30^\circ$ . . . . .	127
3.40	Study the effect of varying the number of rings on $n_{eff}$ for ES-PCF with 7 arms, ratio of 0.42, $\Lambda = 1\mu m$ and $\theta = 30^\circ$ . . . . .	129
3.41	Study the effect of varying the number of rings on $A_{eff}$ for ES-PCF with 7 arms, ratio of 0.42, $\Lambda = 1\mu m$ and $\theta = 30^\circ$ . . . . .	129
3.42	Study the effect of varying the ratio $d/\Lambda$ on $n_{eff}$ for ES-PCF with 6 arms, 3 rings, $\Lambda = 1\mu m$ and $\theta = 30^\circ$ . . . . .	130
3.43	Study the effect of varying the ratio $d/\Lambda$ on $A_{eff}$ for ES-PCF with 6 arms, 3 rings, $\Lambda = 1\mu m$ and $\theta = 30^\circ$ . . . . .	131
3.44	Study the effect of varying the number of arms on $n_{eff}$ for ES-PCF with $d/\Lambda = 0.34$ , 3 rings, $\Lambda = 1\mu m$ and $\theta = 30^\circ$ . . . . .	131
3.45	Study the effect of varying the number of arms on $A_{eff}$ for ES-PCF with $d/\Lambda = 0.34$ , 3 rings, $\Lambda = 1\mu m$ and $\theta = 30^\circ$ . . . . .	132
3.46	Study the effect of varying $\Lambda$ on $n_{eff}$ for ES-PCF with $d/\Lambda = 0.4$ , 4 rings, $\Lambda = 1$ and $4\mu m$ and $\theta = 30^\circ$ . . . . .	133

3.47	Study the effect of varying $\Lambda$ on $A_{eff}$ for ES-PCF with $d/\Lambda = 0.4$ , 4 rings, $\Lambda = 1$ and $4\mu m$ and $\theta = 30^\circ$ . . . . .	133
4.1	Refractive index profile of soft glass SF57 material . . . . .	137
4.2	Cross section of Steiner ES-PCF of 7 arm structure . . . . .	138
4.3	Cross sections of Steiner (left) and ideal (right) ES-PCF of a structures with 7 arms, 3 rings, $d/\Lambda = 0.4$ and $\Lambda = 3\mu m$ . . . . .	139
4.4	Study the effect of varying $N_{arms}$ on $n_{eff}$ for Steiner ES-PCF with $d/\Lambda = 0.4$ and $\Lambda = 3\mu m$ in soft glass SF57. . . . .	140
4.5	Study the effect of varying $N_{arms}$ on $n_{eff}$ for Steiner ES-PCF with $d/\Lambda = 0.4$ and $\Lambda = 1\mu m$ in soft glass SF57. . . . .	141
4.6	Study the effect of varying $\Lambda$ on $n_{eff}$ for Steiner ES-PCF with $d/\Lambda = 0.4$ and $N_{arms} = 6$ in soft glass SF57. . . . .	141
4.7	Study the effect of varying $d/\Lambda$ on $A_{eff}$ for two ES-PCF designs with $\Lambda = 1$ and $3\mu m$ , and $N_{arms} = 6$ (solid lines) and 7 arms (dotted lines), in soft glass SF57. . . . .	142
4.8	Study the effect of varying $N_{arms}$ on dispersion for ES-PCF design with $\Lambda = 1\mu m$ and $d/\Lambda = 0.4$ in soft glass SF57. . . . .	143
4.9	Study the effect of varying $\Lambda$ on dispersion for ES-PCF design with $N_{arms} = 6$ and $d/\Lambda = 0.4$ in soft glass SF57. . . . .	144
4.10	Study the effect of varying $d/\Lambda$ on dispersion for ES-PCF design with $N_{arms} = 7$ and $\Lambda = 1\mu m$ in soft glass SF57. . . . .	144
4.11	(a) Study the effect of varying $d_1$ on dispersion for ES-PCF design with $N_{arms} = 7$ , $d/\Lambda = 0.5$ and $\Lambda = 1\mu m$ in soft glass SF57, and (b) schematic of $d_1$ and $d_2$ the diameters of holes in first and second rings, respectively. . . . .	145
4.12	Study the effect of varying $d_2$ on dispersion for ES-PCF design with $N_{arms} = 7$ , $d/\Lambda = 0.5$ and $\Lambda = 1\mu m$ in soft glass SF57. . . . .	146
4.13	Study the effect of varying $\Lambda$ on dispersion for ES-PCF design with $N_{arms} = 6$ , $d/\Lambda = 0.4$ and $d_c/\Lambda = 0.2$ in soft glass SF57. . . . .	147
4.14	Study of the effect of varying $d_c$ on dispersion for ES-PCF design with $N_{arms} = 6$ , $d/\Lambda = 0.4$ and $\Lambda = 1\mu m$ in soft glass SF57. . . . .	148
4.15	Study the effect of varying $N_{arms}$ on $\gamma$ for ES-PCF design with $d/\Lambda = 0.4$ and $\Lambda = 1\mu m$ in soft glass SF57. . . . .	149
4.16	Study the effect of varying $\Lambda$ on $\gamma$ for ES-PCF design with $N_{arms} = 6$ and $d/\Lambda = 0.4$ in soft glass SF57. . . . .	150

4.17	Study the effect of varying $d/\Lambda$ on $\gamma$ for ES-PCF designs with $\Lambda = 1\mu m$ (solid line) and $3\mu m$ (dotted line), for $N_{arms} = 6$ and $7$ , respectively, in soft glass SF57. . . . .	151
4.18	Study the effect of varying $d_1$ on $\gamma$ for ES-PCF design with $7$ arms, $d/\Lambda = 0.5$ and $\Lambda = 1\mu m$ in soft glass SF57. . . . .	152
4.19	Study the effect of varying $d_2$ on $\gamma$ for ES-PCF designs with $7$ arms, $d/\Lambda = 0.5$ and $\Lambda = 1\mu m$ in soft glass SF57. . . . .	153
4.20	Study the effect of varying spiral parameter $b$ on $\gamma$ and $A_{eff}$ for ES-PCF designs with $6$ arms, $d/\Lambda = 0.4$ and $\Lambda = 1\mu m$ , at wavelength $1.064\mu m$ in soft glass SF57. . . . .	153
4.21	Study the effect of varying $d_c$ on $\gamma$ for ES-PCF design with $6$ arms, $d/\Lambda = 0.4$ , and $d_c/\Lambda = 0.2$ in soft glass SF57. . . . .	154
4.22	Study the effect of varying $d_c$ on $\gamma$ for ES-PCF design with $6$ arms, $d/\Lambda = 0.4$ , and $\Lambda = 1\mu m$ in soft glass SF57. . . . .	155
4.23	A comparison of non-linearity and $A_{eff}$ as a function of core diameter of ASC, H-PCF and ES-PCF designs in soft glass SF57. . . . .	157
4.24	A comparison of Dispersion of ASC, H-PCF and ES-PCF designs in soft glass SF57. . . . .	157
4.25	Normalized $A_{eff}$ for ES-PCF structure as a function of $\Lambda$ in soft glass SF57. . . . .	158
4.26	The effect of varying $\Lambda$ on dispersion of Steiner ES-PCF designs with $6$ arms and $d/\Lambda = 0.67$ in tellurite. . . . .	160
4.27	Varying $d/\Lambda$ to see effect on dispersion for Steiner ES-PCF design with $6$ arms and $\Lambda = 0.75\mu m$ in tellurite. . . . .	161
4.28	Varying the holes diameter of the first ring to see effect on dispersion for Steiner ES-PCF design with $6$ arms, $d/\Lambda = 0.67$ and $\Lambda = 0.75\mu m$ in tellurite. . . . .	162
4.29	Varying the holes diameter of the second ring to see effect on dispersion for Steiner ES-PCF design with $6$ arms, $d/\Lambda = 0.69$ and $\Lambda = 0.75\mu m$ in tellurite. . . . .	163
4.30	Schematic of the cross section of the optimized Steiner ES-PCF structure.	163
4.31	Variation of $n_{eff}$ and $A_{eff}$ with regards to wavelength for the optimum design in tellurite, with $N_{arms} = 6$ , $\Lambda = 0.75\mu m$ , radius of the holes in $1^{st}$ , $2^{nd}$ and $3^{rd}$ rings are $0.1$ , $0.22$ and $1.2134\mu m$ , respectively. . . . .	164
4.32	Dispersion of Steiner ES-PCF in tellurite with $N_{arms} = 6$ , $\Lambda = 0.75\mu m$ , radius of the holes in $1^{st}$ , $2^{nd}$ and $3^{rd}$ rings are $0.1$ , $0.22$ and $1.2134\mu m$ , respectively. . . . .	165

4.33	Slope of dispersion of Steiner ES-PCF in tellurite with $N_{arms} = 6$ , $\Lambda = 0.75\mu m$ , radius of the holes in 1 <sup>st</sup> , 2 <sup>nd</sup> and 3 <sup>rd</sup> rings are 0.1, 0.22 and $1.2134\mu m$ , respectively. . . . .	165
4.34	Non-linearity of Steiner ES-PCF in tellurite with $N_{arms} = 6$ , $\Lambda = 0.75\mu m$ , radius of the holes in 1 <sup>st</sup> , 2 <sup>nd</sup> and 3 <sup>rd</sup> rings are 0.1, 0.22 and $1.2134\mu m$ , respectively. . . . .	166
4.35	Attenuation of tellurite material and Steiner ES-PCF with $N_{arms} = 6$ , $\Lambda = 0.75\mu m$ , radius of the holes in 1 <sup>st</sup> , 2 <sup>nd</sup> and 3 <sup>rd</sup> rings are 0.1, 0.22 and $1.2134\mu m$ , respectively. Inset is a scalable of the lower wavelength region from $1.5 - 2.3\mu m$ . . . . .	167
4.36	Steiner Chains . . . . .	169
4.37	Schematic of 7 arms Steiner ES-PCF preform . . . . .	171
4.38	Schematic of stacking inner tubes of 7 arm Steiner ES-PCF structure .	173
4.39	Schematic of stacking outer tubes of 7 arm Steiner ES-PCF structure .	174
4.40	Comparison of $n_{eff}$ and $A_{eff}$ for the ideal and Steiner ES-PCF in soft glass SF57 with $N_{arms} = 6$ , $N_{rings} = 3$ , $d/\Lambda = 0.4$ and $\Lambda = 3\mu m$ . . . .	175
4.41	Comparison of $n_{eff}$ and $A_{eff}$ for the ideal and Steiner ES-PCF in soft glass SF57 with $N_{arms} = 7$ , $N_{rings} = 3$ , $d/\Lambda = 0.4$ and $\Lambda = 3\mu m$ . . . .	176
4.42	Comparison of dispersion for the ideal and Steiner ES-PCF in soft glass SF57 with $N_{arms} = 6$ , $N_{rings} = 3$ , $d/\Lambda = 0.4$ and $\Lambda = 3\mu m$ . . . .	176
4.43	Comparison of $n_{eff}$ and $A_{eff}$ for the ideal and Steiner ES-PCF in soft glass SF57 with $N_{arms} = 6$ , $N_{rings} = 3$ , $d/\Lambda = 0.4$ and $\Lambda = 1\mu m$ . . . .	178

# List of tables

2.1	$s_k$ values in PML regions . . . . .	77
3.1	Maximum value of $d/\Lambda$ for given number of arms . . . . .	85
3.2	A comparison of structure size for different number of holes . . . . .	87
3.3	Sellmeier coefficients of silica material . . . . .	88
3.4	The values of angle $\theta$ which are divisor of $2\pi$ and should be avoided. . . . .	102
4.1	Sellmeier coefficients of SF57 material . . . . .	138
4.2	Comparison of the $\gamma$ , dispersion and dispersion slope for H-PCF, ASC and ES-PCF structures at pump wavelength of $1064nm$ . . . . .	156
4.3	Sellmeier coefficients of tellurite material . . . . .	159

# Abbreviations

AS	Archimedean Spiral
AS-PCF	Archimedean Spiral Photonic Crystal Fiber
ASaD	Adapted Stack and Draw
ASC	Air Suspended Core
EH	Hybrid mode
ES	Equiangular Spiral
ES-PCF	Equiangular Spiral Photonic Crystal Fiber
F	Fluorine
FDM	Finite Difference Method
FDTD	Finite Difference Time Domain
FEM	Finite Element Method
FS	Fermat's Spiral
FS-PCF	Fermat's Spiral Photonic Crystal Fiber
FWM	Four-Wave Mixing
GeO <sub>2</sub>	Germania
GNLSE	General Non-Linear Schrödinger Equation
GVD	Group Velocity Dispersion
H-PCF	Hexagonal Photonic Crystal Fiber
HC	Hollow-Core
HC-NCF	Hollow-Core Negative Curvature Fiber
HC-PBF	Hollow-Core Photonic Band-gap Fiber
HE	Hybird mode
IR	Infra-Red
LMA	Large Mode Area
LP	Linearly Polarized
M-TIR	Modifier Total Internal Reflection
MCVD	Modified Chemical Vapor Deposition

---

MF	Microstructured Fiber
MMF	Multimode Fiber
MoL	Method of Lines
MoM	Method of Moments
NA	Numerical Aperture
OVD	Outside Vapor Deposition
PBF	Photonic Band-gap Fiber
PBG	Photonic Band-gap
PCF	Photonic Crystal Fibers
PCVD	Plasma Chemical Vapor Deposition
PMD	Polarization Mode Dispersion
PML	Perfectly Matched Layers
SaD	Stack and Draw
SBS	Stimulated Brillouin Scattering
SCG	Supercontinuum Generation
SMF	Single Mode Fiber
SPM	Self-Phase Modulation
SRS	Stimulated Raman Scattering
TE	Transverse Electric
TEM	Transverse Electric and Magnetic
THG	Third-Harmonic Generation
TIR	Total Internal Reflection
TM	Transverse Magnetic
UV	Ultra Violet
VAD	Vapor Axial Deposition
WDM	Wavelength Division Multiplexing
XPM	Cross-Phase Modulation
ZDW	Zero Dispersion Wavelength

# Symbols

$c$	Speed of light in vacuum
$v$	Speed of light in material
$n$	Refractive index of material
$\alpha_c$	Critical angle
$NA$	Numerical Aperture
$\theta_a$	Acceptance angle
$\Delta$	Relative refractive index difference
$V$	V parameter
$\lambda$	Wavelength
$k_0$	Wave number of free space
$\beta$	Propagation constant of the mode
$n_{eff}$	Modal effective index
$b$	Normalized propagation constant
$B$	Birefringence
$N_m$	Number of modes
$\lambda_c$	Cut-off wavelength
$\alpha$	Attenuation coefficient
$D$	Dispersion
$I_0$	Intensity of light
$n_2$	Non-linear refractive index
$n_0$	Linear refractive index
$\mathbf{D}$	Electric flux density
$\epsilon$	Permittivity
$\mathbf{E}$	Electric field intensity
$\mathbf{P}$	Induced electric polarizations
$\gamma$	Non-linearity
$\Lambda$	Pitch

$d$	Diameter of holes
$A_{eff}$	Effective area
<b>H</b>	Magnetic field intensity
<b>B</b>	Magnetic flux density
$\mu$	Permeability
$\omega$	Angular frequency

# Chapter 1

## Introduction to Optical Fibers

An optical fiber is a tiny cylindrical medium in which light is launched to interact with the medium to measure different parameters, amplify signals, carry information or be used as laser. Optical fibers have improved the standard of life of human beings where they are used in a variety of fields. They are widely used in telecommunications as a media for transferring information from point to point such as transoceanic cables [1, 2] and more recently, fiber to the home [3], which enables high Internet data rates. They are used in sensing to measure physical perturbations of temperature, rotation, acoustic and/or other quantities [4], optical sensors can be used in extreme environments with high temperature, high voltage or other stress factors [5]. Moreover, optical fibers can be used for signal amplification [6], power delivery, imaging and much more.

Therefore, optical fiber technology is one of the active scientific research areas for physicists and engineers. Huge amounts of resources and funds have been implemented to improve optical fiber properties and explore new types for various purposes such as medicine, spectroscopy, sensors and telecommunications which are the primary uses of optical fibers.

In this chapter, an overview of the basics of optical fibers is presented to understand the fundamental concepts of how optical fibers operate and their properties. An explanation of the conventional optical fibers and the different types of optical fibers are introduced, also the essential laws and parameters related to optical fibers are represented starting with Snell's law. The major optical properties of optical fibers which influence system performance such as attenuation, dispersion and non-linearity are discussed. The Photonic Crystal Fibers (PCF), which are the focus of this work, are introduced. Then the guiding mechanism of different types of PCF, fabrication process and special properties of PCF are discussed.

The analysis and understanding of the optical fibers and devices requires experimental or numerical studies to be carried out. The former is time consuming and requires huge amounts of physical resources. The study in this thesis is based on numerical simulations to study a special type of PCF. The numerical method adapted is the Finite Element Method (FEM) because of its feasibility and versatility in presenting any arbitrary boundaries. The mathematical derivation of the formula used in the FEM and the procedure of implementing the method in solving electromagnetic problems is shown in Chapter 2.

This thesis presents the result of the studies of a special type of PCF coined in regards to the holes distribution as Spiral PCF. The main factors in PCF that control the propagation and properties of light are the holes position and size. A spiral is a mimic of natural shapes of various creatures and planets. These shapes have different mathematical presentations which are presented by different spirals. In this work three spirals (Equiangular, Archimedean and Fermat's spirals) are explored in the design of PCF. The objective of this work is to understand the effect of varying the different parameters of the spiral on the optical properties so that a design with the desirable properties can be made with analysis of the systematic studies presented. Furthermore, each spiral has a unique hole distribution which indicates that the spirals effect the properties differently. This would widen the implementation of spirals in different applications.

The results are divided into two parts; the first part is the general study of the effect of varying the parameters of spirals. Each spiral results are shown in a separate section in Chapter 3. The second part of the results is more in depth analysis of the Equiangular Spiral PCF (ES-PCF) design for non-linear effect, namely Supercontinuum Generation (SCG), and a propose fabrication procedure for ES-PCF that proved the adaption of Stack and Draw (SaD) technique for exotic structure is possible. The second part of the results is presented in Chapter 4.

## 1.1 Optical Fiber Technology

Conventional glass-core optical fiber technologies have improved significantly since the first successful glass fiber was made in 1957 [7]. However the era of optical fiber communications started in 1970s, when a fiber with loss less than  $20\text{dB}/\text{km}$  was launched [7]. The development of erbium-doped fiber amplifier in 1980s, reduced the cost of long distance communication because the optical signal could be amplified directly without converting it to electrical signal thus reducing the number of repeaters

[6]. Nowadays, optical fibers are one of the best communications media for long haul communications. They exhibit very low losses, immunity to electromagnetic interference and have wide bandwidth hence providing highest data rates. Optical fibers are used in undersea Internet cables which provide a robust and high speed Internet. Moreover, optical fibers and integrated optical waveguides are finding a wide range of usage in other different areas.

In optical telecommunications, the wavelength spectrum is divided into three windows; first, second and third which positioned at wavelengths  $850nm$ ,  $1300nm$  and  $1550nm$ , respectively. In the following section an explanation of basic concepts and terminologies of optical fibers is presented.

### 1.1.1 Optical fibers

An optical fiber is a cylindrical dielectric waveguide. It is constructed of a high index core in which the light propagates. The core is surrounded by a cladding which has a slightly lower refractive index than the core [8], and a coating which provides mechanical protection to the fiber from physical damage and protects the glass surface from moisture and dust particles [7, 9]. A schematic of an optical fiber is shown in Figure (1.1). The core size and the index difference between core and cladding play a major role in determining the fiber properties.

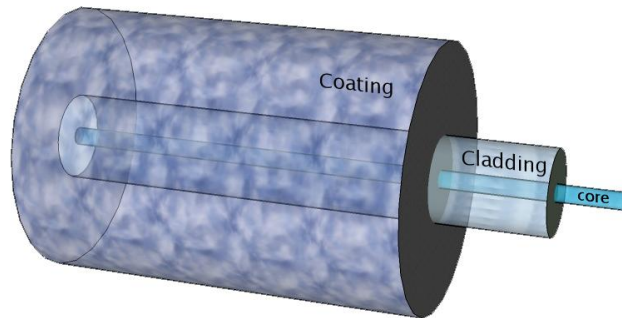


Fig. 1.1 Typical optical fiber structure

An important optical parameter of any transparent medium is the refractive index ( $n$ ) which defines the optical density of the material i.e the relative speed of light in the material ( $v$ ) compared to that in vacuum ( $c$ ) [10].

$$n = \frac{c}{v} \quad (1.1)$$

The refractive index change with wavelength is related to an important property of optical fibers, which is the broadening in pulse duration (temporal) and length (spatial)

[11]. This is known as dispersion in optical technology. Figure (1.2) shows the refractive index of the fused silica material as a function of wavelength. The change in refractive index at lower wavelengths is very sharp, leading to a high value of dispersion.

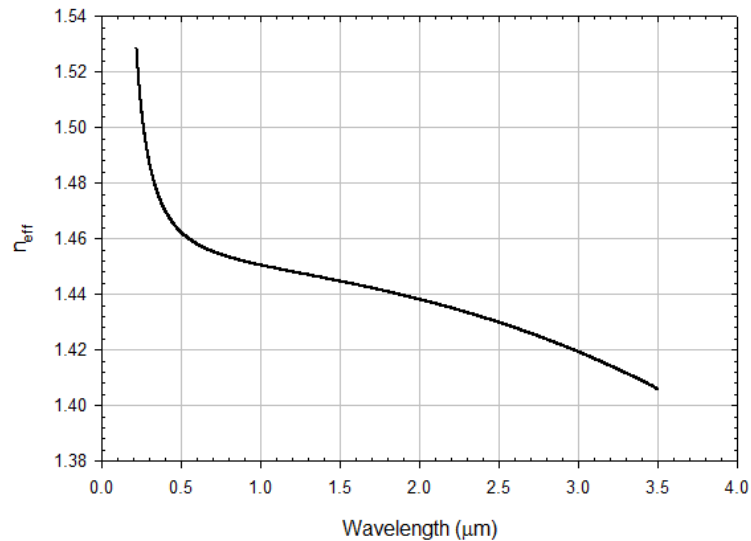


Fig. 1.2 Refractive index profile of fused silica material [12]

Figure (1.3) shows the material dispersion of fused silica. The Zero Dispersion Wavelength (ZDW) is near the second window at  $1.28\mu\text{m}$  [13]. Dispersion is discussed in more depth in Section 1.2.2.

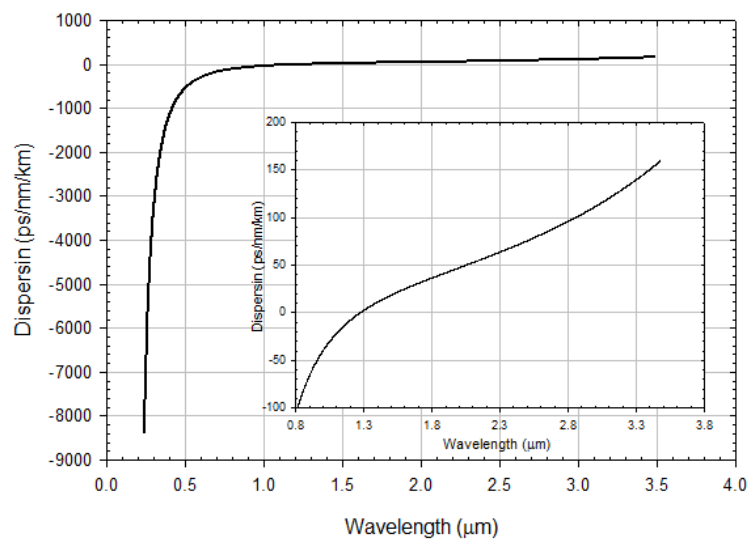


Fig. 1.3 Dispersion of fused silica material [12]

In the following subsection interaction of light as it travels between media with different index is presented.

### 1.1.2 Guiding mechanism

Snell's law gives the mathematical relation that can be used to predict the angle of refraction when a light ray travels from one medium to another [7].

$$n_1 \sin(\alpha) = n_2 \sin(\beta) \quad (1.2)$$

where  $n_1$ ,  $n_2$  are the refractive indices of the high and low density mediums respectively,  $\alpha$  is the angle of incidence and  $\beta$  is the angle of refraction or reflection.

The rays of light traveling from a medium of higher refractive index (Figure (1.4), medium 1) to a lower density medium (medium with a lower refractive index, Figure (1.4), medium 2) are either partly reflected and the rest refracted or completely reflected depending on the angle of incidence. If the angle of incidence is greater than the critical angle the rays get reflected back into medium 1 (Figure (1.4), ray 3), otherwise the rays are refracted into medium 2, the medium with the lower refractive index (Figure (1.4), ray 1). The critical angle ( $\alpha_c$ ) is the value of  $\alpha$  when  $\beta = 90^\circ$  (Figure (1.4), ray 2).

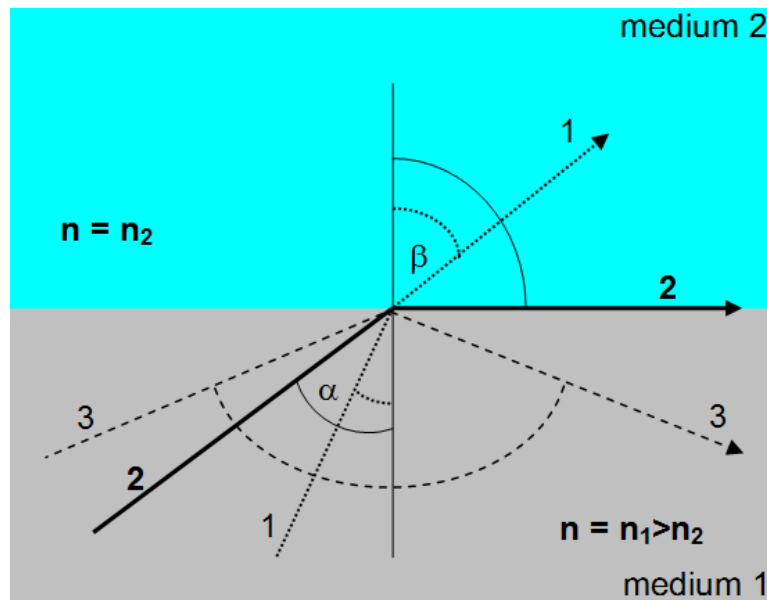


Fig. 1.4 Snell's law of refraction [14]

From Snell's law

$$n_1 \sin(\alpha) = n_2 \sin(\beta).$$

When  $\alpha = \alpha_c$

$$\beta = 90^\circ.$$

Therefore,

$$\alpha_c = \sin^{-1} \left( \frac{n_2}{n_1} \right) \quad (1.3)$$

The propagation of light in an optical fiber can be understood through the application of Snell's law. Rays of light traveling from the core to cladding hit the core/cladding interface at an angle greater than the critical angle suffer Total Internal Refraction (TIR) and travel through the core of the fiber. This happens repeatedly each time the rays hit the core-cladding interface causing light to be guided in the fiber core as shown in Figure (1.5). In contrast, all other rays are refracted and escape from the core and do not propagate in the core.

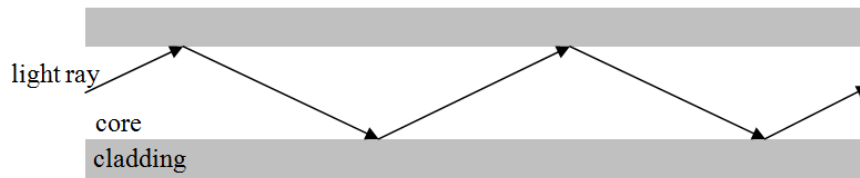


Fig. 1.5 Sketch of TIR in an optical fiber

The light launched in an optical fiber and the amount that couples and propagates in the fiber is measured by two parameters, namely Numerical Aperture ( $NA$ ) and acceptance angle, which are presented below.

The light gathering capability of an optical fiber is determined by the  $NA$  which depends on the index difference between the core and cladding.

$$NA = (n_1^2 - n_2^2)^{\frac{1}{2}} = \sin(\theta_a) \quad (1.4)$$

The optical fiber has a maximal angle, the acceptance angle ( $\theta_a$ ), at which light entering the core can propagate through the fiber. The acceptance angle and  $NA$  are important in determining the amount of light entering the fiber. These parameters are preferred to be large to gather more light.

However, the difference in refractive indices is very small and can not be varied much. The difference in refractive indices of optical fiber is measured as a ratio, known as the relative refractive index difference ( $\Delta$ ) [7]. Telecommunication optical fibers have

a typical value  $\approx 0.01$  of  $\Delta$  [15]. Furthermore, the difference in core and cladding indices is vital in determining the fiber properties.

$$\Delta = \frac{n_1^2 - n_2^2}{2n_1^2} \approx \frac{n_1 - n_2}{n_1} \quad (1.5)$$

The distribution of the field in the transverse direction is called a mode and waves can have identical modes with different frequencies in the optical fibers. The mode defines how the wave travels in the medium and the number of modes that can propagate in the core of a fiber is related to the dimensionless parameter  $V$ , which is given in Equation (1.6) [16]. The  $V$  parameter and modes are discussed in greater details in Section 1.1.4.

$$V = \frac{2\pi a}{\lambda} \sqrt{n_1^2 - n_2^2} \quad (1.6)$$

To sum up, it is a requirement for optical fibers that the core has a higher refractive index than the cladding to guide light as stated by Snell's law. Moreover, the type of optical fiber depends on core size, refractive index difference, and wavelength of operation. The fabrication process and various types of optical fibers are discussed in the following section.

### 1.1.3 Types of optical fibers and fabrication

The interaction of light with matter at high light intensity leads to a non-linear response of the material to the amplitude of the field. In this regime the light waves can interact with each other and generate optical fields at new frequencies [17]. The non-linear effects are discussed in more depth in Section 1.2.3.

In optical systems, the two major properties of concern, that limit the transmission capabilities, are the attenuation (power loss) and dispersion (pulse spreading). Both of them can have a detrimental effect in telecommunications and their values are required to be small or zero so their effect is tolerable. On the other hand, some applications require a non-zero or a larger value of dispersion for the effect to be useful. Such is the case in non-linear effects where a non-zero dispersion is required to have a significant impact on the signal. On the other hand, large values of dispersion are required in dispersion engineered fibers to compensate the dispersion of conventional telecommunication optical fibers. Therefore, the dispersion should be controlled to suite the required application. The dispersion of silica material is given in Figure (1.3) and the intrinsic losses in Figure (1.6).

Conventional telecommunication optical fibers are mostly made of fused Silica, which has a loss of less than  $0.2\text{dB}/\text{km}$  at  $1.55\mu\text{m}$  by doping either the core or the cladding

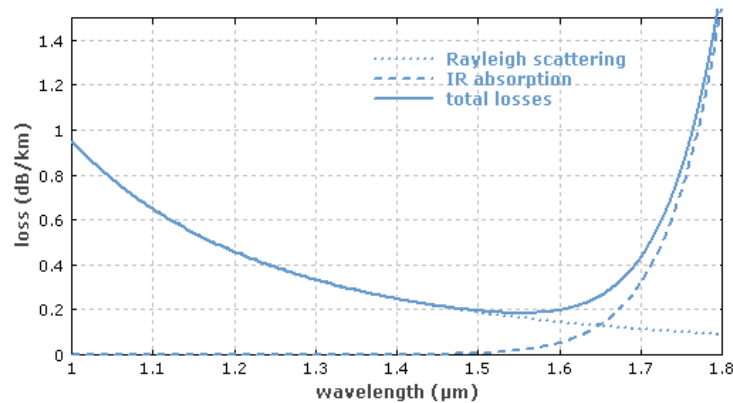


Fig. 1.6 Intrinsic silica material losses [18]

with germania ( $\text{GeO}_2$ ) or fluorine (F) respectively to create a core with higher refractive index. The core rod is fabricated by deposition of the material by one of the various methods popular in the industry: Modified Chemical Vapor Deposition (MCVD) [19, 20], Vapor Axial Deposition (VAD) [21], Outside Vapor Deposition (OVD), and Plasma Chemical Vapor Deposition (PCVD) [22]. The core rod consists of the core and part of the cladding. The overlaying cladding is typically made of lower purity silica by OVD, sol-gel casting, or plasma deposition. The core rod and cladding glass form the preform. Typical length of the preform is  $1m$  and diameter is  $10 - 50mm$ . The preform is drawn down on a drawing tower to form the final optical fiber with dimensions of  $125\mu m$  by softening the silica glass in the temperature range  $1950 - 2250^\circ C$ . Finally, the optical fiber is coated with two polymer layers [7].

There are more sophisticated designs but all of which follow the same rule to satisfy the total internal reflection phenomenon. However, there are two main types of optical fibers: Single Mode Fibers (SMF) and Multimode Fibers (MMF). Figure (1.7) illustrates the standard dimensions of these optical fibers. The core radius of SMF is much smaller than MMF.

In SMF, only the fundamental mode can propagate through the core whereas the number of modes in MMF is roughly  $(V^2/2)$  [23], so MMF suffer from intermodal dispersion. Single mode fibers have lower loss and lower dispersion than the MMF. On the other hand, MMF have higher coupling efficiency than SMF. Although SMF are more expensive than MMF in terms of fabrication, they are preferable in long distance communications because the SMF supports only the fundamental mode hence loss and dispersion is lower which leads to less amplification stages and a lower overall cost.

In the first place, an understanding of a mode is required to see the difference between optical fibers and number of modes which would propagate in the core. The mode

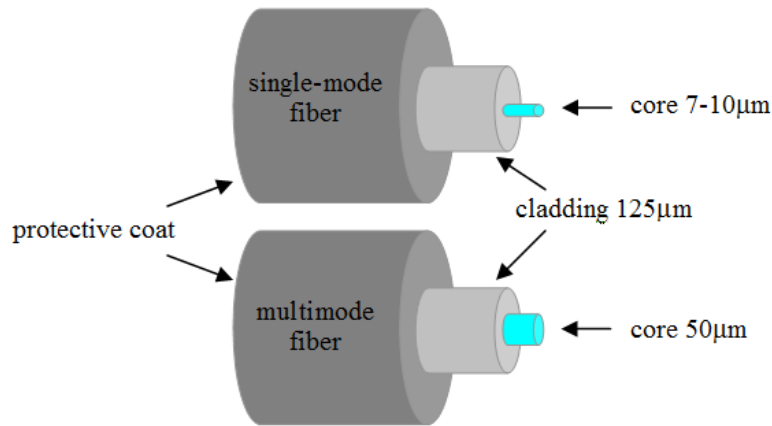


Fig. 1.7 Typical dimensions of SMF and MMF [14]

propagation condition, different types and number of modes are discussed in the following section.

#### 1.1.4 Modes in optical fiber and their properties

A mode is the distribution of the electromagnetic waves in the transverse direction. Mathematically, a mode is a solution of the Helmholtz equation which is derived from Maxwell's equations and boundary conditions [16]. The electromagnetic field variation in the material can be discussed in terms of the quantity  $-(n_i^2 k_0^2 - \beta^2)$  as shown below, where subscript  $i$  stands for media 1 (core with refractive index  $n_1$ ) or 2 (cladding with refractive index  $n_2$ ),  $\beta$  is the mode propagation constant and  $k_0$  is the wave number:

$$k_0 = \frac{2\pi}{\lambda} \quad (1.7)$$

The field variation exhibits sinusoidal behavior when  $n_i^2 k_0^2$  is greater than  $\beta^2$ . When  $n_i^2 k_0^2$  is smaller than  $\beta^2$  the field is evanescent and the variation exhibits an exponential decay [24].

In optical fibers, when  $\beta$  is greater than  $n_1 k_0$  the field is evanescent everywhere and no mode is present. On the other hand, when  $\beta$  is smaller than  $n_0 k_0$  the field oscillates everywhere and does not vanish. The latter are radiation modes and are not guided by the optical fiber. The propagation constant for guided modes falls in the range between  $n_1 k_0$  and  $n_0 k_0$  [24], where  $n_0$  is the refractive index of the air surrounding the cladding. There are two types of guided modes that are present in optical fibers. The first is cladding guided modes which are present when  $n_2 k_0 > \beta > n_0 k_0$ . The second are

core guided modes which have an effective refractive index ( $n_{eff}$ ) with a value range between the core and cladding refractive indices  $n_2 < n_{eff} < n_1$ .

$$n_{eff} = \frac{\beta}{k_0} \quad (1.8)$$

where  $\lambda$  is free space wavelength.

The fiber modes are labeled LP (Linearly Polarized) with subscript integers  $l$  and  $m$ . The  $m$  subscript corresponds to the rays which make different angles with the fiber axis and  $l$  for helicity of the ray. Rays passing through the fiber axis have  $l = 0$  [15]. Figure (1.8) shows the field profile of the modes for  $l = 0, 1, 2$  and  $m = 1, 2, 3$  combination.

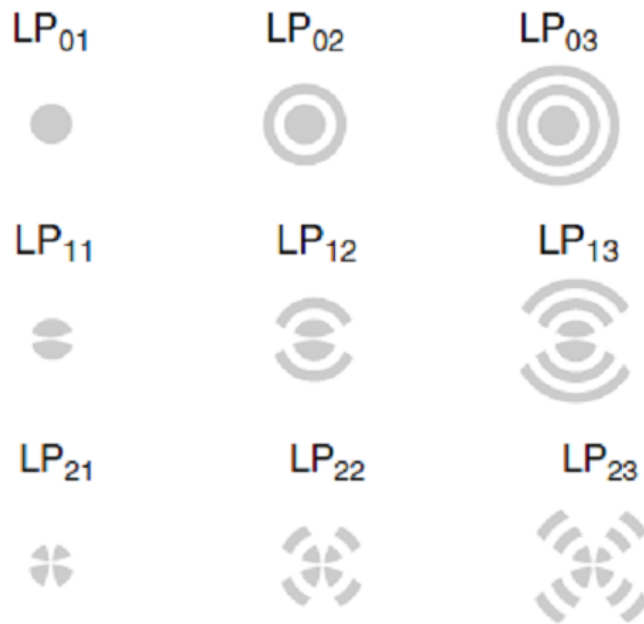


Fig. 1.8 Mode field profiles for low  $LP_{lm}$  [14]

Optical fibers which have a slight difference in refractive index between the core and cladding are considered to be weakly guiding [25]. The modes of optical fibers are not LP modes but in weakly guiding fibers the field can be approximated to LP modes. However, the modes in optical fibers are labeled  $TE_{0m}$  (Transverse Electric, i.e electric field in  $z$  direction  $E_z = 0$ ),  $TM_{0m}$  (Transverse Magnetic, i.e magnetic field in  $z$  direction  $H_z = 0$ ), and the Hybrid modes  $HE_{lm}$  ( $H_z$  and  $E_z$  have similar polarity) and  $EH_{lm}$  ( $H_z$  and  $E_z$  have opposite polarity) [26].

Each mode has a propagation constant and a field profile. The mode with highest propagation constant is known as the fundamental mode and the other modes are higher order modes, with decreasing value of propagation constant.

In a single mode fiber only the fundamental mode propagates within the core. The optical fiber has two degenerated modes (X- and Y-polarized modes) with identical propagation constant and slightly different field configurations [7], any one of which is referred to as the fundamental mode. The notation of the field can be  $E_{lm}^x$  or  $H_{lm}^x$  depending on dominant field electrical or magnetic, respectively. The  $x$  can be either  $x$  or  $y$  depending on the direction of dominant field. An  $H_{11}^x$  is fundamental mode with a dominant magnetic field in the  $x$  direction (the magnetic field amplitude in the  $x$  direction is larger than amplitude in the  $y$  direction) referred to as X-polarized.

The degeneracy between the two fundamental modes is lifted if the optical fiber symmetry is destroyed either accidentally by external stresses and bends, or intentionally like in special designs which are asymmetric for special application such as in elliptical core [27], tie-bow [28], panda [29], and photonic crystal fibers which are discussed later in this chapter. As a result the two modes will have different propagation constant and hence different effective refractive indices. The difference in the effective refractive indices between the two modes is known as Birefringence ( $B$ ).

$$B = \left| n_{eff}^x - n_{eff}^y \right| \quad (1.9)$$

where  $n_{eff}^x$  and  $n_{eff}^y$  are the refractive indices of the two degenerated modes.

The fundamental mode field profile has a Gaussian-like at best shape which is concentrated in the core. The mode field profile spreads into the cladding and decays exponentially. The percentage of the total mode that travels in the core is defined by confinement factor parameter. Higher order modes spread more in the cladding than the fundamental mode.

The number of modes a fiber can support is determined by Equation (1.10) where  $a$  is the core radius. From the formula we notice that the higher the wavelength the fewer the number of modes that can propagate in the fiber. To achieve single mode operation at a given wavelength  $a$  and  $NA$  should be sufficiently small.

$$N_m = 0.5 \left( \frac{2\pi a NA}{\lambda} \right)^2 \quad (1.10)$$

where  $N_m$  is the number of mode in the fiber

The number of modes that propagates in the fiber can be determined from Figure (1.9) by calculating normalized frequency parameter ( $V$ ) from Equation (1.6). In an SMF, the  $V$  value is less than 2.405 [15]. Furthermore, the single mode operation is wavelength dependent. A fiber only supports the fundamental mode if the wavelength of operation

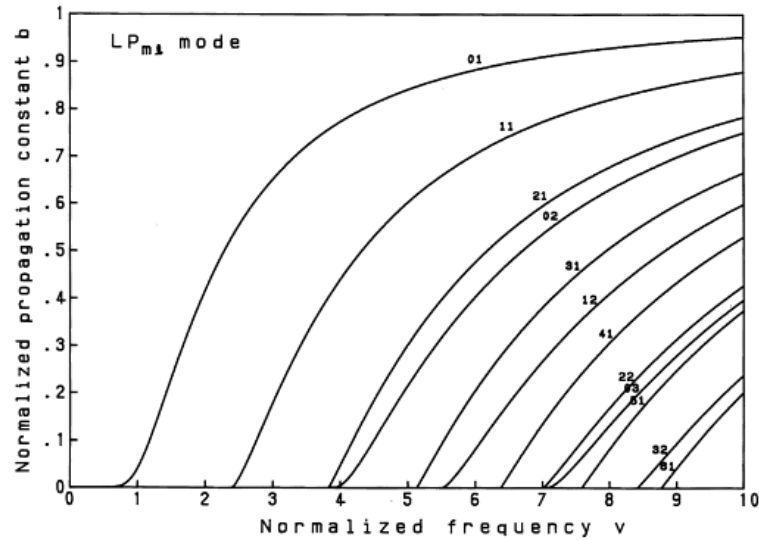


Fig. 1.9 Normalized frequency  $V$  vs normalized propagation constant  $b$  curves for LP modes in step index fiber [30]

is longer than a specific wavelength, the cut-off wavelength ( $\lambda_c$ ). Otherwise, the fiber supports higher order modes at shorter wavelengths.

$$\lambda_c = \frac{2\pi a}{2.405} \sqrt{n_1^2 - n_2^2} \quad (1.11)$$

To conclude this section, the essential laws of optical fibers have been briefly discussed. The physical properties of optical fibers have been introduced and their optical properties are explored in the next section.

## 1.2 Optical Properties of Fibers

The key optical properties which impact the performance of optical fibers are attenuation, dispersion and non-linearity. The attenuation or loss is determinant in any media or/and system as the signal vanishes as it travel through the media [31]. The loss is preferred to be as small as possible for the modes of interest. In contrast, the loss of undesirable modes is preferred to be high so those modes vanish after short distance and do not interfere with the modes of interest such is the case with higher order modes when single mode guidance is required.

Dispersion should be zero or low for some applications like in telecommunications. On the other hand, high values of dispersion is desirable in other application as in the residual dispersion compensating fiber [31]. Other use of dispersion is a non-zero anomalous dispersion for non-linear effects when a non-linear behavior is required.

These properties are more controllable in PCF than in conventional optical fibers due to the different parameters that can be manipulated to get the desired performance [32]. Therefore, it is an important aspect to understand these properties and their effects, and how they can be controlled to have optimal performance. The discussion of attenuation and dispersion is given in following subsections. Then at the end of this section a review of non-linearity which has detrimental affect at high power as a pulse is broadened leading to distortion of the signal. However, recently non-linear effects led to various applications in optical fibers such as Raman amplifiers, optical coherence tomography, high-precision frequency metrology and the most attractive application which was first observed in 2000 [13], and SCG [32].

### 1.2.1 Attenuation

Attenuation is the degradation or loss of optical power as light travels through a medium. In 1965, Kao and Hockham predicated that the fiber losses can be improved significantly because the majority of the loss is due to the impurities in the material and not an intrinsic loss of the glass, silica [15]. Kao was awarded for the Nobel Prize for his work on optical fibers in 2009 [14]. The optical loss is measured in  $(dB/km)$ . The optical losses are either intrinsic or extrinsic. The former depends on the material properties of the waveguide and the fabrication accuracy. This loss is due to the absorption and scattering of light within the medium. The latter arises due to external strains and stresses applied to the waveguide such as bends or thermal effects. Therefore, intrinsic losses can only be reduced at the time of fabrication. On the other hand, extrinsic losses can be reduced or removed after installation of the optical fibers by fixing the problem that leads to loss. The different factors that cause loss are discussed next.

#### **Absorption:**

Absorption is due to impurities trapped in the waveguide material such as metals and moisture. The total attenuation as a function of wavelength for a conventional optical fiber is shown in Figure (1.10). This graph shows the intrinsic losses: impurities result in two peaks in the total loss. The first peak is due to metals and the second large peak is as a result of the vibration of molecules which form in the fabrication process trapping  $H_2O$  molecules in the glass.

Furthermore, at short wavelengths the contribution from the Ultra Violet (UV) absorption is the leading factor. This absorption is caused by electronic transitions stimulated by higher energy excitation. Also, at higher wavelengths Infra-Red (IR) absorption dominates which is resulting from molecular vibrations within the glass [33].

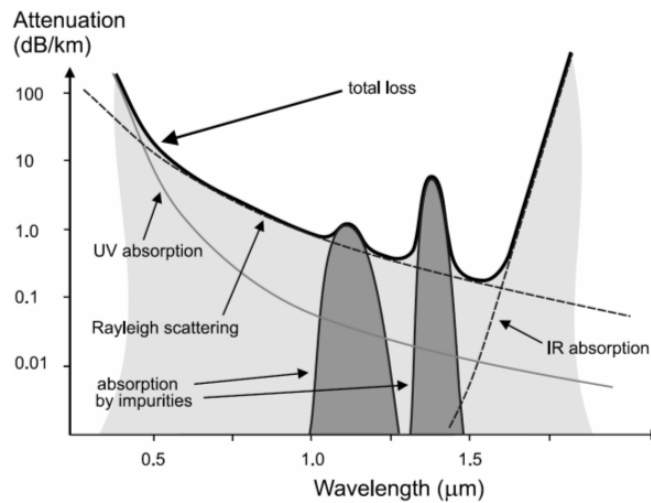


Fig. 1.10 Optical fiber attenuation [14]

The degree of absorption depends on the amount of impurities in the optical fiber and the wavelength of operation. The absorption is an intrinsic loss of the material. There is another intrinsic loss, namely scattering, which is discussed below.

#### Scattering:

Scattering is the reflection of light in all direction as it travels through a waveguide which dominates in much of the visible spectrum range and also the first and second telecommunication windows [14]. The variation of the dopants in the core effects the density and concentration of the glass leading to scattering of the light . There are two main types of scattering which are listed below. Rayleigh scattering is caused by atomic and molecular structure of the glass and inhomogeneities in glass which leads to fluctuations in refractive index that act as tiny scattering centers [34]. The inhomogeneities are regions of different composition or density which are formed naturally, in the glass during the fabrication process. They are much smaller than the wavelength [33]. The amplitude of scattering is proportional to  $\omega^4$  or to the inverse of fourth power of wavelength ( $\lambda^{-4}$ ). Therefore, shorter wavelengths (blue light) are scattered much more than longer wavelengths (red light), this effect is the reason the sky appears blue where sun light scatter due to gas molecules in air [31]. The Rayleigh scattering is negligible at wavelengths greater than  $1.6\mu m$  in comparison with IR absorption [34].

The other type is Mie scattering. It arises from imperfections in optical fiber geometry due to strain, presence of bubbles, core-cladding interface irregularities and refractive index difference through the fiber length [35]. This scattering is usually in the forward direction [35]. Mie scattering can be reduced by controlling fabrication processes [33]. A distinction between both scattering is the size of imperfection in the optical

fiber at which the light is scattered compared to the wavelength of operation. In Rayleigh scattering imperfections are smaller than wavelength of values to one tenth of the wavelength, and in Mie scattering the size is comparable or of similar size to the wavelength [35]. There are other losses which results from bends in the fiber as explained below.

### **Bending:**

Bending losses arise from bends in the optical fiber which are formed during fabrication or poor handling in the installation process. There are two types: macrobends (Figure (1.11)) and microbends (Figure (1.12)). The former is caused intentionally when fibers are bent around corners. There is no light reflected back from cladding to the core in this case. The latter are caused by tensile stress, temperature, or damage and they may conveniently be visible, also light may reflect back [33].

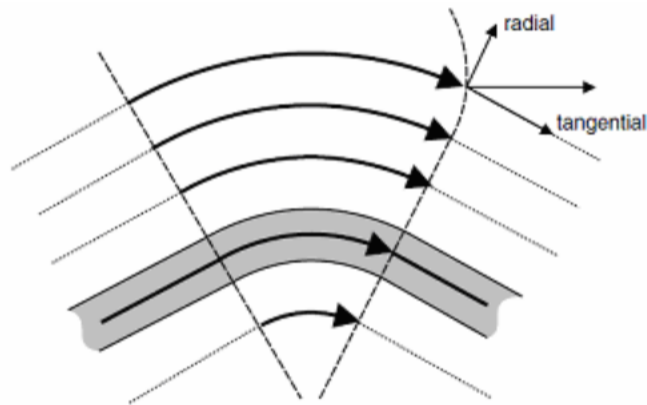


Fig. 1.11 Fiber macrobending [14]

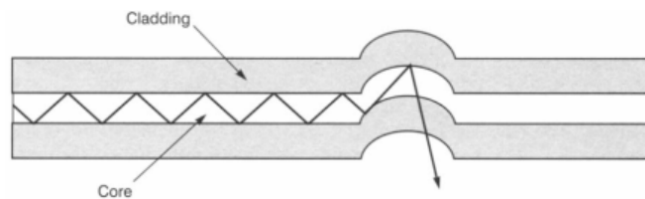


Fig. 1.12 Fiber microbending [14]

The mode in the bent fiber is calculated by transforming the bent fiber to an equivalent straight fiber by the conformal mapping process where the refractive index is modified as shown [36]

$$n' = n \left( 1 + \frac{X}{R} \right) \quad (1.12)$$

where  $X$  is the half thickness of the fiber (radius),  $n$  is the material refractive index and  $R$  is the bend radius.

When bending a fiber the outer side is expanded and the inner side is compressed leading to different speeds of the modal components to maintain its shape. The speed at the outer side increases with decreasing the bend radius to a point where the wave in the cladding would travel with a velocity greater than the speed of light in that material, which is not possible, so the mode escapes from the fiber and hence attenuation increases [37]. Multimode fibers experience higher bending loss than SMF because higher order modes spread more into the cladding region and experience more increase in their velocity and modes couple to the cladding [38].

The attenuation in optical fibers is measured in decibel per unit length. The measurement technique is to launch light with a predetermined power at one end of a sample of the fiber and measuring the output power. The attenuation coefficient ( $\alpha$ ), usually measured for optical fibers in  $dB/km$ , is calculated from Equation (1.13). Then the total loss of the fiber is the product of  $\alpha$  and the length of the fiber ( $L$ ) [15].

$$Loss(dB) = \alpha L = 10 \log_{10} \frac{P_{in}}{P_{out}} \quad (1.13)$$

The loss plays an important role in determining the signal strength at the receiver and thus the efficiency of the system. Another factor which limits the system performance is dispersion. It is considered in the next section.

### 1.2.2 Dispersion

A pulse is broadened as it propagates along the optical fiber because no light pulse is truly monochromatic. In other words, a light pulse has a non-zero spectral width which means the pulse contains different frequency components. In addition to that pulses travel partially in the core and spreads into cladding which has lower refractive index hence velocities of light is higher leading to broadening. If more than one mode is present then their velocities are different and all adds up to the broaden the pulse, this leads to inter-modal dispersion. Therefore, each component in the pulse either in core or cladding propagates with a different velocity in the medium resulting in pulse distortion. This phenomenon is termed dispersion. If a stream of pulses is launched in a fiber and the dispersion is large enough then the pulses will overlap, see Figure (1.13). The effect of dispersion is not desirable in some applications such as telecommunication. However, currently dispersion plays an important role in many applications where dispersion is essential to achieve unique results.

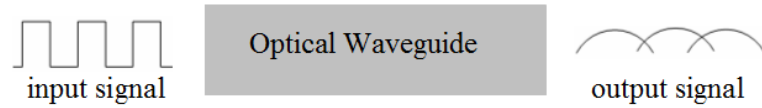


Fig. 1.13 Schematic of effect of dispersion on the signal

In non-linear effects, which are discussed in Section 1.2.3, an anomalous flattened dispersion with zero dispersion near the pump wavelength is desirable to achieve higher non-linear effects. Furthermore, the effective area needs to be small in non-linear applications. The control of both variables in conventional fibers is limited. Luckily, the PCF overcome these limitation and both parameters can be manipulated simultaneously. The dispersion arises from different factors and to control the dispersion an understanding of these factors required. These factors are listed below.

#### **Material Dispersion:**

Material dispersion is an intrinsic property of the material because the refractive index of the material is wavelength dependent [30]. Each spectral component of a light pulse, which is a superposition of different frequencies centered on the frequency of the modulated source, propagates at different speeds. It is a measure for the bulk material and not the waveguide. The material dispersion is the second derivative of refractive index with respect to wavelength. Equation (1.14) shows this relation [14, 26].

$$D_m = -\frac{\lambda}{c} \frac{d^2 n}{d\lambda^2} \quad (1.14)$$

#### **Waveguide Dispersion:**

Waveguide dispersion is dependent on the structure of the waveguide. The light propagation in the core is different from that in the cladding leading to pulse spreading with the effect of the material dispersion. Waveguide dispersion can be utilized to compensate the material dispersion in dispersion compensating fibers and zero dispersion shifted fibers. The waveguide dispersion is calculated by formula [14, 26]:

$$D_w = -\Delta \frac{n}{\lambda_c} V \frac{d^2(Vb)}{dV^2} \quad (1.15)$$

The material and waveguide dispersion combined together yield the chromatic dispersion for the fiber (total dispersion) Figure (1.14) [30]. This dispersion is positive when shorter wavelengths propagate faster than longer wavelengths, or negative which is opposite to the above [39].

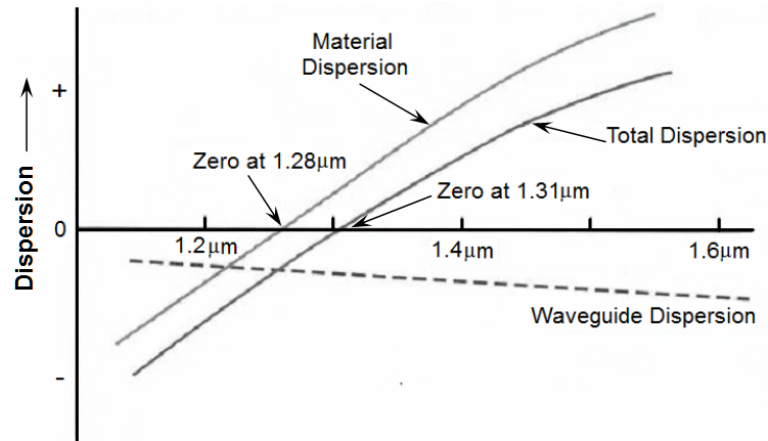


Fig. 1.14 Dispersion of typical single mode optical fibers [40]

The total dispersion is denoted  $D$  and for SMF is the chromatic dispersion which is the sum of the material and waveguide dispersions.

$$D = D_m + D_w \quad (1.16)$$

The dispersion is anomalous if  $D$  is positive, where the change in effective refractive index increases with increasing wavelength. On the other hand, if the change in effective refractive index decreases with increasing wavelength ( $D$  is negative) the dispersion is termed as normal.

#### **Inter-modal Dispersion:**

Different modes in the waveguide are associated with different propagation constant values leading to different propagation velocities. This type of dispersion exists in MMF because various modes propagate within the core and arrive at the output at different times. In MMF, Inter-modal dispersion is the dominant effect and chromatic dispersion is relatively small, therefore it can be neglected [26].

In MMF there are several modes and even if the fiber is long the separation between generated pulses is small and the result is a broadened output pulse [26].

#### **Polarization Mode Dispersion (PMD):**

Optical fibers have an anisotropic perturbation due to variation in refractive index, which results at fabrication or/and due to stress and bends in the fiber. Therefore, optical fibers do not have a perfectly rotational symmetry which results in the degeneracy between the two fundamental modes being lifted and this leads to dispersion between these two modes [41, 42]. This type of dispersion effect was neglected in calculations. However, today requirements of higher data rates and compensation of other dispersions, lead to consideration of this dispersion [35]. One way tested on

conventional fibers for reducing unwanted polarization effect is to rotate the preform during the drawing process, this is known as fiber spinning. This process reduces the PMD [37].

There are different factors that would impact the dispersion such as choosing the right operating wavelength. The transmitter choice is an important factor in controlling the input pulse width and hence the dispersion. Laser has a narrow width while LEDs have a wide frequency spectrum [33]. The optical fiber plays an important role in producing the desirable dispersion. The dispersion is controlled for the application of interest with high or low values and its variation with wavelength. In the next chapter the dispersion is discussed further in relation to the result obtained for this thesis.

The two properties that affect the system performance at low power intensity have been considered in the preceding sections. However, at high power intensity loss and dispersion still have vital impact but there are other effects which influence optical fiber. They are the non-linear effects which are summarized in the next section.

### 1.2.3 Non-linearity

The non-linearity has a positive impact on the implementation of optical fiber in different fields. The non-linear effects are more observed in optical fibers and with the advance in optical fiber fabrication techniques and material side point of view, has made them an interesting media for generation of non-linear effects, in industry and research fields. Non-linearity can however also have a negative impact on the performance of optical fibers in telecommunication [43]. The basic concepts of non-linearity are discussed first, followed by the major types of non-linear effects in optical fibers.

In the linear regime, when the intensity of light is low, the refractive index of the material is independent of the intensity of light and the optical response of the material is linear to light intensity. On the contrary, at high intensity the optical properties of the media vary as the light intensity changes. The material responds in a non-linear manner to the intensity where the refractive index becomes a function of light intensity as shown in Equation (1.17) and the optical properties of the material are altered. [16, 17].

$$n = n_0 + I_0 n_2 \quad (1.17)$$

where  $n_0$  is the linear refractive index,  $n_2$  is the non-linear refractive index coefficient of the medium and  $I_0$  is the light intensity.

Therefore, the non-linearity is the dependence of the change in optical properties of the material on the intensity of light launched. Non-linearity is mainly due to the

conversion of power from one wavelength to another. Before digging deeper into non-linear effects the intensity of light should be defined to understand the general concept why optical fibers are more powerful in studying non-linear effects.

The optical intensity is the power divided by the area in which the field is distributed, or the power per unit area. The efficiency of non-linear effect is the product of intensity of light and effective length of the media that the light travels through ( $L_{eff}$ ). In bulk materials the intensity of light is focused to a spot of radius ( $\sigma$ ) is given by Equation (1.18) [32]. The intensity increases with decreasing the focal radius, though the effective length decreases as radius decreases as can be seen from Equation (1.19) [32].

$$I_0 = \frac{P_0}{\pi\sigma^2} \quad (1.18)$$

where  $P_0$  is the incident optical power.

$$L_{eff} = \frac{\pi\sigma^2}{\lambda} \quad (1.19)$$

Therefore, the non-linearity efficiency in bulk material is given by Equation (1.20). It is observed that non-linearity is proportional to the incident power at given wavelength and as a result, to increase the non-linear effect in bulk material, the incident power has to be increased.

$$(I_0L_{eff})_{bulk} = \left(\frac{P_0}{\pi\sigma^2}\right) \frac{\pi\sigma^2}{\lambda} = \frac{P_0}{\lambda} \quad (1.20)$$

On the other hand, the effective length in optical fiber is limited by loss coefficient ( $\alpha$ ) because the spot-size ( $\sigma$ ) can be maintained through the entire length of the optical fiber. The intensity across the length is defined as in the Equation (1.21) [32], and  $I_0$  is defined as in Equation (1.18), where  $P_0$  is the power coupled into the optical fiber.

$$I(z) = I_0 \exp(-\alpha z) \quad (1.21)$$

The efficiency of non-linearity in optical fiber is

$$(I_0L_{eff})_{fiber} = \int_0^L I(z) \exp(-\alpha z) dz = \frac{P_0}{\pi\sigma^2\alpha} [1 - \exp(-\alpha L)] \quad (1.22)$$

For long fiber non-linear effects can be enhanced by a factor of

$$\frac{(I_0 L_{eff})_{fiber}}{(I_0 L_{eff})_{bulk}} = \frac{\lambda}{\pi \sigma^2 \alpha} \quad (1.23)$$

From the above discussion it is clear that the effects of non-linearity are much higher in optical fibers than in their bulk material counter part, as the field is confined in the core for long distances. Therefore, non-linearity is of high importance in optical fibers where non-linear effects have enhanced significantly, as a consequence optical fibers are finding new applications such as Raman amplifiers, frequency generation [44], optical parametric oscillator [45] and SCG [13]. However, conventional optical fibers still lag behind compared to PCF because the two factors that impact non-linearity are dispersion and the mode area, which can be controlled more efficiently in PCF.

In silica fibers the enhancement factor is  $10^7$  in the visible region and up to  $10^9$  in the second telecommunication window where loss is minimum. However, the non-linear effects are weak in a short span of silica based fibers. The non-linear coefficient of silica glass is in the range of  $2.2 - 3.4 \times 10^{-20} \text{ m}^2/\text{W}$  [32] depending on composition. Most non-linear materials have a value of  $n_2$  higher than silica by 2 orders of magnitude. Therefore, highly non-linear materials are used for applications that require short length fibers [32].

The non-linear effects in optical fibers are observed by launching short pulses with high powers. The pulse propagation in a non-linear material, i.e. optical fiber, requires to solve Maxwell's equations given in Chapter 2 with a modification in the constitutive relation to include the non-linearity term. The equation is rewritten as

$$\mathbf{D} = \epsilon \mathbf{E} + \mathbf{P} \quad (1.24)$$

where  $\mathbf{E}$  is electric field intensity,  $\mathbf{D}$  is electric flux density, ( $\epsilon$ ) is permittivity and  $\mathbf{P}$  is the induced electric polarization which is defined as [39, 46]

$$\mathbf{P} = \epsilon_0 \left( \chi^{(1)} \cdot \mathbf{E} + \chi^{(2)} : \mathbf{E}\mathbf{E} + \chi^{(3)} : \mathbf{E}\mathbf{E}\mathbf{E} + \dots \right) \quad (1.25)$$

where  $\chi^{(1)}$  is the linear susceptibility and has the dominant effect on  $\mathbf{P}$ . Its effects are included through refractive index and attenuation coefficient.  $\chi^{(2)}$  is the second-order susceptibility and is responsible for non-linear effects such as second-harmonic generation and sum-frequency generation. The value of  $\chi^{(2)}$  is zero for materials that have symmetry for example, molecules such as silica [30, 39]. And  $\chi^{(3)}$  third-order susceptibility is responsible for Third-Harmonic Generation (THG), Four-Wave Mixing

(FWM) and non-linear refraction. Non-linear phenomena which result in the generation of new frequencies require phase matching, otherwise their effect is not efficient in optical fibers [39]. The phase matching is the process of choosing the polarizations and directions in order to eliminate the wave vector mismatch [47]. The non-linear processes in optical fibers should be represented in a mathematical formula to study their effects. The procedure to derive the formula for pulse propagation in non-linear dispersive media in slow varying envelope is to start with Maxwell's equations and apply the slowly varying envelope approximation to obtain the General Non-linear Schrödinger Equation (GNLSE) [39].

$$\begin{aligned} \frac{\partial A}{\partial z} + \frac{\alpha}{2}A + \frac{i\beta_2}{2} \frac{\partial^2 A}{\partial T^2} - \frac{\beta_3}{6} \frac{\partial^3 A}{\partial T^3} \\ = i\gamma \left( |A|^2 A + \frac{i}{\omega_0} \frac{\partial}{\partial T} (|A|^2 A) - T_{RA} \frac{\partial |A|^2}{\partial T} \right) \end{aligned} \quad (1.26)$$

where  $A$  is the envelope,  $T_R$  is Raman response function,  $\beta_2$  and  $\beta_3$  are dispersion coefficients, and  $T = t - \beta_1 z$ . The left-hand side of the equation models the propagation of the linear effect and the right-hand side models the non-linear part [48].

There are five major types of non-linear effects that can be stimulated in optical fibers; Self-Phase Modulation (SPM), Cross-Phase Modulation (XPM), FWM, Stimulated Brillouin Scattering (SBS) and Stimulated Raman Scattering (SRS). The first three arise from the Kerr effect and the last two from stimulated inelastic scattering [31]. The non-linear effects are discussed below.

#### **Self-Phase Modulation:**

The phase modulation of a pulse is due to the inhomogeneous phase velocity of the pulse components [49]. The light beam changes the refractive index of the medium and the phase of the light beam changes with refractive index thus the signal changes its own phase, which is termed Self-Phase Modulation. In 1967, SPM was first observed in  $CS_2$  liquid by Shimizu [39, 50]. The study of SPM in optical fibers was first carried in a fiber filled with  $CS_2$  in 1974 [51] and the study of SPM in silica optical fibers started in 1978 [39, 50, 52].

When a pulse propagates in an optical fiber, the intensity at the center of the pulse is higher than at the edges, leading to an increase in refractive index at the center and the center of the pulse would slow down. This will lead to an increase in the separation of waves in the leading edge and compression in trailing edge see Figure (1.15). The resulting pulse is called a chirped pulse. The chirped pulse has a larger frequency

bandwidth thus the pulse spectrum is broadened because different frequencies travel with different speeds [16].

The pulse phase and amplitude change with distance due to the SPM effect. The phase change in optical field due to SPM is given by

$$\phi = (n_0 + n_2 I) k_0 L \quad (1.27)$$

where  $L$  is the length of the fiber, and non-linear phase change given as

$$\phi_{NL} = n_2 k_0 L I \quad (1.28)$$

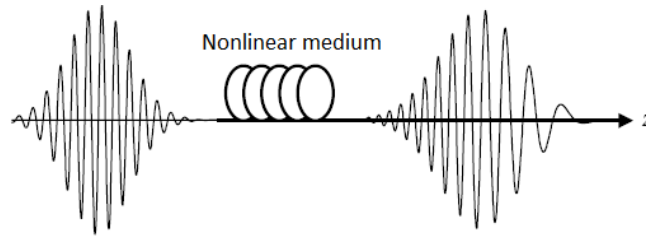


Fig. 1.15 Chirped pulse [16]

The dispersion can be compensated with the implementation of the non-linear effects. Then a pulse can propagate without broadening. If pulses propagate in the anomalous dispersion region, the SPM counteracts the broadening due to induced dispersion, this generates pulses which do not change their shape as they travel in the fiber; these types of pulses are solitons [16, 53]. Solitons are formed under certain conditions of pulse shape and peak power. The relation between pulse shape and peak power  $P_0$  is given by Equation (1.29).

$$P_0 \approx 1.55 \frac{\lambda_0^2 |D|}{\pi c \gamma \tau_f^2} \quad (1.29)$$

where  $\lambda_0$  is the wavelength of the soliton,  $D$  is the dispersion of the fiber, and  $\tau_f$  is the full width at half maximum of the soliton pulse.

If only the linear effect of dispersion is considered for a pulse propagating in the anomalous dispersion regime, where the higher frequencies travel faster than lower ones, then the output pulse at the end of the optical fiber is chirped as shown in Figure (1.16) (b). On the other hand, if considering a pulse propagating under non-linear Kerr effect, the pulse will have higher frequency at trailing edge and lower frequency at leading edge as shown in Figure (1.16) (c). The two effects change the frequency of the pulse at opposite position; this results in both effects balancing each other. This

is how solitons are formed. Solitons are used in optical telecommunication systems because they propagate for long distance without broadening. However, the pulse power decreases as it propagates through the fiber and therefore the non-linear effects will decrease. To overcome this problem amplifiers are used to amplify the signal [16].

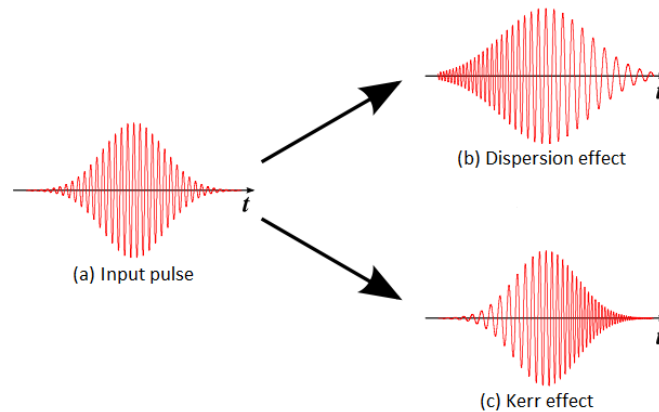


Fig. 1.16 Solitons - Linear and non-linear effects on pulses (a) is input pulse, (b) a pulse propagate in dispersive media where leading edge of the pulse is compressed and trailing edge is expanded, and (c) a pulse propagates under Kerr non-linear effect and pulse is compressed in the trailing edge and expanded in the leading edge of the pulse [54].

### Cross-Phase Modulation:

In an optical fiber, if more than one pulse propagates at the same time at different wavelengths, each pulse will result in a change in the refractive index of the material, which leads to impact other pulses. This effect is Cross-Phase Modulation. If temporal overlap of the signals occurs, the impact of the XPM on the signals is strong. Therefore, it is better to operate at non-zero dispersion wavelength because at low dispersion regime the signals do no overlap [16]. The implementation of XPM is in pulse compression and optical switching [32]. One of the advantages of XPM is on SCG in optical fibers. In the formation process of SCG different phenomena lead to broadening of the spectrum such as Raman effect and generation of dispersive waves. These have widely separated spectra but when an overlap occurs in the time domain the XPM effect takes place and the dispersive wave spectrum would increase which in turn broaden the SCG in the short wavelengths side of input pulse [46]. The drawback of XPM is in the implementation of Wavelength Division Multiplexing (WDM) as multiple signals travel in the fiber each will affect the spectrum of the other signal [16].

In both SPM and XPM, the frequency chirp induced on pulses can be used for pulse compression. Anyhow, for SPM the pulse intensity and energy should be high, whereas

XPM can compress weak input pulses because the chirping is induced by the pump pulse which can have intense power [32].

#### Four-Wave Mixing:

When three pulses travel at adjacent equally spaced frequencies ( $f_1, f_2$  and  $f_3$ ) for a long distance then these waves mix and generate a new wave at a different frequency ( $f_4$ ) as shown in Figure (1.17). This effect is FWM [31].

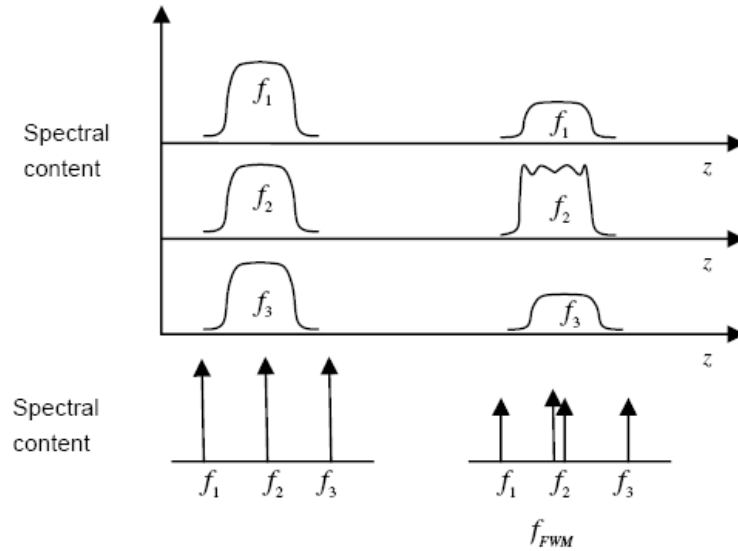


Fig. 1.17 Four-wave mixing [31]

$$f_4 = f_1 + f_2 - f_3 \quad (1.30)$$

There are two types of FWM; one that generates a photon from three photons as explained above. The phase matching condition for this type is hard to be achieved in optical fibers. The second type is when two photon are annihilated and two new photons are produced at different frequencies [39]. The phase matching condition is  $\Delta k = 0$  which is  $\Delta k = \beta_1 + \beta_2 - \beta_3 - \beta_4$ .

$$f_4 + f_3 = f_1 + f_2 \quad (1.31)$$

In the special case of  $f_1 = f_2$  this will generate two sidebands located symmetrically at frequencies  $f_3$  and  $f_4$  from one pump wave. Physically, this case appears in a similar way to SRS [39].

The efficiency of FWM depends on phase matching [30]. Therefore, the operating wavelength should be near the zero dispersion wavelength, because different wavelengths only travel with same velocity when the optical fiber dispersion is close to

zero. Four-wave mixing can be employed to generate new frequencies [55] for different applications; wavelength conversion, high-speed time-division multiplexing, and pulse compression [16]. However, FWM leads to cross-talk in WDM which results in system degradation [56]. To eliminate the effect of FWM, the operating wavelength should have a nonzero dispersion similar to the case of XPM. The dispersion should be increased as the channel frequency spacing is decreased [16].

#### Stimulated Raman Scattering:

Stimulated Raman scattering is an example of photon-phonon interaction, where a photon (with an energy  $hf_1$ ) is absorbed by a molecule leading to the transfer of the molecule from initial energy state ( $E_I$ ) to higher energy state ( $E_R$ ). Thereafter the molecule decays to a lower energy state ( $E_F$ ) and emits a photon with an energy ( $hf_2$ ) lower than the incident photon energy, i.e the light will be red-shifted. The difference in energy of the two photons is the energy of the produced phonon [31].

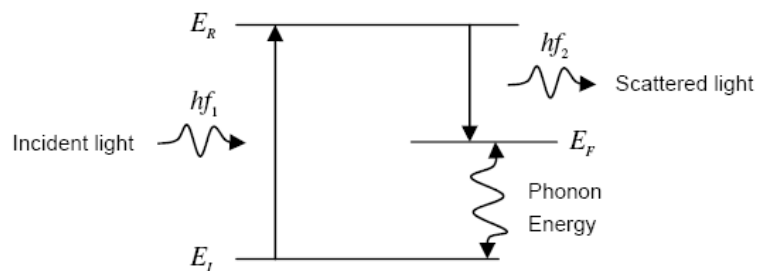


Fig. 1.18 Stimulated Raman scattering [31]

Stimulated Raman Scattering leads to transfer of energy from shorter wavelengths to longer wavelengths, which has negative impact on signals in WDM system [31]. On the other hand, SRS process can be useful in producing Raman lasers [57–59] and Raman amplifiers [60–62] from optical fibers. Raman lasers can be tuned over a wide frequency range of  $\sim 10THz$ . Raman amplifiers offer the advantage of using the same optical fiber as an amplifier by pumping a strong wave to amplify the weak signal [32].

#### Stimulated Brillouin Scattering:

The increase in the power of the pumped wave beyond the Brillouin threshold leads to generation of acoustic waves which in turn modulate the refractive index of the medium. A new wave is generated in the direction of propagation opposite to the direction of the incident wave and carries most of the input power see Figure (1.19). Therefore, their effect has detrimental impact on communication systems where it limits channel power. Moreover the peak power of the generated pulse can exceed the input power of input pulse which may result in fiber damage [39]. This is a limiting factor in delivery of high power and fiber laser applications. The power level at which SBS occurs is much

lower than level for SRS. However, when the pulse width is narrow (width  $< 1\text{ns}$ ) SBS hardly occurs [39]. Stimulated Brillouin Scattering is the interaction of a light wave with acoustic waves and it results in high attenuation which increases with an increase in the input power [31, 32]. Similar to SRS, the SBS can be useful in making Brillouin amplifiers, lasers and sensors. The pump and injected signal in Brillouin amplifiers must propagate in opposite directions [32].

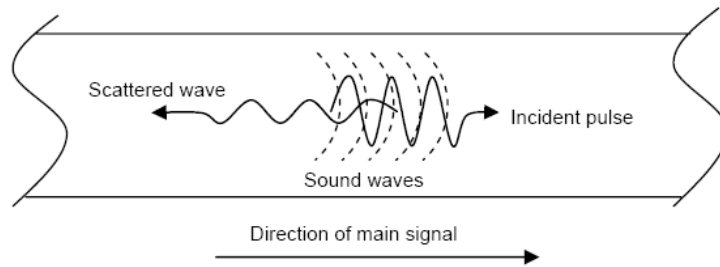


Fig. 1.19 Stimulated Brillouin scattering [31]

The main difference between SRS and SBS is that optical phonons participate in SRS while acoustic phonons participate in SBS. Another fundamental difference between stimulated inelastic scattering in optical fiber is that SBS only occurs in the backward direction when it occurs in SMF, whereas SRS occurs in both directions [32].

#### **SuperContinuum Generation:**

Supercontinuum generation is a phenomenon in which an ultrashort pulses undergoes extreme spectral broadening resulting in a broadband spectrally continuous output due to non-linearity. The spectrum is broadened by a factor of more than 200 times in less than  $1\text{m}$  fiber length [32]. The broadened spectrum very often is white light. It was first reported in 1970 by Alfano and Shapiro in bulk BK7 glass with a spectrum from 400 to 700nm [63, 64]. Similar results were published independently in the same year [65]. Although, there were reports of non-linear spectral broadening before Alfano [49, 66–68], his experiment was distinguished due to the spectral width which was 10 times wider than all previously published results [48]. The generation of SC in bulk material is a complex process as the spatial and temporal effects require a complicated coupling. However, SCG in optical fiber requires only temporal dynamical processes. One of the advantage of studying SCG in optical fibers is understanding the temporal non-linear effect which will help in understanding the picture of SCG in bulk material [48].

The first observation of SCG in optical fiber was in an experiment in 1976. A high power pulse in visible region was injected in standard silica fiber which has zero Group Velocity Dispersion (GVD) at  $1.3\mu\text{m}$ . The broadened spectrum was from the mutual

interaction of SRS and SPM [60]. Similar results were obtained in other experiments which used visible pulses in the range  $10ps - 10ns$ . These experiments clarified the importance of the mutual interaction between SRS and SPM [69], role of XPM [70] and FWM [71].

Numerical studies have proven that SCG occurs in three stages; initial spectral broadening and temporal compression, then fission into a series of distinct fundamental soliton components, and the propagation of solitons. The last stage leads to continuous shift to longer wavelengths due to Raman effect and for short wavelengths the dispersive waves are generated [48]. The emergence of PCF has had a significant impact on SCG. The possibility to shift the ZDW to shorter wavelengths [72] and reducing effective area of the mode would improve the Kerr effect [73].

It is reported that SCG is generated in SMF due to SRS where the spectrum broadens to longer wavelengths. The FWM broadens the spectrum in both directions leading to wider SCG [74]. The combination of these two properties were demonstrated in 2000, by Ranka et al., in SCG spanning over one octave by launching  $100fs$  nano-joule energy pulse at  $770nm$  in a  $75cm$  PCF with ZDW in the region  $765 - 775nm$  [13]. These broad spectra were generated in bulk material but with higher energy pulse and complex sources. An additional advantage of PCF in SCG is the single-mode guidance which results in a uniform spatial SCG profile. In 2000, an experiment on  $9cm$  tapered standard optical fiber of radius  $2\mu m$  generated octaves spanning spectra comparable to PCF [75]. This experiment is one of the crucial steps in understanding SCG in PCF. The combination of SRS and FWM effects on SCG were observed in  $10m$  of PCF injected with  $40nJ$  pulse of  $60ps$  width, the SC spectrum  $400 - 1000nm$  [76]. The first reported use of the GNLSE was in this work. The dominant linear effects participate in SCG spectral broadening in PCF are similar to conventional fibers, where the Raman effect and soliton fission are responsible for long wavelengths and dispersive waves generate short wavelengths component [48]. This is an overview of the milestones in the progress of SCG in the field. Further discussion of SCG is given (in relevant section) with the results of this work in Chapter 4.

To conclude, the optical properties are interconnected where a change in one property may lead to manipulation of other properties. For example, even though dispersion increases the bit error rate in channels, a small dispersion value at high intensity powers is still desirable to either reduce or increase the different non-linear effects depending on the applications. Therefore, a complete study of the problem requires to take into account the different factors and properties that may get altered. In conventional optical fibers the index difference that can be produced is limited due to the nature of their design as not much more can be done and the properties of optical fibers

cannot improve significantly to suit the different applications and demand of the evolving technologies. Therefore, other means of obtaining desired properties are sought. Photonic crystal fibers offer more flexibility in their design parameters to produce the required characteristic for the application of interest such as controllable dispersion, desirable spatial field profile distribution, high degree of field confinement [77] and much more. The next section presents a discussion on PCF.

## 1.3 Photonic Crystal Fibers

Photonic Crystal fibers have periodic microstructured index profile in the transverse direction [78]. They share similarities with conventional optical fibers with respect to guidance (the basic mechanism is TIR) however unlike the latter PCF have properties that depend on the wavelength more strongly. Their properties can be manipulated to suit the desired application where they have more design parameter flexibility that can be controlled. They can exhibit single mode guidance over a broad wavelength range [79, 80], low or high non-linearity [31] and controllable dispersion [72, 81]. Photonic crystal fiber designs include Large Mode Area (LMA) [82], hollow core [83], multicore fibers [84] and can show high birefringence [85]. All this is possible with the advance in the fabrication process that PCF can be manufactured with accuracies of  $10nm$  on scale of  $1\mu m$  so the key properties can be controlled remarkably well [78].

These fibers are also known as Microstructured Fibers (MF) [77, 86] or PCF [15, 77, 86], in this thesis the latter convention is used to refer to the general classification of these fibers. Photonic crystal fibers were first invented in the seventies but only in the nineties they have found more interest as fabrication technologies have improved [87]. Recently, PCFs attract more and more attention of scientists and technologists as they have several applications. A good starting point is to briefly mention the milestones and developments in the field of PCF. An overview of this is given in the following section.

### 1.3.1 Brief history of photonic crystal fibers

Before the development of modern silica fiber technology, capillaries were investigated as a candidate for optical telecommunications in the 1960s [74, 88]. In the 1970's at Bell Laboratories, Kaiser reported the fabrication of microstructured air-silica optical fibers [87]. Philip Russell reported the first working example of a solid core PCF in 1996 [79, 87], even though the concept of PCF goes back to 1991 [89]. The light guiding mechanism of solid core PCF, high-index guiding, is similar to conventional

fibers where light is guided by Modified-TIR (M-TIR). One of the most remarkable application of PCF was the SCG reported in 2000 [13].

The concept of hollow-core Bragg fibers was proposed in the mid 1970s [78, 90]. A solid core Bragg fiber was made in 2000 [78]. Worldwide research followed the discovery of Photonic Band-Gap (PBG) concept in 1987 by Sajeev John [91] and Eli Yablonovitch [92]. The creation of a band-gap was announced in 1989 by Eli Yablonovitch [93] and in the same paper the name photonic crystal was introduced [94]. The first photonic crystal material was fabricated by drilling holes in a material in 1991 [95]. In the same year, Russell proposed a fiber that can guide light in a Hollow-Core (HC) by forming a 2D photonic crystal in the cladding [95]. The first air-guiding Hollow-Core Photonic Band-gap Fiber (HC-PBF) was fabricated in 1999 [83]. An interesting fiber design was developed in 2002 with a similar concept to a HC-PBF but with a different guiding mechanism. The light was confined to the core with anti-resonant effect [96]. Antiresonance has been known to enable the confinement of light in a media with a refractive index lower than the surroundings [97]. The design has holes arranged in a Kagome lattice in the cladding region [98]. A novel type of fiber with negative curvatures in the core boundaries was proposed in 2010 where the light is confined to a core of lower refractive index than cladding in similar concept to Kagome [99]. The name coined for this type of fiber is Hollow-Core Negative Curvature Fibers (HC-NCF). There are numerous designs of PCF, and it would not be possible to introduce them all here. However, the guiding mechanism of other PCF would fall in one of these categories. In the next section the optical fibers classification is given.

### 1.3.2 Types of photonic crystal fibers

The design of PCF is different from conventional silica fibers, where they can be made of a single material with two dimensional photonic crystals or periodic lattices of air holes parallel to the fiber axis to produce a form of cladding and core [78]. A few types of PCFs are shown in Figure (1.20); *a.* fiber with a pure silica core surrounded by air-holes in the cladding. *b.* air-guiding fiber in which light is confined to a hollow core by band-gap effect. *c.* core is made of pure silica while the holes in the cladding are filled with a high index liquid. *d.* hollow cylindrical multilayer fiber with an all solid cladding, Bragg fiber.

Photonic crystal fibers can be classified into two main categories according to the light propagation mechanism; high-index guiding fibers in which light propagation satisfies M-TIR [100] in a similar manner to conventional fibers. These are referred to as PCF.

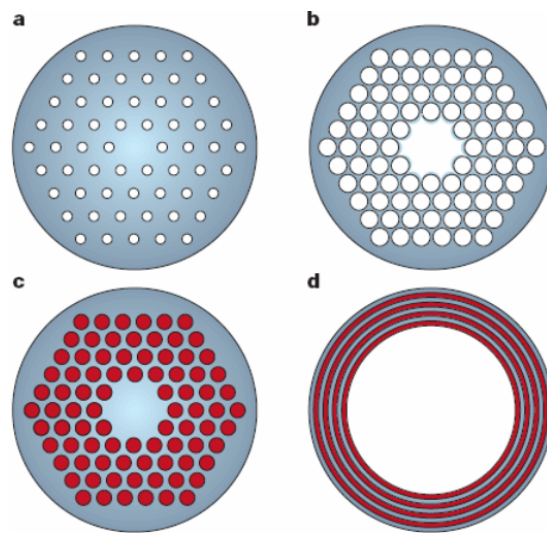


Fig. 1.20 Different designs of PCF (a) fiber with a pure silica core surrounded by air-holes in the cladding, (b) air-guiding fiber in which light is confined to a hollow core by band-gap effect, (c) core is made of pure silica while the holes in the cladding are filled with a high index liquid, and (d) hollow cylindrical multilayer fiber with an all solid cladding (Bragg fiber) [88].

The second is low-index guiding fibers known as Hollow-Core fibers. The core of HC fibers is made of a lower index material than the cladding and the light is guided either by PBG [74] or anti-resonant effect [96]. HC fibers are further sub-classified into HC-PBF [83], Bragg Fibers [101], Kagome fibers [98], and HC-NCF [99]. A brief description of each of these types are given below.

#### **Hollow-Core Photonic Band-gap Fibers:**

These fibers, HC-PBF, are two-dimensional photonic band-gap fibers which are made of a single material with array of holes in the transverse direction forming a photonic crystal cladding such that refractive index changes periodically. The core is formed by omitting one or several unit cells of the material in the center. They are pioneered by Russell [7], and first fiber was fabricated in 1999 at The University of Bath [83]. In HC-PBF the light is confined to the low index core through the photonic band-gap effect [83, 102]. The PBG results in light propagation for certain frequencies in the core/defect while propagation in the photonic crystal surrounding/cladding region is not possible. The light is confined in the core regardless of the refractive index difference between core and cladding. Even though dielectric materials exhibit good transparency at optical wavelengths, the loss in PBFs is higher compared to index guiding fibers. The lowest loss of HC-PBF is  $1.2\text{dB}/\text{km}$  [103, 104]. Therefore, the drawbacks of HC-PBF are high loss due to air glass interface roughness and the main drawback is the nature of

PBG limits transmission window to tens of nanometers [105]. A schematic of HC-PBF is shown in Figure (1.21).

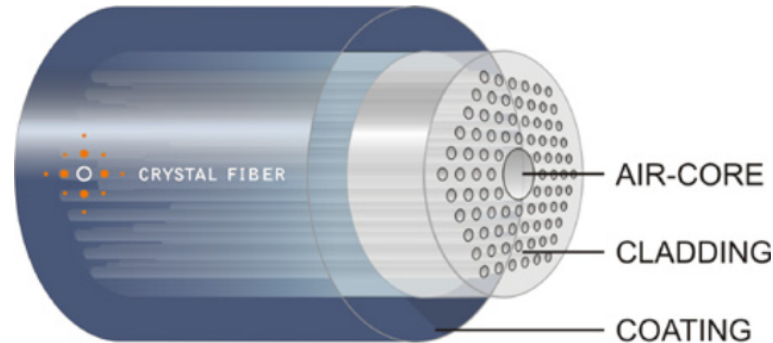


Fig. 1.21 Hollow-core photonic band-gap fiber [106]

### **Bragg Fibers:**

Bragg fibers are a sub type of HC-PBF with a 1D photonic band-gap which has a photonic crystal periodicity in one direction. Theoretical proposals for a new fiber with a periodic structure in the cross section were made in the 1960s [107]. The structure consists of array of rings of high and low refractive index concentric with the central core which is air. In 2000, a solid core version was made using MCVD [78, 101]. A non silica Bragg fiber of similar structure was reported with loss of  $1\text{dB}/\text{m}$  at  $10\mu\text{m}$  wavelength [108]. A schematic of the transverse cross direction is shown in Figure (1.20) (d).

### **Kagome Fibers:**

Kagome fibers was reported in 2002 by Benabid [98]. The structure has a periodic lattice in the cladding with no PBG [104]. The light is guided in Kagome fiber by means of an anti-resonant effect [96]. The transmission spectrum in these fibers is broader than the one achieved in HC-PBF. This type has wide range spectrum from visible to near-IR. The loss in Kagome fibers is higher than the loss of index guiding fibers due to lack of PBG. The loss is related to core size where large core sizes have low loss [109]. The complex cladding structure does not have noticeable impact on the confinement losses [110]. Kagome fibers have a wide range of application; gas-light interaction [111] and terahertz applications [112], due to their low loss and extended transmission window in comparison with HC-PBF [96]. The transverse cross section of Kagome fiber is shown in Figure (1.22).

### **Hollow-Core Negative Curvature Fibers:**

Hollow-Core Negative Curvature Fibers are a new type of HCF, they were first observed in 2010 by Wang [99] when he noticed unexpected low attenuation on a Kagome fiber that has a negative curvature on the core boundary. The name is coined from the

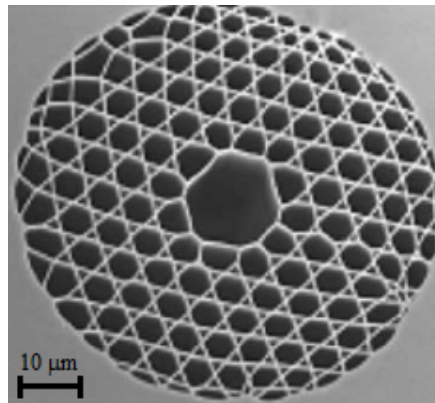


Fig. 1.22 Cross section of Kagome fiber [74]

structure of the core boundary which has a convex shape if seen from the center [96]. In the year following the discovery of HC-NCF, a silica HC-NCF with no lattice in the cladding was fabricated which has a transmission window from UV to far-IR [113]. A study predicted a loss of less than  $1\text{dB}/\text{km}$  is possible [114]. These fibers have been proposed for applications in surgical laser [115] and high power laser delivery [116, 117]. Figure (1.23) shows different designs of HC-NCF.

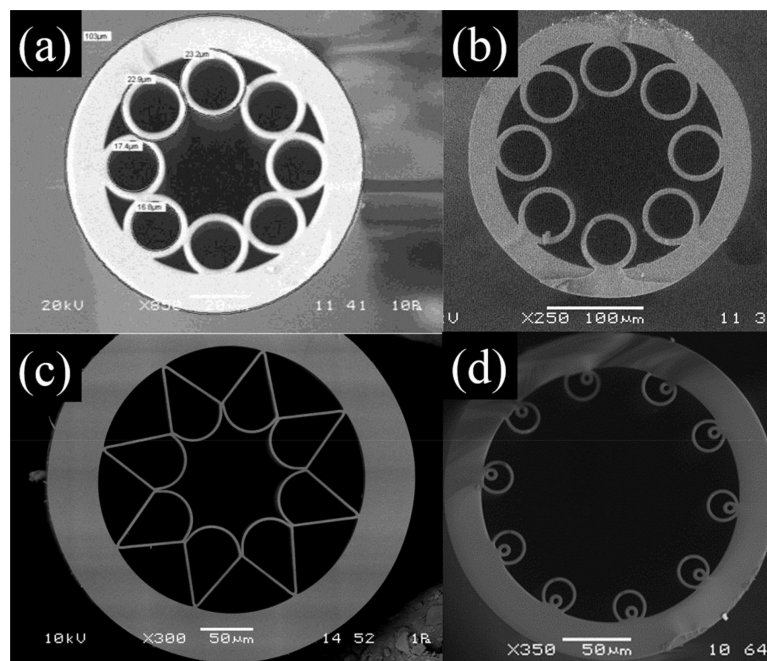


Fig. 1.23 Cross sections of different HC-NCF designs with; (a) touching capillaries in the cladding, (b) non-touching capillaries in the cladding, (c) double nested capillaries in the cladding, and (d) ice-cream cone shape capillary in the cladding [118]

To have a robust guidance in all types of HC fibers, inner claddings must contain small portion of the solid material, a filling fraction of solid material of less than 10% by area [104].

#### Photonic Crystal Fibers:

In the case of index guiding fibers, shown in Figure (1.24), the core is a higher index solid material and the photonic crystal cladding consists of an array of air holes which leads to a reduction in the average refractive index in the cladding region. Therefore light will be confined to the core by M-TIR. The guiding mechanism is defined as ‘modified’ because the photonic crystal cladding refractive index is not a constant value, as in standard optical fibers; it changes with wavelength. When the wavelength increases the field expands more into air holes so the interaction with the material and air changes according to the structure and leads to change in the average refractive index of the photonic crystal cladding. At shorter wavelengths the field is concentrated in the material and as the wavelength increases the field expands more inside the air-holes leading to change in the refractive index. Therefore, PCF are very dispersive and this leads to improvement in controlling the waveguide dispersion.

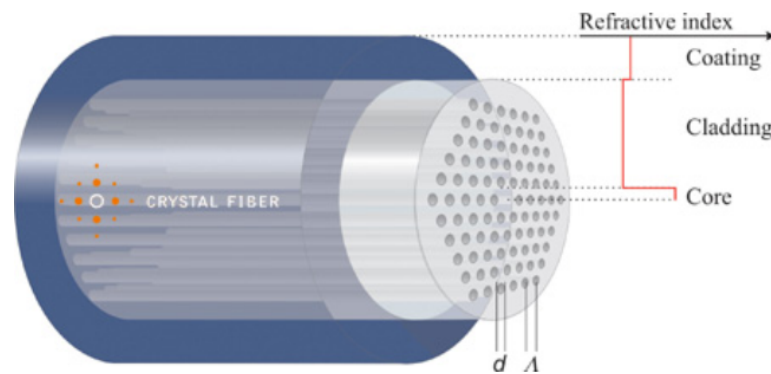


Fig. 1.24 High-index guiding photonic crystal fiber [106]

To sum up, the PCF types differ in terms of guiding mechanism where each type has superiority in some applications. Furthermore, the arrangement, size, number and shape of air-holes can be controlled to manipulate the properties of the optical fiber to achieve better results. Controlling these parameters can yield low attenuation and adjustable dispersion.

The fiber cross-section can be designed to achieve different guiding mechanisms and to exploit various physical phenomena such as single mode operation over an extended wavelength range (endlessly single-moded) [80], hollow-core guidance [83], non-linear effects [39, 74, 88] and much more. The hexagonal or triangle lattice structure is the first and most investigated design. It offer endless single mode operation [79, 80] and

controllable dispersion. In the next section, the cross section of the triangle lattice structure is explored.

### 1.3.3 Hexagonal photonic crystal fiber

Hexagonal Photonic Crystal Fiber (H-PCF) is the first PCF proposed and fabricated [79] and the most investigated PCF for different applications. This section introduces the H-PCF and its structure. Figure (1.25) shows a schematic of the H-PCF which has a triangular lattice of holes in the transverse section,  $d$  is the hole diameter and  $\Lambda$  is the pitch (hole to hole spacing) [80].

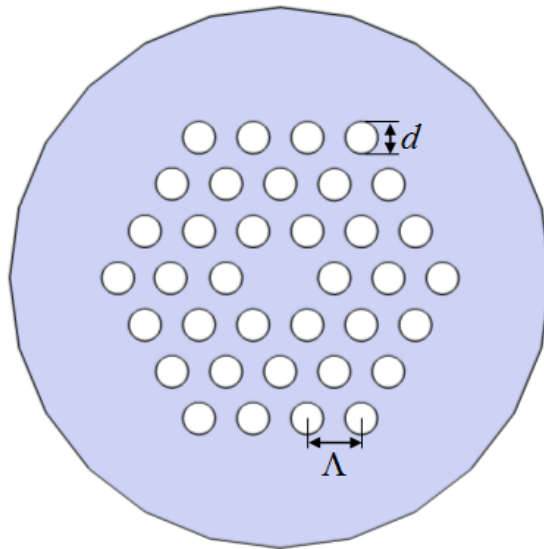


Fig. 1.25 A schematic of hexagonal photonic crystal fiber transverse section

The number of modes a PCF supports is determined in a similar way to conventional optical fibers with the  $V$  parameter. The formula is manipulated slightly to suit PCF as there is not a well defined core or a constant refractive index value for the cladding. The cladding refractive index is a function of the wavelength which changes according to the interaction of light with the two materials (core and air) of the cladding region. At longer wavelengths, the light spreads inside the holes and leads to change in refractive index depending on the design. The  $V_{PCF}$  formula is shown below [15].

$$V_{PCF} = \frac{2\pi\Lambda}{\lambda} \sqrt{n_1^2 - n_{cl}^2(\lambda)} \quad (1.32)$$

where  $n_{cl}(\lambda)$  is the average refractive index of the photonic crystal cladding.

The single mode guidance depends on the refractive index of the core and the average index of the photonic crystal cladding which is a function of wavelength. In conventional optical fibers, the fiber has a cut-off frequency where the fiber is not single

moded below that wavelength. In contrast, the region for single mode guidance in PCFs expands over a wider band because the average refractive index of the photonic crystal is wavelength dependent. At shorter wavelength, the modal field is more concentrated in the glass material as wavelength increases the field expands more into the air-holes. Therefore, at shorter wavelengths the average index of the cladding region is close to the material index. This results in a small index difference between core and cladding so that  $V_{PCF}$  value is small even at shorter wavelengths. Due to refractive index dependence on wavelength the PCF can be designed to have endlessly single mode guidance [80]. The single mode guidance for PCF is satisfied under the condition  $V_{PCF} < \pi$  [15, 119].

The endlessly single mode property is discussed in more depth in the next section. Other unique properties of PCF are discussed as well.

### 1.3.4 Properties of photonic crystal fibers

The properties of an optical fiber depend on two factors, the intrinsic materials properties and the structure of the optical fiber. The former is fixed and cannot be changed for a specified material. Even though it is possible to use different materials for different applications such as chalcogenide glasses are used for non-linear applications to enhance the output of the non-linear effects due to their high non-linear coefficients, but it is still limited to the nature of the material. In this case, the only possible way to intensify this further is to explore an alternative material with enhanced properties for the desired application. On the other hand, the optical fiber structure can be altered to control or optimize the optical properties.

The conventional optical fibers offer limited enhancement to their properties compared with PCFs. Moreover, PCF lead to unique properties which cannot be achieved by conventional fibers. This great flexibility in managing guiding properties is due to dispersion shown by the effective index of the cladding [80]. The three fundamental properties discussed in Section 1.2 can be controlled more efficiently with PCF designs. The dispersion is manipulated more smoothly and many designs have proven a high degree of control. This reason combined with modal field size leads to enhancement in non-linear applications. Even though the loss of PCF is higher than conventional optical fibers, they are still acceptable for applications which do not require a long span of the fiber. Conventional optical fibers perform better in telecommunication but in other field such as sensors, medicine and fiber laser, PCF have many advantages. In sensing, the holes can be filled with gases or liquids for special applications. The PCF

can have a LMA for fiber lasers and power delivery. There are different applications for PCFs, some of which are given below.

Various PCFs designs are proposed and fabricated with unique optical properties for different applications. To name some of these designs and their applications: the most well known PCF (H-PCF) structure is endlessly single moded [79, 80] and offers low and flat dispersion [80, 120]; Air-Suspended Core (ASC) for small effective area [121]; LMA PCFs for high power lasers and power delivery [15]; honeycomb design for band-gap guidance [15]; designs having different hole size [122] or elliptical holes [123] to break the symmetry and have high birefringence [124]. These properties are discussed in more detail below.

In this thesis a new class of PCF proposed. It is based on a spiral photonic crystal in the cladding region. There are a range of spirals in the world. In this work, Equiangular, Archimedean and Fermat's spirals were adapted in the simulated structures. The results are discussed in following chapters, The unique optical properties of PCF are discussed below.

#### **Endlessly single mode:**

There are many parameters that can be controlled in H-PCF such as; hole size, separation between holes ( $\Lambda$ ) and core size. The most striking property of PCF is the endlessly single mode which is possible when the lower index region (air) within the cladding are small enough [80] such that the  $d/\Lambda$  ratio decreases below certain value,  $d/\Lambda < 0.4$  [125], the fiber supports only single-mode propagation regardless of the core size and/or wavelength. This is unlike the SMF which is single-moded only in a small wavelength range and requires a small core size [80]. This is valid when the PCF core is made of one missing hole. Whereas, the endlessly single mode condition is  $d/\Lambda < 0.25$  or  $d/\Lambda < 0.15$  when the PCF core is made of three or seven missing holes, respectively [15]. The single mode behavior with large core is beneficial for telecommunication where light can be injected with high power without suffering from non-linear effects and damaging the fiber because the power intensity is low. Therefore, distance between repeaters is increased [86]. The endlessly single mode operation is at all the wavelengths within the transparency window of the fibers and for any core size as long as the  $d/\Lambda$  condition is satisfied, however for large core size the bending losses increase. The requirement for large core fiber with single mode operation is for high power delivery and its applications.

#### **Large mode area:**

Large mode area fibers can carry high power without being damaged or giving rise to non-linear effects. They are used in delivery of high powers, fiber amplifiers and fiber lasers [8, 74]. The single mode operation of H-PCFs is controlled only by the ratio  $d/\Lambda$

therefore the structure is scalable which permits the fabrication of single mode PCF with LMA. Since the first years of discovering PCF, a fiber with core size of  $22\mu\text{m}$  has been reported in the literature with single mode operation at  $458\text{nm}$  wavelength in 1998 [82]. In 2005, single mode silica PCFs with effective areas of  $1417\mu\text{m}^2$  have been reported at wavelength  $1550\text{nm}$  and  $\gamma < 0.1\text{W}^{-1}\text{km}^{-1}$  [126]. In PBF values of  $A_{\text{eff}} \approx 20\mu\text{m}^2$  at wavelength  $1060\text{nm}$  have been reached by year 2006 [37]. Moreover, a huge portion of the guided mode is located in the air and a tiny fraction of less than 1% in silica of the cladding and  $\gamma$  values of as low as  $0.01\text{W}^{-1}\text{km}^{-1}$  is achievable in HC-PBF [37]. Recently, a theoretical study proposed triangular PCF with a mode effective area of  $1500\mu\text{m}^2$  with low bending loss of  $10^{-5}\text{dB/km}$  at bend radius  $40\text{cm}$  at wavelength  $1064\text{nm}$  [127].

The development of LMA fibers is important in many practical applications, most notably those which require high powers. The quality of the spatial mode is important in most of these applications [37]. The low power intensity minimizes the occurrence of non-linear optical effects [15]. However, there is a limit to the scalable dimension as the fiber becomes sensitive to inhomogeneities and small bends when ( $\Lambda > 10\lambda$ ). Therefore, the bending loss limits the use of LMA fibers and an understanding of bend losses is important in designing LMA fibers. Generally speaking, hole size controls the window of operation, larger holes result in a broader window [37]. The center of the window is related to the hole to hole distance and the minimum bending loss is approximately located at  $\Lambda/2$  [128].

#### **Tuneable dispersion:**

The dispersion of PCF can be controlled more efficiently than conventional optical fibers due to the fact that the photonic crystal cladding holes have a large impact on the dispersion. The configuration of PCF cladding has strong influence when the features of the cladding are on the scale of the wavelength of operation with small core [37]. The refractive index difference between core material and air-holes is large and by varying holes size, separation between air-holes and the core the dispersion can be managed. The flexibility in variation of the photonic crystal structure has made it possible to fabricate PCF with desirable dispersion for both linear [129, 130] and non-linear [13, 131] applications. The linear applications of dispersion are, and not limited to only these, PCF for dispersion compensation [132–136], flattened dispersion [120, 137, 138], telecommunication in WDM [135] and very low dispersion for high power delivery have also been successful. Photonic crystal fibers have been fabricated with anomalous dispersion over the visible spectrum [13, 81] down to  $550\text{nm}$  [37]. Such specifications have many applications for SCG [48] and soliton-based devices [139]. Even though a huge range of dispersion profiles can be made, it is not always possible

to obtain all required properties for a particular application within one fiber. Photonic crystal fiber with large values of normal dispersion may appear to be attractive to compensate the dispersion of communication fibers. Unfortunately, for large dispersion a fiber with small core is required, which would introduce large losses when integrated with a conventional communication system and degradation of the linear polarization of the mode [37].

**Non-linearity:**

The efficiency of non-linear effects increase with increasing power intensity which requires a small core and a well confined field. This is not possible in SMF because as the core radius is reduced the field will be less confined. In contrast, PCF with small core size and large air-holes have small effective area ( $A_{eff}$ ) and it is possible to manipulate dispersion allowing for large interaction with air and thus improve efficiency of non-linear effects. The effective non-linearity ( $\gamma$ ), is calculated according to Equation (1.33).

$$\gamma = \frac{2\pi}{\lambda} \frac{n_2}{A_{eff}} \quad (1.33)$$

The effective non-linearity for a given wavelength can be enhanced by either using a material with higher  $n_2$  or minimizing the mode field area. The non-linearity can be estimated theoretically for a given material by calculating the minimum core size where the  $A_{eff}$  should be compatible at the operating wavelength for the field to be well confined [37]. If the core size is smaller than wavelength, the core would be too small to guide a well confined field as the mode starts to broaden. In ASC fibers a value of  $\gamma \approx 70(W \cdot km)^{-1}$  has been reported [37] and a design with similar value has been manufactured [140]. In PCF, light can be more confined in the core made of glasses with higher refractive index, leading to smaller  $A_{eff}$ . Silicate glass has high  $n_2$  values and values of  $\gamma \approx 1860(W \cdot km)^{-1}$  have been reported [141]. Photonic crystal fibers have enhanced the conventional non-linear processes and allowed the establishment of new phenomena [77]. One of most successful applications of non-linearity is SCG from pico- and femto-second laser pulses [74].

In contrast, non-linearity has drawbacks in telecommunications and high power delivery. High-power laser pulses are important in many technological and scientific applications such laser amplifiers, multiphoton spectroscopy, fiber lasers and photodynamic therapy. In conventional fibers the non-linearity limits the use of ultrashort pulses to energies no higher than a nano-Joule [142]. To over come non-linearity effects a low  $n_2$  material could be used with LMA.

**Loss:**

The process of extension of preform to a fiber has a detrimental effect on fiber loss where the fiber cross section should be kept invariant along its length to minimize the loss. The other factors that affect loss in PCF are the percentage of light in the glass material, and the roughness at the glass-air interface. Other loss factors similar to those in conventional fibers are confinement and bending losses. Confinement loss can be reduced by increasing the number of holes [74]. All these factors are managed in the fabrication process apart from bending which is managed at installation. In solid core PCF the lowest loss reported is  $0.28\text{dB}/\text{km}$  [74] which is slightly higher than SMF loss. Whereas, the best reported loss in HC-PCF is  $1.2\text{dB}/\text{km}$  [? ], the best loss figure reported is  $0.025\text{dB}/\text{m}$  at wavelength  $1064\text{nm}$  in a 7 capillary cladding HC-NCF. These losses are due to the roughness of glass-air interface. However, HC-PCFs are expected to exhibit loss lower than that of conventional fibers with an advance in the fabrication technologies because light travels inside the Hollow-core (usually air). Furthermore, the bending losses can be very small even for LMA [82]. In theory, scattering losses of HC fibers could be 1000 times less than the loss in conventional fibers, which would have an impact on telecommunication and quantum information applications [142].

**Birefringence:**

The fiber has two fundamental modes which will be degenerate if the structure has symmetry. If the symmetry is broken to two fold symmetry or less then the fiber will have birefringence [123]. The possibility of realizing high birefringence values in PCF due to a higher intrinsic index contrast compared to conventional fibers [125] makes PCF an excellent choice for applications such as sensing [143, 144] and high bit-rate transmission systems [145]. The value of birefringence achieved in PCF is orders of magnitude higher than that of conventional fibers [124]. The symmetry of H-PCF is six-fold and the idea is to break this symmetry into two-fold, to increase the birefringence, either by changing the size of two holes [122] or use elliptical holes [123]. Furthermore, asymmetry can either be introduced in the cladding by distribution of air-holes, or in the shape of the core. However, no fiber in practice is perfectly symmetric due to structural imperfections which combined with small core size and large index contrast lead to birefringence. The effect is more noticeable when the fiber is highly non-linear [37]. Birefringence values of  $3.7 \times 10^{-3}$  in 2000 [124] and  $4.56 \times 10^{-2}$  in 2014 [146] have been reported. The latter was in a square lattice PCF where some of the holes were elliptical and rotated  $45^\circ$  [146]. Moreover, the birefringence of PCF is 100 time less sensitive to temperature than conventional fibers. This is important in many applications [147]. The temperature dependence is due to the fact that conventional fibers are made of two materials with different thermal expansion

coefficients [74] whereas in PCF only the thermal expansion of the core material (and air which has a negligible thermal coefficient) has to be taken into account. Therefore the fiber performance is almost insensitive to temperature variation.

When the fiber is birefringent then it is polarization maintaining. It is possible to design single-mode single-polarization PCF which can eliminate the polarization mode dispersion [86]. Even in PCF the fiber spinning during drawing process has reduced the PMD by an order of magnitude [148].

There are various advantages of PCF over conventional fibers such as, in air cladding PCF, the large index contrast can provide very large numerical apertures from arbitrary small values to  $NA = 0.9$  [149].

To sum up, PCFs have significantly improved optical properties and offer unique properties which are not available in conventional optical fibers. The fabrication processes of PCFs is discussed in the following section.

### 1.3.5 Fabrication of photonic crystal fibers

There are a number of techniques for fabrication of optical fibers which were developed to suit the varieties in the material properties. Therefore, a knowledge of the material properties is necessary in choosing the most appropriate fabrication technique. The fabrication of optical fibers involves two stages; preparing a preform which contains the structure of interest on a macroscopic scale, and drawing the preform to elongate to fiber dimensions. The preform preparation may require more than one step to get it ready to be drawn down on a fiber-drawing tower. The main difference in the fabrication processes lies in the preform preparation stage. The second stage, drawing, does not differ much because the same procedure, with some changes in parameters which control the process such as heat temperature, speeds and pressure inside fiber holes to make them preserve their shape and not collapse, is followed. The most common techniques are discussed below.

The fabrication process is one of the most important aspects in designing and developing new types of optical fibers. Optical fibers fabricated using silica have been accurately analyzed, partly because most conventional optical fibers are produced from fused silica [88]. In the fabrication process of PCF, a preform needs to be prepared first. Usually, the most challenging step in the process of fabrication is the preform fabrication [37]. One possible way of fabrication is the drilling of several holes in a periodic arrangement into the preform. Another way is extrusion by using dies which contain the structure of interest [150–155]. The Stack and Draw technique [79] was developed and introduced to PCF by Birks *et al.* in 1996 [95] from the tube stacking technique investigated at

Bell Laboratories [156]. This technique has become the preferred fabrication technique in the last few years, since it allows relatively fast, clean, low cost, and flexible preform manufacture. The first PCF was fabricated by drilling silica rods to form tubes which then stacked to form the preform [87]. Due to the expanding research in PCF there are new designs with complex air-hole distributions which require different techniques such as cigar-rolling [157], sol-gel casting [158] and most recently the 3D printing [159] which is a promising method for complex designs.

**Stack and draw technique:**

The stack and draw fabrication process for PCF is shown in Figure (1.26), where the process involves the stacking of silica capillary tubes and rods in a mm-scale radius preform in a hexagonal pattern forming the desired air-silica structure. Typical dimensions of preform are 1m long with a diameter of 20mm [88]. Creating the preform in this way allows high level of design flexibility to control the core size and shape as well as the arrangement of air-hole in the cladding region, which gives the ability to fabricate fibers with different properties. After the stacking process, the capillaries and rods are held together by thin wires and fused together during an intermediate drawing process, where the preform is drawn into preform canes. This bundle is then drawn down by heating and pulling in a conventional fiber-drawing tower [80, 125] to extend its length and reduce its cross-section to produce the fiber. The stack and draw is a common method in PCF fabrication. It is widely used to fabricate silica PCF [79] and chalcogenide fibers [153, 160, 161].

Conventional optical fibers are usually drawn at temperatures around 2100°C whereas for PCF the draw temperature is kept at 1900°C, since the surface tension can otherwise lead to the collapse of the air-holes [95]. When producing LMA fibers the preform draw process is done in one step, whereas in micro-scale  $\Lambda$  it is done in two steps; draw preform to cane of 1 – 2mm diameter, second phase to draw the cane into the final dimension.

At drawing cane or fiber the hole shape and size are not easy to control and it is one of the challenging tasks in the fabrication process. The size of holes can change during drawing due to effects of temperature gradient, surface tension and pressure inside holes [37]. During the drawing process, a slight overpressure is applied to the inside of the preform relative to the surroundings, and to properly adjust the drawing speed. This is in order to carefully control the size of the air-holes. During the drawing process holes can survive the spinning of the preform, which is used to control the fiber geometry [148, 163]. Finally, the fibers are coated to provide a protective standard jacket.

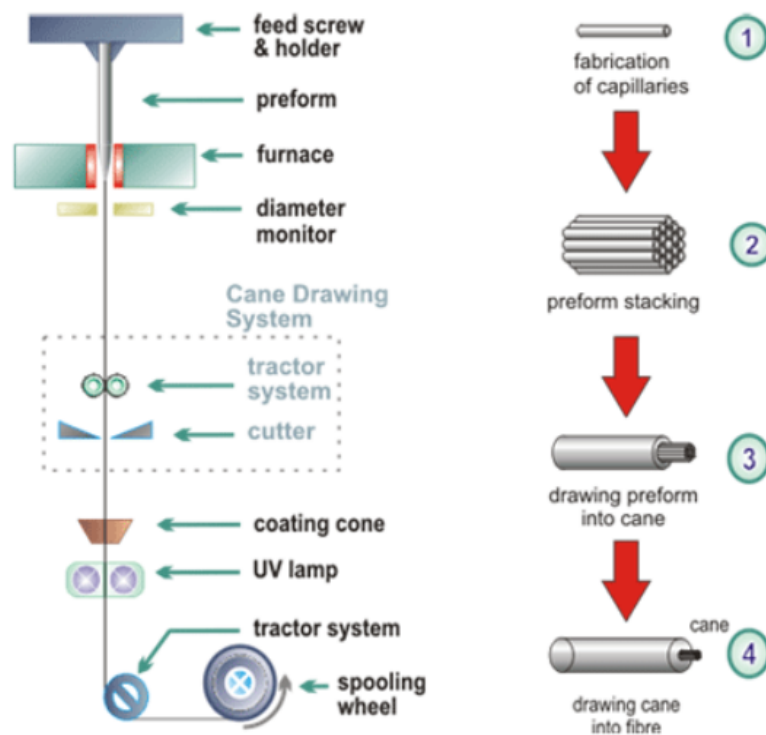


Fig. 1.26 Fabrication process of PCF [162]

The stack and draw fabrication processes of PCFs and HC-PBFs are almost the same with the only difference that in the center of HC-PBFs some (7 or 19) rods are omitted from the center, which produce a large air core [37]. The drawing process is similar and adaptable to other methods. The drawback of stacking that it is labor intensive and quality depends on the craft of the fabricator of the preform [37]. If the distribution of the air-holes is complex, then it will not be possible to use SaD. Therefore other methods should be investigated to design such structures.

#### **Extrusion technique:**

Extrusion is forcing molten glass through a die containing the design pattern of holes in millimeter-scale features [37]. In extrusion a fiber is drawn from bulk glass directly and allows the production of complex geometries in one step and so can be used to produce almost any design if a die is present. However, selective doping of rare-earth ions is difficult [74]. It is not possible to use extrusion for silica as there is no die material that can withstand the processing temperature without contaminating the glass. Extrusion works well for other materials with relatively low softening temperature like compound silica glasses [8], soft glasses (including sulfur hexafluoride (SF<sub>6</sub>) [150], lead silicate (SF57) [151, 152], chalcogenides [153] and tellurites [155]) and polymers [154]. All these materials have been fabricated using extrusion. The thermal processing in some

glasses may lead to increase in the fiber losses due to formation of crystals during the extrusion process [37].

**Drilling technique:**

This method is defining the structure of the preform by direct drilling of bulk material. A broad range of geometries can be fabricated with drilling and it is suitable in producing PCF in many diverse materials such as chalcogenides glasses, soft-glass [164] and polymer [154] as their hardness is not as high as silica glass [165]. Extra care should be taken of rotation and forward speeds of the drilling device [165]. The drawbacks of drilling are the time length required to make a structure with many features, introduced roughness at surface, and as complexity of structure increase the preform yield is reduced [37].

**Sol-gel method:**

The method has been around for decades and recently it is being used for processing different glasses and ceramics [166]. It was developed to fabricate optical fibers at Bell Labs, the solution comprises of colloidal silica particles [167, 168]. The name of this method is coined from the two steps involved. The method starts with preparing a solution (sol) containing small portion of metal ions so the mixture is uniform to a nanoscale. Then the solution is solidified by gelling (gel). The design would have the shape of the mold or the surface on which the solution is poured on. One of the advantages of a solution is that even if it consists of multi-components, it is homogeneous. The method facilitates the control of the homogeneity, the composition and high concentration of dopants [158]. The gelling process is through chemical reactions which take place at room temperature leading to more homogeneous materials not like other methods that require high temperatures [158].

**Cigar-rolling technique:**

There are other techniques used to fabricate photonic crystal fibers such as the cigar-rolling technique which is used in fabrication of HC-PBF [157]. In this technique, a multilayer mirror is rolled up to form a preform with a hollow core. This design is different from the others discussed above where it uses two solid materials in a way that results in radial variation in the refractive index. This provides intrinsic advantages for forming hollow-core fibers. Guiding light in a hollow core is much easier because there is only a single periodicity involved. On the contrary, the use of two solid materials limits the choice to those with compatible thermal and thermo-mechanical properties. This method is not limited to HC-PBF where a PCF with solid core and array of air-holes in the cladding is fabricated with this method [169]. The process is simple where a pattern is created on sheet of planar glass and then the sheet is rolled into a cylinder [169].

**Casting:**

The glass is molded in a silica cast made of capillaries and capillary guides, the cast is removed in a hydrofluoric acid bath [170]. The inhomogeneities at the interface between capillaries is greatly reduced with this method, which is the cause of high losses [170]. This method is implemented to fabricate polymer [171], SF<sub>6</sub> [172] and chalcogenide [170] fibers. The former two used metallic moulds which can be removed by heating or cooling either the preform or the metallic cast. In the latter a metal cast is not a choice due to the large difference in thermal expansion, so a silica mould can be used [170].

**3D printing:**

The process starts by making a digital file that contains the design of interest to be printed on a 3D printer. The printing is done layer by layer to produce a 3D structure, preform, using powdered metal or plastic material [173]. It is expected that silica based glasses fiber can be printed in the near future using 3D printers [159]. This technology was introduced to fabricate PCF because usually one material is used to make the fiber, the fabrication of two material all solid fiber has been demonstrated by using a dual head 3D printer [159]. Any arbitrary design can be printed in 3D with high precision; this is the most important advantage of this method [173]. Three factors impact the optical transparency; printing speed should be slow, temperature should be high and the layer should be thin [173].

In this discussion, it is noted that the choice of the fabrication method is more related to the material which is used to make the fiber. Therefore, some knowledge of the different materials and their properties is a requirement. In the next section a brief description is given on the important materials used in optical fiber fabrication.

## 1.4 Materials for Fiber Fabrication

Fused silica glasses have been the core material of optical fibers since their invention and silica is still in use with new classes of optical fibers such HC-NCF, and Kagome. Optical fibers made of silica offer a range of unique characteristics, low loss, feasibility in fabrication process as silica based fibers are being made for more than 40 years. However, the transmission spectrum of silica material is limited to the visible and near-IR range due to strongly increasing absorption at mid-IR and color-center-related damage in deep-UV [174]. The loss of silica is very high, above  $60\text{dB}/\text{m}$ , at wavelengths  $> 3\mu\text{m}$  [175]. The necessity to use different wavelengths for different application requires the use of new materials. The popular materials used in optical

fibers fabrication with a brief introduction on their optical properties (wavelength band, loss ...etc) are listed below. The most important optical parameter is the refractive index. It is calculated by the Sellmeier equation [12] (Equation (1.34)) where each material has different coefficients. The simulations in this work have been carried out with silica, tellurite and SF57 materials.

$$n^2 - 1 = \sum \frac{B_j \lambda^2}{\lambda^2 - (A_j)^2} \quad (1.34)$$

### 1.4.1 Soft-Glasses

Silica based fibers have superiority over other materials in telecommunication but in almost all other applications silica is not the material of choice. Non-silica glasses have been adapted in many optical fibers applications such as non-linear effects, i.e. SCG [176], mid-IR and UV applications [177] and even in telecommunications there are promising glasses with lower loss than silica [178]. These glasses are known as soft or compound glasses with reference to the lower melting temperature compared to silica and are composed of more than one chemical component [37].

#### **Chalcogenide:**

Chalcogenide glasses are based on one of the chalcogen elements *S*, *Se*, and *Te*, with addition of other element such *Ge*, *As*, *Ga*, *Sb*, etc... [179]. They have very high Kerr non-linearity coefficient, some chalcogenide glasses such as ( $As_2Se_3$ ) has a non-linear coefficient value of 500 times higher than silica [180] and even higher up to 1000 times higher for selenium and tellurium based glasses [170]. The composition  $As_{24}S_{38}Se_{38}$  has highest  $n_2 = 1.75 \times 10^{-14} cm^2/W$  [179]. They are used in non-linear applications [179]. However, chalcogenides are more complicated to control than silica because their chemical stability is low [181]. They have a wide transparency window from visible (300 – 700nm) to mid-IR (10 – 20 $\mu m$ ) [181], and higher refractive index ( $n = 2.0 - 3.5$ ) [181]. Transition temperature ranges from 116 to 550 °C depending on composition [180]. The fabrication of the first non-silica (chalcogenide) PCF was reported in 2000 using stack and draw [153].

#### **Tellurite:**

Tellurite glasses have useful characteristics which are not present in silica such as high refractive index in the range 2-2.2 [182] at 1.55 $\mu m$ , good transparency in a wide range (0.4 – 7 $\mu m$ ) [182] including the mid-IR region, and high Kerr non-linear coefficient ( $n_2 = 20 - 50 \times 10^{-20} m^2/W$  [182] ) [155]. The tellurite glasses are good candidate for high non-linear application namely SCG. In the simulation of this work, tellurite

PCF has been investigated to generate a flat dispersion for wide-band SCG. The results are discussed in Chapter (4).

**Lead Silicate:**

The first single mode non-silica glass PCF was fabricated from extruded preform of a SF57 glass [152, 183]. The softening temperature for SF57 is low ( $519^{\circ}C$ ) [152, 183], therefore the preform can be extruded from bulk glass. SF57 has a refractive index of 1.8 at  $1.53\mu m$  [183] and a Kerr non-linear coefficient of  $4.1 \times 10^{-19} m^2/W$  at  $1.06\mu m$  [184]. The material loss at wavelength  $1.55\mu m$  is  $0.3dB/m$  [183].

**ZBLAN:**

ZBLAN was discovered in 1975 and is a promising material to replace fused silica in telecommunications. The transparency window of ZBLAN extends from UV to mid-IR ( $0.2$  to  $7.8\mu m$ ), so it has advantage of transparency in UV where silica suffers from solarization below wavelength  $380nm$ . Solarization is the damage of the fiber due to operating at the UV region [178]. The loss at wavelength  $2.5\mu m$  is  $0.01dB/km$  where silica loss  $0.185dB/km$  at wavelength  $1.55\mu m$ . However, drawing ZBLAN is extremely hard because its viscosity is stable only in a narrow temperature range [178].

## 1.4.2 Polymers

Polymer PCF offer key advantages over glass PCF such as low cost at manufacture, mechanical robustness and chemical flexibility [37, 154]. However, the loss of polymer fibers is much higher than glass fibers [185]. Even though the loss of polymers is high, they are finding applications in various fields including, and not limited to, THz applications [44, 186], sensing [187, 188] and imaging [188]. The first polymer PCF was fabricated in 2001 [95].

**PMMA:**

The preform of the first microstructured polymer fiber was fabricated using extrusion of Poly(methyl methacrylate) PMMA in 2001. The draw process was at a temperature of  $175^{\circ}C$  and speed rate of  $10m/min$  on a polymer drawing tower [154]. The drawing temperature could be varied in wide range without significant change to the fiber unlike glass PCF. The temperature range for PMMA when drawn to a fiber is from  $150^{\circ}C$  to  $200^{\circ}C$  [154]. PMMA has a loss of  $55dB/km$  at the wavelength  $567nm$  and a corresponding refractive index of 1.49 [189].

**Teflon:**

Teflon is used for THz applications. Teflon has many advantages in THz regime such as low refractive index ( $\sim 1.4$ ) [190] which means low index difference between Teflon and air in the PCF thus scattering loss would be reduced and it would be possible

to obtain flat dispersion for non-linear effects to generate THz waves [44]. The first demonstration of Teflon based PCF was in 2004 for THz guidance in the range 0.1 – 1.3 THz [191]. Other advantages of Teflon include its flexibility and that it is a low cost material. A long fiber can be drawn from Teflon compared to other polymers [44].

**Topas:**

Topas is used in THz regime applications similar to Teflon. Two PCF fibers were fabricated in 2009 with large and small mode area with loss less than  $0.09\text{cm}^{-1}$  in the range 0.35 – 0.65 THz [192]. In Topas, the THz region falls between microwave and IR and has applications in identification of hidden objects, sensing, medical diagnostics, defence, etc... [44, 186].

The wide range of materials used to study and fabricate PCF, alongside the diversity in design of PCF and their unique properties have made PCF feasible to many applications like sensors [193, 194], frequency metrology [195], optical coherence tomography [196], high power fiber lasers [197], laser machining , welding [88], and many more applications.

## 1.5 Summary

To conclude, this chapter presents an introduction to optical waveguides with a focus on optical fibers and photonic crystal fibers. The relevant information from literature is included to clarify the properties and advantages of PCF. These properties can be enhanced more through investigating the designs in depth and propose new ones. However, it is not possible to predict the characteristics of a design before fabrication and characterization and the fabrication process is relatively costly and time consuming. Therefore, the design is first analyzed, investigated and optimized with the use of simulation methods to reduce the cost and time required to produce the optimal design. The analysis of optical fibers requires the implementation of Maxwell's equations to study the interaction of light with the medium and find the modes. The next chapter discusses Maxwell's equations, and the simulation method, FEM, employed in this work to obtain modal solutions.

# Chapter 2

## Methodology

The optical properties of a device are an important matter in choosing the right design to meet a specific application. In optical system design, the amount of time and money to produce a device is a significant factor in the final cost of the device. If a device is made without appropriate design, it may fail to meet specifications. Experimental techniques are time consuming and expensive. Furthermore, the flexibility in variation of parameters is usually limited by the resource availability [198]. For these reasons, there is a requirement for a way to study and predict the characteristics of a device before it is made. In photonics and optical science, computational methods have been developed and employed to simulate optical devices. Moreover, computational methods facilitate the study of designs and phenomena which cannot be achieved with available technologies.

The computational simulations lead to vast improvement in performance and reduction in cost and time required to make a device. The process requires initial simulation to test a design. The simulation results are processed and analyzed to compare with the target application. If specifications are not met then a redesign of the device and retesting is carried out. There may be several stages of redesign and retest until the specifications are met. At that stage the design is fabricated. The simulation process demands less time and money than fabrication. Therefore, the design can be manipulated and improved more efficiently to meet specifications.

The work presented in this thesis is simulations of spiral Photonic Crystal Fibers (PCFs) to study some of their optical properties. The method adapted in this work is the Finite Element Method (FEM) and most of this chapter is dedicated to explain how the method is implemented to study optical waveguides. The reason behind choosing FEM in this work is that any arbitrary index profile can be presented more efficiently and also the approximation is more accurate than other methods in the frequency domain.

Simulation of optical waveguides and devices require the implementation of the electromagnetic field theory. The starting point is Maxwell's equations which are introduced in the next section followed by the derivation of the wave equation. Thereafter, computational methods are discussed in brief. The rest of the chapter is concerned with the FEM and how it is implemented. An in depth discussion of the method is given with reference to optical waveguides.

## 2.1 Introduction to Electromagnetism

The study of physical phenomena requires the problem of interest to be presented in a mathematical formula to be solved either in very limited situations analytically such that it has exact solution. Otherwise, if the problem has a solution which can not be found analytically then the mathematical problem can be approximated where assumptions are made [199].

This section begins with Maxwell's equations and lists the assumption made to derive the wave equation. The wave equation is then solved by the computational methods to find the modal solution of the optical waveguide. Maxwell's equations can be written in integral or differential formulae. In this thesis, only the latter are discussed.

### 2.1.1 Maxwell's equations

Maxwell's equations are partial differential equations which relate electrical and magnetic fields and their fluxes with the sources (currents and charges). There are four Equations (2.1) - (2.4) which are stated as Faraday's law (2.1), the Maxwell-Ampere law (2.2), Gauss's law electric (2.3), and Gauss's law magnetic (2.4) [200, 201].

$$\nabla \times \mathbf{E} = -\frac{\partial \mathbf{B}}{\partial t} \quad (2.1)$$

$$\nabla \times \mathbf{H} = \frac{\partial \mathbf{D}}{\partial t} + \mathbf{J} \quad (2.2)$$

$$\nabla \cdot \mathbf{D} = \rho \quad (2.3)$$

$$\nabla \cdot \mathbf{B} = 0 \quad (2.4)$$

where  $\mathbf{E}$  is electric field intensity in *volt/meter* ( $V/m$ ),  $\mathbf{B}$  is magnetic flux density in *weber/meter<sup>2</sup>* ( $Wb/m^2$ ),  $\mathbf{H}$  is magnetic field intensity *ampere/meter* ( $A/m$ ),  $\mathbf{D}$  is elec-

tric flux density *coulomb/meter<sup>2</sup>* ( $C/m^2$ ),  $\mathbf{J}$  is electric current density *ampere/meter<sup>2</sup>* ( $A/m^2$ ), and  $\rho$  is electric charge density *coulomb/meter<sup>3</sup>* ( $C/m^3$ ) [200, 201].

The electric/magnetic field strength and the corresponding flux are dependent on each other through the medium properties. The relation for a lossless, homogeneous and isotropic medium is defined through the following two equations. These equations relate the electric quantities to the permittivity of the medium ( $\epsilon$ ) and the magnetic quantities to the permeability of the medium ( $\mu$ ), respectively. These relations are known as the constitutive relations [201]:

$$\mathbf{B} = \mu\mathbf{H} = \mu_0\mu_r\mathbf{H} \quad (2.5)$$

$$\mathbf{D} = \epsilon\mathbf{E} = \epsilon_0\epsilon_r\mathbf{E} \quad (2.6)$$

where  $\mu_0 = 4\pi \times 10^{-7}(H/m)$  and  $\epsilon_0 = 8.854 \times 10^{-12}(F/m)$  are the permeability and permittivity of vacuum,  $\mu_r$  and  $\epsilon_r$  are the relative permeability and permittivity, respectively [200, 201].

A relation for the continuity of current or conservation of charge is obtained by applying the divergence to Equation (2.2) and substituting Equation (2.3) in:

$$\nabla \cdot \mathbf{J} = -\frac{\partial \rho}{\partial t} \quad (2.7)$$

The Maxwell's equations and constitutive relations can be solved to obtain a general solution in free space or one infinite medium [201]. However, optical waveguides and/or devices consist of different media with finite dimensions and Maxwell's equations are not enough to solve for a unique solution for such boundary value problems. Therefore, boundary conditions are required to solve for solutions. The boundary conditions are discussed in the next section.

### 2.1.2 Boundary conditions

In the previous section, Maxwell's equations and the constitutive relation were given. Both can be used to get a general solution for electromagnetic problems. In this section, the boundary condition will be discussed. Thus a unique solution can be obtained by enforcing boundary conditions. There are boundaries at the physical dimension of the waveguide and the boundary continuity condition at the interface between two media should be satisfied to ensure continuity of the field through the interface [201].

The boundary condition at the interface between two media is shown in Figure (2.1), when there is no surface charge ( $\rho = 0$ ) nor surface current ( $\mathbf{J} = 0$ ), this is the case if

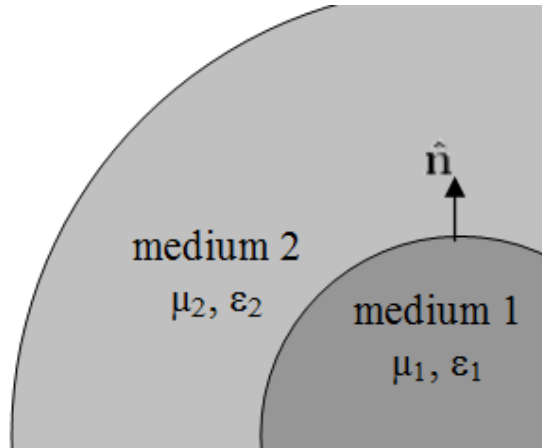


Fig. 2.1 Interface between two media [201]

both materials are perfect dielectrics [201]. This gives rise to the following continuity between field components across the interface:

1. The tangential components of the electric field must be continuous.

$$\begin{aligned}\hat{\mathbf{n}} \times (\mathbf{E}_1 - \mathbf{E}_2) &= 0 \\ \therefore \mathbf{E}_{t1} &= \mathbf{E}_{t2}\end{aligned}\tag{2.8}$$

2. The tangential components of the magnetic field must be continuous.

$$\begin{aligned}\hat{\mathbf{n}} \times (\mathbf{H}_1 - \mathbf{H}_2) &= 0 \\ \therefore \mathbf{H}_{t1} &= \mathbf{H}_{t2}\end{aligned}\tag{2.9}$$

3. The normal components of electric flux density must be continuous.

$$\begin{aligned}\hat{\mathbf{n}} \cdot (\mathbf{D}_1 - \mathbf{D}_2) &= 0 \\ \therefore \mathbf{D}_{n1} &= \mathbf{D}_{n2}\end{aligned}\tag{2.10}$$

From Equation (2.6), and since permittivity of the two media are different ( $\epsilon_1 \neq \epsilon_2$ ), then

$$\begin{aligned}\epsilon_1 \mathbf{E}_{n1} &= \epsilon_2 \mathbf{E}_{n2} \\ \therefore \mathbf{E}_{n1} &\neq \mathbf{E}_{n2}\end{aligned}\tag{2.11}$$

4. The normal components of magnetic flux density must be continuous.

$$\begin{aligned}\hat{\mathbf{n}} \cdot (\mathbf{B}_1 - \mathbf{B}_2) &= 0 \\ \therefore \mathbf{B}_{n1} &= \mathbf{B}_{n2}\end{aligned}\tag{2.12}$$

From Equation (2.5), and since permeability for most non-magnetic media are 1 ( $\mu_1 = \mu_2 = 1$ ), then

$$\begin{aligned}\mu_1 \mathbf{H}_{n1} &= \mu_2 \mathbf{H}_{n2} \\ \therefore \mathbf{H}_{n1} &= \mathbf{H}_{n2}\end{aligned}\tag{2.13}$$

where subscripts 1 and 2 indicate the two media, subscripts  $n$  and  $t$  indicate normal and tangential components, respectively, and  $\hat{\mathbf{n}}$  is the unit vector normal to the interface between the two media.

The tangential and normal components conditions are dependent on each other. If the tangential component conditions (Equations (2.8) and (2.9)) at the interface are satisfied then the normal component conditions (Equations (2.10) and (2.12)) will also be satisfied. These conditions are called natural condition [201]. Therefore, natural boundary condition can be left free because they are satisfied automatically [202].

There are two other conditions when one medium is a perfect electric conductor, in absence of electrical charge ( $\rho$ ) and current ( $\mathbf{J}$ ), the tangential magnetic field components ( $\mathbf{H}$ ) vanishes, see Equation (2.14). Likewise, when the medium is a perfect magnetic conductor the tangential electric field components ( $\mathbf{E}$ ) vanish and magnetic field continuity is ensured, Equation (2.15) [200].

$$\mathbf{n} \times \mathbf{E} = 0 \quad \text{or} \quad \mathbf{n} \cdot \mathbf{H} = 0\tag{2.14}$$

$$\mathbf{n} \times \mathbf{H} = 0 \quad \text{or} \quad \mathbf{n} \cdot \mathbf{E} = 0\tag{2.15}$$

On the other hand, when the conditions are not natural then the field must be defined at the boundaries. These condition are termed forced conditions and implemented at different cases so some implementations are discussed in the following text. A waveguide has finite dimensions but the surroundings are infinite and in numerical analysis the domain has to be finite so an artificial boundary condition is imposed to make the dimension finite. This boundary is made to absorb the optical field so it does not reflect back to the structure. In this work the boundary implemented to limit the structure to finite dimensions is the Perfectly Matched Layers (PML) [201], which is discussed in Section (2.3.6). The forced conditions are classified as follow:

$$\text{Homogeneous Dirichlet} \quad \phi = 0 \quad (2.16)$$

$$\text{Inhomogeneous Dirichlet} \quad \phi = k \quad (2.17)$$

$$\text{Homogeneous Neumann} \quad \partial\phi/\partial\mathbf{n} = 0 \quad (2.18)$$

The forced conditions (PEC and/or PMC) can also be implemented when there is a symmetry in the waveguide structure so that the computational domain is reduced and hence economize the computational resources. The structure could be symmetric on one axis where one-half of the structure is enough to be simulated to find a solution, half symmetry, or symmetric on two axes and a quarter of the structure can be simulated. In rare cases there are further symmetries [203, 204].

However, the symmetry conditions are not discussed further in this thesis because the structures studied in this work are asymmetric. In the next section, the derivation of the wave equation is given.

### 2.1.3 Wave equation

The analysis of optical waveguide problems involve the solution of Maxwell's equations. In modal solutions the time dependence can be included as frequency operator. Therefore, the four Maxwell's equations are combined to produce a second-order differential equation, know as the wave equation, which can be solved numerically to obtain solutions [200].

Furthermore, it is not an easy task to apply the coupled Maxwell's differential equations when solving boundary-value problems [198]. Moreover, the computational requirement for storing all field components is memory consuming [200]. The derivation of the wave equation from Maxwell's equations is explained below by substituting Equation (2.5) into (2.1).

$$\nabla \times \mathbf{E} = -\mu \frac{\partial}{\partial t} \mathbf{H} \quad (2.19)$$

Apply curl to both sides of equation

$$\nabla \times (\nabla \times \mathbf{E}) = -\mu \frac{\partial}{\partial t} (\nabla \times \mathbf{H}) \quad (2.20)$$

and substitute (2.2) and then (2.6)

$$\nabla \times (\nabla \times \mathbf{E}) = -\epsilon\mu \frac{\partial^2}{\partial t^2} \mathbf{E} \quad (2.21)$$

In the frequency domain, the time harmonic assumption of the electromagnetic field is used to eliminate the time dependence from the field vector. This is related to the steady-state of the field, which is a function only of space and not time [198]. The field vectors can be expressed in the phasor form as:

$$\mathbf{E}(x, y, z, t) = \mathbf{E}(x, y, z) e^{j\omega t} \quad (2.22)$$

where  $\omega$  is the angular frequency

The phasor form enables the replacement of time derivative with  $j\omega$  as illustrated in the following equations.

$$\therefore \frac{\partial e^{j\omega t}}{\partial t} = j\omega e^{j\omega t} \quad (2.23)$$

$$\therefore \frac{\partial}{\partial t} = j\omega \quad (2.24)$$

Substitute equation (2.24) into (2.21)

$$\nabla \times (\nabla \times \mathbf{E}) = \omega^2 \epsilon \mu \mathbf{E} \quad (2.25)$$

The previous equation is for the electric field ( $\mathbf{E}$ ). In a similar manner an equation for the magnetic field ( $\mathbf{H}$ ) can be derived:

$$\nabla \times \frac{1}{\epsilon} (\nabla \times \mathbf{H}) = \omega^2 \epsilon \mu \mathbf{H} \quad (2.26)$$

From the vector calculus relation  $\nabla \times (\nabla \times \mathbf{E}) = \nabla(\nabla \cdot \mathbf{E}) - \nabla^2 \mathbf{E}$ , rewrite  $\nabla(\nabla \cdot \mathbf{E}) = -\nabla(\ln \epsilon) \cdot \mathbf{E}$ , substitute in Equation (2.25) and rearrange to obtain the E-field vector wave equation:

$$\nabla^2 \mathbf{E} + \omega^2 \epsilon \mu \mathbf{E} = -\nabla(\ln \epsilon) \cdot \mathbf{E} \quad (2.27)$$

Similarly the H-field vector wave equation can be obtained:

$$\nabla^2 \mathbf{H} + \omega^2 \epsilon \mu \mathbf{H} = -\nabla(\ln \epsilon) \times \nabla \times \mathbf{H} \quad (2.28)$$

The formulae in Equations (2.27) and (2.28) are the vector form of the electric and magnetic wave equation, respectively. These formulae contain both longitudinal and transverse components of the field and are coupled. In homogeneous media (material property independent of position), the right hand side of Equation (2.27) vanishes because  $\nabla \cdot \epsilon = 0$ , thus the longitudinal and transverse components are decoupled [200].

These assumptions hold even when the medium has weak inhomogeneity because the change in the refractive index is small ( $\nabla\epsilon/\epsilon$  is small compared over length scale that E and H progress in space) [205]. The result is the scalar E-field wave equation (Equation (2.29)). The scalar formulation is used whenever possible due to its simplicity in comparison with vector formulation. It can be used in homogeneous isotropic material, anisotropic waveguide and open boundary problem. However, if the longitudinal field component is not small enough to be neglected, and may couple with the transverse component, then the latter formulation has to be used [200].

$$\nabla^2 E = \omega^2 \epsilon \mu E \quad (2.29)$$

Similarly the H-field scalar equation is obtained.

$$\nabla^2 H = \omega^2 \epsilon \mu H \quad (2.30)$$

In this thesis, the vector formula is implemented to solve for the modes of the waveguides studied. The computational methods are discussed in the next section along with a discussion on the advantages and disadvantages of the different methods.

## 2.2 Numerical Methods

The analysis of optical devices requires a sophisticated process and requires a huge amount of mathematical operations to find a solution. The time taken to solve such problems would be impossible without the aid of computational resources. Therefore, analytical and numerical methods are employed intensively. The performance of computational methods is improving rapidly due to two reasons; the advance in computer technology and the improvement in algorithms [199]. In this section the analytical and numerical approaches are discussed.

### 2.2.1 Analytical methods

Analytical methods have been implemented to solve for solutions of electromagnetic problems. They are used in simple structures like in slab, buried and rib waveguides. Although analytical methods give accurate solutions, they are limited and are not applicable to many real-world cases [199] which involve complex geometries and inhomogeneous domains [206]. Analytical methods were more applicable before computers and there are various methods implemented to solve boundary-value problems. Some of these methods are Effective Index Method [207], Marcattili's Method [208] and

Variational Method [200]. However, they have an important role in the development of numerical methods [201].

There are a variety of analytical methods used to obtain solutions for simple optical waveguides, however, obtaining a solution for complex optical waveguide structures with inhomogeneity in the spatial domain is not possible with the aid of analytical methods. Therefore, approximations and assumptions are made to problems to be solved with numerical methods. In the next section, some of the common numerical methods used in modeling of electromagnetic problems are introduced.

### 2.2.2 Numerical methods

The lack of analytical solutions to complex real-world problems has led to the development of numerical solutions. The approximation or numerical methods, as the name indicates, are based on approximating the solution by applying assumptions to the problem of interest which leads to some error that can be tolerated. The approximations made are either numerical or to the physics. Hence, the numerical methods are classified according to these approximations into two main classes.

The first class is the asymptotic methods. These methods require fundamental approximation in the Maxwell's equations. The approximation in physics limits the use of these methods for general cases [209, 210]. They are usually used for electrical large metallic objects, which is a drawback of these methods. Their advantages are low computational resources and high efficiency [210].

The other class of numerical methods is the full-wave methods. In these methods, approximation are made numerically and there is no initial physical approximation. These methods are further classified according to the formula used, integral or differential, and according to the domain they operate in, time or frequency [209]. However, this classification is general because some of the methods can be implemented with either formula and/or in both domains.

The frequency domain methods are suitable for studying steady-state narrow-band applications, whereas time domain methods are suitable for wide-band transient applications. The discretization in integral formula involves the important surface of the problem thus the computational resources are reduced. This comes with the price of poor presentation of complex structures and inhomogeneous materials [211]. The integral formula can be used to study scattering and open domain problems. In differential formulae, the discretization involves the full volume which is computationally consuming but can present inhomogeneous media and complex structures efficiently. The differential formulae can be implemented in a boundary problem. Therefore, from

the discussion above it is clear that there is no universal choice of best method in all cases. In each case there are advantages and disadvantages of the methods and the appropriate method is chosen.

There are general steps required for all full-wave methods. A common aspect of full-wave numerical methods is to discretize the system domain into smaller sub-domains and thus the solution is almost independent of the system [201]. Full-wave methods generally speaking involve three major steps to solve the problem. First, the problem of interest should be defined by a governing equation which is obtained from Maxwell's equations. However, every method differs in preprocessing of Maxwell's equation to obtain the final formula. The second step is discretization of the domain into non-overlapping sub-domains in order to present arbitrary inhomogeneous dielectric waveguides such that every sub-domain or element is homogeneous. Discretization results in a set of equations which are described in a matrix form. The final step requires the solution of the matrix of unknowns using efficient algorithms [201]. The most popular full-wave methods in the field are listed with an introduction to each in the following paragraphs.

**Method of moments:**

The Method of Moments (MoM), also known as boundary element method, has advantage in problems involving open regions. It is mostly applied in frequency domain. It has been the most widely used method in antenna engineering [209]. The mathematical formulation representing electromagnetic fields is implemented in MoM by discretizing the integral equation [210]. It is computationally efficient but it requires sophisticated mathematics than other methods [203]. It is the preferred method for frequency domain scattering and radiation problems [209].

**Finite difference method:**

The Finite Difference Method (FDM) is the most widely used method in electromagnetic problems due to being straightforward and ease of implementation. The domain is divided into a mesh and the solution is found for each grid point. It implements the differential Maxwell's equations to derive the wave equation to find the modal solution. The differential operator is replaced by difference operators by using central difference formula. There is another method which shares the same concept of meshing, which is known as the Finite-Difference Time-Domain (FDTD) method. It is used in the analysis of time domain problems by directly discretizing the Maxwell's equations. Both methods are very efficient as they require few operations on each point on the grid [199].

The back draw of FDM is that the grid should be uniform for the method to work well.

It also uses staircase approximation of boundaries which are not in alignment with the grid [199]. Moreover, the solution is only available at the nodes [200].

**Finite element method:**

The Finite Element Method is capable of representing complex domains accurately as it discretizes the domain into a grid of unstructured elements and thus approximates boundaries better. The typical element is a triangle in 2D and tetrahedron in 3D. FEM can be implemented in frequency domain problems [199]. Also, it can be implemented in time domain but it was developed for frequency domain. FEM is efficient for microwave device and eigenvalue problem simulations [209].

This method and the previous two are the fundamental methods in electromagnetic analysis [203]. Therefore, the first point of choice to analysis optical fibers and waveguides is one of these methods. In this work, due to the arbitrary boundaries of PCF structures the FEM is chosen because it can approximate boundaries better. The steps of implementing FEM in optical waveguide problems are described in the next section.

**Transmission line matrix method:**

The Transmission Line Matrix (TLM) method solves field problem by the use of circuit equivalents [198]. It is used generally for wave propagation in the time domain where the waveguide is discretized into a 3D lattice. The method uses differential formula [211]. It is similar to FDTD method apart from using an array of short transmission lines instead of direct discretization of Maxwell's equations [209]. It can also be implemented in the frequency domain [211].

**Method of lines:**

The Method of Lines (MoL) has similarity with FDM. For a system of partial differential equations the independent variables are all discretized except one which is obtained analytically therefore the computational time of MoL is efficient [212].

## 2.3 Finite Element Method

The finite element method was first proposed in 1940s. It was deployed in various fields in structural mechanics, thermodynamics and aero engineering in 1950s. In 1960s, it was implemented for solving electromagnetic problems. It has the widest implementation range among computational method in most of physical and engineering fields due to its versatility in dealing with complex designs [209, 213, 214].

The basic ideology of FEM is to divide a domain into sub-domains/elements and approximating the solution in each element with a basis function, usually polynomial,

which has a non-zero value over the element and zero else where [201]. The solution at any point in the element can be computed because the interpolation function is continuous inside the element. Each element has its interpolation function for the unknown field ( $\Psi$ ) and the field in the element,  $e$ , is expressed as

$$\Psi^e = \sum_{i=1}^m N_i \Psi_i \quad (2.31)$$

where  $m$  is the number of nodes in the element,  $N_i$  is the interpolation function and  $\Psi_i$  is field value at node  $i$ .

Higher-order interpolation function leads to more accurate solution but the formulation is complex and more difficult to derive because the mathematics is challenging [215]. Moreover, the bandwidth of the system of equations increase when using higher-order interpolation functions [213]. The field across the boundary of adjacent elements is continuous since the elements share nodes and field interpolation is defined at the nodes. Therefore, the boundary condition can be integrated in the implementation of FEM smoothly [200, 206].

The solution of boundary value problem involves the use of either variational approach (Rayleigh-Ritz method) or weighted residuals (Galerkin method) to set up FEM and both lead to an expression which can be reduced by FEM to eigenvalue matrix equations [216]. The concept of the variational method is concerned with the stationary point of the functional value and this can be found by minimizing or maximizing an expression of variables. The result obtained by minimizing or maximizing the functional yields the associated Euler-Lagrange equation. The variational principle exists if and only if the Euler-Lagrange equations correspond to the physical problem under consideration. If a variational principle exists then a solution can be obtained by trying a set of basis functions with unknown coefficients in the formula. The derivative of the functional with respect to coefficients vanishes [200, 201]. The steps to produce the  $\mathbf{H}$  field formula using the variational principle are shown below.

The wave equation (Equation (2.26)) can be presented as an eigenvalue equation

$$L\mathbf{H} - \lambda M\mathbf{H} = 0 \quad (2.32)$$

where operators are  $M = \mu$  and  $L = \nabla \times \epsilon^{-1} \nabla \times$ , and the eigenvalue is  $\lambda = \omega^2$ . When the  $L$  operator is self-adjoint which means ( $\langle L\phi, \psi \rangle = \langle \phi, L\psi \rangle$ ) then minimizing or maximizing the functional gives:

$$F(\tilde{H}) = \frac{1}{2} \langle L\tilde{H}, \tilde{H} \rangle - \frac{\lambda}{2} \langle M\tilde{H}, \tilde{H} \rangle \quad (2.33)$$

where the symbol  $\langle \rangle$  is the inner product which is defined as follows

$$\langle f, g \rangle = \int g^* \cdot f dV \quad (2.34)$$

where \* stands for conjugate

The stationary value of the functional is when  $F(\tilde{H}) = 0$  then

$$\lambda = S.V. \frac{\langle L\mathbf{H}, \mathbf{H} \rangle}{\langle M\mathbf{H}, \mathbf{H} \rangle} \quad (2.35)$$

where *S.V.* stands for the stationary value

Therefore, the full vectorial  $\mathbf{H}$  field functional obtained from the Rayleigh-Ritz method is

$$\omega^2 = S.V. \frac{\iint (\nabla \times \mathbf{H})^* \cdot \epsilon^{-1} (\nabla \times \mathbf{H}) dV}{\iint \mathbf{H}^* \cdot \mu \mathbf{H} dV} \quad (2.36)$$

The minimization formula obtained as an eigenvalue problem is

$$[A]\mathbf{x} = \lambda [B]\mathbf{x} \quad (2.37)$$

where *A* is the mass matrix, *B* is the stiffness matrix,  $\mathbf{x}$  is the eigenvector and  $\lambda$  is the eigenvalue.

In simple words, the procedure for the variational method requires finding a functional whose minimum corresponds to the differential equation of the problem under the given boundary conditions. The variable of the functional is defined, generally speaking, as a polynomial with unknown coefficients. The boundary conditions are applied to the polynomial which may reduce the coefficient. Then substituting the polynomial in the functional and performing integration. A partial derivatives of the result with respect to each coefficients is set to zero to obtain the approximate solution.

The matrices generated by this method are symmetric and this simplifies the computation. Moreover, the natural boundary condition in the formula is the perfect electric conductor and can be left free in most electromagnetic problems. Therefore, it is easy to set up numerical methods with the variational principle. The draw-back is that the method cannot be implemented in all problems and only applied when the variational principles exists [200]. Therefore, the problem should be tested if the variational principle exist.

The alternative to Rayleigh-Ritz method is the Galerkin method which does not require a knowledge of the functional [200, 217]. It can be presented in terms of an operator equation:

$$Lu = v \quad (2.38)$$

where  $L$  is a differential operator,  $v$  is the source of excitation and  $u$  the unknown function.

The unknown function is determined by expanding it with some known basis functions with unknown coefficients. The coefficients are chosen to minimize the residual error, which is defined as in Equation (2.39), and forced to zero [200, 217].

$$R(s) = Lu - v \quad (2.39)$$

If the basis functions and unknown coefficients represent the exact solution of the problem, only then the residual error can be zero. Otherwise, the error is minimized by choosing weight functions which are orthogonal to the residual error. Therefore, the weighted integral of the residual is set to zero [200, 217]. These steps leads to a matrix form:

$$[L][u] = [v] \quad (2.40)$$

where, in the case of electromagnetics, the unknown function  $u$  is the magnetic field, the operator  $L = \nabla \times \epsilon^{-1} \nabla \times - \omega^2 \mu$ , and the source  $[v] = 0$ .

The advantage of this method is that it can be used even when the variational approach cannot be applied. However, the natural boundary conditions need extra care as they are not easily satisfied as in the Rayleigh-Ritz method [200]. Although any one of these methods can be applied to set up the FEM, in this thesis the variational method is utilized. The vector and scalar formulations of FEM are discussed in the next section.

### 2.3.1 Formulation

The FEM can be implemented to solve both the vector and scalar wave equations. If the change in the refractive index is small then the weakly guiding approximation (when  $\nabla \epsilon / \epsilon$ ,  $\nabla \mu / \mu$  are small compared with the length that the fields evolve over) holds and the right hand side of the vector wave equations (Equation (2.27) and (2.28)) can be neglected. This leads to decoupling of the longitudinal and transverse field components. Therefore, the scalar wave formulation can be used because the equation is less complex. However, the vector formulation is used in this work due to the

complexity of the refractive index profile and the use of the scalar formulation would not be possible to find a solution. In this section, the scalar formulation is presented and then the derivation of the vector formulation is given in the following section [200].

The scalar formulation can be presented in two ways depending on the dominant field in the transverse direction where the magnitude of the longitudinal components is very small and it is sufficient to solve one of the scalar Equations (2.29) or (2.30) for electric and magnetic fields, respectively. The modes in waveguides are not purely transverse electric or transverse magnetic. Thus the fields are expressed either as quasi-transverse electric (TE) or quasi-transverse magnetic (TM) modes. In the case of TE where the electric field ( $E_x$ ) is dominant, the functional formulation is described by Equation (2.41), and for TM mode ( $H_x$ ) dominant the functional is shown in Equation (2.42) [200].

$$L = \iint_{\Omega} \left[ \left( \frac{\partial E_x}{\partial x} \right)^2 + \left( \frac{\partial E_x}{\partial y} \right)^2 - k_0 n^2 E_x^2 + \beta^2 E_x^2 \right] d\Omega \quad (2.41)$$

where  $\Omega$  is the cross section of the waveguide.

In (2.41)  $\beta^2$  would be the eigenvalue for given  $k_0$  and in (2.42)  $k_0^2$  is the eigenvalue for a given  $\beta$ .

$$L = \iint_{\Omega} \left[ \frac{1}{n^2} \left( \frac{\partial H_x}{\partial x} \right)^2 + \frac{1}{n^2} \left( \frac{\partial H_x}{\partial y} \right)^2 - k_0 H_x^2 + \frac{1}{n^2} \beta^2 E_x^2 \right] d\Omega \quad (2.42)$$

The Equations (2.41) and (2.42) have the continuity of  $\frac{\partial E_x}{\partial \hat{n}}$  and  $\left( \frac{1}{n^2} \right) \left( \frac{\partial H_x}{\partial \hat{n}} \right)$  as the natural boundary condition, respectively, where  $\hat{n}$  is the outward normal unit vector. The vector formulation is discussed in the following section.

### 2.3.2 Vector formulation

The vector formulation is used when the modes are hybrid and both longitudinal and transverse components may couple. The vector formulation can be derived in different ways depending on the field components used in the derivation. The formulation can be derived by the use of:

- transverse electric field components.
- transverse magnetic field components.
- both transverse field components.
- both longitudinal field components.

- all six field components.
- all electric (**E**-field formulation) field components.
- all magnetic (**H**-field formulation) field components.

The latter two are more efficient in terms of computational resources. However, the **E**-field formulation requires further integration to impose the boundary conditions when the material changes at the boundary between the two elements. In contrast, in the **H**-field formulation, the change in the material at the boundaries does not require imposing the boundary condition because both material are non-magnetic. The use of six components does not have much advantage over the **H**-field formulation and requires more computational resources for storing and processing. Therefore, **H**-field formulation is used in this work and its derivation is given in the following discussion. The Rayleigh-Ritz procedure is used to obtain the matrix equation. First, the functional of the vector **H**-field formulation is defined as:

$$F = \iint_{\Omega} (\nabla \times \mathbf{H})^* \left( [\epsilon_r]^{-1} \nabla \times \mathbf{H} \right) d\Omega - \omega_0^2 \iint_{\Omega} \mathbf{H}^* \cdot \mathbf{H} d\Omega \quad (2.43)$$

The domain is divided into small elements and the field in each element is defined as:

$$\mathbf{H} = \sum_{i=1}^m N_i H_i \quad (2.44)$$

where  $m$  is the number of nodes in the element,  $H_i$  is the magnetic field at the node  $i$ , and  $N_i$  is the basis functions (shape functions).

The matrix form of Equation (2.44) is:

$$\mathbf{H} = [N]^T \{H\}_e \quad (2.45)$$

where  $T$  stands for transpose,  $[N]^T$  matrix of basis function and  $\{H\}_e$  column vector of nodal field values.

Substituting (2.45) into (2.43) and applying the variational principle, then:

$$\iint_{\Omega} (\nabla \times [N]^T \{H\}_e)^* [\epsilon_r]^{-1} \nabla \times [N]^T \{H\}_e - \omega_0^2 [N]^T \{H\}_e^* [N]^T \{H\}_e d\Omega = 0 \quad (2.46)$$

Writing it in matrix form:

$$[A]\{H\} - \omega_0^2 [B]\{H\} = 0 \quad (2.47)$$

where  $\omega_0^2$  is the eigenvalue and  $\{H\}$  is the eigenvector.  $[A]$  is a complex Hermitian matrix and can be reduced to real symmetric, in the case of lossless dielectrics, and  $[B]$  is a real symmetric matrix. Both matrices are defined as:

$$[A] = \iint (\nabla \times \mathbf{H})^* \cdot \epsilon^{-1} \cdot (\nabla \times \mathbf{H}) d\Omega \quad (2.48)$$

$$[B] = \iint \mathbf{H}^* \cdot \mu \cdot \mathbf{H} d\Omega \quad (2.49)$$

The solution to Equation (2.47) may contain spurious solutions which are nonphysical. These solutions occur because some mathematical eigenvalue solutions of the equation do not satisfy the divergence condition ( $\nabla \cdot \mathbf{H} = 0$ ) automatically, which must be satisfied by physical solutions. Therefore, the penalty function method is implemented to eliminate or suppress the spurious solutions. The goal of the penalty function is to impose the divergence free constraint on the solution variables [216]. The result of employing the penalty function is an additional term called penalty term ( $\alpha$ ). The value of the penalty term controls the number of the spurious solutions. The higher the term value the fewer the spurious solutions are. However, a reasonable value for  $\alpha$  is  $1/\epsilon$ , where  $\epsilon$  is the permittivity of the core material. The use of penalty function results in manipulation of the  $[A]$  matrix [200]. However, the matrix size does not change with the use of penalty function and it has a negligible extra processing time [218]. The formulation would be as shown:

$$\omega^2 = \frac{\iint (\nabla \times \mathbf{H})^* \cdot \epsilon^{-1} \cdot (\nabla \times \mathbf{H}) d\Omega + \left(\frac{\alpha}{\epsilon}\right) \iint (\nabla \cdot \mathbf{H})^* (\nabla \cdot \mathbf{H}) d\Omega}{\iint \mathbf{H}^* \cdot \mu^{-1} \cdot \mathbf{H} d\Omega} \quad (2.50)$$

The formulation has been derived and penalty term is included in the vector formulation, which is used to find the modal solutions of waveguides of this work. Implementation of the penalty function is discussed in Section (2.3.5). The next issue is the discretization of the domain into smaller sub-domains to implement the FEM and is discussed in the next section.

### 2.3.3 Domain discretization

The domain discretization or meshing is a critical step in FEM as the mesh determines the computational requirements such as storage and processing time. Furthermore, the mesh plays an important role in accuracy of the results. Meshing is the process of dividing the domain into small subdivisions (elements) which do not overlap. The

elements should be adjacent with no space in between to cover the whole domain. There are different types of elements depending on the domain to be discretized. The elements range from simple lines to more complex elements. The basic finite elements for 1, 2 and 3D are shown in Figure (2.2).

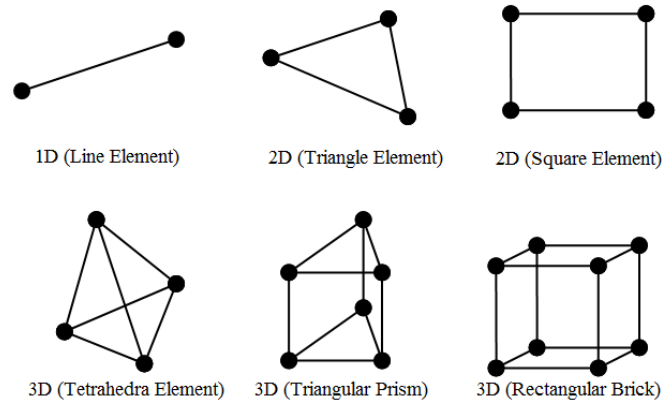


Fig. 2.2 Basic finite element in 1, 2 and 3D [213]

For a 1D problem a line element is used with two nodal points, one at each end for first-order elements. In 2D, which is the case considered in this work, the element is either triangular or rectangular. A first-order triangular element has three nodal points and a square element has four. Higher order elements have more nodal points depending on the degree of the element hence they are more accurate. However, higher order elements result in complicated formulation because the degree of the interpolation function is related to the degree of the element. Triangles can represent complex domains more accurately than rectangles because arbitrary boundaries can be approximated more accurately with triangles as illustrated in Figure (2.3) [219]. Therefore, they are implemented in this work.

In Figure (2.4) triangular elements of first- second- and third-order are shown. In 3D a tetrahedron is the common element also there are triangular prisms and rectangular brick elements [200, 213].

The element is represented by an interpolation function which should approximate the field in the element with respect to the real physical problem. The accuracy of the solution is related to the computational resources. Therefore, a trend to compensate between the accuracy and the available/affordable resources is required. The error should be tolerable and the computer storage and processing time need to be acceptable. The most popular interpolation functions to represent elements are polynomials. The polynomial should contain all possible terms to be complete. This implies that the polynomial is unique and the orientation of the coordinates has no effect on the shape

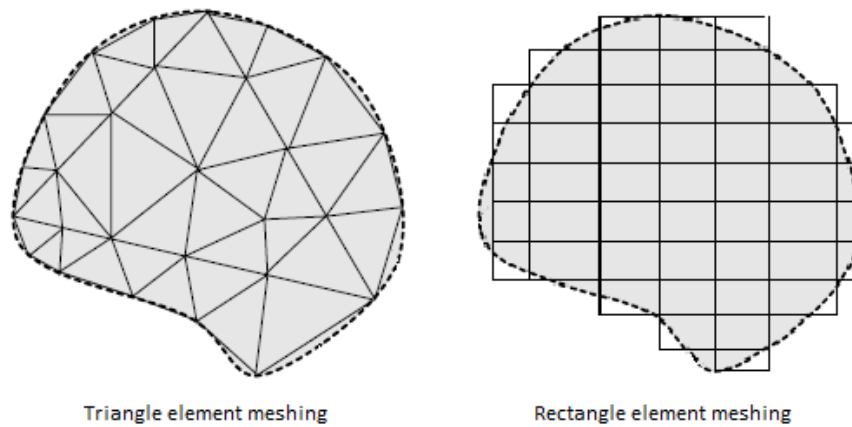


Fig. 2.3 Mesh comparison of triangular (left) and rectangular (right) elements [219]

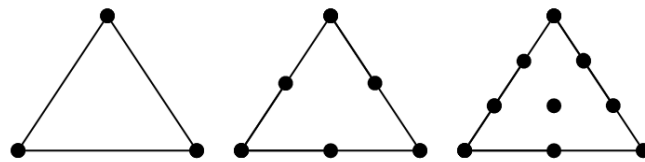


Fig. 2.4 First- second- and third-order triangular elements (left to right) [200]

function. The polynomial must have number of terms equivalent to the nodal points to be unique. In first-order triangular element, there ought to be three terms to form a complete polynomial. The number of terms required for a polynomial defined by Pascal triangle as shown in Figure (2.5), where the polynomial of an element of any order contains all terms in the same order line and the lines above of the Pascal triangle.

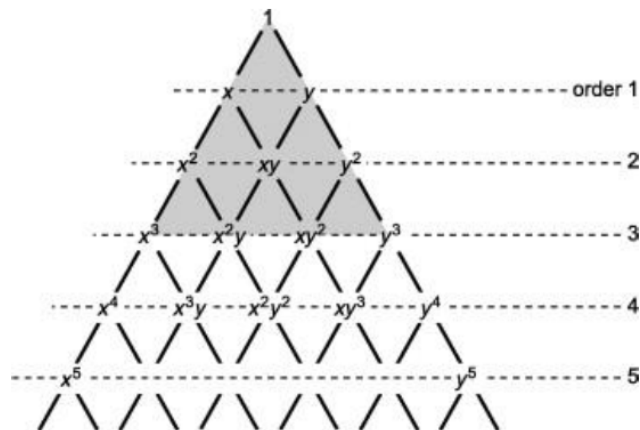


Fig. 2.5 Pascal triangle and number of terms for a complete polynomial [200]

The field value at the nodal points of each element is defined by a shape function. The shape function is set as a polynomial which is fit to the field at the nodes and the coefficients are determined for every element. The shape function for a first order

triangular element can be a polynomial ( $a + bx + cy$ ) to represent the field in the nodes. The field in each element ( $\phi_e$ ) is defined by:

$$\phi_e(x, y) = a + bx + cy \quad (2.51)$$

where  $a, b, c$  are constants. The field at nodes is:

$$\phi_e(x_i, y_i) = \phi_i \quad i = 1, 2, 3 \quad (2.52)$$

Therefore, the field at the three nodal points is expressed as

$$\begin{aligned} \phi_1 &\equiv \phi_e(x_1, y_1) = a + bx_1 + cy_1 \\ \phi_2 &\equiv \phi_e(x_2, y_2) = a + bx_2 + cy_2 \\ \phi_3 &\equiv \phi_e(x_3, y_3) = a + bx_3 + cy_3 \end{aligned} \quad (2.53)$$

In the matrix form

$$\begin{Bmatrix} \phi_1 \\ \phi_2 \\ \phi_3 \end{Bmatrix} = \begin{bmatrix} 1 & x_1 & y_1 \\ 1 & x_2 & y_2 \\ 1 & x_3 & y_3 \end{bmatrix} \begin{Bmatrix} a \\ b \\ c \end{Bmatrix} \quad (2.54)$$

The constants  $a, b, c$  are determined as

$$\begin{aligned} a &= \frac{1}{2A_e} [\phi_1(x_2y_3 - x_3y_2) + \phi_2(x_3y_1 - x_1y_3) + \phi_3(x_1y_2 - x_2y_1)] \\ b &= \frac{1}{2A_e} [\phi_1(y_2 - y_3) + \phi_2(y_3 - y_1) + \phi_3(y_1 - y_2)] \\ c &= \frac{1}{2A_e} [\phi_1(x_3 - x_2) + \phi_2(x_1 - x_3) + \phi_3(x_2 - x_1)] \end{aligned} \quad (2.55)$$

where  $A_e$  is the area of the triangle element and expressed as

$$A_e = \frac{1}{2} \begin{vmatrix} 1 & x_1 & y_1 \\ 1 & x_2 & y_2 \\ 1 & x_3 & y_3 \end{vmatrix} = \frac{1}{2} [(x_2y_3 - x_3y_2) + (x_3y_1 - x_1y_3) + (x_1y_2 - x_2y_1)] \quad (2.56)$$

Substituting Equation (2.55) into Equation (2.51) and rearranging

$$\begin{aligned} \phi_e(x, y) &= N_1(x, y) \cdot \phi_1 + N_2(x, y) \cdot \phi_2 + N_3(x, y) \cdot \phi_3 \\ \phi_e(x, y) &= [N] \{\phi_e\} \end{aligned} \quad (2.57)$$

where  $N_i$  are the shape functions and are defined as

$$\{N\}^T = \begin{bmatrix} N_1 \\ N_2 \\ N_3 \end{bmatrix} = \frac{1}{2A_e} \begin{bmatrix} x_2y_3 - x_3y_2 & y_2 - y_3 & x_3 - x_2 \\ x_3y_1 - x_1y_3 & y_3 - y_1 & x_1 - x_3 \\ x_1y_2 - x_2y_1 & y_1 - y_2 & x_2 - x_1 \end{bmatrix} \begin{bmatrix} 1 \\ x \\ y \end{bmatrix} \quad (2.58)$$

The shape function matrix can also be

$$\{N\}^T = \begin{bmatrix} N_1 \\ N_2 \\ N_3 \end{bmatrix} = \frac{1}{2A_e} \begin{bmatrix} a_1 + b_1x + c_1y \\ a_2 + b_2x + c_2y \\ a_3 + b_3x + c_3y \end{bmatrix} \quad (2.59)$$

$a_i, b_i, c_i$  and  $i = 1, 2, 3$  are calculated as

$$\begin{aligned} a_1 &= x_2y_3 - x_3y_2 \\ b_1 &= y_2 - y_3 \\ c_1 &= x_3 - x_2 \end{aligned} \quad (2.60)$$

Similarly  $a_2, b_2, c_2, a_3, b_3$  and  $c_3$  can be calculated by cyclic exchange of  $1 \rightarrow 2 \rightarrow 3$  in Equation (2.60). The shape function  $N_i$  has a value of 1 at node  $i$  and 0 where else.

The domain discretization and shape functions have been discussed. The derivation of matrix of unknown coefficients at nodal points is listed. Every node in the element has a local number, corresponding local coordinates and also a global number. A first-order triangular element has three nodes with local numbers 1, 2 and 3. The total number of nodes in the domain are numbered using a global node number scheme. In the global matrices, the entry value has contribution from all elements which belong to that node. The local and global numbers mapping represents the contribution of nodes in the global matrices [200]. The mapping and adding of element coefficient matrices to the global coefficient matrix entries is called the assembly process. The element coefficient matrix dimension is equal to the number of the nodes in the element. The dimension of a first-order triangular element matrix is  $9 \times 9$ . However the matrix is symmetric only lower triangular matrix is stored and zeros are not stored which minimize the size of the required memory [219]. The next step is the generation of the global and element matrices. The formation of these matrices is given in the next section.

### 2.3.4 Element and global matrices

The formation of matrices, that represent the matrix eigenvalue equation derived from the wave equation by FEM, is discussed in this section. They are the global and element

matrices. In Equation (2.45), the field is expressed in matrix form, and as the interest is in all field components ( $H_x$ ,  $H_y$  and  $H_z$ ) then the equation can be expanded

$$\{H\}_e = [\{H_x\}_e \{H_y\}_e \{H_z\}_e]^T \quad (2.61)$$

and

$$[N]^T = \begin{bmatrix} \{N\} & \{0\} & \{0\} \\ \{0\} & \{N\} & \{0\} \\ \{0\} & \{0\} & j\{N\} \end{bmatrix} \quad (2.62)$$

where  $\{N\} = [N_1 N_2 N_3]^T$  and  $\{0\}$  is null vector.

The  $j$  term in matrix is for lossless cases when the component of  $H_z$  is  $90^\circ$  out of phase with transverse component. By substituting Equation (2.62) into (2.45) then

$$\{H\}_e = \begin{bmatrix} N_1 & N_2 & N_3 & 0 & 0 & 0 & 0 & 0 & 0 \\ 0 & 0 & 0 & N_1 & N_2 & N_3 & 0 & 0 & 0 \\ 0 & 0 & 0 & 0 & 0 & 0 & jN_1 & jN_2 & jN_3 \end{bmatrix} \begin{pmatrix} H_{x1} \\ H_{x2} \\ H_{x3} \\ H_{y1} \\ H_{y2} \\ H_{y3} \\ H_{z1} \\ H_{z2} \\ H_{z3} \end{pmatrix} \quad (2.63)$$

The global matrices  $[A]$  (mass matrix) and  $[B]$  (stiffness matrix) in Equation (2.47) are determined as follows:

$$(\nabla \times \mathbf{H})_e = [\nabla \times] [N]^T \{H\}_e = \begin{bmatrix} 0 & -\partial/\partial z & \partial/\partial y \\ \partial/\partial z & 0 & -\partial/\partial x \\ -\partial/\partial y & \partial/\partial x & 0 \end{bmatrix} [N]^T \{H\}_e \quad (2.64)$$

Equation (2.64) can also be written as

$$(\nabla \times \mathbf{H})_e = [Q]^T \{H\}_e \quad (2.65)$$

where  $[Q]$  is

$$[Q] = \begin{bmatrix} \{0\} & j\beta\{N\} & \partial\{N\}/\partial y \\ -j\beta\{N\} & \{0\} & -\partial\{N\}/\partial x \\ -\partial\{N\}/\partial y & \partial\{N\}/\partial x & \{0\} \end{bmatrix} \quad (2.66)$$

Then  $A$  is given as

$$A = \sum_e [A]_e = \sum_e \iint_e \frac{1}{\epsilon_e} [Q]^* [Q]^T dx dy \quad (2.67)$$

$$A = \begin{bmatrix} [A_{xx}] & [A_{xy}] & [A_{xz}] \\ [A_{yx}] & [A_{yy}] & [A_{yz}] \\ [A_{zx}] & [A_{zy}] & [A_{zz}] \end{bmatrix} \quad (2.68)$$

where

$$[A_{xx}] = \iint_e \left[ \beta^2 \{N\} \{N\}^T + \frac{\partial\{N\}}{\partial y} \frac{\partial\{N\}^T}{\partial y} \right] dx dy \quad (2.69)$$

$$[A_{xy}] = \iint_e -\frac{\partial\{N\}}{\partial y} \frac{\partial\{N\}^T}{\partial x} dx dy \quad (2.70)$$

$$[A_{xz}] = \iint_e \beta \{N\} \frac{\partial\{N\}^T}{\partial x} dx dy \quad (2.71)$$

$$[A_{yy}] = \iint_e \left[ \beta^2 \{N\} \{N\}^T + \frac{\partial\{N\}}{\partial x} \frac{\partial\{N\}^T}{\partial x} \right] dx dy \quad (2.72)$$

$$[A_{yz}] = \iint_e \beta \{N\} \frac{\partial\{N\}^T}{\partial y} dx dy \quad (2.73)$$

$$[A_{zz}] = \iint_e \left[ \frac{\partial\{N\}}{\partial y} \frac{\partial\{N\}^T}{\partial y} + \frac{\partial\{N\}}{\partial x} \frac{\partial\{N\}^T}{\partial x} \right] dx dy \quad (2.74)$$

and the  $B$  matrix is

$$B = \sum_e \iint_e [N]^* [N]^T dx dy \quad (2.75)$$

$$B = \begin{bmatrix} [B_{xx}] & [0] & [0] \\ [0] & [B_{yy}] & [0] \\ [0] & [0] & [B_{zz}] \end{bmatrix} \quad (2.76)$$

$$[B_{xx}] = [B_{yy}] = [B_{zz}] = \sum_e \iint_e [N]^* [N]^T dxdy \quad (2.77)$$

Matrices  $A$  and  $B$  are the general form of global matrices for any 2D shape functions. In the discussion to follow, the element matrices are given for a first-order triangle element. The size of the matrices is 9x9.

$$\int_e N_1^2 dxdy = \int_e N_2^2 dxdy = \int_e N_3^2 dxdy = \frac{A_e}{6} \quad (2.78)$$

$$\int_e N_1 N_2 d\Omega = \int_e N_2 N_3 d\Omega = \int_e N_1 N_3 d\Omega = \frac{A_e}{12} \quad (2.79)$$

$$\iint_e \{N\} \{N\}^T dxdy = \frac{A_e}{12} \begin{bmatrix} 2 & 1 & 1 \\ 1 & 2 & 1 \\ 1 & 1 & 2 \end{bmatrix} \quad (2.80)$$

$$\frac{\partial \{N\}}{\partial x} = \frac{1}{2A_e} \begin{bmatrix} b_1 \\ b_2 \\ b_3 \end{bmatrix} \quad (2.81)$$

$$\frac{\partial \{N\}}{\partial y} = \frac{1}{2A_e} \begin{bmatrix} c_1 \\ c_2 \\ c_3 \end{bmatrix} \quad (2.82)$$

$$\left[ \iint_e \frac{\partial \{N\}}{\partial p} \frac{\partial \{N\}^T}{\partial q} dxdy \right]_{ij} = A_e C_{pi} C_{qj} \quad p, q = x, y \quad (2.83)$$

$$\left[ \iint_e \frac{\partial \{N\}}{\partial p} \{N\}^T dxdy \right]_{ij} = \frac{A_e}{3} C_{pi} \quad (2.84)$$

$$[A]_{e(1,1)} = \frac{1}{\epsilon} \int_e -\beta^2 N_1^2 + \left( \frac{\partial N_1}{\partial y} \right)^2 dxdy = \frac{1}{\epsilon} \left[ \frac{-\beta^2 A_e}{6} + c_1^2 A_e \right] \quad (2.85)$$

$$[A]_{e(1,4)} = \frac{1}{\epsilon} \int_e \frac{-\partial N_1}{\partial y} \frac{\partial N_1}{\partial x} d\Omega = -\frac{1}{\epsilon} c_1 b_1 A_e \quad (2.86)$$

Then calculating  $B$  the matrix element

$$[B]_{e(1,1)} = \mu \int_{\Delta} N_1^2 d\Omega = \mu \frac{A_e}{6} \quad (2.87)$$

$$[B]_{e(1,4)} = 0 \quad (2.88)$$

The stiffness element matrix contain several 0 entries. It is shown below

$$B_e = \begin{bmatrix} \frac{A}{6} & 0 & 0 & \frac{A}{12} & 0 & 0 & \frac{A}{12} & 0 & 0 \\ 0 & \frac{A}{6} & 0 & 0 & \frac{A}{12} & 0 & 0 & \frac{A}{12} & 0 \\ 0 & 0 & \frac{A}{6} & 0 & 0 & \frac{A}{12} & 0 & 0 & \frac{A}{12} \\ \frac{A}{12} & 0 & 0 & \frac{A}{6} & 0 & 0 & \frac{A}{12} & 0 & 0 \\ 0 & \frac{A}{12} & 0 & 0 & \frac{A}{6} & 0 & 0 & \frac{A}{12} & 0 \\ 0 & 0 & \frac{A}{12} & 0 & 0 & \frac{A}{6} & 0 & 0 & \frac{A}{12} \\ \frac{A}{12} & 0 & 0 & \frac{A}{12} & 0 & 0 & \frac{A}{6} & 0 & 0 \\ 0 & \frac{A}{12} & 0 & 0 & \frac{A}{12} & 0 & 0 & \frac{A}{6} & 0 \\ 0 & 0 & \frac{A}{12} & 0 & 0 & \frac{A}{12} & 0 & 0 & \frac{A}{6} \end{bmatrix} \quad (2.89)$$

These matrices are implemented in computer codes of FEM to solve for a mode. However, there are spurious solutions which can be eliminated by using a penalty function method, as mentioned in the previous section. The penalty function matrix formation is discussed next.

### 2.3.5 Penalty function

There are spurious solution in all vector formulations and a penalty function is introduced to eliminate and suppress these solutions [200, 220]. The implementation of the penalty function leads to manipulation in the global matrix system. The elements of the matrix generated due to the penalty function are clarified below. Equation (2.47) is written in a matrix form with explicit penalty term as:

$$\left( [A] + \frac{\alpha}{\epsilon} [C] \right) \{H\} - \omega_0^2 [B] \{H\} = 0 \quad (2.90)$$

where

$$C = \sum_e [C]_e = \begin{bmatrix} [C_{xx}] & [C_{xy}] & [C_{xz}] \\ [C_{yx}] & [C_{yy}] & [C_{yz}] \\ [C_{zx}] & [C_{zy}] & [C_{zz}] \end{bmatrix} \quad (2.91)$$

$$[C_{xy}] = \iint_e \frac{\partial \{N\}}{\partial x} \frac{\partial \{N\}^T}{\partial x} dxdy \quad (2.92)$$

$$[C_{xy}] = [C_{yx}]^T = \iint_e \frac{\partial \{N\}}{\partial x} \frac{\partial \{N\}^T}{\partial y} dxdy \quad (2.93)$$

$$[C_{xz}] = [C_{zx}]^T = \iint_e \beta \frac{\partial \{N\}}{\partial x} \{N\}^T dx dy \quad (2.94)$$

$$[C_{yy}] = \iint_e \frac{\partial \{N\}}{\partial y} \frac{\partial \{N\}^T}{\partial y} dx dy \quad (2.95)$$

$$[C_{yz}] = [C_{zy}]^T = \iint_e \beta \frac{\partial \{N\}}{\partial y} \{N\}^T dx dy \quad (2.96)$$

$$[C_{zz}] = \iint_e \beta^2 \{N\} \{N\}^T dx dy \quad (2.97)$$

The formulation including the penalty function has been derived for FEM. The last topic to be discussed in this chapter is the PML which eliminates the problem of reflections due to domain truncation. It is introduced in the next section.

### 2.3.6 Perfectly matched layers

The physical dimension of the problem are infinite in space but the computational resources are limited. Therefore, to present the physical problem to be modeled on a computer, the domain should be truncated to finite by introducing boundaries. The wave at the boundaries can reflect back and result in non-physical radiation to the structure of interest so two techniques were proposed and used in defining the boundary that is used to truncate the domain to finite. The first technique is purely mathematical in which an operator can be defined: either global or local. The global mathematical technique [221] results in a fully populated matrix which is a drawback and cannot be used in large meshes. The local mathematical technique [222] defines the local operator which cancels the field at the boundaries. Its disadvantage is that it requires trial and error to find the boundary position which cannot be placed near the source [200].

The other technique is to place a physical layer of artificial medium. Berenger has proposed the concept of PML in 1994 [223] and since then it has been implemented in numerical methods in particular in FDTD and FEM. The concept of PML is to place an artificial medium with permittivity similar to the material in the main domain. The impedance of both is identical thus no reflection occurs at interface. The PML boundary absorbs waves traveling outwards from the main domain at any angle and frequency. The magnitude of the wave decays exponentially inside PML and no radiation is reflected back to the domain [200, 224].

The first proposed PML was proposed for FDTD and it cannot be easily implemented in unstructured meshes which are used in FEM. The PML is implemented as stretching of the complex coordinate in FEM.

$$x \rightarrow \tilde{x} = \int_0^x s_x(x') dx' \quad (2.98)$$

where  $s_x(x)$  is complex stretching variable.

This results in a change in the nabla operator,  $\nabla$ , which is written as:

$$\nabla \rightarrow \tilde{\nabla} = \hat{x} \frac{\partial}{\partial \tilde{x}} + \hat{y} \frac{\partial}{\partial \tilde{y}} + \hat{z} \frac{\partial}{\partial \tilde{z}} = \hat{x} \frac{1}{s_x} \frac{\partial}{\partial x} + \hat{y} \frac{1}{s_y} \frac{\partial}{\partial y} + \hat{z} \frac{1}{s_z} \frac{\partial}{\partial z} \quad (2.99)$$

Then the Maxwell's equations can be written with  $\tilde{\nabla}$  instead of  $\nabla$ , and the time derivative  $\frac{\partial}{\partial t}$  is replaced with  $j\omega$

$$\tilde{\nabla} \times \mathbf{E} = -j\omega \mathbf{B} \quad (2.100)$$

$$\tilde{\nabla} \times \mathbf{H} = j\omega \mathbf{D} \quad (2.101)$$

$$\tilde{\nabla} \cdot \mathbf{D} = \rho \quad (2.102)$$

$$\tilde{\nabla} \cdot \mathbf{B} = 0 \quad (2.103)$$

This leads to a modification of Equation (2.26). The obtained equation is as shown below where  $\omega^2 \mu \varepsilon = \frac{\omega^2}{c^2} = k_0^2$ .

$$\nabla \times ([p] \nabla \times \mathbf{H}) - k_0^2 [q] \mathbf{H} = 0 \quad (2.104)$$

where

$$[p] = \begin{bmatrix} \frac{s_y s_z}{s_x} \boldsymbol{\varepsilon}_{xx} & s_z \boldsymbol{\varepsilon}_{xy} & s_y \boldsymbol{\varepsilon}_{xz} \\ s_z \boldsymbol{\varepsilon}_{yx} & \frac{s_z s_x}{s_y} \boldsymbol{\varepsilon}_{yy} & s_x \boldsymbol{\varepsilon}_{yz} \\ s_y \boldsymbol{\varepsilon}_{zx} & s_x \boldsymbol{\varepsilon}_{zy} & \frac{s_x s_y}{s_z} \boldsymbol{\varepsilon}_{zz} \end{bmatrix}^{-1} \quad (2.105)$$

and

$$[q] = \begin{bmatrix} \frac{s_y s_z}{s_x} & 0 & 0 \\ 0 & \frac{s_z s_x}{s_y} & 0 \\ 0 & 0 & \frac{s_x s_y}{s_z} \end{bmatrix} \quad (2.106)$$

By following steps of FEM the Equation (2.104) can be written in matrix form as shown in Equation (2.107) which is similar to Equation (2.47).

$$[A] \{\mathbf{H}\} - k_0^2 [q] \{\mathbf{H}\} = 0 \quad (2.107)$$

where

$$[A] = [Q]^T [p] [Q] \quad (2.108)$$

and

$$[Q] = \begin{bmatrix} 0 & 0 & 0 & j\beta N_1 & j\beta N_2 & j\beta N_3 & c_1 & c_2 & c_3 \\ -j\beta N_1 & -j\beta N_2 & -j\beta N_3 & 0 & 0 & 0 & -b_1 & -b_2 & -b_3 \\ -c_1 & -c_2 & -c_3 & b_1 & b_2 & b_3 & 0 & 0 & 0 \end{bmatrix} \quad (2.109)$$

The PML absorbs waves traveling in a particular direction. A simulation window terminated by PML boundary is shown in Figure (2.6) where PML regions are numbered 1 to 8. The  $s_x$  and  $s_y$  values for each of the PML regions are shown in Table (2.1). The values are 1 in non-PML region and  $s_k$  in PML region, where  $s_k$  is complex and are defined as

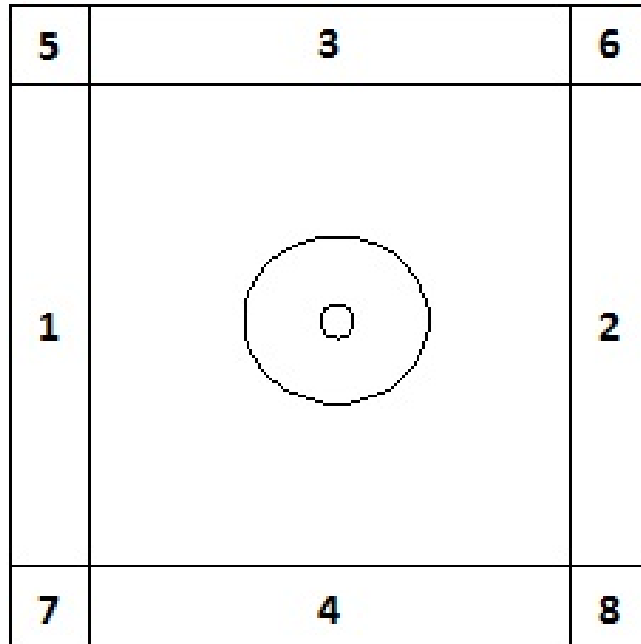


Fig. 2.6 A schematic diagram of simulation window of a conventional fiber structure with PML boundaries [200]

PML parameter	PML region							
	1	2	3	4	5	6	7	8
$s_x$	$s_1$	$s_2$	1	1	$s_1$	$s_2$	$s_1$	$s_2$
$s_y$	1	1	$s_3$	$s_4$	$s_3$	$s_3$	$s_4$	$s_4$

Table 2.1  $s_k$  values in PML regions [200]

$$s_k = 1 - j\alpha_k \quad (2.110)$$

where  $k = 1, 2, 3$  and  $4$ .

$$\alpha_k = \alpha_{k,max} \left( \frac{\rho}{d_k} \right)^2 \quad (2.111)$$

$$\alpha_{k,max} = \frac{3\lambda}{4\pi nd} \ln \left( \frac{1}{R_{max}} \right) \quad (2.112)$$

where  $\rho$  is the distance from the PML,  $d_k$  is thickness of the  $k$ th layer and  $R_{max}$  is tolerance or maximum reflection.

The PML not only absorb unwanted non-physical reflected radiations at boundaries but it provides a mechanism to measure confinement and bending losses of the waveguide. The loss results which are shown in the next chapter are calculated using PML. This is the last and not the least part to explain in the methodology and at the end a summary of the discussion is given in the following section.

## 2.4 Summary

The chapter began with the four coupled Maxwell's differential equations side along the constitutive relations. The vector wave equation has been derived and the assumption made to get the scalar form. Boundary condition have been explained. Then a general view of the analytical and numerical methods given with description of the well known full-wave methods in field of electromagnetics. Thereafter, the steps of implementing FEM have been discussed starting with deriving the formula using the variational principle and weighted residual method. The meshing and formation of global and element matrices were explained. Finally, the penalty function and PML were described.

The results of this work have been obtained by the use of a full vectorial FEM formulation to obtain a modal solution of optical waveguides. The penalty function method was used to suppress the spurious solutions. The PML boundary was imposed to truncate

the domain to finite dimensions. The results obtained are discussed in the following chapters.

## Chapter 3

# Spiral Photonic Crystal Fibers

In the previous chapters the basics of fibers and the propagation of light are discussed; the simulation tools to study the light propagation in fibers are reviewed and the Finite Element Method (FEM) is explained. The results obtained by the FEM simulations are explained in this and the following chapter. This thesis is concerned with the study of Equiangular Spiral Photonic Crystal Fibers (ES-PCF) and other spiral PCF designs so the start of this chapter is an introduction to ES and followed by ES-PCF properties. The Archimedean and Fermat's spiral PCFs are introduced and investigated and the study of their parameters is explained with brief simulation results.

The results discussed in this chapter were obtained to test the effect of various parameters of the spiral PCF on the optical properties. Conventional fibers and a huge range of PCF are fabricated and investigated in silica material so the general simulations of the studies of the parameters are all based on silica material. However, the concept is the same for other materials and this is shown in the next chapter when discussing simulation results in SF57 and Tellurite materials which is used in the published paper for SuperContinuum Generation (SCG) [225].

The refractive index difference between the core and cladding plays an important role in the optical properties. The position and sizes of the holes, and the size of the core are the parameters that effect the effective refractive index of the cladding. The core size can be varied for most PCF designs freely but the hole position is fixed for most structures such as Hexagonal Photonic Crystal Fiber (H-PCF). On the other hand, the spiral PCFs have more parameters to control the design which make spiral PCFs unique. The position of holes is controlled more efficiently with varying the different parameters. These parameters requires knowledge for their effect on the optical properties so that for a specific objective the parameters can be chosen appropriately. In the results presented in this chapter all the parameters are varied independently to understand their effects.

The spiral that has most parameters to vary is the ES-PCF which is the focus of this thesis. The general definition of a spiral is given below then each spiral is discussed individually with comparison of results to preceding spirals whenever possible.

### 3.1 Definition of Spiral

This world is full of different shapes and curves that represent the universe in a beautiful way. These shapes are being investigated, analyzed and represented in mathematical formulae to understand natural phenomenon and employ them in various fields of life. One of these shapes is a spiral which can be noticed in small creatures as snails, flowers, or in huge big galaxies, spreading all over. A spiral is a shape rotated around itself in a systematic way.



Fig. 3.1 Spirals in Nature [226–231]

In a mathematical form, a spiral is a plane curve following a mathematical expression that is described more easily in polar coordinates with a distance  $r$  from the center dependent on an angle  $\theta$ , where it is represented by a point revolving round the center with an increasing  $r$ . The above definition is a description of two dimensional spirals,

but there are more sophisticated three dimensional spirals which have another variable, height, which is a function of  $\theta$  as well. In this thesis, only a discussion of two dimensional spirals is given.

Spiral shapes have been observed thousands of years ago where some spirals have been defined by ancient Greeks [232]. Spirals are important in understanding many natural phenomena. Furthermore, spirals are found in many architectural designs, art works and different objects. Different images of natural spirals are shown in Figure (3.1).

There are different types of spirals in this universe such as Fermat's, Archimedean, lituus, hyperbolic and logarithmic spirals. The latter is also known as Equiangular Spiral (ES) and it is implemented in this work to design PCF with spiral hole distributions. The equiangular spiral is discussed in the next section.

## 3.2 Equiangular Spiral

The history of the Logarithmic spiral goes back to 1638 when Rene Descartes first developed and described its equation. Evangelista Torricelli worked on it independently and found the rectification of the curve's length. Later on it was extensively investigated by Jacob Bernoulli where he found its properties of self-reproduction and in 1692 called it *spira mirabilis* [232].

### 3.2.1 Equiangular spiral curve

The equiangular spiral is represented mathematically in polar coordinates as defined by Descartes in 1638 [232]

$$r = ae^{\theta \cot(\alpha)} \quad (3.1)$$

where the term  $\cot(\alpha)$  is referred to as  $b$  in this thesis and the equation is written as [233]

$$r = ae^{b\theta} \quad (3.2)$$

The  $b$  coefficient controls the tightness of the spiral and in which direction it grows. If  $b = 0$  then the spiral becomes a circle of radius  $a$ . On the contrary, when  $b$  approaches infinity the shape tends to be a straight line. The spiral grows in an anti-clockwise for positive values of  $b$  and in a clockwise for negative values. The value of  $a$  is only a scalar to scale the whole curve and does not have an impact on its shape. Both coefficients  $a$  and  $b$  are arbitrary real constants and  $\theta$  is the angle measured from the

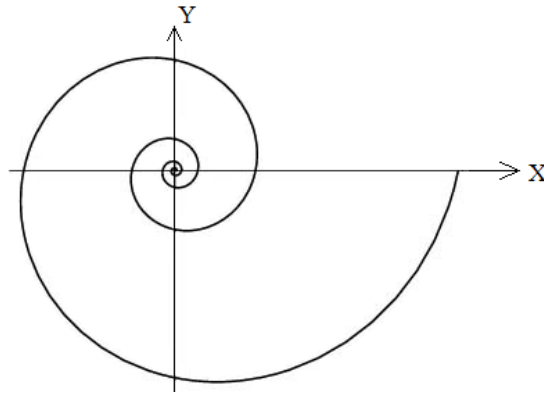


Fig. 3.2 Equiangular spiral [233]

X-axis. The value of  $\theta$  controls the number of turns the curve has. One turn of the curve requires a value of  $\theta = 2\pi$ .

### 3.2.2 Characteristics of equiangular spiral

The distances between the turnings increase in geometric progression, which distinguishes the equiangular spiral from the Archimedean Spiral (AS). Another property of the equiangular spiral is that all radii produce constant angles with the curve, which is the reason to call it "Equiangular spiral" [232]. In natural sea-shells spirals, the growth of an organism is proportional to the size of the organism.

### 3.2.3 ES-PCF

The uniqueness of PCF in performance and adaptability to diverse applications led researchers to investigate and analyzes vast number of designs. In Chapter 1 the main classification of PCF has been given with reference to guiding mechanisms. The designs studied in this work are index-guiding PCF, in which light is guided by M-TIR [100]. The hexagonal structure, also introduced in the same chapter, is compared with the proposed designs in this work. The discussion of H-PCF structure and the parameters of interest are introduced to help in the explanations throughout the thesis. Figure (3.3) shows a schematic of the H-PCF cross section.

The three structural parameters that can be varied in a H-PCF are the pitch ( $\Lambda$ ), hole size ( $d$ ) and number of rings. The latter does not have much effect when number of rings  $> 4$  as the mode is well confined in the core and holes in higher rings do not influence the modal field. However, higher rings have impact on bending loss at small bending radius. The other two parameters are related to each other as a ratio  $d/\Lambda$  which is the most important factor which impacts the guidance properties. The maximum

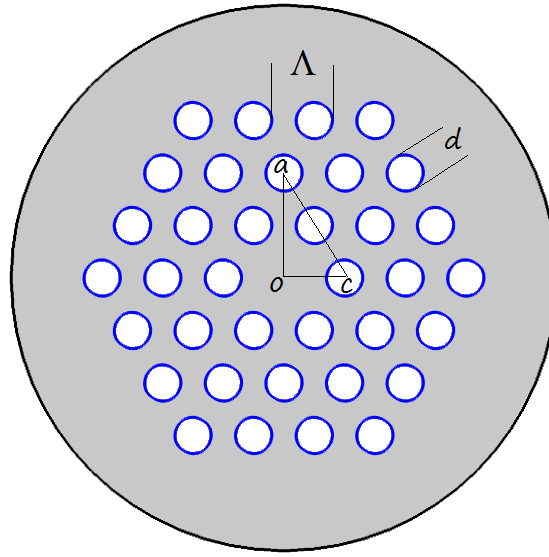


Fig. 3.3 A schematic of H-PCF cross section in transverse direction

theoretical value this ratio can have is 1 when each hole touches neighboring holes. In practice that is not possible because there would be no barrier between holes and it would be one big gap with a core suspended in air without being held by any strut. However, if holes are replaced by solid material then the ratio can be 1. The distance from center of the structure to the center of the hole of the second ring which lies at  $30^\circ$  angle from holes in the first ring is marked as point ( $a$ ) in Figure (3.3). This distance ( $oa$ ) equals, by applying Pythagorean theorem, to  $\sqrt{(ac)^2 - (oc)^2}$  which is

$$oa = \sqrt{3} \Lambda \quad (3.3)$$

This distance  $oa$  in H-PCF is fixed by this relation and it is not possible to adjust the position of the holes. In contrast, the position of holes in ES-PCF can be managed more freely as clarified in the following discussion. The formula in Equation (3.2) is used to calculate the center of holes with respect to the center of the structure which is set as the origin point, and  $a$  in the formula is referred to in ES-PCF as  $\Lambda$  in this thesis. The parameters of ES-PCF used to manipulate the structure in this work are six; number of arms ( $N_{arms}$ ), number of rings in each arm ( $N_{rings}$ ), the angle between two successive holes of the same arm ( $\theta$ ), the spiral growth rate ( $b$ ) which is defined in this thesis as in Equation (3.4), therefore it is fixed for a given number of arms in the ES-PCF, and the last two parameters which are related to each other as a ratio of hole size ( $d$ ) and

pitch ( $\Lambda$ ) are similar to the case in H-PCF. There is however one difference in this ratio: the maximum value is not always 1 but varies with  $b$ ,  $N_{arms}$  and  $\theta$  as explained below.

$$b = \cot \left( \frac{(N_{arms} - 2)\pi}{2N_{arms}} \right) \quad (3.4)$$

The distance from center of the structure to the first hole is calculated using formula 3.2, where the angle with the X-axis equals zero, similarly the distance of the second hole ( $r_2$ ) is calculated with the angle with the X-axis being equal to  $\theta$ , the third hole is at an angle  $2 \times \theta$ , and so on with every hole added in the arm, the angle is incremented by one times its initial value, and for the  $n^{th}$  hole the angle is  $(n - 1)\theta$ . The same procedure is followed for each arm but the axis is rotated by an angle of  $\pi/N_{arms}$  radian. Therefore, the distance of the second hole from the center is  $r_2 = \Lambda e^{b\theta}$ . Figure (3.4) show a schematic cross section of a six arms 3 rings ES-PCF structure. The holes in the figure are numbered as  $(i, j)$  where  $i$  is the arm number and  $j$  is the ring number. To make a comparison between H-PCF and ES-PCF parameters are  $N_{arms} = 6$ ,  $N_{rings} = 3$ ,  $b = 0.577$  and  $\theta = \frac{\pi}{N_{arms}}$ , no value is set to the rest of the parameters because they are considered to be similar in both structures. In this case, by the use of Equations (3.4) and (3.2), the second hole is located at distance from center

$$r_2 = 1.353\Lambda \quad (3.5)$$

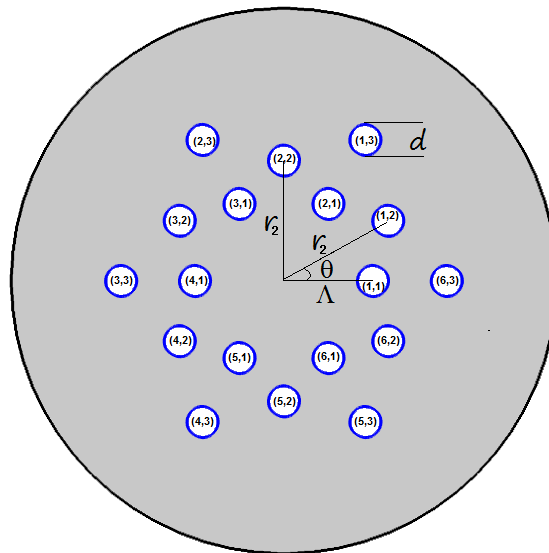


Fig. 3.4 A schematic of ES-PCF cross section in transverse direction

This distance is smaller than the distance of the second hole from the center in the H-PCF (Equation (3.3)) and this point will be referred to when the results are discussed. Moreover, this distance varies with  $b$  where the value of  $b$  for which the ratio  $d/\Lambda$  can take the maximum value of 1 is calculated by setting  $r_2 = \sqrt{3} \Lambda$  and substituting in Equation (3.2). In this assumption the distance of the holes in the second ring of ES-PCF from the center is identical to the distance of holes in second ring of H-PCF.

$$b = \frac{\ln \sqrt{3}}{\theta} \approx 1.05 \quad (3.6)$$

where  $\theta$  is in radian, and this condition is only true for the parameters given above. The discussion above is valid when  $N_{arms} = 6$  where there are six holes in the first ring. As the number of holes increase in the first ring the maximum value of  $d/\Lambda$  is decreased and vice versa, the general formula for any value of  $N_{arms}$  is

$$\left(\frac{d}{\Lambda}\right)_{max} = \frac{2 \times (x - 1)}{x + 1} \quad (3.7)$$

where

$$x = \frac{1 + \sin\left(\frac{\pi}{N_{arms}}\right)}{1 - \sin\left(\frac{\pi}{N_{arms}}\right)} \quad (3.8)$$

Both Equations (3.7) and (3.8) are derived from Steiner Chains rule which is discussed in Section (4.3.1). The maximum values of  $d/\Lambda$  for  $N_{arms}$  from 4 to 9 are shown in Table (3.1). These values are calculated in regard to the first ring and are valid if the holes of the second ring are at a distance far enough not to overlap with the holes in the first ring. This can be realised by calculating appropriate values of  $b$  and  $\theta$ .

Table 3.1 Maximum value of  $d/\Lambda$  for given number of arms

$N_{arms}$	4	5	6	7	8	9
$d/\Lambda$	1.414	1.176	1	0.868	0.765	0.684

The value of  $\theta$  is the most important parameter that influences the maximum value of  $d/\Lambda$ . There are two scenarios to consider; first when  $N_{arms}$  is equal or smaller than 6. In this case, with increasing hole size, the first merge occurs between second hole with either the first hole of the same arm or the first hole of the neighboring arm. The former merge occurs when  $\theta < \pi/N_{arms}$ , the latter when  $\theta > \pi/N_{arms}$  and at values of  $\theta = \pi/N_{arms}$  the merge occurs at both holes at the same time.

The second scenario is when  $N_{arms} > 6$  the merge occurs between the third hole and the first hole of neighboring arms at values of  $\theta$  even less than  $\pi/N_{arms}$ . Therefore, there is not a universal rule for all cases but the best practice is to use a computer program to calculate the maximum value of  $d/\Lambda$  for a given structure. The procedure is to calculate  $r$  of first and second/third holes of one arm and the first hole of the adjacent arm and find the distance between the center of holes of the two arms. This can be done by converting from polar to Cartesian coordinates and obtaining the square root of the difference in coordinates of both axes. Then the smallest value among the holes combination is considered as  $d$  to calculate the maximum ratio.

The microstructured cladding width of H-PCF and ES-PCF, with approximate equally number of holes, are compared in the Table (3.2). Although the size of ES-PCF is smaller, as shown in the table, the H-PCF can have higher air filling fraction. Actually, with H-PCF the maximum air filling fraction is achieved as holes are packed in a uniform way so that no space is left between adjacent holes in all directions. However, for a given hole size the ES-PCF would have the advantage of the second ring of holes being closer to the center leading to better confinement of the modal field and lower losses are achieved. Some structures can be presented by a different combination of arms and rings such as 60 rings can be presented by  $N_{arms} = 6$  and  $N_{rings} = 10$  which has a distance of  $15\Lambda$  from center of structure to the center of the farthest hole thus the confinement of light is not as good as when using more arms and fewer holes per arm as shown in Table (3.1), the number can be approximately represented by 8 arms and 9 rings with distance of  $3.67\Lambda$  or even by 10 arms and 6 rings with distance of  $1.67\Lambda$ . The field is better confined with smaller distance because the air filling fraction is higher.

One more advantage of the ES-PCF is that any number (apart from prime numbers) of holes can be presented with the combination of  $N_{arms}$  and  $N_{rings}$ . On the other hand, the number of holes in H-PCF is defined by the formula

$$\sum_{i=1}^N 6i \quad (3.9)$$

where  $N$  is the number of rings.

In this thesis the value of  $b$  is fixed for a given number of arms as in Equation (3.4) thus all results were obtained with this condition. To conclude this discussion, ES-PCF has more parameters than H-PCF to control the number and distribution of holes in the structure. However, the ES-PCF requires more knowledge of the effect on optical properties by varying the various parameters. For this reason, a study of each parameter is included in this chapter, in the following sections.

Table 3.2 A comparison of structure size for different number of holes

Holes	Structure	$N_{rings}$	$N_{arms}$	Total holes	Size ( $\Lambda$ )
6	ES-PCF	1	6	6	1
	H-PCF	1	-	6	1
18	ES-PCF	3	6	18	1.83
	H-PCF	2	-	18	2
36	ES-PCF	5	7	35	2.37
	H-PCF	3	-	36	3
60	ES-PCF	9	8	62	3.67
	H-PCF	4	-	60	4
90	ES-PCF	10	9	90	3.14
	H-PCF	5	-	90	5

### 3.3 Study of the ES-PCF Parameters

The layout of the holes, for a given material, is the factor that controls the properties and performance of a PCF. In H-PCF, the holes have fixed positions and the two parameters that can be varied are  $\Lambda$  and  $d$ . There are other factors that have an impact on the properties, such as number of rings and core size which is related to the number of missing holes at the center (1, 7 or 19). In this discussion, the typical H-PCF (one central hole missing and with uniform circular holes of same size) is considered and the typical ES-PCF (with circular uniform hole size).

The ES-PCF has more parameters than H-PCF to control the hole distribution for this reason the two parameters, namely  $N_{arms}$  and  $\theta$ , which influence the holes position are varied and the corresponding transverse cross sections are shown in Figure (3.5). It can be noticed that some structures have densely packed holes and some very loose as there are large gaps in between holes. It is very much related to  $\theta$  where some structures have similar arms with different  $\theta$ . The first from top left corner has four arms and  $\theta = 35^\circ$ , the one on its right has 5 arms and  $\theta = 45^\circ$ , and the last two at the bottom right corner both have 9 arms with  $\theta = 60^\circ$  and  $70^\circ$ , respectively. The holes in the last two figures show that the one on the left has more densely packed holes than the other one. The most dense distribution is when  $\theta = \pi/N_{arms}$  in which the second hole is located exactly above the middle of two holes of the first ring. In this section, studies on the effect on the optical properties of changing these two parameters and others is carried out with the relevant discussion of the outcomes. The base material in this

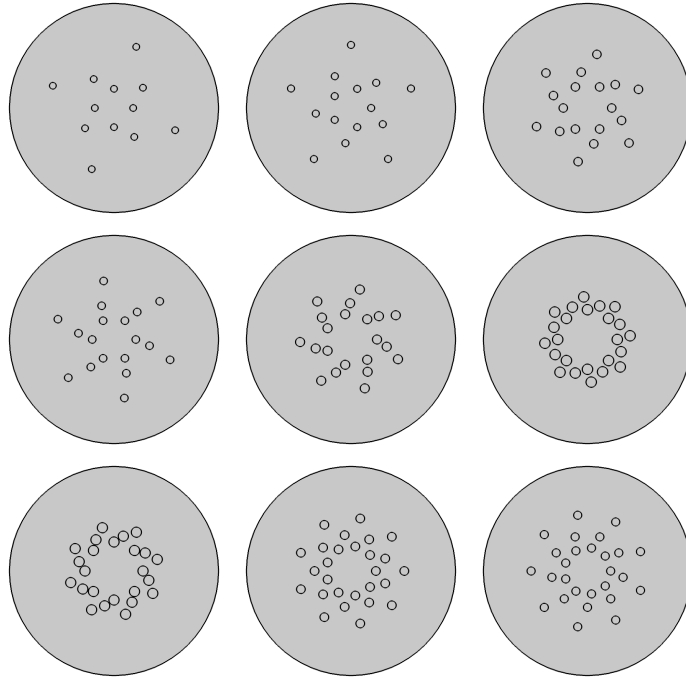


Fig. 3.5 Schematics of different ES-PCF holes distribution with  $N_{rings} = 4$  where  $N_{arms}$  and  $\theta$  are different. Starting from top left corner and moving to the right, the values are defined as set of pairs  $(N_{arms}, \theta)$  as  $(4, 35^\circ)$ ,  $(5, 45^\circ)$ ,  $(6, 40^\circ)$ ,  $(6, 50^\circ)$ ,  $(7, 40^\circ)$ ,  $(8, 25^\circ)$ ,  $(8, 30^\circ)$ ,  $(9, 60^\circ)$ ,  $(9, 70^\circ)$ .

section is silica and the refractive index is calculated according to Sellmeier equation [12] (Equation (1.34)) and the Sellmeier coefficients [12] for silica are shown in Table (3.3).

Table 3.3 Sellmeier coefficients of silica material [12]

Sellmeier Coefficient	1	2	3
$A_j$	0.0684043	0.1162414	9.896161
$B_j$	0.6961663	0.4079426	0.8974794

The wavelength of operation is  $1.55\mu m$  for all results shown in this chapter apart from the case where the wavelength is the parameter investigated to see its effects.

### 3.3.1 Study of number of arms ( $N_{arms}$ )

The number of arms can be varied in practice from 3 to slightly above 10 as the holes get packed close together for higher values of  $N_{arms}$ , the optimum range is 5 to 8 to gain the unique characteristic of the ES design. For smaller values of  $N_{arms}$  the holes size should be large to confine the light in the core and a 3-arm structure is somewhat

similar to Air Suspended Core (ASC) [152, 181]. However, it is still possible to have a large number of arms for large pitches and small  $d/\Lambda$  ratio structure for LMA.

The modal field plots and change in  $n_{eff}$ ,  $A_{eff}$  and loss with varying number of arms are shown in Figure (3.6) for an ES-PCF, where  $N_{rings} = 3$ ,  $\theta = 30^\circ$ ,  $d/\Lambda = 0.35$  and  $b$  is set according to Equation (3.4). The range of  $N_{arms}$  is chosen to be from 5 to 8 for the reasons discussed above.

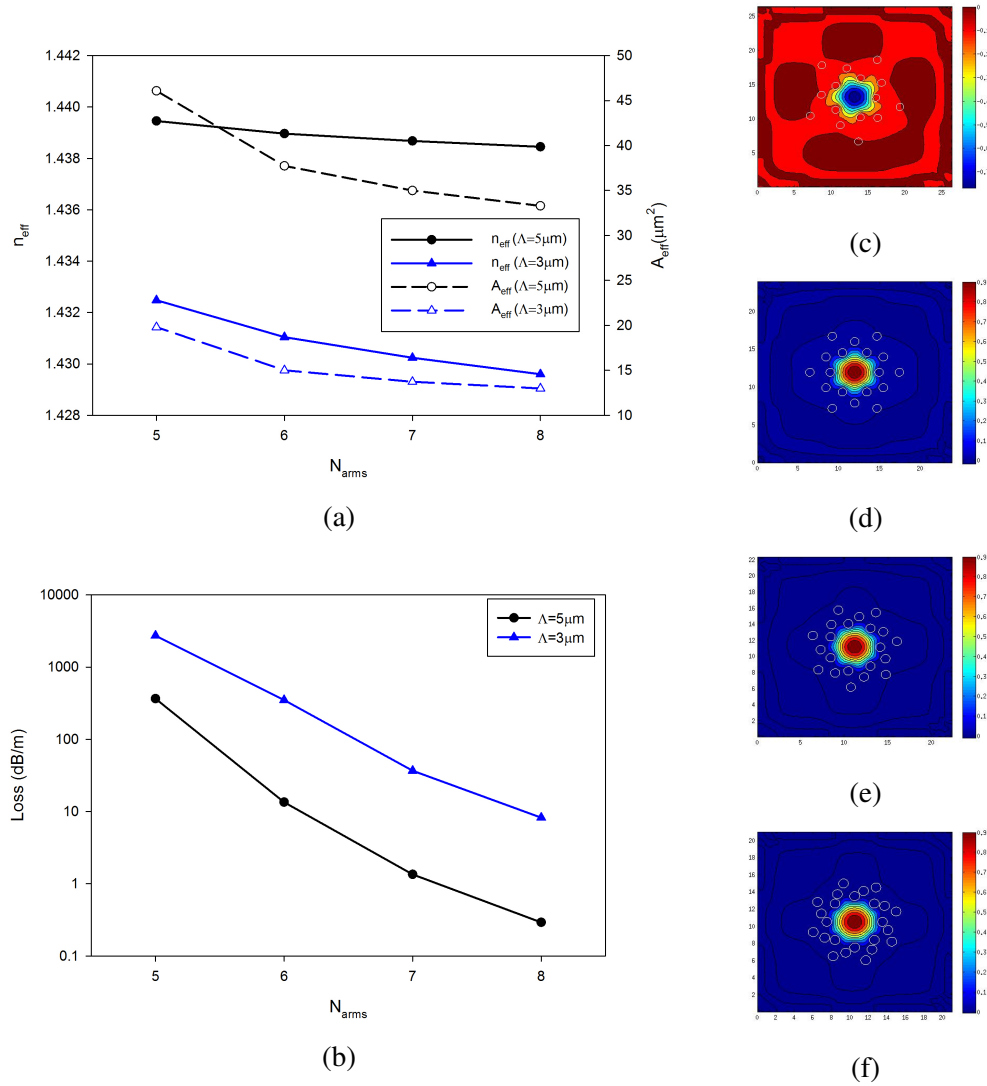


Fig. 3.6 Change in (a)  $n_{eff}$ ,  $A_{eff}$  and (b) loss with varying  $N_{arms}$ , and (c-f) the corresponding field plots of 5, 6, 7 and 8 arms structures, respectively. Structure parameters are  $N_{rings} = 3$ ,  $\Lambda = 3\mu m$ ,  $d/\Lambda = 0.35$  and  $\theta = 30^\circ$ .

The field profile is more confined as the number of arms increased as can be seen from the  $A_{eff}$  plots, which is due to several factors. There are more holes in first ring in higher values of  $N_{arms}$  and the other reason is holes in  $2^{nd}$ ,  $3^{rd}$  and if any further rings

present, are packed closer to the center and therefore this leads to a larger refractive index difference between the core and the effective cladding region. This can be justified from the effective index graph (Figure (3.6a)) as the number of arms increase  $n_{eff}$  decreases because the field encounters more air-holes.

Furthermore, there are two sets of different  $\Lambda$ ,  $\Lambda = 3$  and  $5\mu m$  shown in Figure (3.6a) where the change in  $n_{eff}$  is sharper at smaller  $\Lambda$  because the field is influenced by the cladding air region more. In contrast, the  $A_{eff}$  change is sharper at large value of  $\Lambda$  as the field spreads more widely at lower refractive index difference when  $N_{arms}$  is small. The field plots of  $N_{arms} = 5$  to 8 are shown in Figures (3.6c) and (3.6f), respectively, with a schematic of the position of the air-holes.

The loss for both structures is shown in Figure (3.6b), where loss decreases as number of arms increased due to more confinement of the field. Furthermore, the loss at larger pitch is lower because the core size is larger and the field is more concentrated in the core and not in cladding.

### 3.3.2 Study of number of rings ( $N_{rings}$ )

The parameter  $N_{arms}$  discussed in the previous Section, (3.3.1), is related to  $N_{rings}$  as both of them together determine how many holes would be in the structure. The total number of holes is  $N_{arms} \times N_{rings}$  therefore almost any number of holes can be present unless the total number of holes is a prime number. However, only the primes 5, 7 and 11 can be presented as larger primes would result in large number of holes packed together. In general, a prime numbers of holes is not practical as only one ring can be present and then the field won't be well confined and losses would be high. The loss can be reduced by having more holes either by adding more arms or rings. The number of arms is limited as it would not be practical to have a design with  $N_{arms} > 10$  so the best choice to increase holes is by increasing  $N_{rings}$ . Therefore, the number of rings factor is studied in this section.

The number of rings in ES-PCF has been varied to study the change in  $A_{eff}$  and  $n_{eff}$ . The structure has 6 arms,  $\Lambda = 2\mu m$ ,  $\theta = 30^\circ$  and  $d/\Lambda = 0.35$ , the results are shown in Figure (3.7a). The two curves of  $n_{eff}$  and  $A_{eff}$  have similar change where the curves have high values at  $N_{rings} = 2$  which is as a result of the few holes in the structure (12 holes) so the field is not well confined. The change in  $n_{eff}$  is as expected where it decreases slightly as  $N_{rings}$  increases from 3 to 7. The change is small because the field is confined and does not expand to holes in further rings. The curve of  $A_{eff}$  increases with number of arms slightly from  $N_{arms} = 4$  to 7 where at  $N_{arms} = 7$  the increase is more noticeable. This is believed to be due to the fact that the field expands slightly

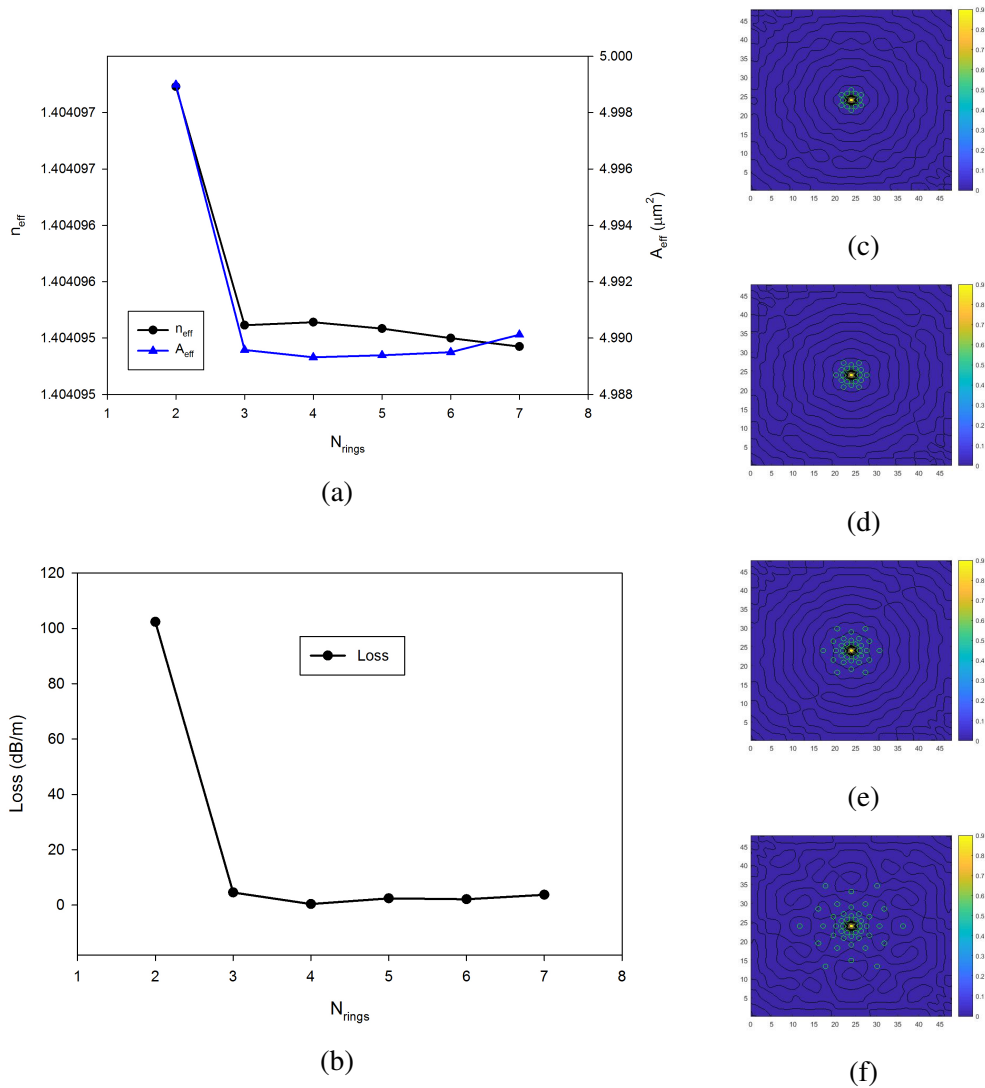


Fig. 3.7 Change in (a)  $n_{eff}$ ,  $A_{eff}$  and (b) loss with varying  $N_{rings}$ , and (c-e) the corresponding field plots of 2, 3, 5 and 7 rings structures. Structure Parameters are  $N_{arms} = 6$ ,  $\Lambda = 2\mu\text{m}$ ,  $d/\Lambda = 0.35$  and  $\theta = 30^\circ$ .

when the air filling fraction of the cladding is reduced. In the ES-PCF the distance between two holes from the same arm is increasing (the distance between second and third holes is larger than distance between first and second hole and so on) as explained in Section (3.2.2). The distance of the holes is increased and the effective cladding area grows more even if the increase in distance is similar the area increases more because  $area = \pi r^2$ . Therefore in ES-PCF as the  $N_{rings}$  increases and the hole size in fixed in all arms the total air filling fraction of the effective cladding region is reduced.

From Figure (3.7b), the loss curve has similar behavior to  $A_{eff}$  and this is for the same reason explained above due to decrease in the air filling fraction. Therefore, in most

cases 3 rings are sufficient enough to confine the field if the ratio  $d/\Lambda$  is larger than 0.3 and  $N_{arms}$  is 6 or larger. The other method which can be used is to have different sizes for the holes. The holes in first ring are small and as ring number increases the hole size increase [234], in this way the air filling fraction can be kept constant if the growth ratio of the hole size is large enough. The field plots of the 2, 3, 5 and 7 rings are shown in Figures (3.7c) - (3.7f), respectively.

### 3.3.3 Study of pitch size ( $\Lambda$ )

The number of arms and rings have been discussed in the previous sections with regards to their effect on  $n_{eff}$  and  $A_{eff}$  of the modal field at wavelength  $\lambda = 1.55\mu m$ , all results shown in this section are at this wavelength. The core size is mainly related to the  $\Lambda$ , with the core size being equal to  $\Lambda - (d/2)$ . The core size in PCF, as discussed in Chapter 2, can be of small or large sizes unlike in conventional fibers. Furthermore, in H-PCF core size depends on  $d/\Lambda$  ratio where as in ES-PCF the core size can be large with proportionally small holes which cannot be achieved with a similar characteristic of strong confinement of the field in H-PCF.

The range of  $\Lambda$  chosen in this study varies from 1 to  $8\mu m$ . Smaller and larger values can be used but for the smaller values extra care should be taken as the field won't be well confined and the design may be in the cut-off region. On the other hand large values lead to more sensitivity to bending losses. The change in  $n_{eff}$  and  $A_{eff}$  as a function of  $\Lambda$  are shown in Figure (3.8). The parameters are  $N_{arms} = 6$ ,  $N_{rings} = 3$ ,  $\theta = 30^\circ$ , and there are two sets with different ratio  $d/\Lambda$  of 0.6 and 0.35.

The effective area increases with increase in pitch size due to increases in the core size and the field spreads inside the core. For smaller  $d/\Lambda$  ratio the  $A_{eff}$  is larger for two reasons; core size is bigger and confinement of light is less because index difference between core and cladding region is smaller due to lower air filling fraction as holes are smaller. The difference in  $A_{eff}$  is higher at larger pitch size because as the pitch sizes increases the difference in core sizes between the two structures increases proportionally with  $\Lambda$ .

On the other hand,  $n_{eff}$  increases with increase in  $\Lambda$  due to more interaction of the mode with the material. This results from increase in  $\Lambda$  and keeping  $d$  fixed so the ratio  $d/\Lambda$  is reduced. The increase in  $n_{eff}$  at lower value of  $\Lambda$  is sharper in structures with larger holes as the field is more confined and holes are closer to each other. The step drop in  $n_{eff}$  at  $\Lambda = 1\mu m$  is due to the cut off as can be observed from Figure (3.8b) where normalized  $A_{eff}$  is plotted versus  $\Lambda$ . The normalized  $A_{eff}$  increases with decrease in  $\Lambda$  to a point where the mode gets cut off as shown in the graph. There are

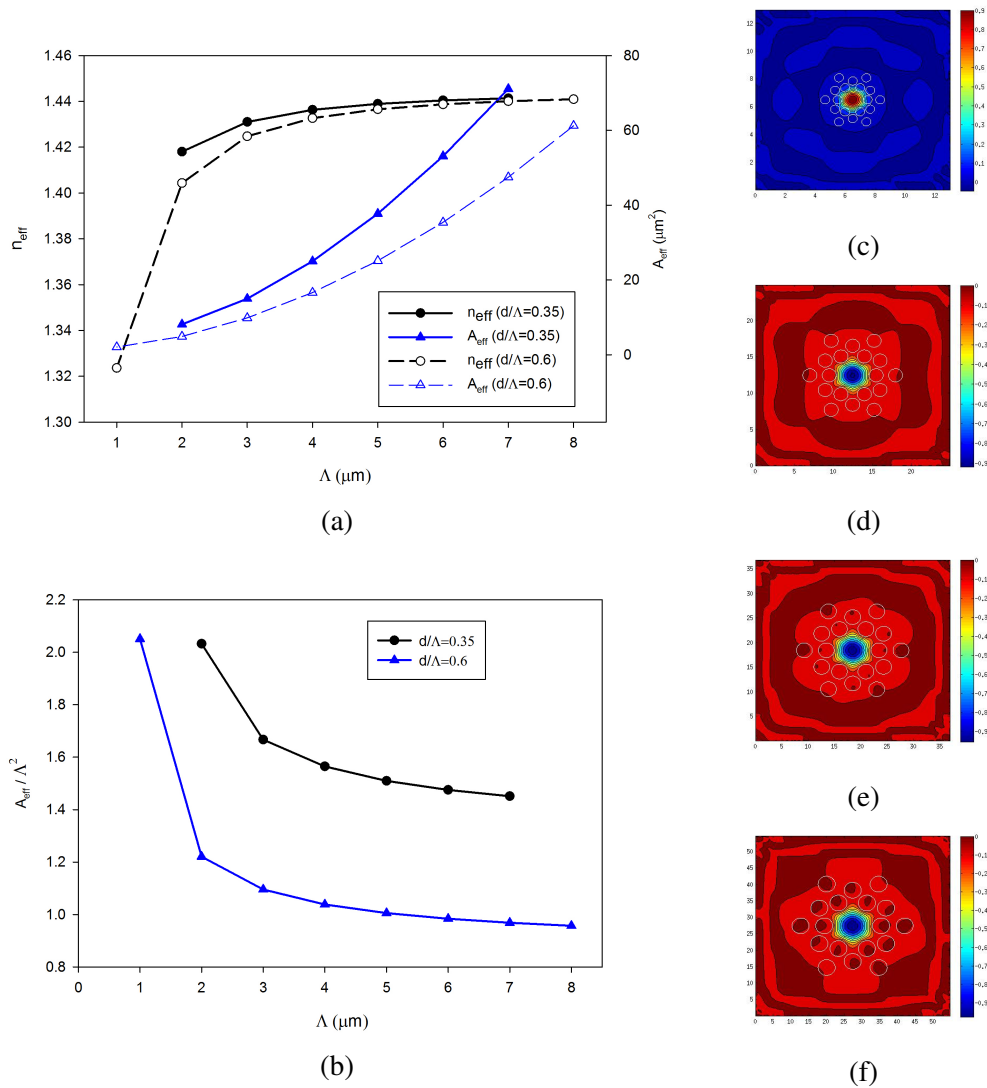


Fig. 3.8 Change in (a)  $n_{\text{eff}}$ ,  $A_{\text{eff}}$  and (b) normalized  $A_{\text{eff}}$  with varying  $\Lambda$ , and (c-f) the corresponding field plots of pitch size 1, 3, 5 and  $8\mu\text{m}$  for  $d/\Lambda = 0.6$ . Structure Parameters are  $N_{\text{arms}} = 6$ ,  $\Lambda = 3\mu\text{m}$ ,  $d/\Lambda = 0.35$  and  $0.6$ , and  $\theta = 30^\circ$ .

four field plots for the set with larger hole for  $\Lambda = 1, 3, 5$ , and  $8\mu\text{m}$  shown in Figure (3.8c), (3.8d), (3.8e), and (3.8f), respectively. The field is well confined at higher value of  $\Lambda$ . The change of three parameters has been discussed so far, in this section the  $\Lambda$  has been varied for two different ratios  $d/\Lambda$ , in the next section the effect of the variation of this ratio on the modal field is discussed.

### 3.3.4 Study of the ratio ( $d/\Lambda$ )

From the previous section it is noticed that the higher the ratio  $d/\Lambda$  the more well confined the field which is due to larger holes hence higher air filling fraction which

results in larger index difference between core and effective cladding region. The ratio  $d/\Lambda$  can be varied by changing either  $d$ ,  $\Lambda$  or both together with different values. It is more efficient to study the effect on the ratio by variation in one parameter. In this section  $d$  is changed hence this discussion is valid for both hole size and ratio  $d/\Lambda$ . Even though  $d$  is varied, the discussion in this section refers to  $d/\Lambda$  throughout, and more focus on the effect of varying  $d/\Lambda$  is discussed as all other parameters are kept the same through the study, where  $N_{arms} = 6$ ,  $N_{rings} = 3$ ,  $\Lambda = 5\mu\text{m}$  and  $\theta = 30^\circ$ .

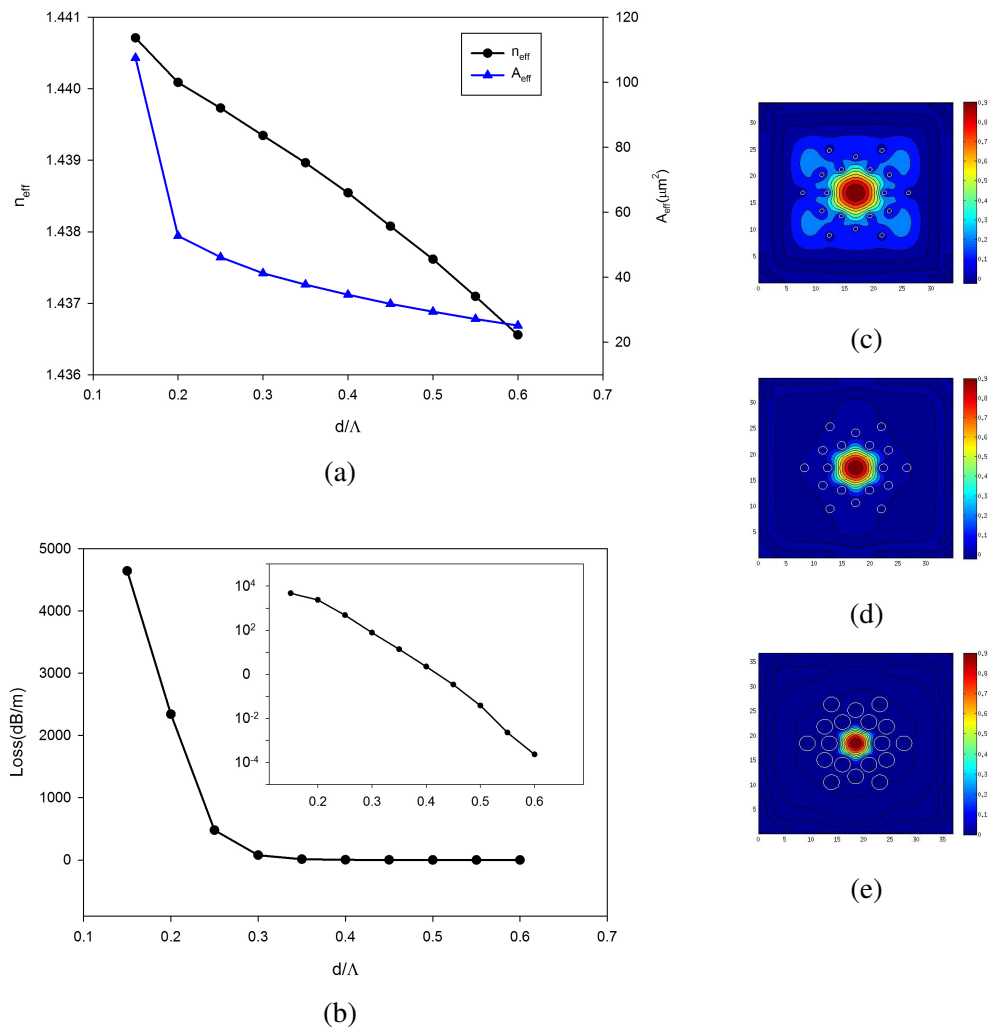


Fig. 3.9 Change in (a)  $n_{eff}$ ,  $A_{eff}$  and (b) loss with varying  $d/\Lambda$ , and (c-e) the correspondence field plots for  $d/\Lambda = 0.15, 0.3$  and  $0.6$ . Structure parameters are  $N_{arms} = 6$ ,  $N_{rings} = 3$ ,  $\Lambda = 5\mu\text{m}$  and  $\theta = 30^\circ$ .

The variation of  $n_{eff}$  and  $A_{eff}$  with  $d/\Lambda$  is shown in Figure (3.9a). The effective index decreases as  $d/\Lambda$  increases because the modal field interacts with more air in the cladding region as a result of the bigger holes. The field is more confined at higher

values of  $d/\Lambda$  and thus the effective area decreases with increase in  $d/\Lambda$  and at small values of  $d/\Lambda = 0.15$  the field is poorly guided in the core where it expands in the cladding region as can be seen from the plot in Figure (3.9c).

The loss is related to many factors but in general as the index difference is increased the loss decreases. The index difference can be increased by increasing the air filling fraction. The loss for different  $d/\Lambda$  is shown in Figure (3.9b). The loss increases as  $d/\Lambda$  decreases but at large values the change is small at values of  $\Lambda > 0.4$  where loss is less than  $10dB/m$  as it can be seen in the inset figure (log-scale). However, the loss increases rapidly at small  $d/\Lambda$  values due to field expansion in the cladding region. The value of  $d/\Lambda$  should be kept at values larger than 0.35 for a loss of less than  $20dB/m$  where the field is not well confined below  $d/\Lambda = 0.2$ . In the case of small  $\Lambda$ , the air filling fraction can be increased by increasing  $N_{arms}$  and/or  $N_{rings}$  to confine the field and lower the loss.

### 3.3.5 Study of angle ( $\theta$ )

The most unique parameter in the spiral structure is the angle between two successive holes. The change in this parameter can have huge impact on the propagation properties of the field. As discussed earlier, the distribution of holes is mainly determined by  $\theta$  and  $N_{arms}$ . The holes can be rotated in a way to confine the field strongly in the core ( $\theta = \pi/N_{arms}$ ) or can be loose (at values close to  $2\pi/N_{arms}$ ) and at some angles it has been noticed that higher order modes do not propagate in the core and the fiber supports only the fundamental mode.

The effect of change of  $\theta$  is investigated in a structure with  $N_{arms} = 6$ ,  $N_{rings} = 3$ ,  $\Lambda = 3\mu m$  and  $d/\Lambda = 0.35$ , where the results are shown in Figure (3.10). The effective index increases with increase in  $\theta$ , this is due to the fact that at lower values of  $\theta$  the holes are closer to the core thus the field interacts with the holes more. As the value of  $\theta$  increases holes spread further from core and the interaction with air is less. On the other hand, the field spreads more into cladding region at higher values of  $\theta$  and this might be expected to lead to lower  $n_{eff}$  but the opposite is true as mentioned. The reason is that when  $\theta$  is increased the holes divert away from each other and the field can spread in between holes in the material of the fiber as is observed from the fields plot where angle increases from top field plot (Figure (3.10c)) where  $\theta = 28^\circ$  to the bottom (Figure (3.10f)) where  $\theta = 42^\circ$  and the field expands in cladding region. The increase in  $n_{eff}$  is not perfectly monotonic and seems to have steps where the value of  $n_{eff}$  is similar, before jumping to the next step. This is in part because of the distribution of the holes is similar for a small range of values of  $\theta$  and therefore the confinement of the modal field

is similar within this range. When  $\theta$  is increased sufficiently so that the distribution of holes changes enough to make a noticeable change in the confinement of the field a corresponding change in  $n_{eff}$  is observed. Figure (3.11) shows the distribution of the holes for the range of  $\theta$  chosen ( $28^\circ$ ,  $30^\circ$ ,  $32^\circ$ ,  $34^\circ$ ,  $35^\circ$ ,  $37^\circ$ ,  $40^\circ$  and  $42^\circ$ ) starting from top left moving to the right then second row from left to the right. The designs in the first row have their holes closely packed and no large gaps between hole for the field to expand. In the second row the holes divert from their optimum position as  $\theta$  increases causing gaps between holes in which the field can expand out of the core.

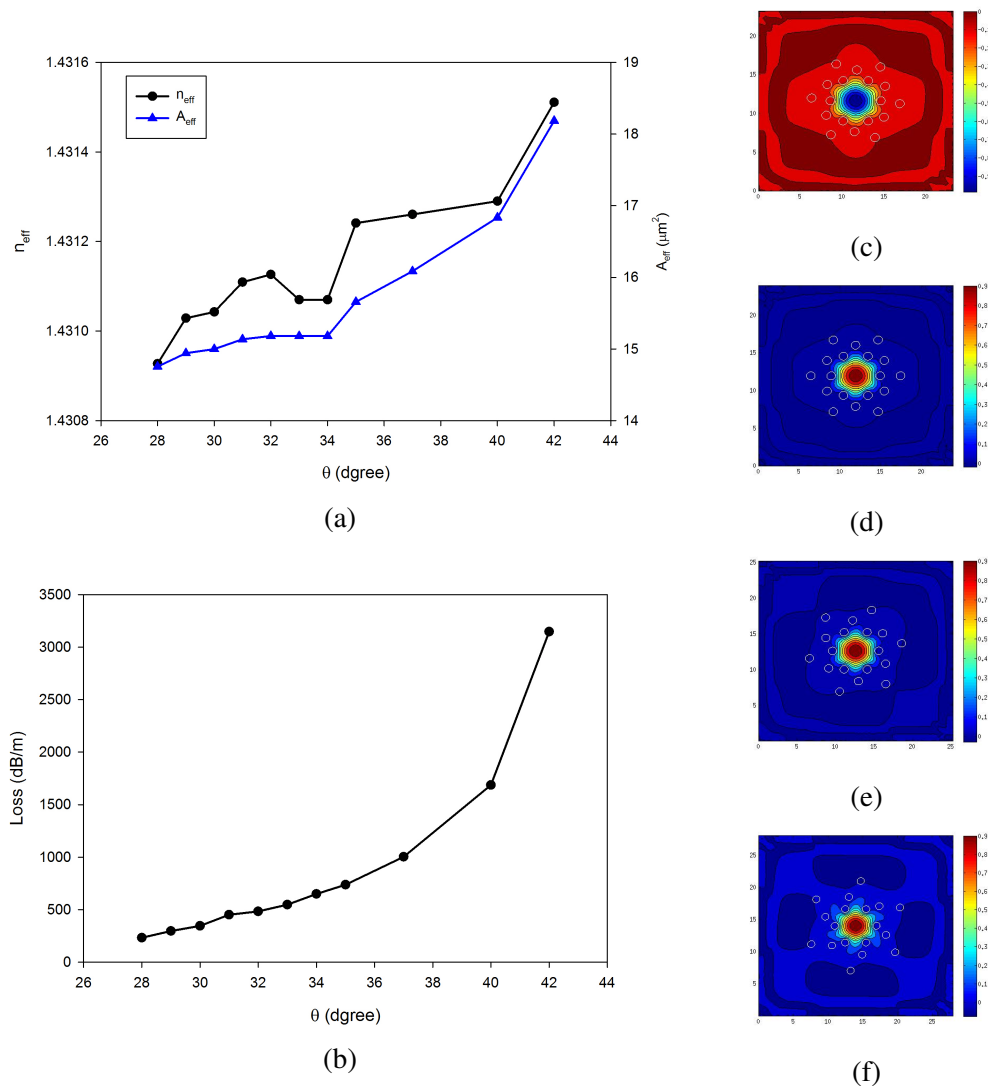


Fig. 3.10 Change in (a)  $n_{eff}$ ,  $A_{eff}$  and (b) loss with varying  $\theta$ , and (c-f) the corresponding field plots for  $\theta = 28, 30, 32$  and  $42^\circ$ . Structure parameters are  $N_{arms} = 6$ ,  $N_{rings} = 3$ ,  $\Lambda = 3\mu m$  and  $d/\Lambda = 0.35$ .

The loss follows the same trend as the  $A_{eff}$  where at lower  $\theta$  loss is small and increases with increase in  $\theta$  and at higher values the increase is sharper due to a wider gap and more field spreading thus more light escapes out of the core.

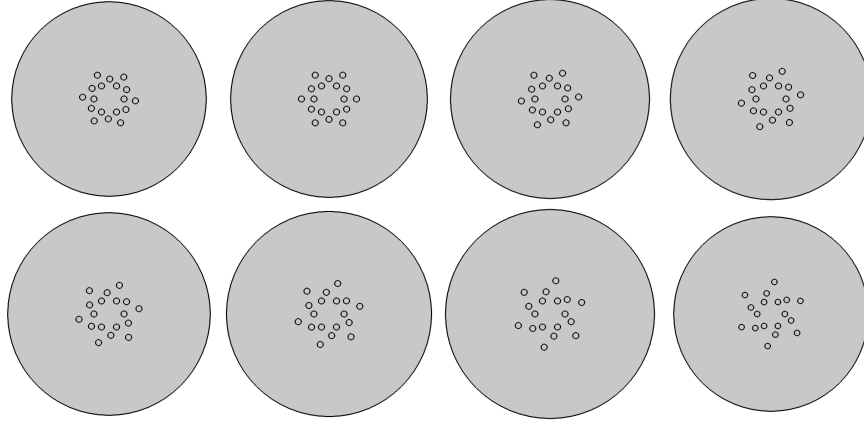


Fig. 3.11 Schematics of different ES-PCF holes distribution with  $N_{arms} = 6$ ,  $N_{rings} = 3$ ,  $\Lambda = 3\mu m$ ,  $d/\Lambda = 0.35$  and  $\theta$  varied. Starting from top left corner and moving to the right, the values of  $\theta$  are  $28^\circ$ ,  $30^\circ$ ,  $32^\circ$ ,  $34^\circ$ ,  $35^\circ$ ,  $37^\circ$ ,  $40^\circ$  and  $42^\circ$ .

The study of the ES-PCF parameters have been discussed by varying each parameter individually to get an overview of the possibilities to design PCF with the required specifications. However, there are other factors that can manipulate the optical properties of the structure such as introducing a small hole in the center, or use of elliptical or semi-circular holes, or other manipulation in the design. The final step in this parameter study is to study the change of wavelength of operation which is discussed next.

### 3.3.6 Study of wavelength ( $\lambda$ )

Variation of parameters is important to understand how each parameter effects the properties. One of the values to study, which is not a ES parameter, is the wavelength of operation. In any media the change in wavelength leads to change in optical properties of the field. In this part the ES-PCF has  $N_{arms} = 6$ ,  $N_{rings} = 3$ ,  $\theta = 30^\circ$ ,  $\Lambda = 5\mu m$ , and  $d/\Lambda = 0.3$  and  $0.5$  for two structures. The wavelength range in this study is from  $0.6$  to  $1.9\mu m$  in which silica is transparent. The refractive index of the fused silica is shown in Figure (3.12a) along side with  $n_{eff}$  of both structures. The change in  $n_{eff}$  of the structure with larger holes is more due to higher air filling fraction thus lower  $n_{eff}$  values. At shorter wavelengths the difference between both structures is small due to the fact that the field is small enough to be well confined in the core. However, at longer wavelength the field expands more leading to additional interaction of the field

with the air in the holes. The loss is shown as well in the same graph and as expected larger holes lead to lower losses.

The normalized  $A_{eff}$  is shown as a function of normalized wavelength in Figure (3.12b). The change in both structures with wavelength is stable as the normalized  $A_{eff}$  increases with increase in wavelength. The effective area is larger for smaller holes due to less confinement of the field thus leading to a larger modal field profile.

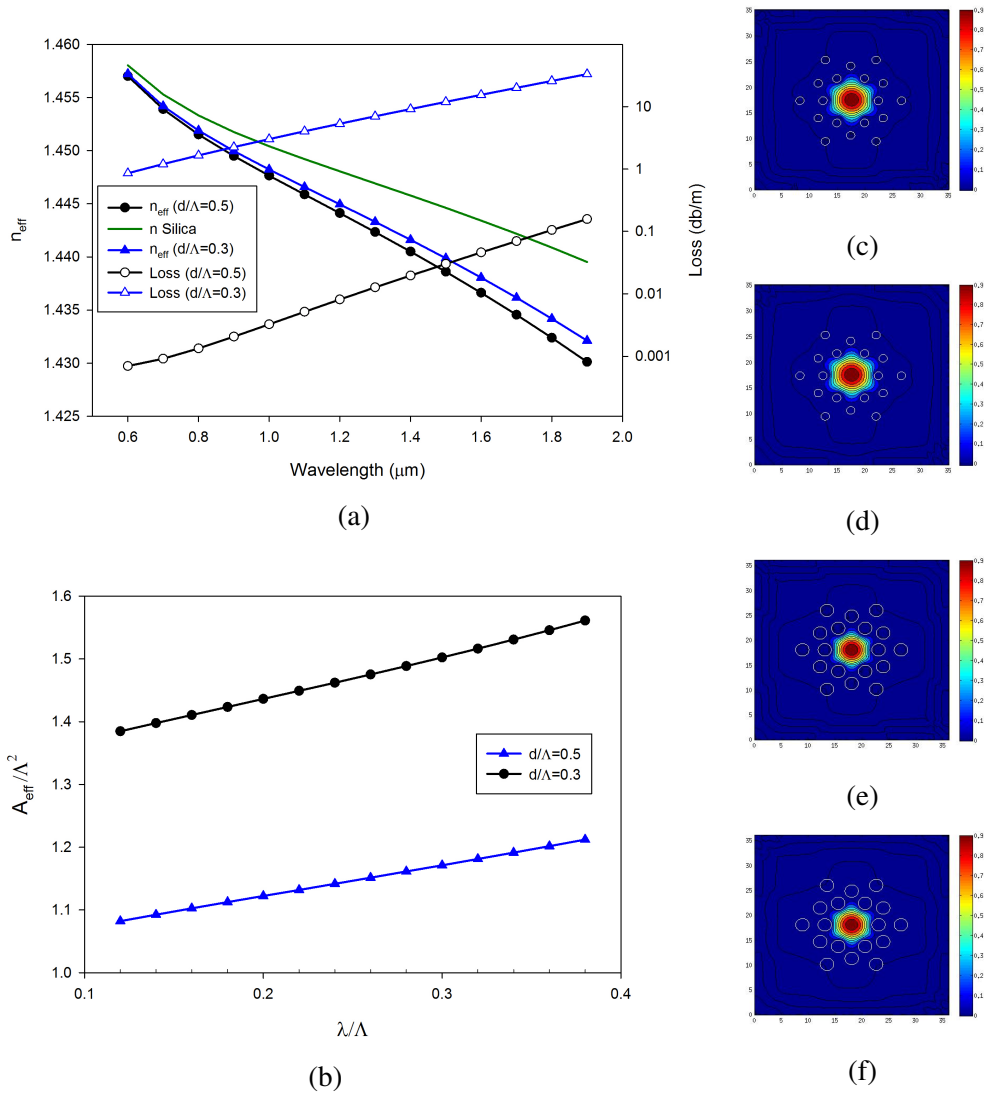


Fig. 3.12 Change in (a)  $n_{eff}$ , loss and (b) normalized  $A_{eff}$  with varying  $\lambda$ , and (c-f) the corresponding field plots at  $\lambda = 0.6$  and  $1.5 \mu m$  for  $d/\Lambda = 0.3$  and  $0.5$ , respectively. Structure parameters are  $N_{arms} = 6$ ,  $N_{rings} = 3$ ,  $\theta = 30^\circ$ ,  $\Lambda = 5 \mu m$ , and  $d/\Lambda = 0.3$ .

The dispersions of the two structures are calculated for the wavelength range shown and plotted along side with the silica material dispersion as shown in Figure (3.13). The dispersion is blue shifted and the Zero Dispersion Wavelength (ZDW) is shifted from

$1.3\mu\text{m}$  wavelength to around  $1.15\mu\text{m}$ . The structure with larger holes has diverted further from the material dispersion than the other one because the interaction with air is more and thus the change in effective index is higher. However, it is not always the case that the dispersion of the structure has a uniform change from the material dispersion. In some structures the change is varying where some wavelengths are blue shifted and others are red shifted which leads to dispersion profiles with low flat dispersion for a wide range of wavelengths. The dispersion profile is a major factor in the efficiency of non-linear effects along side with the  $A_{eff}$ . Therefore, more detailed studies on the effect of varying the ES-PCF parameters on the dispersion and  $A_{eff}$  are carried out in the latter part of this chapter. The next few sections are an introduction to different spiral (ES, AS and FS) PCFs with some general results of the effect of varying their parameters on the optical properties of the fiber. Archimedean spiral is discussed first then followed by discussion of Fermat's spiral, the three spirals are compared and in the end of the chapter the ES-PCF is revisited for more in depth studies.

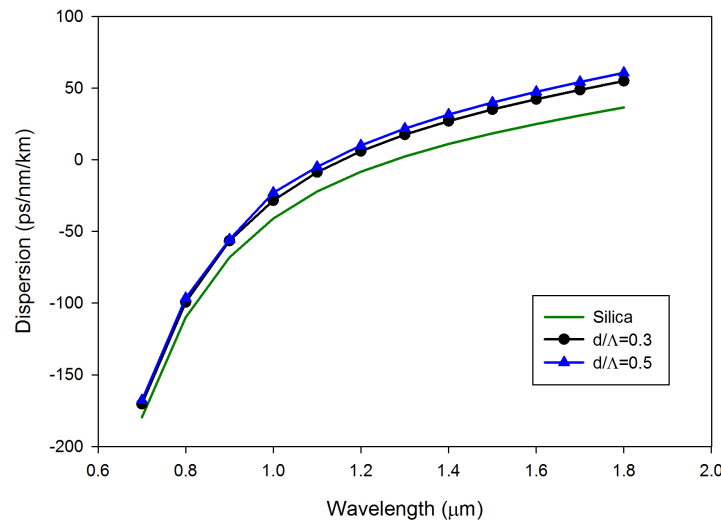


Fig. 3.13 Dispersion of ES-PCF  $N_{arms} = 6$ ,  $N_{rings} = 3$ ,  $\theta = 30^\circ$   $\Lambda = 3\mu\text{m}$  and  $d/\Lambda = 0.3$  and  $0.5$

### 3.4 Archimedean Spiral (AS)

Archimedean spiral was named after the Greek mathematician Archimedes who discussed the spiral in 3rd century BC [235]. It is represented graphically by a point moving away from the origin point with constant speed along the radius,  $r$ , which rotates with a constant angular velocity.

### 3.4.1 AS curve

The first step in the discussion to begin with is the equation of the AS. Similar to the ES, the equation of AS can be represented mathematically in a polar coordinates. The formula of the evolving AS in space is

$$r = a + b\theta \quad (3.10)$$

The spiral starting point depends on the value of the constant  $a$ , and the separation distance between two successive turnings is controlled by the coefficients  $\theta$  and  $b$ . That distance is of constant value, equal to  $2\pi b$  where  $\theta$  is measured in radians, and that is what distinguishes it from the equiangular spiral. The Archimedean spiral consists of two arms, one for positive value of  $\theta$  and the other for negative value of  $\theta$ . Only one arm is shown in Figure (3.14). The second arm is the reflection image of this arm across the Y-axis. These two arms are connected at the center.

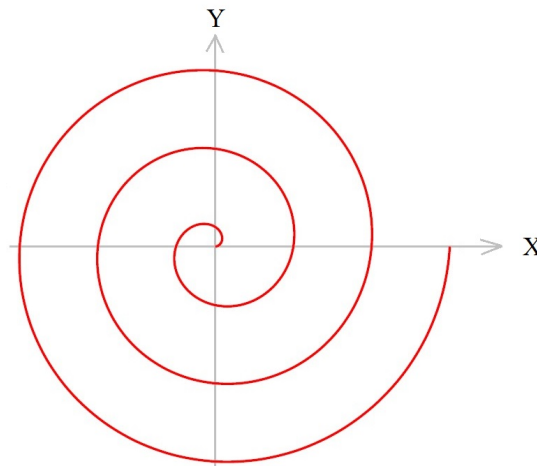


Fig. 3.14 Archimedean Spiral [233]

### 3.4.2 AS-PCF

The formula of the AS represented above is implemented in designing the AS-PCF. The design has characteristics which are explained in a similar manner to the ES section. There are five parameters that can be varied in the AS-PCF structure. Three of them are in the equation, which are  $a$ ,  $b$  and  $\theta$ , and the other two are number of holes ( $N_{holes}$ ) and diameter of the holes ( $d$ ). The  $a$  parameter is similar to the  $\Lambda$  in both ES-PCF and H-PCF designs, where it is the distance from center of the core to the center of the first hole and it controls the core size. The second parameter  $b$  is the tightness of the spiral

or the separation between turns, i.e. controls the ratio of distance between holes from center to the outward direction. The angle  $\theta$  is similar to ES-PCF as it is the angle between two successive holes, however the way the value of the angle is chosen in AS-PCF is totally different from that in ES-PCF. In AS-PCF all holes are in one arm and  $\theta$  should be chosen carefully as large value of  $\theta$  values would result in large gaps between holes which leads to poor/no light confinement in the core. This happens with the values of  $\theta$  which are the divisor of  $2\pi$  as shown in Figure (3.15) (3 figures at 1<sup>st</sup> row with  $\theta = 36, 45$  and  $60^\circ$  from left to right).

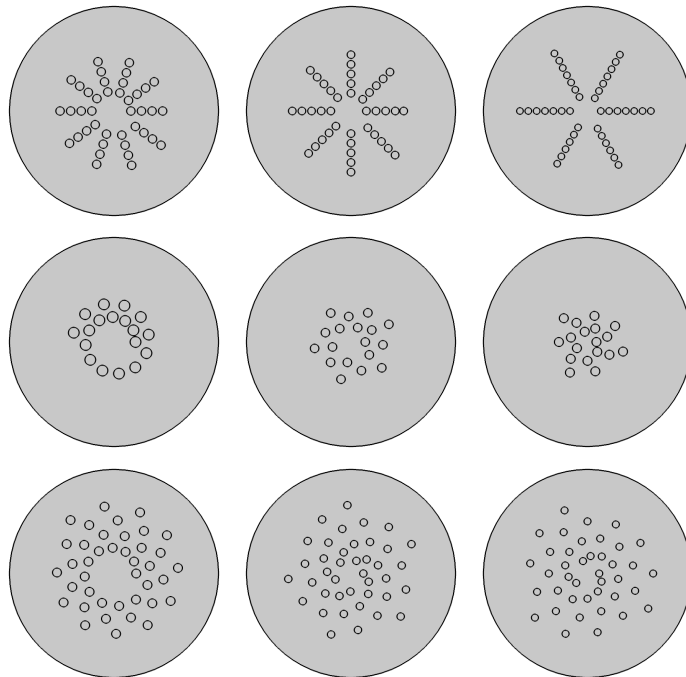


Fig. 3.15 Schematics of different AS-PCF hole distribution with  $N_{rings} = 18$  (middle row) and 40 (upper and lower rows) for different  $\theta$  values. Starting from top left corner and moving to the right, the values of  $\theta$  are 36, 45, 60, 31, 67, 105, 31, 67, and  $110^\circ$ .

Table (3.4) shows the value of  $\theta$  in degrees that should be avoided as the holes are located in straight lines from the center to the circumference of the fiber. The value of  $\theta$  should be chosen to be in the middle between any two adjacent values shown in the table. The values at the start and the end of the table would not lead to practical designs. For the large values of  $\theta$  (above  $90^\circ$ ) the holes are scattered with no distinct core being defined Figure (3.15) (2<sup>nd</sup> row 3<sup>rd</sup> column). On the small value side the holes are packed close to each other so only one complete circle of holes surrounding the core is formed Figure (3.15) (2<sup>nd</sup> row 1<sup>st</sup> column). The best values for  $\theta$  from physical layout viewpoint are in the mid range around  $65^\circ$  Figure (3.15) (2<sup>nd</sup> row 2<sup>nd</sup> column). However, this discussion is valid when the number of holes is small ( $N_{holes} < 30$ ).

In contrast, when there are a large number of holes,  $\theta$  can be small as holes would form a few circles surrounding the core Figure (3.15) (3<sup>rd</sup> row 1<sup>st</sup> column). For large values of  $\theta$  the value of  $\Lambda$  needs to be large to form a reasonable core size in relation to space between holes in the cladding region Figure (3.15) (3<sup>rd</sup> row 3<sup>rd</sup> column). The middle range is similar in both scenarios.

Table 3.4 The values of angle  $\theta$  which are divisor of  $2\pi$  and should be avoided.

<i>Divisor</i>	10	9	8	7	6	5	4	3	2
$\theta$	36	40	45	51.4	60	72	90	120	180

In the following studies the parameters are chosen as follow  $N_{holes} = 18$ ,  $\Lambda = 3\mu m$ ,  $d = 1\mu m$ ,  $b = 0.3$  and  $\theta = 65^\circ$ . In each case the parameter of interest is varied while the rest of the parameters are kept fixed to these values.

### 3.5 Study of the AS-PCF Parameters

The performance of PCF mainly relies on the core size and effective index of the cladding region. The core size is strongly dependent on  $\Lambda$  and the size of the holes in the first turn of the spiral, where core radius equals  $(\Lambda - d/2)$  in the case of circular holes. The cladding effective index depends both on the distribution of holes and their sizes. In AS-PCF, the hole distribution is managed by three parameters;  $N_{holes}$ ,  $b$  and  $\theta$ . The hole size is calculated through the diameter,  $d$  parameter. These parameters are varied in simulations and the results of each individual parameter are presented below.

#### 3.5.1 Study of number of holes ( $N_{holes}$ )

The holes in AS-PCF are all distributed over one arm and their number should be large enough to form at least one complete ring of holes around the center of the structure to produce a form of core and cladding for light to propagate. The number of holes  $N_{holes}$  in this study is varied from 14 up to 32 to study the effect on the basic optical properties. The effect of the variation of the  $N_{holes}$  is shown in Figure (3.16a). The effective area curve is almost constant with no change in the middle. However, it has a slight increase when number of holes increases beyond 28 and higher values at  $N_{holes} = 16$  and 14. The former one is believed to be a numerical error and the latter behavior at  $N_{arms} = 16$  and 14 is supposed to be a physical effect as reducing number of holes leads to less confinement of the field and hence higher  $A_{eff}$  and loss. The loss curve is shown in Figure (3.16b), which shows a similar trend to the  $A_{eff}$  curve.

The change of  $N_{holes}$  does not effect the  $n_{eff}$  as can be seen from Figure (3.16a) where the line is straight. This is due to the field being well confined in the core because the pitch size is large. Therefore, the number of holes does not have a noticeable impact on  $n_{eff}$  and  $A_{eff}$  unless a few holes are chosen then the confinement of the field would be poor and the optical properties such as loss and  $A_{eff}$  are increased as the number of holes is decreased.

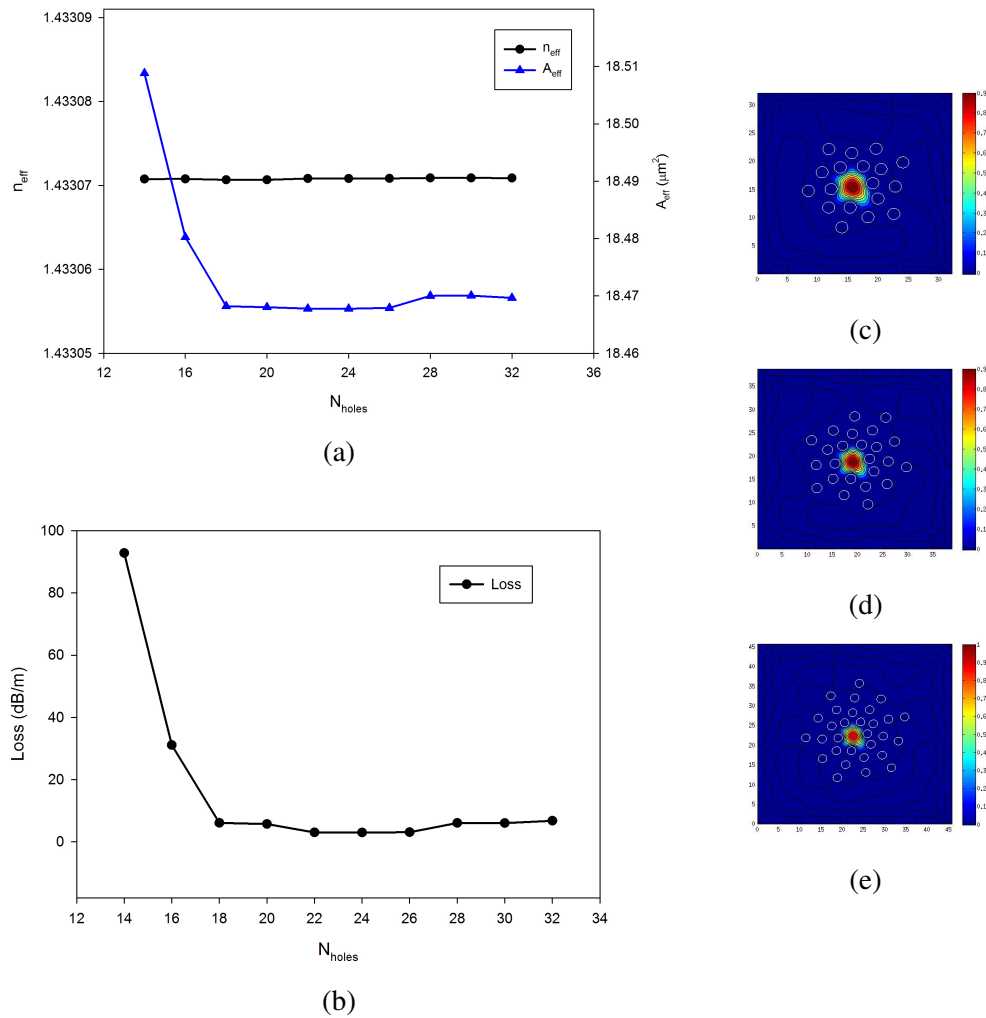


Fig. 3.16 Change in (a)  $n_{eff}$ ,  $A_{eff}$  and (b) loss with varying  $N_{holes}$ , and (c-e) the corresponding field plots for  $N_{holes} = 18, 24$  and  $30$ . Structure parameters are  $\Lambda = 3\mu m$ ,  $d = 1\mu m$ ,  $\theta = 65^\circ$  and  $b = 0.3$ .

### 3.5.2 Study of pitch size ( $\Lambda$ )

The pitch ( $\Lambda$ ) is the main factor that controls the core size as mentioned before. The core size can be large with a small  $d/\Lambda$  of 0.05 or smaller as the holes can be packed close to each other which is not possible in H-PCF.

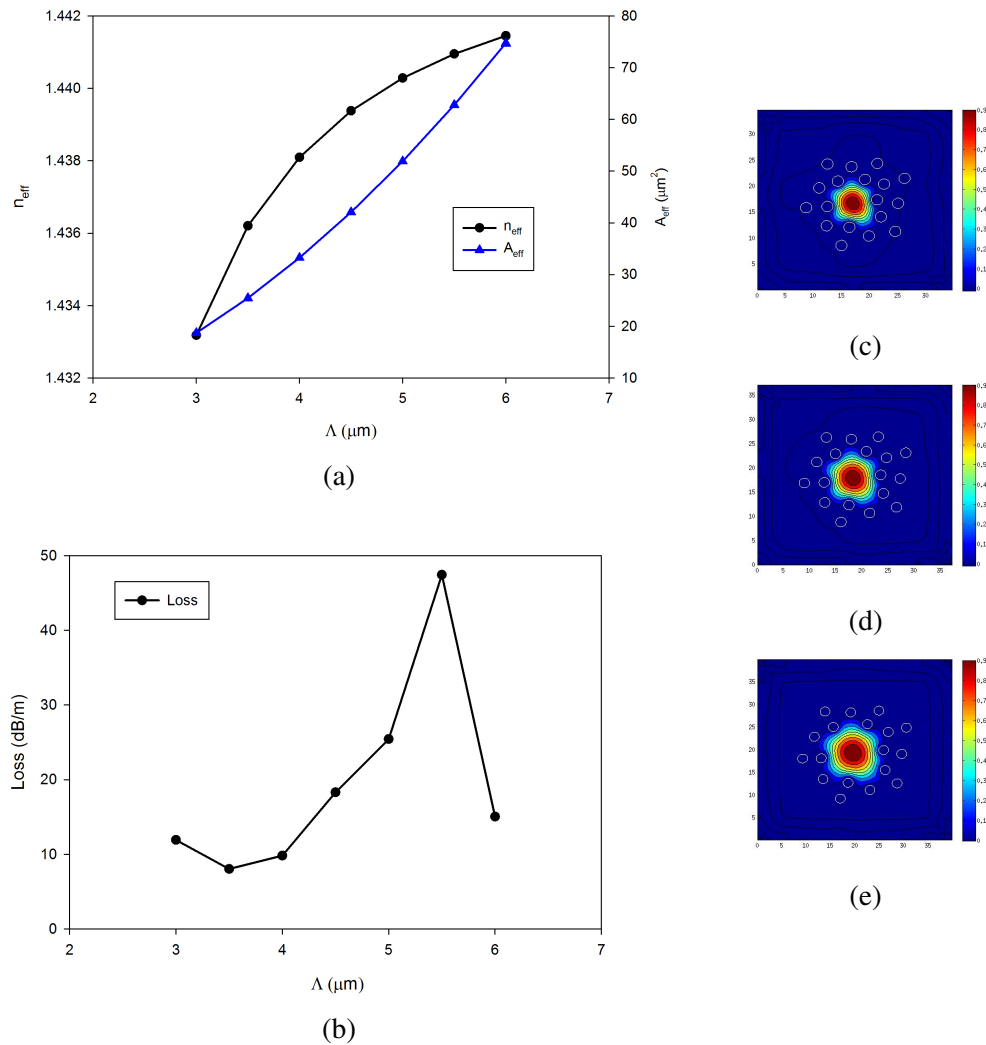


Fig. 3.17 Change in (a)  $n_{eff}$ ,  $A_{eff}$  and (b) loss with varying  $\Lambda$ , and (c-e) the corresponding field plots for  $\Lambda = 4, 5$  and  $6 \mu\text{m}$ . Structure parameters are  $N_{holes} = 18$ ,  $d = 1 \mu\text{m}$ ,  $\theta = 65^\circ$  and  $b = 0.3$ .

The pitch size has been varied from 3 to  $6 \mu\text{m}$  in this structure. The change in  $A_{eff}$  and  $n_{eff}$  due to varying ( $\Lambda$ ) are shown in Figure (3.17a). The effective area increases steadily with increase in  $\Lambda$  which agrees with the discussion on ES-PCF as in both cases the field spreads more in the larger core leading to higher values of  $A_{eff}$ . Another reason for increasing  $A_{eff}$  is due to the air filling fraction is being reduced when  $\Lambda$  is

increased and holes kept at a fixed diameter  $d$ . The loss of the fiber is discussed to check the variation which is shown in Figure (3.17b). The loss increases with increasing  $\Lambda$  as the air filling fraction is getting reduced so the loss increases. However, increasing  $\Lambda$  from  $5$  to  $6\mu\text{m}$  leads to decrease in the loss and this is believed to be the reason that the core size is large enough for the light to be confined within the core smoothly.

### 3.5.3 Study of hole size ( $d$ )

In previous sections both  $N_{holes}$  and  $\Lambda$  have been discussed. In this section, the impact of the related parameter ( $d$ ) which plays a major role in the air filling fraction value is discussed.

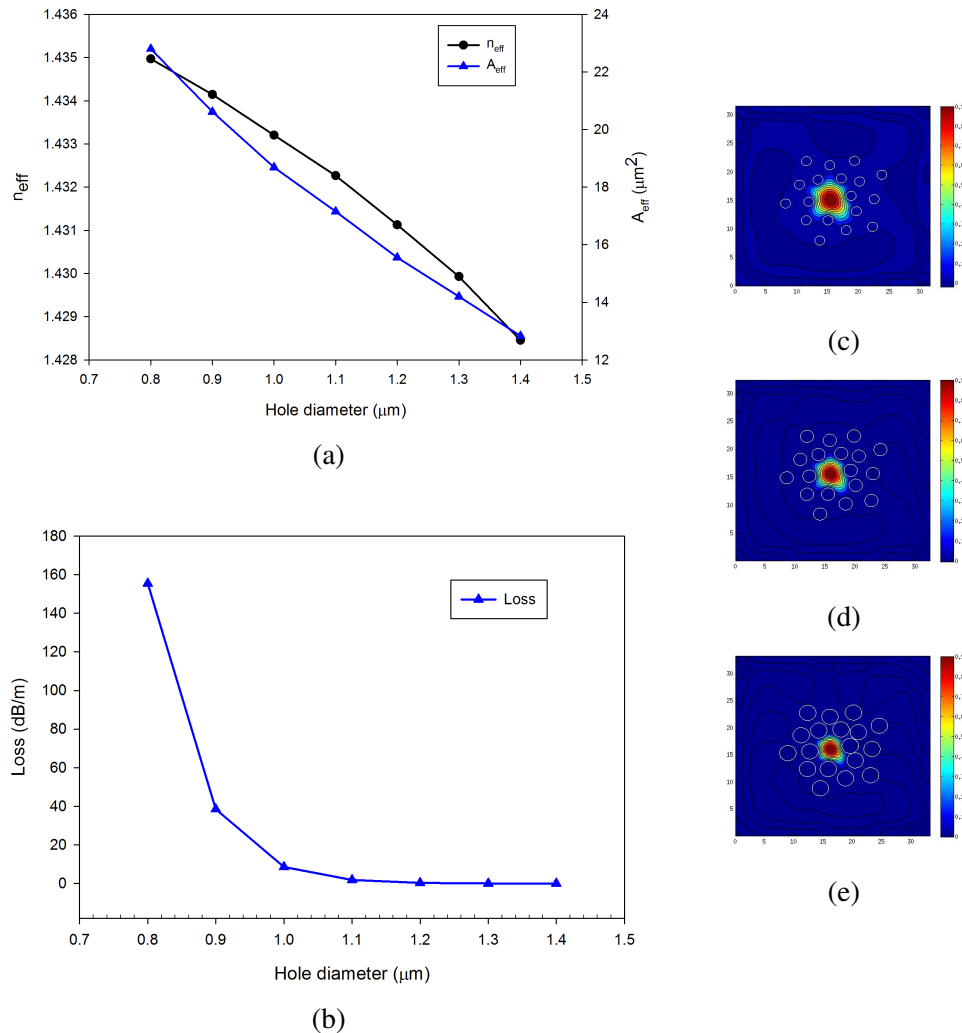


Fig. 3.18 Change in (a)  $n_{eff}$ ,  $A_{eff}$  and (b) loss with varying  $d$ , and (c-e) the corresponding field plots for  $d = 0.8, 1.1$  and  $1.4\mu\text{m}$ . Structure parameters are  $N_{holes} = 18$ ,  $\Lambda = 3\mu\text{m}$ ,  $\theta = 65^\circ$  and  $b = 0.3$ .

The other parameter which has an impact on air filling fraction is  $N_{holes}$ . However, the hole radius has more impact as the effective cladding region radius is changed slightly with a value similar to increase in  $d/2$ . The change in effective cladding region when  $N_{holes}$  increased is depending on the number of holes added. Higher air filling fraction leads to a strong field confinement in the core. The effect of the size of the holes on optical properties are explained in a structure in which  $d$  varied from 0.8 to  $1.4\mu m$ . The effective area decreases as the hole size is increased as shown in Figure (3.18a), this is due to stronger confinement factor with larger holes. The effective refractive index decreases in a similar manner to  $A_{eff}$  and that is for the same reason: the field interacts with more air when the holes are bigger. In Figure (3.18b), the loss curve shows a stable value for  $d > 1.1\mu m$  and at lower values the loss increases exponentially. The field plots with holes distributions are shown in Figures (3.18c), (3.18d) and (3.18e) for  $d$  values of 0.8, 1.1 and  $1.4\mu m$ , respectively.

#### 3.5.4 Study of turns spacing factor ( $b$ )

The factor  $b$  is the factor that controls the tightness of the spiral, at lower value the spiral is more packed together and turns are closer to each other and at higher values holes are distributed apart from each other. A typical value of  $b$  would be in the range of 0.3 to 0.5 as lower values results in squeezed turns and higher value lead to gaps between turns of the structure. The results for a structure with  $b$  varied from 0.2 to 0.6 are shown in Figure (3.19). The change in the values of  $A_{eff}$  and  $n_{eff}$  with  $b$  is shown in Figure (3.19a), where both values increase with increase in  $b$ . The reason is that for closely packed holes, the light is well confined in the core and as  $b$  value increases  $A_{eff}$  and  $n_{eff}$  increase because holes are spread further away from each other and the air filling fraction is decreased. This leads to the struts/silica regions between holes in the structure getting larger and larger and light spreading, leading to larger  $A_{eff}$ . The loss of AS-PCF increases with increase in  $b$  as shown in Figure (3.19b). The increase in loss is due to the separation of holes increasing, therefore the air filling fraction decreases and the gap between holes increases. These reasons lead to expansion of the field which leads to increase of the loss. The loss increases in an exponential way with increase in  $b$ . The scale of the loss axis is log and for an increase of 0.05 in the  $b$  factor shows a quadruple increase in the value of the loss.

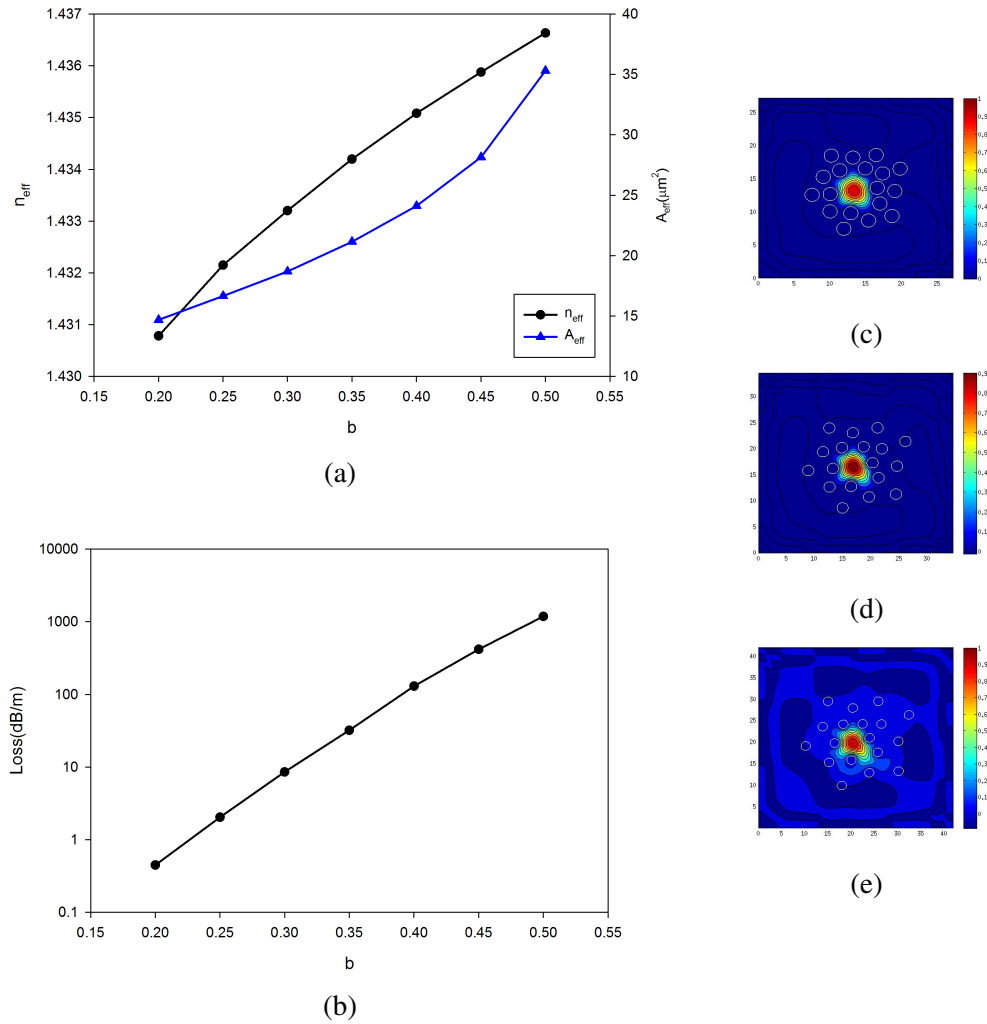


Fig. 3.19 Change in (a)  $n_{eff}$ ,  $A_{eff}$  and (b) loss with varying  $b$ , and (c-e) the corresponding field plots for  $b = 0.2, 0.35$  and  $0.5$ . Structure parameters are  $N_{holes} = 18$ ,  $\Lambda = 3\mu m$ ,  $d = 1\mu m$  and  $\theta = 65^\circ$ .

### 3.5.5 Study of angle ( $\theta$ )

The angle ( $\theta$ ) controls the position of holes in respect to the longitudinal axis or it controls the positions of holes along the spiral curve which is the angular distance through the curve. The explanation of the effect of  $\theta$  is somewhat complex as change in  $\theta$  does not follow a uniform trend for the entire range but in the ranges between the values shown in the Table (3.4). The reason is that as the value of  $\theta$  is increased or decreased, it shifts the holes close to the values at which  $\theta$  is a divisor of  $2\pi$ . This leads to holes lying in a straight lines from the center moving outwards. Therefore, the deviation of holes from these position to the right or left side leads to better field confinement when holes get distributed more randomly to fill gaps in between.

The results are shown in Figure (3.20a) for  $A_{eff}$  and  $n_{eff}$  curves. The range for varying  $\theta$  lies between  $64$  and  $68^\circ$ . The  $A_{eff}$  increases slightly with increase in  $\theta$  and at larger  $\theta$  the change is steep due to the holes deviating and creating larger struts causing the field to spread out of the core region. The change in  $n_{eff}$  is similar to  $A_{eff}$  with slight difference at lower  $\theta$ . The  $n_{eff}$  decreases at the beginning then starts to increase. The loss graph is on a log-scale and shown in Figure (3.20b) for the fiber under consideration. The loss increases slightly and at higher values of  $\theta$  loss has a step increase. This is because holes deviate from the position in which light along a AS-PCF curve is blocked from escaping.

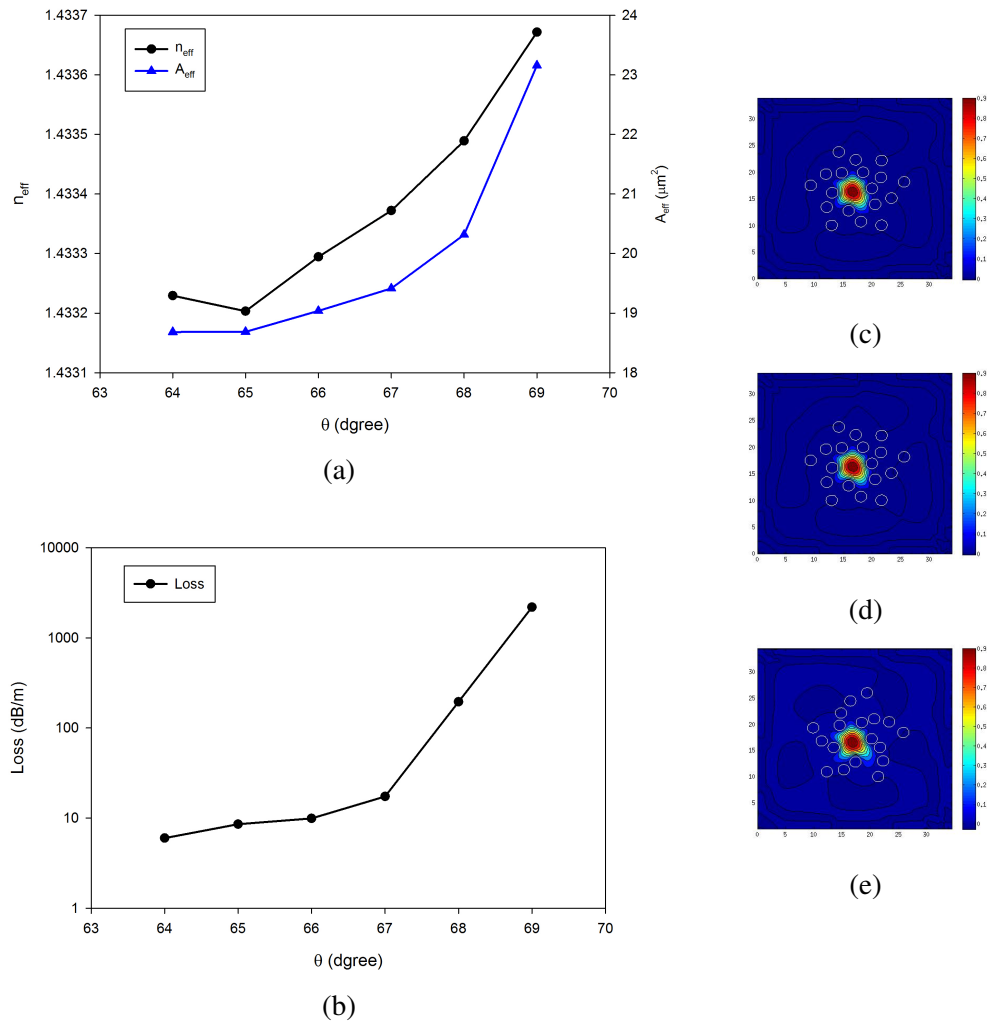


Fig. 3.20 Change in (a)  $n_{eff}$ ,  $A_{eff}$  and (b) loss with varying  $\theta$ , and (c-e) the corresponding field plots for  $\theta = 64, 66$  and  $68^\circ$ . Structure parameters are  $N_{holes} = 18$ ,  $\Lambda = 3\mu\text{m}$ ,  $d = 1\mu\text{m}$  and  $b = 0.3$ .

In this section the AS has been reviewed and the equation of the progression of the curve is implemented to arrange holes in the AS-PCF design. Even though AS has less parameters to control than the ES, the holes still can be controlled smoothly. Actually, for a large number of holes the AS is better in the arrangement of holes as the holes can be packed close together where the distance between turns in AS is constant whereas in ES the distance is increasing in geometric progression. Therefore the outer holes of ES-PCF with large  $N_{rings}$  are distributed far from each other. The way to overcome this is to use different size for the holes where the size of the holes increase in a progression with the ring number (Figure 3.21), as in the work published in OWTNM 2015 Conference [234]. The diameter of the hole ( $d_i$ ) is related to its position, holes closest to the core (first ring) have smallest diameter size ( $d_{min}$ ) and increases as the holes shifted away from the core according to the formula in Equation(3.11) and the holes with largest diameters ( $d_{max}$ ) are the outermost. However, making PCF with holes of different size is more challenging task.

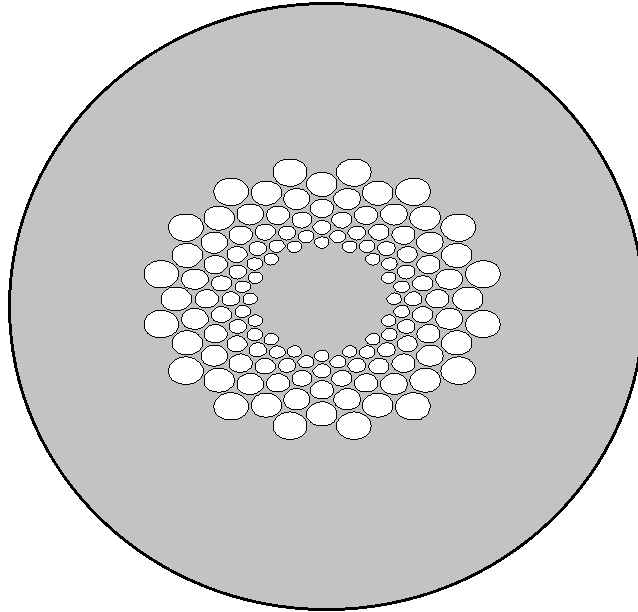


Fig. 3.21 A schematic of a cross section of the transverses direction of an ES-PCF with varying hole size. Structure parameters are  $N_{arms} = 16$ ,  $N_{rings} = 8$ ,  $\theta = 33.75^\circ$ ,  $\Lambda = 5\mu m$ ,  $d_{min} = 1\mu m$ ,  $d_{max} = 2.2\mu m$  and  $p = 1.5$ .

$$d_i = d_{min} + \left( \frac{i-1}{N_{rings}-1} \right)^p (d_{max} - d_{min}) \quad (3.11)$$

where  $i$  is the hole position and  $p$  is the ratio at which the hole size increase with position.

On the other hand the AS-PCF can be fabricated with extrusion, drilling or casting similar to ES-PCF, but the AS-PCF can be even fabricated using glass rolling. A sheet of glass is etched from one side or both (depending on the structure of interest) to form the holes and then the sheet of the glass is rolled to produce the preform which contains the AS-PCF structure [169]. One of the differences between AS-PCF and ES-PCF is the core symmetry; in an ES-PCF all the holes of each ring are equidistant from the center. In contrast, there are no two holes at same distance from the center in AS-PCF because holes are distributed over one arm which is rotating while the distance from center  $r$  increases. This leads to asymmetry in the core shape which leads to birefringence. However, the asymmetric core of the AS-PCF is not leading to high values of birefringence as the core has a sort of circular shape. Luckily, there are various spirals and different spirals can be implemented in PCF for different applications. In the next section a discussion of a spiral (Fermat's spiral) which has a non circular core (asymmetric), which can have higher values of birefringence than AS-PCF, is given.

## 3.6 Fermat's Spiral (FS)

The Fermat's spiral was explained in 1636 by the French lawyer, Pierre de Fermat, who studied mathematics in his spare time [233]. This spiral is also known as the parabolic spiral. In this section, the mathematical formula of FS is presented. In a similar manner to the ES and AS, a study of the spiral parameters is carried out to understand the effect of each parameter to control the design.

### 3.6.1 FS curve

The mathematical formula for the spiral is given by the polar equation [233]:

$$r = \theta^{1/2} \quad (3.12)$$

where  $r$  is the radial distance, and  $\theta$  is the angle in polar coordinates.

For any given positive value of  $\theta$ , there are two corresponding values of  $r$  which have opposite signs. Hence the resulting spiral is symmetrical about the origin and line  $y = -x$  [233]. The general graphical representation of the spiral is given in Figure (3.22). Dixon [236] and also Naylor [237] determined that a divergence in Fermat's spiral of  $222.5^\circ$ , which is  $360/\tau$  and  $\tau = 1.618$  (the Golden Ratio), results in a true daisy. Dixon also concluded that many plants demonstrate this pattern such as sunflowers, daisies, pineapples and pine cones [236], where Naylor included the

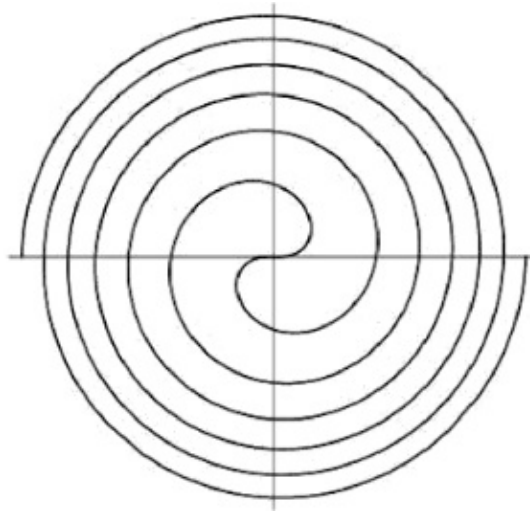


Fig. 3.22 Fermat's Spiral [233]

golden flower [237]. The Golden Ratio provides that the seeds are distributed in an equally spaced manner. The Golden Ratio is used in all the simulation of this section as this ratio yields the most packed distribution and mimics closely natural structures.

### 3.6.2 FS-PCF

The hole distribution in a Fermat's spiral is shown in Figure (3.23), which has an angle of  $222.5^\circ$  to mimic the arrangement of seeds in natural plants. The holes are at a distance of  $r_i$  from the center of the spiral (center of structure).

$$r_i = \Lambda \sqrt{i} \quad (3.13)$$

where  $i$  is the hole number

The position of the holes in the Cartesian coordinates are calculated by

$$\begin{aligned} x_i &= r_i \cos(\theta) \\ y_i &= r_i \sin(\theta) \end{aligned} \quad (3.14)$$

The position of the holes are calculated from the formulae shown with  $\theta = 222.5^\circ$ . From the formula it is clear that there are fewer parameters to vary in the ES-PCF than in the other two spirals discussed. The parameters that are varied in ES-PCF are number of holes ( $N_{holes}$ ), hole size and pitch size ( $\Lambda$ ). The core size is dependent on  $\Lambda$ , similar to other spiral designs. The difference in this spiral is that the value of  $\Lambda$  is chosen small in comparison with hole size where the  $d/\Lambda$  ratio can exceed 1. The core is formed by omitting the first hole so a core is formed. Therefore, the core is more

controlled in this spiral PCF by the number of omitted holes rather than the  $\Lambda$  value alone. The advantage of omitting holes in FS-PCF leads to totally different core shape than be the H-PCF where the core shape does not change by omitting holes from the center. The change in the core shape can offer different properties for every FS-PCF structure.

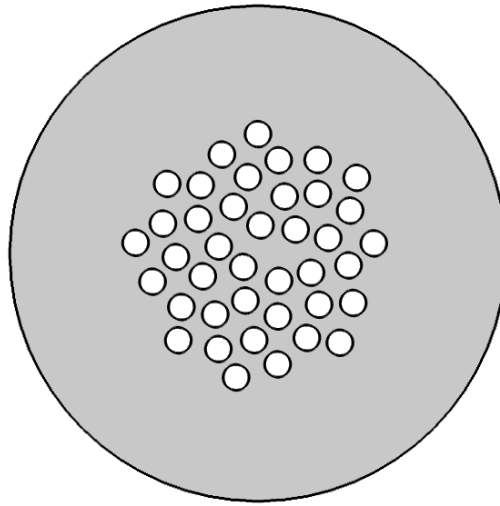


Fig. 3.23 Hole distribution of Fermat's spiral

### 3.7 Study of the FS-PCF Parameters

In this chapter, the ES and AS have been presented and their parameters have been studied in the previous sections (Sections (3.3) and (3.5)). It is noticed that similar effects have been observed when varying identical parameters in the designs of both spirals. In this section, the FS parameters are studied to obtain their effects and compare the change in optical properties with previous structures studied in this chapter. The parameters varied in this design are number of holes, hole diameter and pitch size, all have the same abbreviation or symbol as used in other sections, as  $N_{holes}$ ,  $\Lambda$  and  $d$ , respectively.

#### 3.7.1 Study of number of holes ( $N_{holes}$ )

This spiral is similar to an Archimedean in that the holes are distributed on one arm. The angle between holes is fixed one to  $222.5^\circ$  in all simulation for the two reasons mentioned above. The Fermat's spiral PCF should have a slightly large number of holes compared to ES and AS if holes are of small size in comparison to the

structure dimensions. In this comparison  $N_{holes}$  is varied from 10 to 70 and the optical properties are examined. The two fundamental modes are no longer degenerate because this structure is asymmetric, and in this case both modes are studied. The effective refractive index of both modes are presented graphically in Figure (3.24a), where both have similar trend. When  $N_{holes}$  is less than 20 the  $n_{eff}$  changes slightly because field is not well confined as  $N_{holes}$  is small and there are few holes for the field to interact with, as the  $N_{holes}$  increases to 20 and beyond the change in  $n_{eff}$  is stable. Therefore, the effective refractive index decreases with increase in  $N_{holes}$  because the air filling fraction is increased and more air in the cladding region is present for the field to interact with.

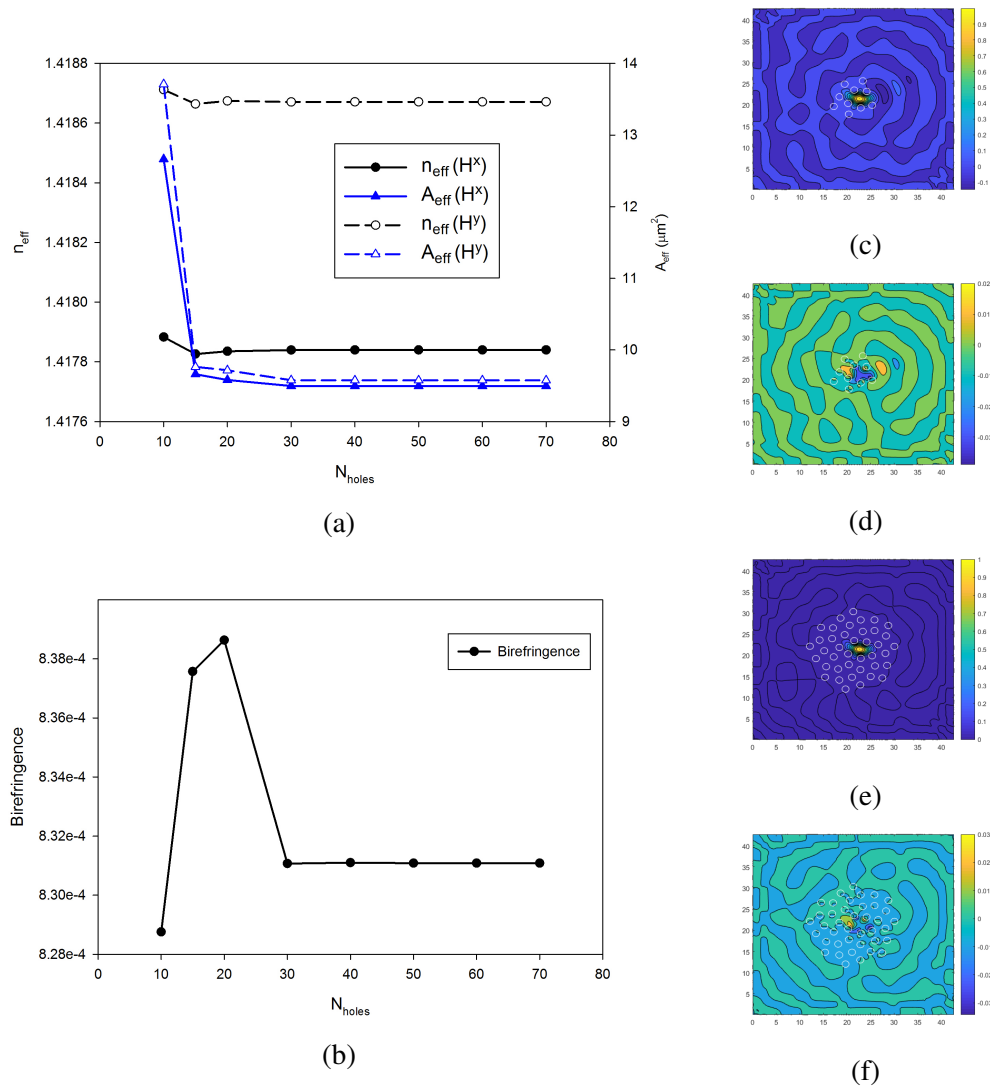


Fig. 3.24 Change in (a)  $n_{eff}$ ,  $A_{eff}$  and (b) birefringence with varying  $N_{holes}$ ,  $\Lambda = 1.5\mu m$  and  $d = 0.75\mu m$  with one missing hole in the center, and (c-e) the corresponding field plots for  $N_{holes} = 10$  and 40 for x polarized  $H_{11}^y$  and  $H_{11}^x$  fields.

The effective area curve shows that the fields have constant value for structure with  $N_{holes}$  equal to/larger than 30. The value of  $A_{eff}$  increases as the number of holes is reduced to 20 and increased slightly when reaching 15 holes. The curves of  $A_{eff}$  show steep increase as number of holes reduced to 10 due to few holes being present in the cladding region so the field is poorly confined in the core. The birefringence has constant value ( $8.31 \times 10^{-4}$ ) for the number of holes from 30 to 70. But at 20 and 15 holes the birefringence increases then drops when number of holes is reduced to 10. This fluctuation is due to the field being in the cut-off region.

The field plot shown in Figures (3.24c) and (3.24d) are for the  $H_{11}^y$  and  $H_{11}^x$  field for the x polarization, respectively. The field shows single polarization which is due to the asymmetry of the structure.

In the previous results only one value of  $n_{eff}$  is mentioned and studied in all ES-PCF and AS-PCF designs. In this design as mentioned there are two  $n_{eff}$  and the absolute difference between them is the birefringence which is introduced in Chapter 1. The birefringence is shown in Figure (3.24b) with a value of  $1.7 \times 10^{-4}$ . The number of holes does not effect the birefringence because  $n_{eff}$  for both modes are not showing any change.

### 3.7.2 Study of pitch size ( $\Lambda$ )

The study of number of holes show that when the value of  $N_{holes}$  should be large enough to confine the field. In this section the pitch is varied and results are presented in Figure (3.25). The effective area and  $n_{eff}$  of both fundamental modes increases smoothly with increasing  $\Lambda$ . This is similar to the case of ES-PCF and AS-PCF where the field expands as the core size is made larger hence higher  $n_{eff}$  and larger  $A_{eff}$ . The changes in the  $n_{eff}$  and  $A_{eff}$  of both modes are of similar trend.

The birefringence decreases with increase in  $\Lambda$  due to the fact that field at higher  $\Lambda$  is more inside the large core and less affected by the asymmetry of the holes of the structure. If the change in birefringence is compared to the case of varying  $N_{holes}$ , it is noticed that the curve follow a smooth change and the value is doubled as  $\Lambda$  decreases from 4.3 to  $3.8\mu m$  where in the case of varying  $N_{holes}$  (Figure (3.24b)) the curve is constant and there is no change in the value of birefringence at values larger than 30 holes and when number of hole is small the field is in the cut-off region and the birefringence fluctuates. The field plots for both modes are shown in Figures (3.25c), (3.25d), (3.25e) and (3.25f) for  $\Lambda = 4.3$  and  $3.8\mu m$ , respectively.

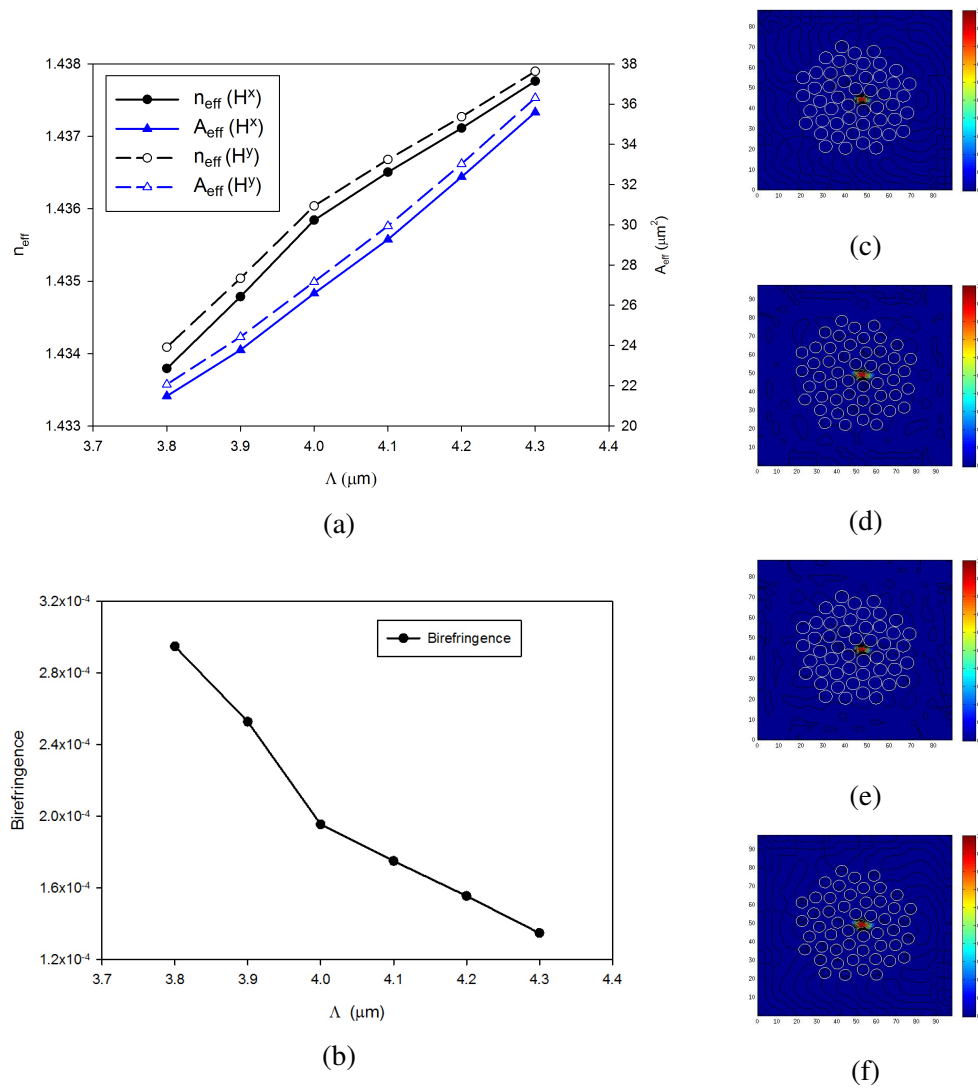


Fig. 3.25 Change in (a)  $n_{\text{eff}}$ ,  $A_{\text{eff}}$  and (b) birefringence with varying  $\Lambda$ ,  $N_{\text{holes}} = 50$  and  $d = 6\mu\text{m}$  with one missing hole in the center, and (c-e) the corresponding field plots for  $\Lambda = 3.8$  and  $4.3\mu\text{m}$  for  $H_{11}^x$  and  $H_{11}^y$  fields.

### 3.7.3 Study of hole size ( $d$ )

Another parameter that can be varied in the FS-PCF is the hole radius as shown in Figure (3.26). The effective area and  $n_{\text{eff}}$  for both modes decrease with increase in hole radius. Similar to the case of varying  $\Lambda$  where  $n_{\text{eff}}$  and  $A_{\text{eff}}$  follow similar trends. The hole radius has an opposite effect to  $\Lambda$  because if hole size is increased the core becomes slightly smaller and the space between holes decreases. This is the same scenario as when  $\Lambda$  is decreased where core decreases and space between holes is reduced. Therefore, the effect of both parameters is opposite to each other if only one parameter is varied and the other is kept constant.

Similarly, the birefringence increases with an increase in hole radius which in contrast to the case when  $\Lambda$  increased the birefringence decreased as shown in Figure (3.25b).

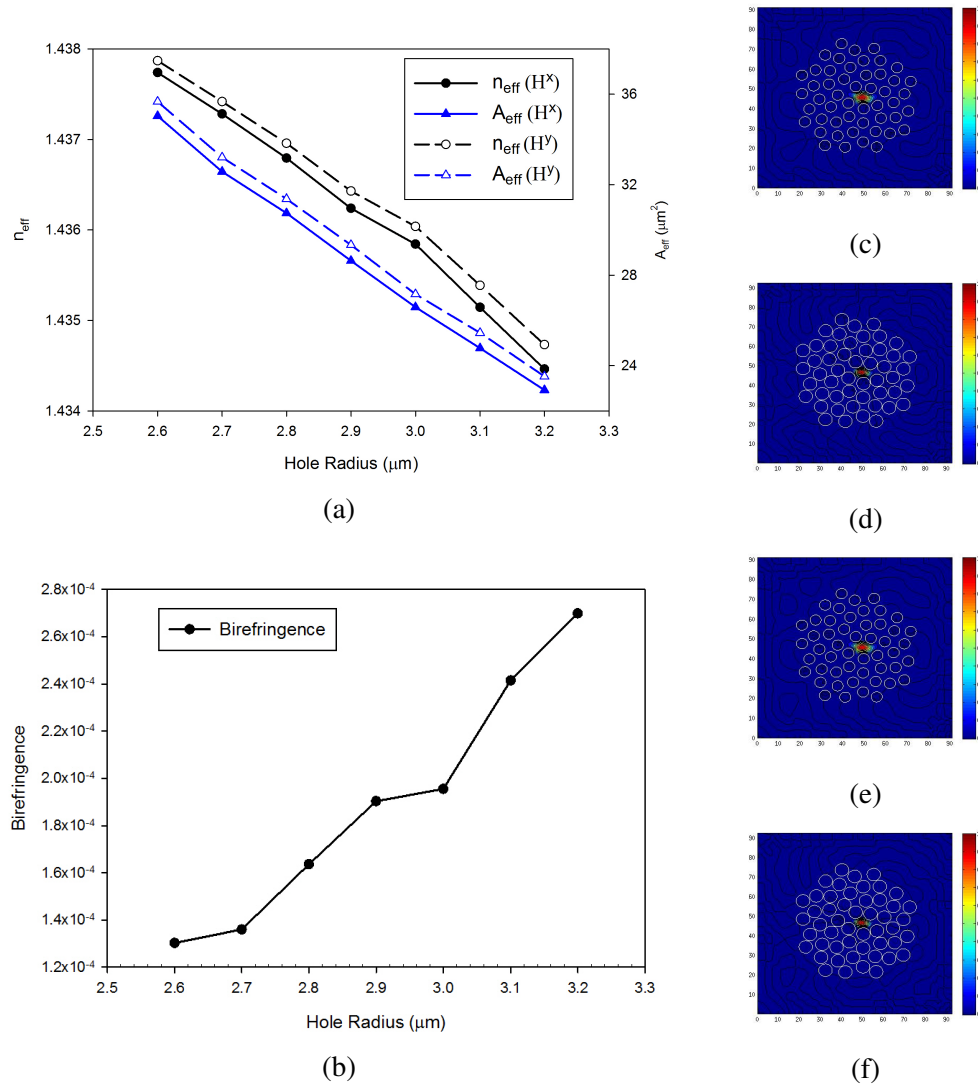


Fig. 3.26 Change in (a)  $n_{eff}$ ,  $A_{eff}$  and (b) birefringence with varying  $d$ ,  $N_{holes} = 50$  and  $\Lambda = 4\mu\text{m}$  with one missing hole in the center, and (c-e) the corresponding field plots for  $d = 2.6$  and  $3.2\mu\text{m}$  for  $H^x$  and  $H^y$  fields.

From the discussion of the three spirals presented in Sections (3.3), (3.5) and (3.7) it is obvious that every structure has advantages and disadvantages compared to others. For example, the most suitable spiral for birefringence is FS-PCF and simulation results of high birefringence values have been published [238]. The high birefringence is due to the asymmetry of the structure which results from core shape and holes distribution. The core shape is the main reason for high birefringence values and as stated before the core shape can be changed by omitting more holes and/or holes omitted at different

positions. The distribution of the holes leads to the core shape and also the holes near the core have impact on the field. The other spirals can have slightly high birefringence if the distribution of the holes is chosen to break the symmetry. However, the FS-PCF has been proven to perform better in terms of high birefringence.

The best hole distribution when the number of holes is large can be obtained by AS-PCF. In ES-PCF the distance of the holes from the center increase in progression with the number of rings. Other application of spiral PCF is non-linear effects and the most appropriate is ES-PCF and results were published for SCG [184, 225]. This section provides an introduction to the results of the different spirals as both AS-PCF and FS-PCF are presented to emphasize the unique properties of spirals in PCF designs. In the next section, two ES-PCF structures of different hole size are compared alongside AS-PCF and ES-PCF structures. The comparison of the results is obtained to highlight the main differences between the three spiral (ES, AS and FS) PCF designs.

### 3.8 Comparison of Spiral PCFs

The results of each spiral from the three spiral (ES, AS and FS) PCFs presented in this work have been given in a separate section. A full comparison between the three spirals in terms of their optical properties is given in this section. The designs have similar structural parameter values to observe the different effects of their structure. The structures compared are ES-PCF, AS-PCF and two FS-PCF which have different  $d/\Lambda$  value of 0.6 and 1.2, and the former two designs have  $d/\Lambda = 0.6$ . The total number of holes in every structure is 18 where ES-PCF has 6 arms and 3 rings, the pitch size  $\Lambda = 2\mu m$ , the angle  $\theta$  has a value of  $30^\circ$ ,  $65^\circ$  and  $222.5^\circ$  for ES, AS and FS-PCFs, respectively. The last parameter is the  $b$  value of AS-PCF, which equals 0.3. The parameters of the designs are given and the best point to start at is the distribution of the holes in the cladding. The layouts of the holes in the transverse direction are shown in Figure (3.27). The structures are sorted left to right as ES-PCF, AS-PCF, FS-PCF with  $d/\Lambda = 0.6$  and FS-PCF with  $d/\Lambda = 1.2$ ; the graphs have the same aspect ratio. The first three have similar  $d/\Lambda$  hence the holes are identical in size. The most dense packed distribution is formed by ES-PCF where holes are surrounding the core tightly. The two in the middle have scattered holes distribution where holes in FS-PCF are spread more. The fact is that holes distributed over one arm are not as flexible as when having two distinct variables to control the holes such as in ES-PCF. The number of arms can be increased to have very dense holes in the first ring.

Another difference between the structure with various arms (ES-PCF) and one arm structures (AS-PCF and FS-PCF) is the core symmetry. In one arm structure the core is not symmetric because the distance of the holes from the center is changing with the hole number (increases as the hole number increase) from the formulae of the AS-PCF (Equation (3.10)) and FS-PCF (Equation (3.13)). On the other hand, the ES-PCF structure can have a symmetric core if number of arms chosen is even. Furthermore, if  $N_{arms}$  is even and  $\theta$  is chosen to be  $\pi/N_{arms}$  then the entire structure has a symmetry (First graph in Figure (3.27) has six-fold symmetry). However, the core of ES-PCF structure has a kind of circular shape because all holes of each ring are at fixed distance. The last comment on the figure is that the last two graphs are identical in all parameters but one, which is the  $d/\Lambda$ . The hole size  $d$  is doubled in the last graph and its effect is discussed in the results.

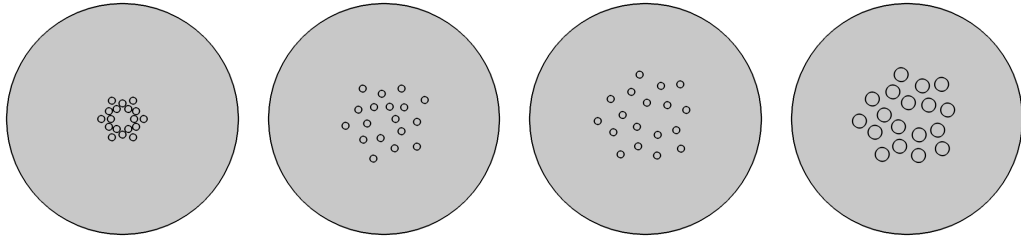


Fig. 3.27 Schematics of cross sections of four structures: ES-PCF has  $N_{arms} = 6$ ,  $N_{rings} = 3$ ,  $d/\Lambda = 0.6$  and  $\theta = 30^\circ$ ; AS-PCF has  $N_{holes} = 18$ ,  $d/\Lambda = 0.6$ ,  $b = 0.3$  and  $\theta = 65^\circ$ ; and two FS-PCF has  $N_{holes} = 18$ ,  $\theta = 30^\circ$  and  $d/\Lambda = 0.6$  and  $1.2$ . All structures has  $\Lambda = 2\mu m$ .

In all sections  $n_{eff}$  is the first property discussed due to its importance. The change in  $n_{eff}$  with wavelength of the four structures is shown in Figure (3.28). The highest change (dark-green line) is in the ES-PCF structure due to dense packing of holes near the core. The field interacts with the air in the holes and  $n_{eff}$  is decreased as the air filling fraction increases within the field interaction space. The change in  $n_{eff}$  of AS-PCF (black line) is higher than in the FS-PCF with the same  $d/\Lambda$  (blue line) because the holes are distributed in a way which blocks the field better than the case in FS-PCF hence the field expands in the holes more. This can be justified by comparing FS-PCF structure with larger hole (blue dashed line) which has lower  $n_{eff}$  than same structure with small holes and even lower than AS-PCF. The large holes led to an increase in the air filling fraction and struts between holes are reduced in size so the field cannot expand freely in the material. The field expands in holes and interaction with air increases. A general remark on Figure (3.28) is the change in  $n_{eff}$  is small

at lower wavelength and increases at higher wavelengths as the field expands with increase in wavelength.

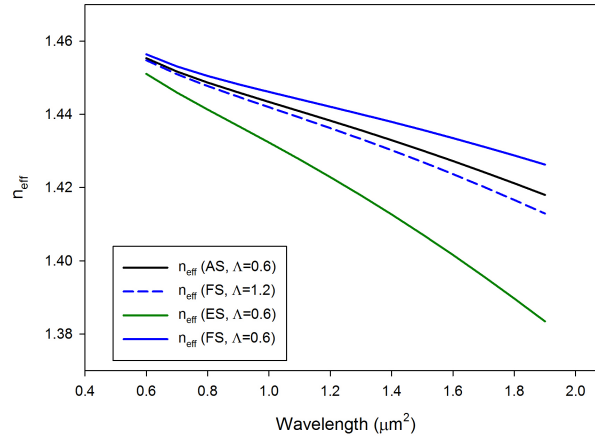


Fig. 3.28 Comparison of the change in  $n_{eff}$  with wavelength. The structures parameters are: ES-PCF has  $N_{arms} = 6$ ,  $N_{rings} = 3$ ,  $d/\Lambda = 0.6$  and  $\theta = 30^\circ$ ; AS-PCF has  $N_{holes} = 18$ ,  $d/\Lambda = 0.6$ ,  $b = 0.3$  and  $\theta = 65^\circ$ ; FS-PCF has  $N_{holes} = 18$ ,  $\theta = 30^\circ$  and  $d/\Lambda = 0.6$  and 1.2. All structures have  $\Lambda = 2\mu m$ .

The asymmetry of the core leads to different propagation constants for the two fundamental modes. The result is two modes with different  $n_{eff}$  values. The difference between those values is the birefringence and it is shown in Figure (3.29) for three structures. The fourth structure (ES-PCF) has symmetric core and the two modes are alike. The birefringence of AS-PCF is higher than FS-PCF with holes of similar size but the birefringence increases when hole size increased for FS-PCF. The reason is that at larger hole size the field is affected more by the holes where core size is reduced and the struts between holes are shrunk (see Figure (3.27)). The smaller core leads to more interaction of the field with the asymmetric core hence higher birefringence. If the core size is very large compared to the wavelength of operation then the asymmetry of the core does not have huge impact on the birefringence. The field is expanded in the core freely and the interaction between field and the core edges is small. The shrinking in size of the struts forces the field to interact with holes instead of expanding through large struts. The increase in the holes in AS-PCF would not increase the birefringence sufficiently due to two reasons. The first one is the holes cannot be made as large as in the FS-PCF because the distance between holes is smaller (see Figure (3.27)), and second reason is the increase of the holes in AS-PCF has small effect on the shape of the core due to the distribution of the holes. To sum up, the best birefringence obtained

in spiral PCFs is  $1.6 \times 10^{-2}$  at  $1.55 \mu\text{m}$  in FS-PCF [238] to the best knowledge of the author.

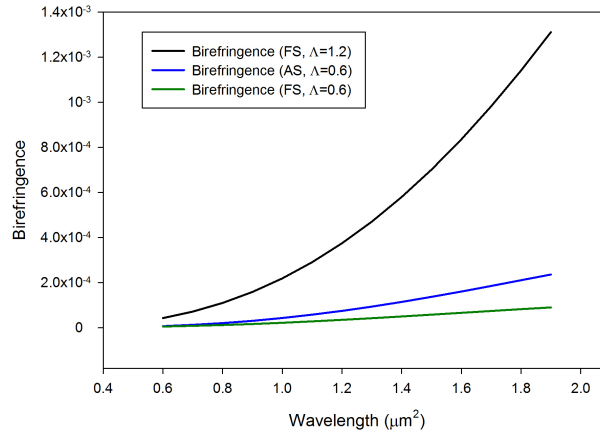


Fig. 3.29 Comparison of the change in Birefringence with wavelength. The structures parameters are: AS-PCF has  $N_{holes} = 18$ ,  $d/\Lambda = 0.6$ ,  $b = 0.3$  and  $\theta = 65^\circ$ ; FS-PCF has  $N_{holes} = 18$ ,  $\theta = 30^\circ$  and  $d/\Lambda = 0.6$  and  $1.2$ . All structures have  $\Lambda = 2 \mu\text{m}$ .

The field in the ES-PCF is well confined because holes are packed together and there is not enough spaces between holes for the field to expand. Therefore, ES-PCF has lowest  $A_{eff}$  among the four designs as shown in Figure (3.30).

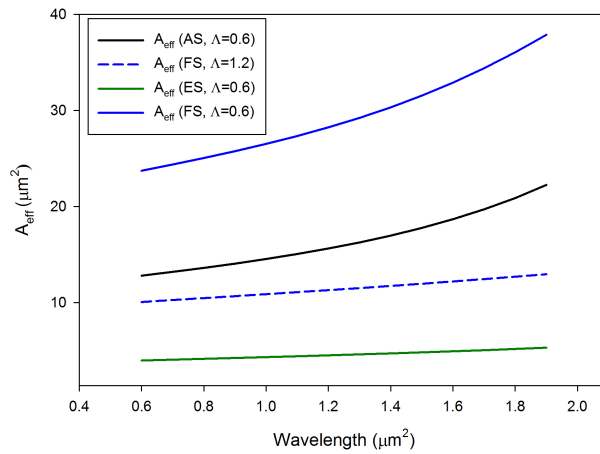


Fig. 3.30 Comparison of the change in  $A_{eff}$  with wavelength. The structures parameters are: ES-PCF has  $N_{arms} = 6$ ,  $N_{rings} = 3$ ,  $d/\Lambda = 0.6$  and  $\theta = 30^\circ$ ; AS-PCF has  $N_{holes} = 18$ ,  $d/\Lambda = 0.6$ ,  $b = 0.3$  and  $\theta = 65^\circ$ ; FS-PCF has  $N_{holes} = 18$ ,  $\theta = 30^\circ$  and  $d/\Lambda = 0.6$  and  $1.2$ . All structures have  $\Lambda = 2 \mu\text{m}$ .

The value of  $A_{eff}$  in the entire range is lower than  $5 \mu\text{m}^2$ . The values of  $A_{eff}$  are ranging from  $12 - 20 \mu\text{m}^2$  for AS-PCF and for FS-PCF values are higher than  $23 \mu\text{m}^2$

at lower wavelength and increase to reach up to  $28\mu m^2$ . The increase of the holes size in FS-PCF leads to a reduction in  $A_{eff}$  values to less than half. These value of  $A_{eff}$  will reflect on the non-linearity; ES-PCF design is thus more favorable for non-linear effects than AS-PCF and FS-PCF.

The non-linearity plots of the four structures are shown in Figure (3.31). The color and style of the lines are kept similar to  $n_{eff}$  figure for each structure. The curves sequence is reversed where the highest in  $A_{eff}$  graph is the lowest in  $\gamma$  graph and this is because the relation is inverse between  $A_{eff}$  and  $\gamma$  as mentioned in Section (1.3.4). The value of  $\gamma$  of ES-PCF is more than twice the value of  $\gamma$  for the other spiral PCFs.

The conclusion from the graphs of  $A_{eff}$  and  $\gamma$  is that ES-PCF is the best design suited for non-linear effects. Other spiral structures have lower  $\gamma$  even with holes double the size. The AS-PCF outperforms FS-PCF with similar holes size.

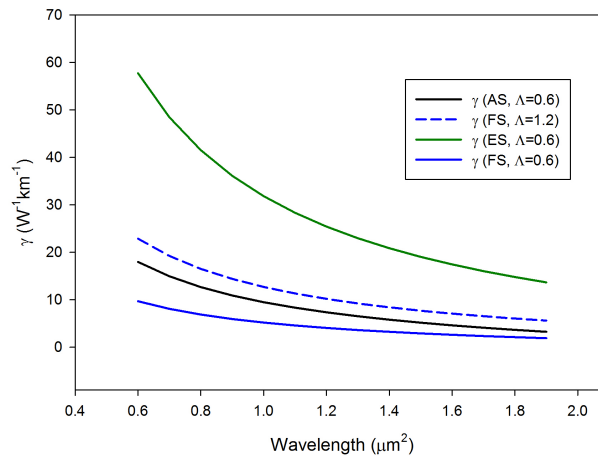


Fig. 3.31 Comparison of the change in  $\gamma$  with wavelength. The structures parameters are: ES-PCF has  $N_{arms} = 6$ ,  $N_{rings} = 3$ ,  $d/\Lambda = 0.6$  and  $\theta = 30^\circ$ ; AS-PCF has  $N_{holes} = 18$ ,  $d/\Lambda = 0.6$ ,  $b = 0.3$  and  $\theta = 65^\circ$ ; FS-PCF has  $N_{holes} = 18$ ,  $\theta = 30^\circ$  and  $d/\Lambda = 0.6$  and  $1.2$ . All structures have  $\Lambda = 2\mu m$ .

The last property compared in this section is the loss of the structures. This is shown as a function of wavelength in Figure (3.32). Although the ES-PCF curve shows a steep change, it still has the lowest loss in the wavelengths below  $1.6\mu m$  with a value of less than  $20dB/m$ . The loss at lower wavelength for both AS-PCF and FS-PCF have values larger than ES-PCF of 5 order of magnitude. The large holes FS-PCF structure has loss lower than AS-PCF and FS-PCF with small holes.

The general results of the spirals are concluded in this section. From these results we can conclude that three spirals have different behavior and offer advantages for different applications. For example, for large birefringence for sensing, gyroscope etc

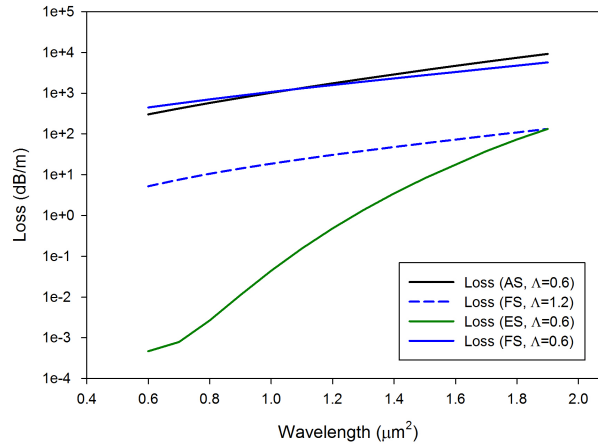


Fig. 3.32 Comparison of the change in loss with wavelength. The structures parameters are: ES-PCF has  $N_{arms} = 6$ ,  $N_{rings} = 3$ ,  $d/\Lambda = 0.6$  and  $\theta = 30^\circ$ ; AS-PCF has  $N_{holes} = 18$ ,  $d/\Lambda = 0.6$ ,  $b = 0.3$  and  $\theta = 65^\circ$ ; FS-PCF has  $N_{holes} = 18$ ,  $\theta = 30^\circ$  and  $d/\Lambda = 0.6$  and 1.2. All structures have  $\Lambda = 2\mu m$ .

the FS-PCF is more suitable, while for non-linear applications the ES-PCF is the best design as it confines the field the most. In the next section the ES-PCF is revisited to study the effect of changing the parameters for two different pitch sizes. The pitch size plays an important role in the properties of the fiber and two values of  $\Lambda$  are chosen to compare the difference.

### 3.9 Results of Ideal ES-PCF

The optical performance of PCF with different spiral have been discussed and results presented for various parameters variation in the previous sections. In this section the ES-PCF is revisited to provide an in depth evaluation of the variation of the parameters over the transparency wavelength window of the silica material, to study the effect of dispersion and how can it be controlled. The term ideal refers to the unmodified spiral as the topic of next chapter is the Steiner ES-PCF which is a modification of ES-PCF. The structures studied in this section are 6, 7 and 8 arms structures with varying  $N_{rings}$  and  $d/\Lambda$ . The angle is fixed at  $\theta = \pi/N_{arms}$  for all structures such that even numbered holes are in the middle of two preceding odd holes. The odd numbered holes lie on the same angle position as the preceding odd hole of the adjacent arm. The optical properties are obtained for the wavelength range  $0.6$  to  $1.9\mu m$ . There are two case studies in this section with the first being for  $\Lambda$  greater than the wavelength of operation. The second case is for  $\Lambda$  being comparable with the wavelength of operation.

Figure (3.33) shows the distribution of air-holes in the ES, which has 7 arms. Each arm has 4 holes, which form a single ES with a radius of  $\Lambda$  and an angular increment of  $\theta$  degrees. The holes have a diameter of  $d$ . The use of dotted lines is only to clarify the direction of growth of the arms and the distribution of holes among the arms.

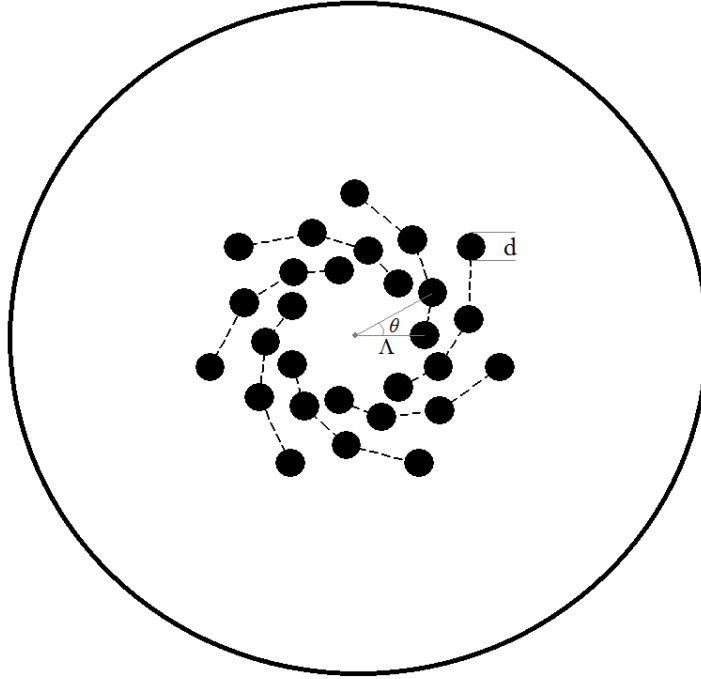


Fig. 3.33 Air-hole arrangements in ES-PCF (7 arms &  $\theta = 30^\circ$ )

### 3.9.1 Large pitch scenario ( $\Lambda = 4\mu m$ )

The study in this scenario is concerned with a large pitch value (hence large core) so the light is well confined in the core and has less interaction with outer holes. This is proven by the study by changing number of rings and comparing the optical properties. Three 7 arm structures with identical parameters and varying number of rings of values 3, 4 and 5 rings have been considered for the comparison. It has been observed that there is no change in  $n_{eff}$  and  $A_{eff}$  with varying  $N_{rings}$  through the entire wavelength range, as shown in Figures (3.34) and (3.35), respectively. A similar study was carried out for two 8 arm structures with 3 and 4 rings (graphs not included here). This study also showed no change in  $n_{eff}$  and  $A_{eff}$ . The latter study serves to confirm the outcome observed in the former case. The observation obtained from the two studies of varying  $N_{rings}$  is that when  $N_{rings} > 3$  the increase in number of rings can be neglected if the size of the core is larger than the wavelength of operation.

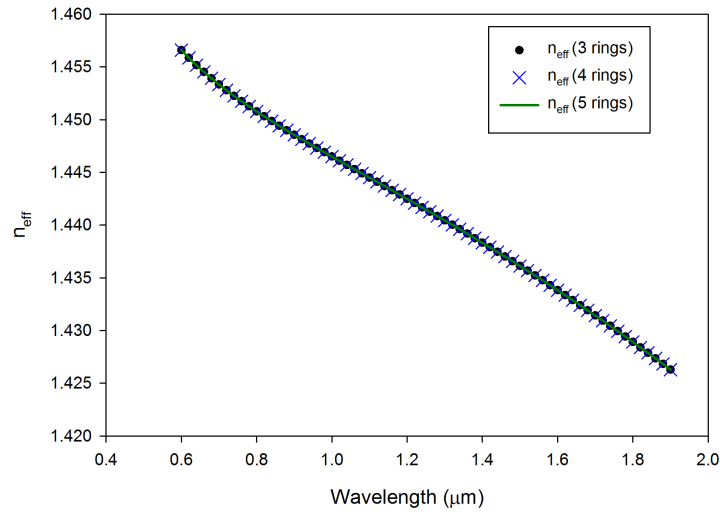


Fig. 3.34 Study the effect of varying  $N_{rings}$  on  $n_{eff}$  for ES-PCF with 7 arms,  $d/\Lambda = 0.42$ ,  $\Lambda = 4\mu m$  and  $\theta = 30^\circ$

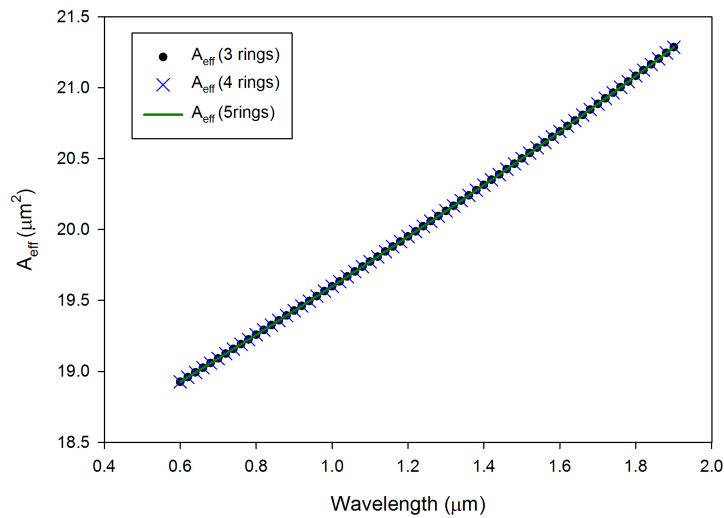


Fig. 3.35 Study the effect of varying  $N_{rings}$  on  $A_{eff}$  for ES-PCF with 7 arms,  $d/\Lambda = 0.42$ ,  $\Lambda = 4\mu m$  and  $\theta = 30^\circ$

The study of varying the ratio  $d/\Lambda$  has shown that this ratio has impacted on optical properties. The difference in the  $A_{eff}$  values, for structures with different  $d/\Lambda$  ratios, is almost constant through out the entire wavelength range of study, see Figure (3.36). The smaller the ratio the larger the  $A_{eff}$ , and this is what is expected as hole size is smaller hence the field is less confined and spreads more. Also the core size depends on  $\Lambda$  and  $d$  as noted in the previous sections. The smaller value of  $d$  leads to smaller  $d/\Lambda$  and larger core size. The field would spread in the core and  $A_{eff}$  will increase.

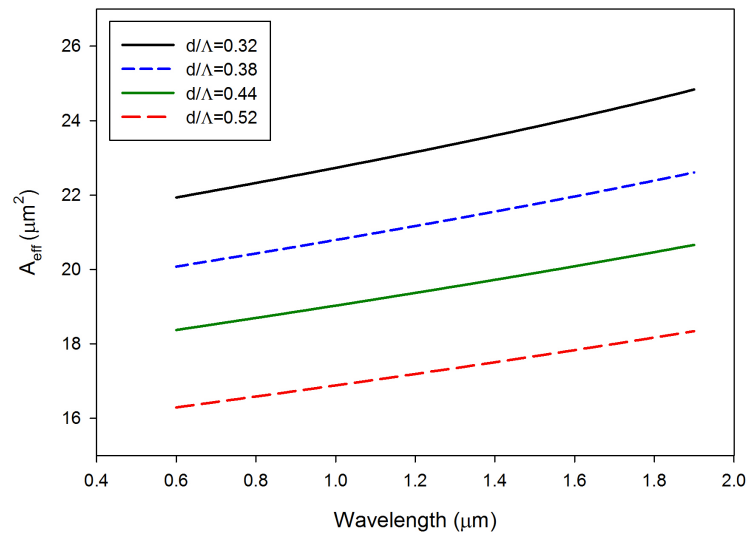


Fig. 3.36 Study the effect of varying the ratio  $d/\Lambda$  on  $A_{eff}$  for ES-PCF with 7 arms, 4 rings,  $\Lambda = 4\mu m$  and  $\theta = 30^\circ$ .

On the other hand, the change in  $n_{eff}$  is small at lower wavelengths and the difference increases with increasing wavelength as shown in Figure (3.37). This change is due to field interaction with air in the holes at higher wavelengths. The field spreads more as wavelength is increased and interacts with holes more leading to different  $n_{eff}$  for different value of  $d/\Lambda$ . The larger the ratio the smaller  $n_{eff}$  is.

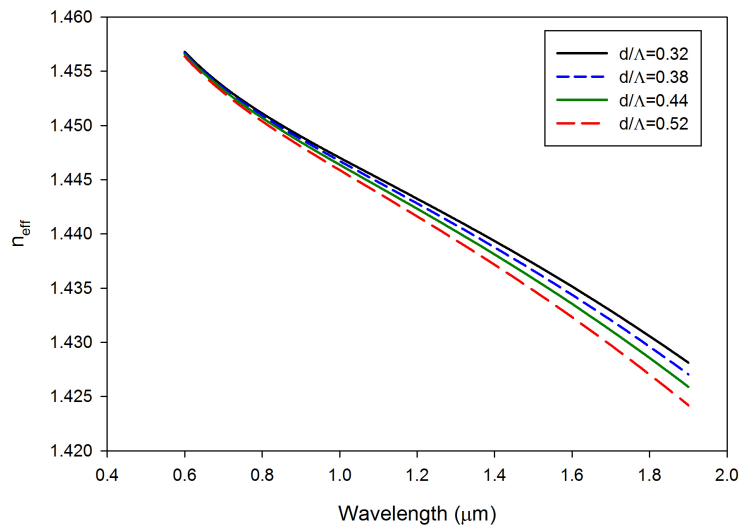


Fig. 3.37 Study the effect of varying the ratio  $d/\Lambda$  on  $n_{eff}$  for ES-PCF with 7 arms, 4 rings,  $\Lambda = 4\mu m$  and  $\theta = 30^\circ$ .

The variation of arms leads to similar behavior to varying  $d/\Lambda$  as both lead to a change in the air filling fraction of the cladding region, and hence to a change in the cladding effective refractive index. However, the change in arms has small effect on  $n_{eff}$  even at higher wavelengths as can be seen from Figure (3.38). The reason behind this is the change in air filling ratio is somehow limited for  $N_{arms}$  to small variation which leads to small change in  $n_{eff}$ . For example if number of arms is varied from 6 to 7 the air filling ratio is increased by a factor of  $1/6$ . The limiting factor is that the number of arms in practical designs should be in the range of 5 to 8 arms as mentioned in Section (3.3.1). On the other hand, the ratio  $d/\Lambda$  can be varied more freely from small to closer to the maximum value possible. Moreover, the change of  $N_{arms}$  leads to change in the hole distribution; hence the properties will be altered by the change in air filling fraction and the position of the holes at the same time. In the case of varying  $d/\Lambda$  only the air filling fraction is changed which makes it practical to control field profile.

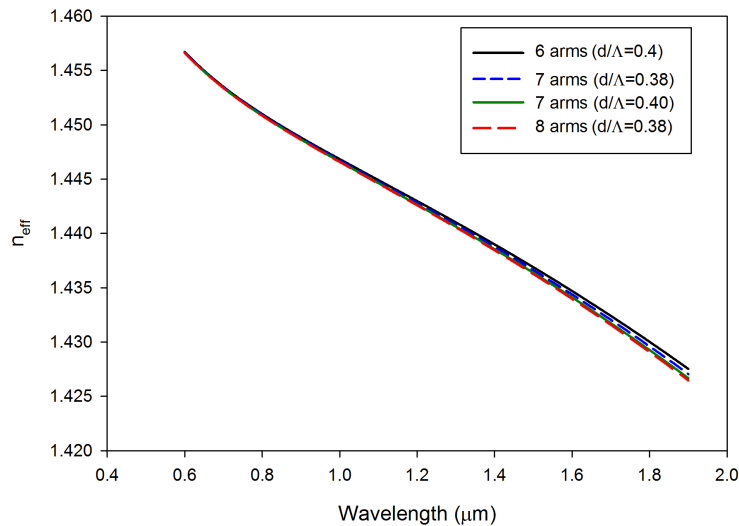


Fig. 3.38 Study the effect of varying the number of arms on  $n_{eff}$  for ES-PCF with 4 rings, ratio of 0.4 and 0.38,  $\Lambda = 4\mu m$  and  $\theta = 30^\circ$ .

From Figure (3.38), varying of arms from 7 (blue dashed lines) to 8 (red dashed lines) with identical  $d/\Lambda = 0.38$  leads to an increase of one seventh (0.1430) in the air filling fraction, where varying  $d/\Lambda$  from 0.38 to 0.4 for 7 arms structure leads to an increase of (0.053) in the air filling fraction. The change when varying the number of arms is higher due to increase in the air filling fraction, which is three times more, but the structures of 7 arms with  $d/\Lambda = 0.4$  and 8 arms with  $d/\Lambda = 0.38$  have very close values which agree with the discussion that the number of arms has less effect.

There is another observation to point out. When varying the number of arms from 6 to 7, with  $d/\Lambda = 0.4$  (solid lines), the change in  $n_{eff}$  is slightly higher than when varying arms from 7 to 8 with  $d/\Lambda = 0.38$  (dashed lines) as can be seen from Figure (3.38). The reason is the air filling fraction increases more in the former case due to change of arms in the former case led to an increase in the air filling fraction by  $1/6$  of its initial value and in the latter case the increase is  $1/7$  of the initial value, where larger change leads to effect the properties of the field more. Moreover, the added holes in the former case are bigger as the ratio  $d/\Lambda$  is larger so more air is introduced. Therefore the change in the percentage of the air filling fraction is larger when varying  $N_{arms}$  from 6 to 7.

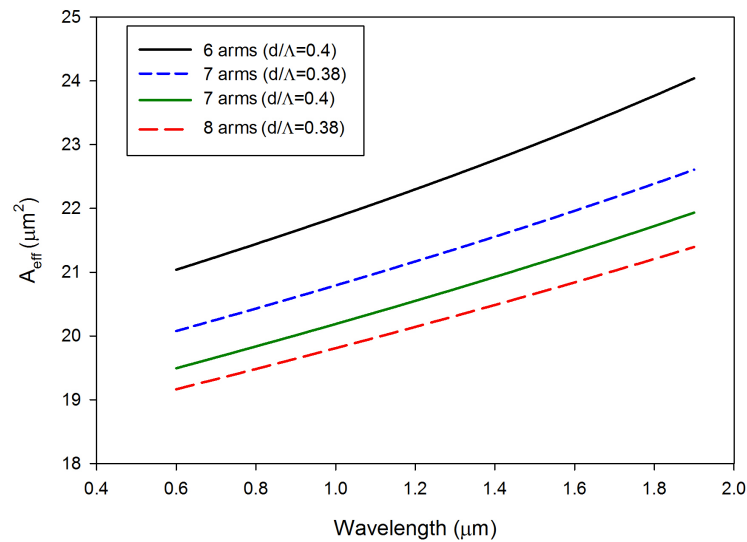


Fig. 3.39 Study the effect of varying the number of arms on  $A_{eff}$  for ES-PCF with 4 rings, ratio of 0.4 and 0.38,  $\Lambda = 4\mu m$  and  $\theta = 30^\circ$ .

The result of  $A_{eff}$  for a similar study of  $d/\Lambda = 0.38$  and 0.4 ratio is shown in Figure (3.39). The change in  $A_{eff}$  is of more than  $1\mu m$  for an addition of one arm to the structure with similar hole size. The effective area decreases as  $N_{arms}$  increases for the entire wavelength range. This behavior holds for different ratios, and the reason is that the holes close to the center will increase by one in each ring which leads to better confinement of the field. In the case of changing from 6 to 7 arms with  $d/\Lambda = 0.4$  (solid lines Figure (3.39)) the change in the value of  $A_{eff}$  is larger then when changing from 7 to 8 arms with  $d/\Lambda = 0.38$  (dashed lines). The reason is that the ratio  $d/\Lambda$  is higher then the added holes of the arm will increase the air filling fraction more and the field will be influenced further and the reason discussed above. The other thing is to compare change in  $A_{eff}$  between 6 to 7 arms (solid lines) and between the two 7 arms curves.

The difference when varying the number of arms is larger, and in this case follows the ratio of change in the air filling fraction. The change in  $d/\Lambda$  value leads to an increment in air filling fraction of 0.053 and the change in  $N_{arms}$  leads to an increment of 0.143 which is roughly three times the increment by changing  $d/\Lambda$ . From Figure (3.39) it is obvious that the change between 6 and 7 arms with  $d/\Lambda = 0.4$  is roughly three times the change between the two 7 arms structures. Therefore, the change in  $A_{eff}$  follows the ratio of change in the air filling fraction but the  $n_{eff}$  responds differently.

The most important point of this study is to focus on one property at a time when optimizing a structure for a specific application as changing more than one parameter at once would have an unexpected behavior and properties cannot be controlled smoothly. To conclude this section, the control of the dispersion in a large  $\Lambda$  design is limited as the effect of varying other parameters has small effect on  $n_{eff}$  which is not adequate to manage the dispersion as required. The second issue is that the core size is large; as  $A_{eff}$  is related to the square root of the field radius, a small increase in the core diameter leads to significant increase in  $A_{eff}$ . The pitch size used in SCG, to the best knowledge of the author, is in the range of less than  $2\mu m$  down to a sub micron [13, 48]. In general values of  $\Lambda$  should be comparable with the operating wavelength for light to interact with the microstructure of the cladding. In the next section a study of small  $\Lambda$  is carried out to investigate the effect of dimensional parameters on the optical properties.

### 3.9.2 Small pitch scenario ( $\Lambda = 1\mu m$ )

The study of large pitch has been discussed and the effect on the optical properties are explained in Section (3.9.1). In this part the study of designs with small pitch sizes, comparable to the wavelength of operation, is carried out and the effect of variation of other parameters on the optical properties is explained. A comparison between the behavior of the large and small pitch designs is also presented. The study is for structures with 6, 7 and 8 arms, with varying parameters as in the previous case of large pitch.

The change of number of rings has shown similar behavior to the case when the pitch size is large. The different structures at lower wavelengths show no change in  $n_{eff}$  for structures with different  $N_{rings}$  below a wavelength of  $1.4\mu m$  and  $A_{eff}$  for wavelengths below  $1.2\mu m$  (see Figures (3.40) and (3.41), respectively). However, at higher wavelengths  $N_{rings}$  has an effect on optical properties which is due to the fact that the field expands out of the core and interacts with holes in outer rings. This happens due to the wavelength of operation being larger than the pitch and the field is not well confined in the core.

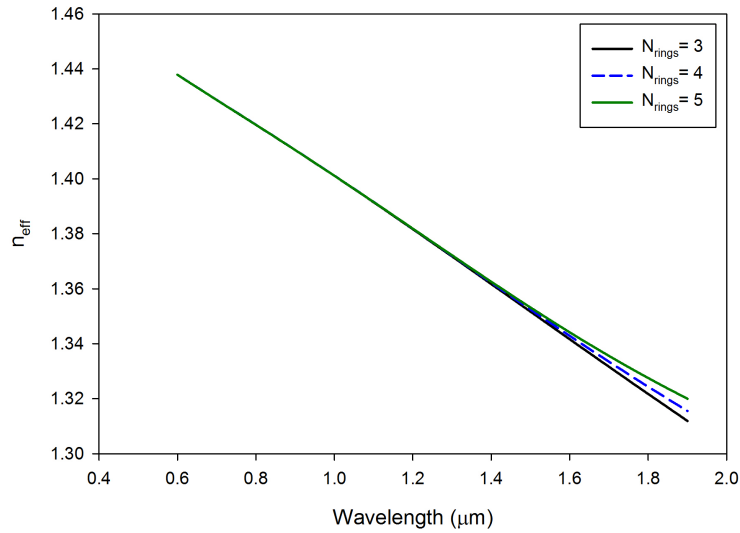


Fig. 3.40 Study the effect of varying the number of rings on  $n_{eff}$  for ES-PCF with 7 arms, ratio of 0.42,  $\Lambda = 1\mu m$  and  $\theta = 30^\circ$ .

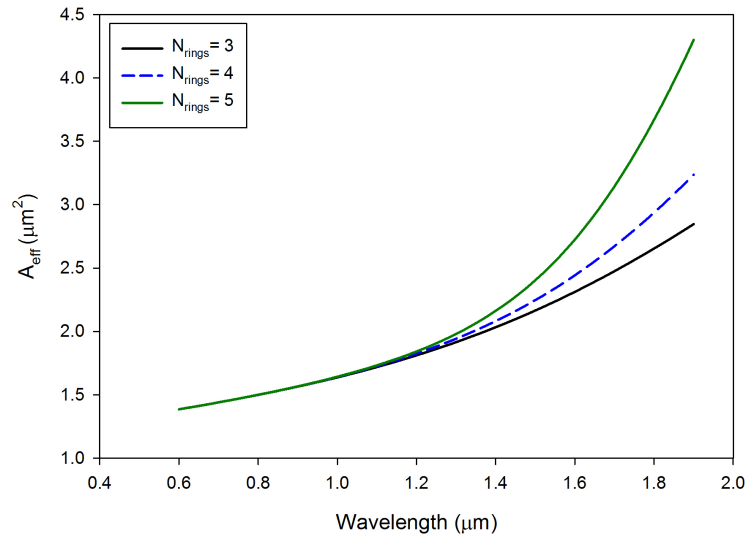


Fig. 3.41 Study the effect of varying the number of rings on  $A_{eff}$  for ES-PCF with 7 arms, ratio of 0.42,  $\Lambda = 1\mu m$  and  $\theta = 30^\circ$

The behavior at higher wavelengths is completely different to what is expected; the higher number of rings structure has a higher  $A_{eff}$ . From a physical point of view, the field should be more confined with more rings in the cladding for otherwise identical (same value of  $N_{arms}$ ,  $\Lambda$  and  $d/\Lambda$ ) structures. The reason for this unexpected behavior is that the size of simulation window is taken to be dependent on the size of the structure. Therefore, the 3 rings window is smaller than the 5 rings window structure which

limits the expansion of the field more which is a non-physical effect and hence the results obtained for  $\Lambda$  above  $1.2\mu\text{m}$  are not accurate. The structure with 5 rings can guide light as the field is expanding rapidly which indicates the field is far enough from the edges of the simulation window. This can be overcome by increasing the size of the simulation window at values of  $\Lambda$  that are comparably similar or smaller than the wavelength of operation.

The study on the comparison of changing the number of rings has shown unexpected behavior in the change of  $A_{eff}$  as discussed above. This is important in the explanation of other results which do not show a clear sign of this unexpected behavior. The example of this is when studying the variation of  $d/\Lambda$  where the change in  $n_{eff}$  shows a normal change (see Figure (3.42)). The higher the value of  $d/\Lambda$  the lower the effective index of the mode and this is due to more interaction with air as the holes are larger.

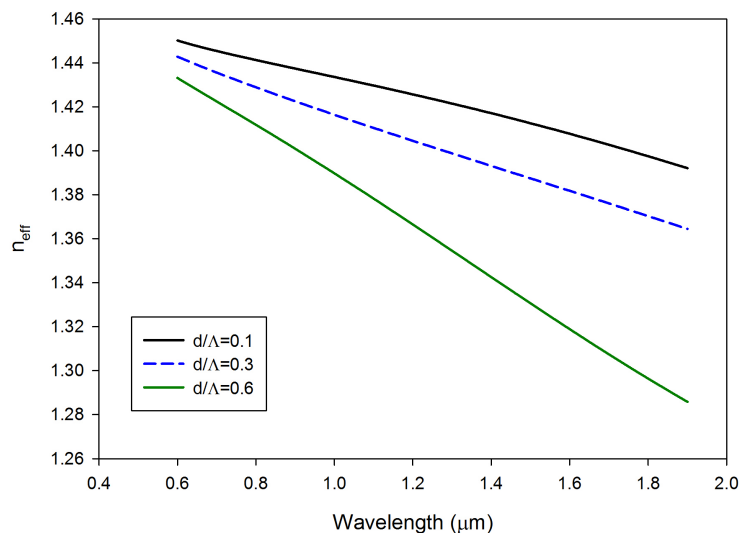


Fig. 3.42 Study the effect of varying the ratio  $d/\Lambda$  on  $n_{eff}$  for ES-PCF with 6 arms, 3 rings,  $\Lambda = 1\mu\text{m}$  and  $\theta = 30^\circ$ .

However, from  $A_{eff}$  curves shown in Figure (3.43) indicate that there is an error in the results. The three curves where  $d/\Lambda > 0.3$  are increasing slowly at lower wavelengths and then the change increases and this is what is expected as the field expands out of the core and approaches the cut-off. The change in the curve for  $d/\Lambda = 0.3$  is linear with trend similar to former curves at higher wavelengths. This is because the field expands outside the core even at lower wavelength region. The upper two curves with smallest  $d/\Lambda$  show sharp changes then the change decreases and both curves get closer at higher wavelengths. The reason behind this behavior is similar to what is explained above where the field is limited by the simulation window and the field is supposed

to be poorly guided/confined. The simulation window should be large enough that the field when expands in the cladding region it does not reach the borders of the window as this limits the expansion of the field. The window size should be chosen large enough for the field to expand freely in the cladding.

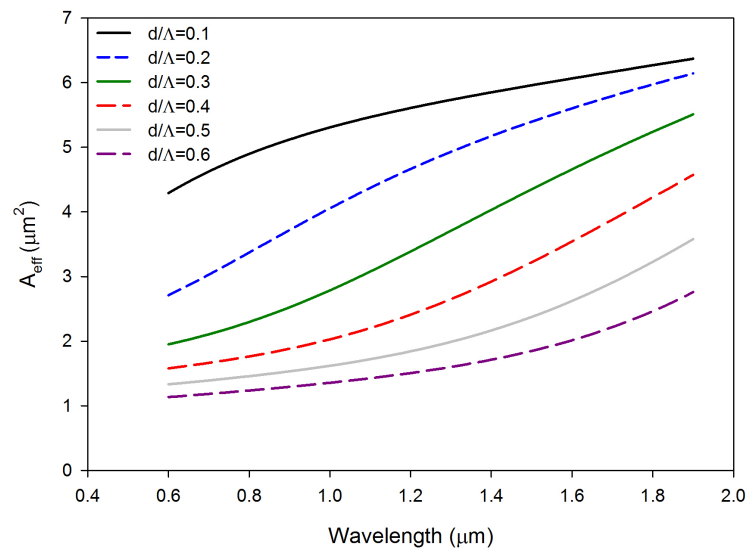


Fig. 3.43 Study the effect of varying the ratio  $d/\Lambda$  on  $A_{eff}$  for ES-PCF with 6 arms, 3 rings,  $\Lambda = 1\mu\text{m}$  and  $\theta = 30^\circ$ .

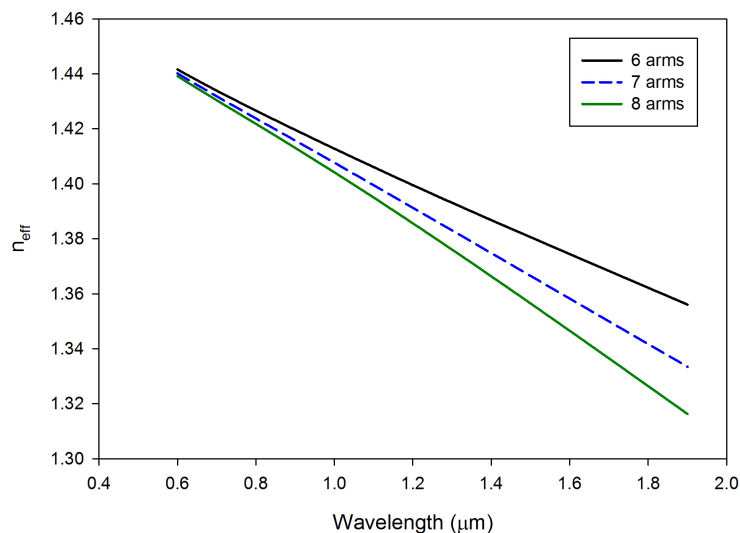


Fig. 3.44 Study the effect of varying the number of arms on  $n_{eff}$  for ES-PCF with  $d/\Lambda = 0.34$ , 3 rings,  $\Lambda = 1\mu\text{m}$  and  $\theta = 30^\circ$ .

The change of number of arms shows a similar behavior to the case of large  $\Lambda$  scenario. The change in  $n_{eff}$  between structures with different arms is small at lower wavelengths and increases with increasing wavelength as shown in Figure (3.44). The field expands more at higher wavelengths and the field interaction with air in the holes increases more for higher number of arms as more holes are close to the core (first ring), also the holes in following rings are closer to the core as the angle is arm dependent. The angle  $\theta$  increases as the parameter  $N_{arms}$  is reduced leading to holes being located farther from the core.

Similarly for  $A_{eff}$  curves the difference between different arms structures is larger at higher wavelengths as shown in Figure (3.45). At 1550nm the  $A_{eff}$  decreases from  $\approx 4\mu m^2$  for the 6 arm design to  $\approx 2.7\mu m^2$  for the 7 arm and to  $\approx 2.3\mu m^2$  for the 8 arm structure. The smaller  $N_{arms}$  has higher  $A_{eff}$  as the field expands more because the air filling fraction is less and the field is less well confined.

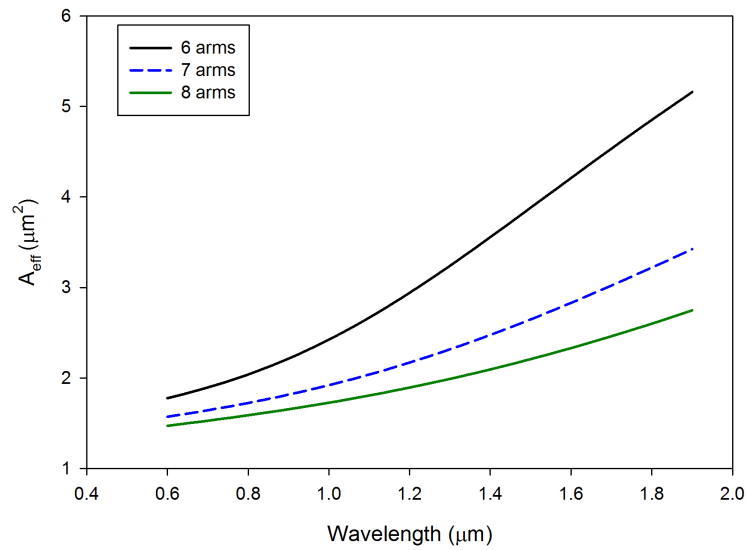


Fig. 3.45 Study the effect of varying the number of arms on  $A_{eff}$  for ES-PCF with  $d/\Lambda = 0.34$ , 3 rings,  $\Lambda = 1\mu m$  and  $\theta = 30^\circ$ .

The final study for the ideal ES-PCF is the comparison of  $\Lambda$  for both scenarios as shown in Figures (3.46) and (3.47)). The difference in  $n_{eff}$  is very small for large  $\Lambda$  and also the change in  $n_{eff}$  with varying wavelength is small compared for small  $\Lambda$ . The difference increases with increase in wavelength for  $\Lambda = 1$  which is a result of the field expanding outside the core when the wavelength is comparable to the core size. Figure (3.47) shows that  $A_{eff}$  is almost constant at high  $\Lambda$  with a slight increase at higher wavelengths. The field is well confined in the core and change in  $A_{eff}$  is linear with varying wavelength. On the other hand, at small  $\Lambda$  the difference between

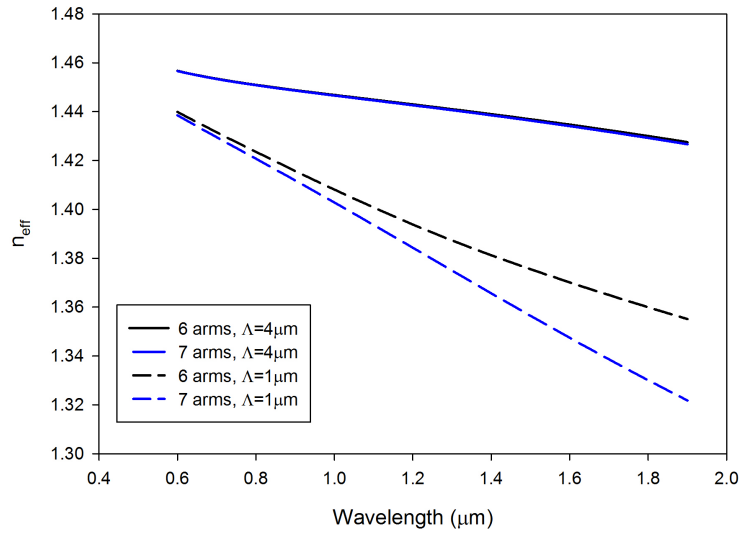


Fig. 3.46 Study the effect of varying  $\Lambda$  on  $n_{eff}$  for ES-PCF with  $d/\Lambda = 0.4$ , 4 rings,  $\Lambda = 1$  and  $4\mu m$  and  $\theta = 30^\circ$ .

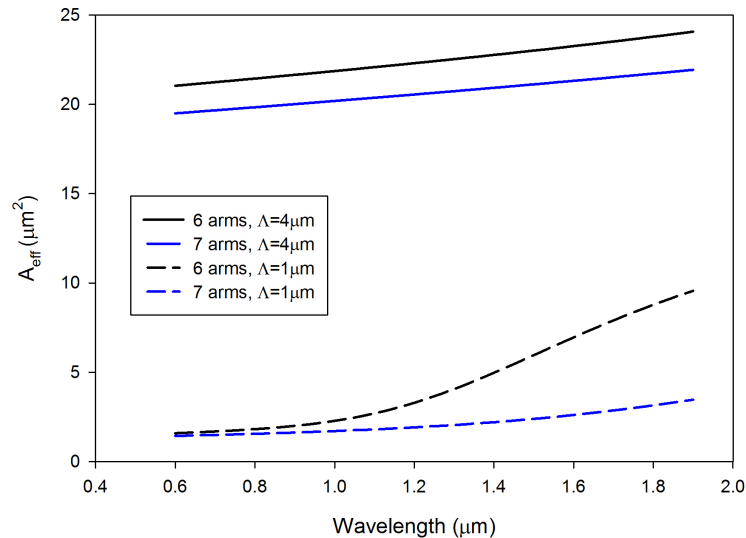


Fig. 3.47 Study the effect of varying  $\Lambda$  on  $A_{eff}$  for ES-PCF with  $d/\Lambda = 0.4$ , 4 rings,  $\Lambda = 1$  and  $4\mu m$  and  $\theta = 30^\circ$ .

structures with different  $N_{arms}$  is small at lower wavelengths and then increases rapidly as shown in Figures (3.47). The curve of the 6 arm structure (dashed black line) indicates that the field is expanding far beyond the core, where  $A_{eff}$  reaches values greater than the area of the core which is  $\pi R_c^2 = 2\mu m^2$ , where  $R_c = \Lambda - (d/2)$ . The field of the 6 arm structure is reaching cut-off at wavelength close to  $1.2\mu m$  and expands rapidly from  $\approx 3\mu m^2$  up to  $\approx 9\mu m^2$  at wavelength  $1.9\mu m$ . The field of the 7

arm structure is not expanding out of the core and remains well confined. The 7 arm structure has higher air filling fraction due to two facts; in every ring there is an extra hole thus the total number of holes in the structure is higher by a value equals to  $N_{rings}$ . The second factor is that the holes of the second and consecutive rings are closer to the core and to each other than their counterpart in the 6 arm structure where the angle  $\theta$  is  $N_{arms}$  dependent. The angle  $\theta$  decreases as the  $N_{arms}$  is incremented as the value of  $\theta$  is set to be equal  $\pi/N_{arms}$  as discussed before.

To conclude this section the dispersion (due to control of  $n_{eff}$ ) is more controllable at small pitch size, i.e. one which is comparable to the operating wavelength or smaller. The higher pitch size the field is mainly in the core where varying other parameters would have unremarkable change on the optical properties. The small pitch is chosen in this thesis and the results in the next chapter are concentrated on small pitch values.

### 3.10 Summary

In conclusion, the spiral is a unique shape which is present in nature and applied in man-made projects and has been adapted to design, simulate and study PCF. The equiangular spiral is implemented in this work where the formula and the how it is adapted to PCF is explained with pointing out the limiting factors of maximum air filling fraction. The advantage over H-PCF is mentioned as the holes in ES-PCF can be packed together more effectively or laid far apart from each other, unlike the H-PCF where the position of the holes are fixed. The design parameters of ES-PCF are investigated to study their effects on the properties of the modal field. The number of arms which leads to more confinement as  $N_{arms}$  is increased and lower losses, similar behavior is observed if the number of holes is increased. The hole size and the ratio  $d/\Lambda$  are related as for a given pitch size if hole size is increased the ratio increases and the field gets more confined, and the effective index decreases as the effective cladding region index decreases due to increase in air filling fraction. The angle between successive holes is more critical as the hole distribution mainly depends on combination of  $N_{arms}$  and  $\theta$ . The optimum value of the angle  $\theta$  for high confinement is to be equal or very close to  $\pi/N_{arms}$ . Last and not the least is the  $b$  parameter which is fixed to the  $N_{arms}$  in this study according to formula shown in the discussion.

The same study carried out was on AS-PCF and FS-PCF, and for both the mathematical formulae governing the growth of the curve have been discussed along with the limiting factors. The parameters have been studied individually to understand the effect of each one. There are common parameters that lead to similar effects in all three spirals, which

are pitch and hole size. The number of holes does not have huge impact if the number is sufficiently large. The hole radius has opposite effect to pitch size as both control the core size and space between holes.

Furthermore, the most important fact to mention is that the field interaction with the holes is weak at large values of  $\Lambda$  and this is good for some applications such as high power lasers and power delivery. In contrast, the focus of this thesis is about the small pitch size ( $\Lambda$  size is compatible with the operating wavelength) scenario where the field interacts strongly with the holes. In this case the dispersion property is significantly manipulated which is required for our goal of generating broadband SCG. For non-linear effects like SCG a small core size (to enhance the non-linear effects) is needed and with a smaller pitch size this is easier to achieve. However, in the ideal spiral design the field expands outside the core at small  $\Lambda$  values and results in poorly guided mode and high losses. This effect is overcome by the Steiner design as the holes in the third ring are large enough to stop the field from expanding too far from the core. This advantage and the feasibility of the fabrication of Steiner design using stack and draw (SaD) is what makes the Steiner design superior to ideal equiangular spiral designs. The Steiner design was invented to allow adapting the SaD to make the spiral PCF. In the next Chapter the Steiner ES-PCF published results [225, 239] and fabrication procedure [240] are presented. There is a discussion on the comparison between the Steiner and the ideal spiral designs which have similar dimensions to compare the difference in optical properties.

# Chapter 4

## Steiner ES-PCF Design

The spirals (equiangular, Archimedean and Fermat's spirals) have been introduced in the previous chapter and their implementation in Photonic Crystal Fiber (PCF) is discussed with the limitation of the physical dimensional factors. The result of varying different parameters have been explained for the three PCF spirals: equiangular, Archimedean and Fermat's spirals with comparison on their shared parameters. The former spiral is the focus of this thesis and in depth results of Equiangular Spiral Photonic Crystal Fiber (ES-PCF) were presented at the end of previous chapter.

The fabrication of the ideal ES-PCF using Stack and Draw (SaD) may not be possible with current available techniques. Therefore, a manipulation in the structure, which does have a small affect on the optical properties of the fiber, is proposed to make the design more practical and can be fabricated and tested experimentally.

This chapter is about the modified structure of ES-PCF (Steiner ES-PCF) design which is an approximation of the ideal spiral. The chapter starts with introduction of the Steiner design with an indication to the differences from the ideal spiral design. The Steiner ES-PCF is simulated to test and observe the effects of the variation of the structural parameters in similar manner to the studies of the ideal spiral which were presented in the previous chapter.

The non-linear applications such as all optical switches, light pulse compression, frequency conversion [241], Raman amplifiers, ultrafast signal processing [39] and SuperContinuum Generation (SCG) require small effective area ( $A_{eff}$ ) and low flat anomalous dispersion. The dispersion can be controlled smoothly in H-PCF in a similar way to ES-PCF but the latter has smaller  $A_{eff}$  which is an advantage for non-linear applications. Even though there are other structures which have smaller  $A_{eff}$  such Air Suspended Core (ASC) but a well engineered (flat with low dispersion at the desired pump wavelength) dispersion profile is not easy to achieve with ASC. Therefore, the

ES-PCF which combines both advantages is more suitable for non-linear applications. The focus of this thesis is on implementing ES-PCF for non-linear applications. Furthermore, the Steiner structure has bigger holes in the third ring thus the field is confined much more than ideal ES-PCF and  $A_{eff}$  is smaller. The Steiner ES-PCF is optimized in this chapter to have low flattened dispersion and small effective area to be used for generating a wide band SCG. The results of SCG are presented and compared with published data. Thereafter, a procedure for fabricating the structure is proposed based on the SaD technique. The fabrication section contains the Steiner Chain concept, the derivation of the structural parameters and the process of stacking the tubes and rods. The Steiner structure is derived to make the fabrication of ES-PCF feasible using SaD technique. Therefore, their optical properties are compared to study the deviation in the results. The study is carried out using identical dimensional parameters apart from third hole which differentiate both designs.

## 4.1 Properties of Steiner ES-PCF

The results of the three different spirals (equiangular, Archimedean and Fermat's) have been presented in the previous chapter. All the previous results are for structures made of silica material with holes filled with air. The material used in the simulation of this section is soft glass SF57 for which the refractive index is obtained using the formula shown in Equation (1.34) and Sellmeier coefficients of SF57 material are shown in Table (4.1). The refractive index as a function of wavelength is shown on Figure (4.1).

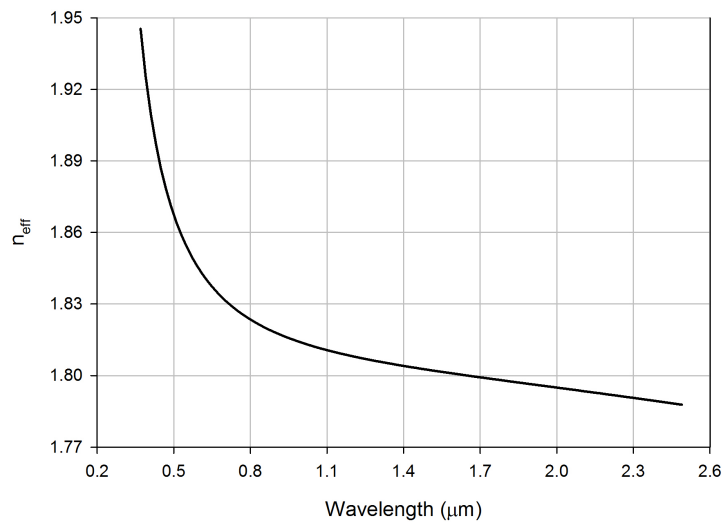


Fig. 4.1 Refractive index profile of soft glass SF57 material [242]

The soft glass SF57 has a large non-linear coefficient which makes this material more suitable choice for non-linear applications than silica [184]. Furthermore, it is feasible to fabricate SF57 fibers using different techniques such as extrusion [152, 183] to make complex structures which are not possible by the SaD technique.

Table 4.1 Sellmeier coefficients of SF57 material [242]

Sellmeier Coefficient	1	2	3
$A_j$	0.0143704198	0.0592801172	121.419942
$B_j (\mu m^2)$	1.81651371	0.428893641	1.07186278

The structure studied in this section is a modified ES-PCF which has larger holes in the third ring as shown in Figure (4.2). This structure is a modification of the ideal spiral presented in the previous chapter. There are two assumptions in this structure which are  $N_{rings}$  is fixed to 3 and the value of  $\theta$  is fixed to  $\pi/N_{arms}$ . The only difference from ES-PCF is that the distance of 3<sup>rd</sup> hole from the center is much larger and these holes are bigger in size. One of the characteristics of this structure is the maximum size of the holes in the third ring is reduced as the value of  $N_{arms}$  is increased. Actually, for a given  $\Lambda$  the overall structure size is reduced as  $N_{arms}$  increases. The other thing to notice is the gap between the edges of the holes in the second and third rings. This gap can be significant if the radius of the holes in the third ring is reduced.

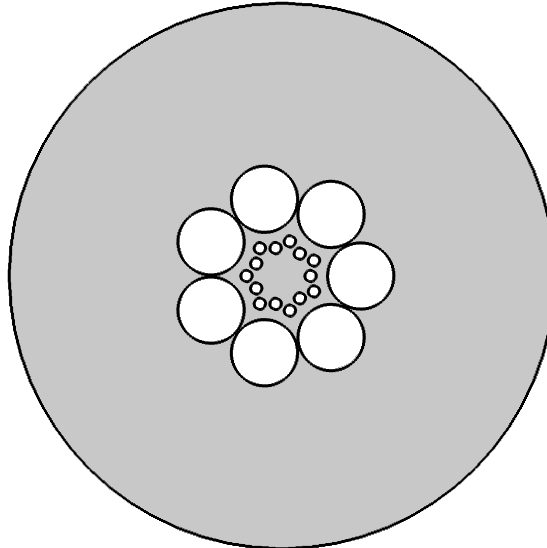


Fig. 4.2 Cross section of Steiner ES-PCF of 7 arm structure

This structure is studied because the fabrication of ideal ES-PCF using a conventional SaD technique is not possible, therefore a procedure was proposed to fabricate the

ES-PCF using SaD with some assumptions and modifications to the design as noted above. The algorithm proposed to fabricate this structure is given in Section (4.3). Moreover, this design offers better field confinement as mentioned.

The cross section of the ideal and Steiner ES-PCF structures with identical parameter values apart from holes in third ring which have different position and size are shown in Figure (4.3). The two structures shown in the figure have 7 arms, 3 rings,  $d/\Lambda = 0.4$  and  $\Lambda = 3\mu m$ .

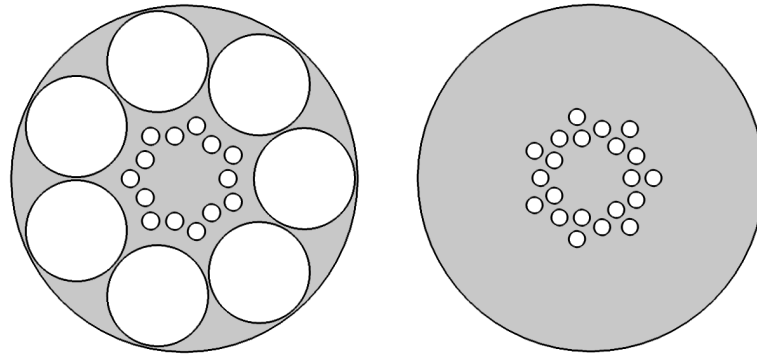


Fig. 4.3 Cross sections of Steiner (left) and ideal (right) ES-PCF of a structures with 7 arms, 3 rings,  $d/\Lambda = 0.4$  and  $\Lambda = 3\mu m$

In this section the results of the Steiner design are presented and at the end of the chapter a comparison between ideal and Steiner designs is given. The studies in this section are sorted in accordance to the optical properties rather than the dimensional parameters. The effective index is studied first then dispersion which is mainly related to  $n_{eff}$ . Then both properties  $A_{eff}$  and  $\gamma$  are studied together as they are related. In the studies the parameters are varied to observe their effect and estimate the value range for the final studies. At the end of the section a comparison of the results with other PCF is given.

#### 4.1.1 Study of the effective refractive index

The first optical property studied is  $n_{eff}$  and curves for different designs are represented with explanation on the change and relate it to the structure design. The first parameter that is varied is  $N_{arms}$  to observe its effect on  $n_{eff}$ . The results are for two structures with different  $\Lambda$  similar to the comparison of Section (3.9) where small and large pitch size structures were simulated. The structures with the large pitch are discussed first and the results are shown in Figure (4.4). There is not a significant change in  $n_{eff}$  as  $N_{arms}$  is varied. Actually, at lower wavelengths they are almost identical while the change occurs at higher wavelengths. The change is small which would not have

an impact on other properties such as dispersion. The reason is that the field is well confined in the core and interaction with holes even in first ring is small.

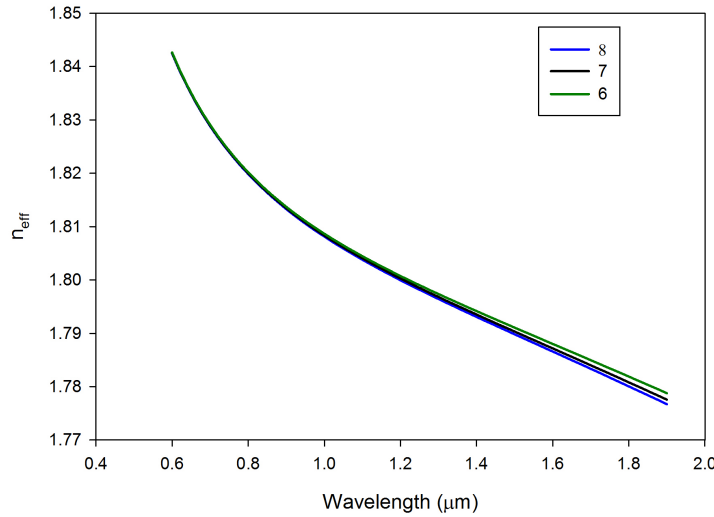


Fig. 4.4 Study the effect of varying  $N_{arms}$  on  $n_{eff}$  for Steiner ES-PCF with  $d/\Lambda = 0.4$  and  $\Lambda = 3\mu m$  in soft glass SF57.

The pitch size of  $1\mu m$  has more affect as the field interacts with holes and the refractive index decreases with increase in air filling fraction which results from having more arms present in the structure, see Figure (4.5). At lower wavelengths the difference in  $n_{eff}$  is small as the field is not expanding into the cladding due to the wavelength being smaller than the core size. At higher wavelengths the field profile spreads more into the holes leading to a bigger difference in  $n_{eff}$  values for the different  $N_{arms}$  structures. The effect of the variation of  $N_{arms}$  on dispersion is discussed in the next section.

The above discussion has proven that the pitch size can have detrimental effect on the optical properties. Therefore, a study of the effect of  $\Lambda$  is performed and results of  $n_{eff}$  are presented in Figure (4.6). It is clear that the  $n_{eff}$  decreases with increase in  $\lambda$ . However, the change is small when the core size is larger than wavelength of operation (black and dark-green lines). When the size of the core decreased to be compatible with the operating wavelength or smaller then the change can be significant (blue line). The core size or  $\Lambda$  has to be small when interaction of the field with holes is required to change the dispersion and also for small  $A_{eff}$  values, which are the most important factors in this thesis as the main objective of this work are to optimize a structure with flat low dispersion in the anomalous region and small  $A_{eff}$  for SCG. The optimized design for SCG has been obtained and results for this design are discussed in Section (4.2.2).

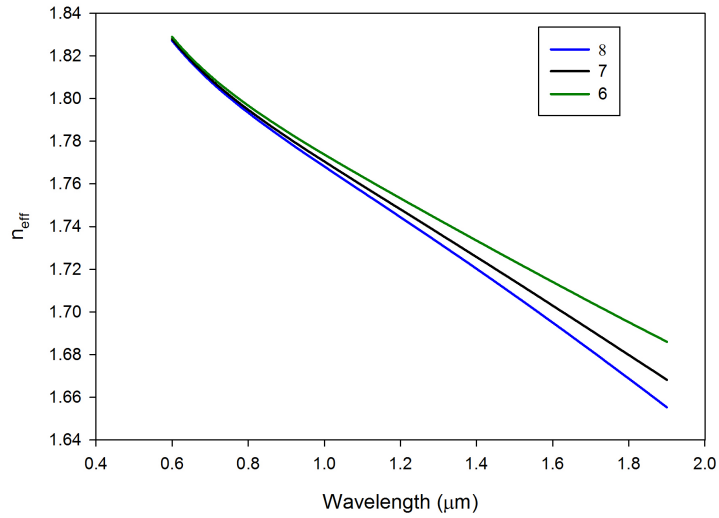


Fig. 4.5 Study the effect of varying  $N_{arms}$  on  $n_{eff}$  for Steiner ES-PCF with  $d/\Lambda = 0.4$  and  $\Lambda = 1\mu m$  in soft glass SF57.

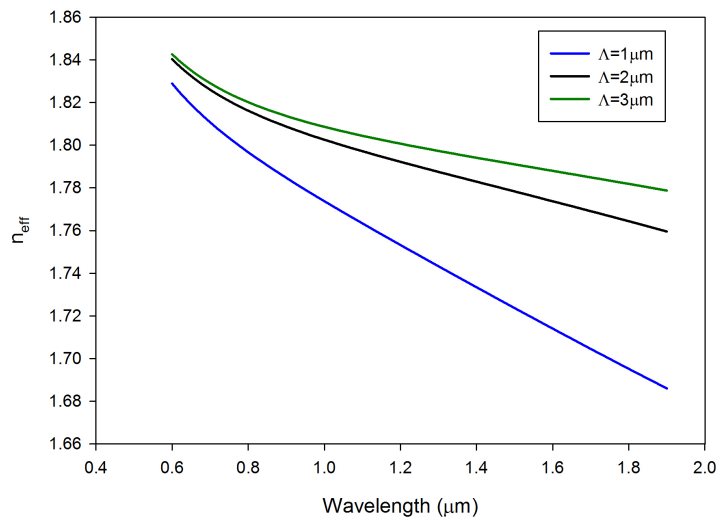


Fig. 4.6 Study the effect of varying  $\Lambda$  on  $n_{eff}$  for Steiner ES-PCF with  $d/\Lambda = 0.4$  and  $N_{arms} = 6$  in soft glass SF57.

The pitch size is varied in two structures with a different number of arms and the results are shown in Figure (4.7). The solid lines show results for 6 arms structures with  $\Lambda = 3\mu m$  and dashed lines show result for structures of 7 arms with  $\Lambda = 1\mu m$ . The former shows small change even at higher wavelengths, whereas the latter case the change is large and increases with increasing wavelength. However, both sets share a similarity in terms of that the  $n_{eff}$  decreases with increase in  $d/\Lambda$  because air filling fraction increases and field interacts with more air.

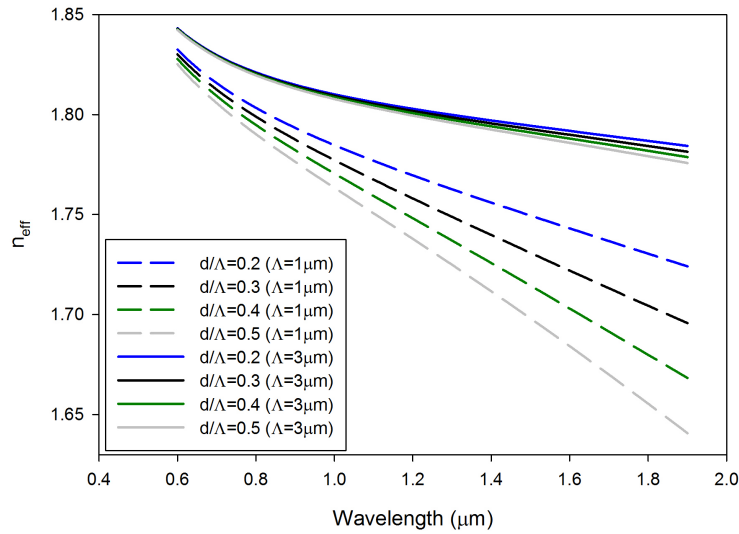


Fig. 4.7 Study the effect of varying  $d/\Lambda$  on  $A_{eff}$  for two ES-PCF designs with  $\Lambda = 1$  and  $3\mu m$ , and  $N_{arms} = 6$  (solid lines) and 7 arms (dotted lines), in soft glass SF57.

The slope of the change in the refractive index with respect to wavelength is an important property of optical fibers which is dispersion. It is discussed in the next section with reference to  $n_{eff}$  in the explanation.

### 4.1.2 Study of the dispersion

Dispersion has been studied extensively since the emergence of optical fibers due to its impact on signals traveling in fibers. However, the dispersion can be implemented in positive ways in non-linear applications to enhance the effect of these phenomena. This section is dedicated to study dispersion due to its importance. The dispersion calculated in this work is carried by using Equation (1.14) where  $n = n_{eff}$ .

The dispersion results presented are for small  $\Lambda$  structures because in the case of large  $\Lambda$  the variation of parameters does not have a noticeable impact on the dispersion. The dispersion results at small  $\Lambda = 1\mu m$  are presented in this section, varying different parameters. The change in dispersion with respect to  $N_{arms}$  is shown in Figure (4.8). The dispersion at lower wavelengths does not change much with an increase in  $N_{arms}$ , but at wavelengths above  $1\mu m$  the dispersion increases as the number of arms is incremented. The 6 arms curve has a negative dispersion value at all wavelengths which is the normal dispersion region. In contrast, the other two have positive dispersion value which is the anomalous dispersion region and this is the region of interest for non-linear applications. Therefore, the change of  $N_{arms}$  leads to shifting the curve up if  $N_{arms}$  is incremented and down if decremented. The other important point is the zero crossing of the curve

or ZDW which is the point where the curve changes sign. The effect of moving the curve up or down affects the ZDW; if the curve is shifted up ( $N_{arms}$  incremented) then the ZDW is blue shifted towards shorter wavelengths and vice versa.

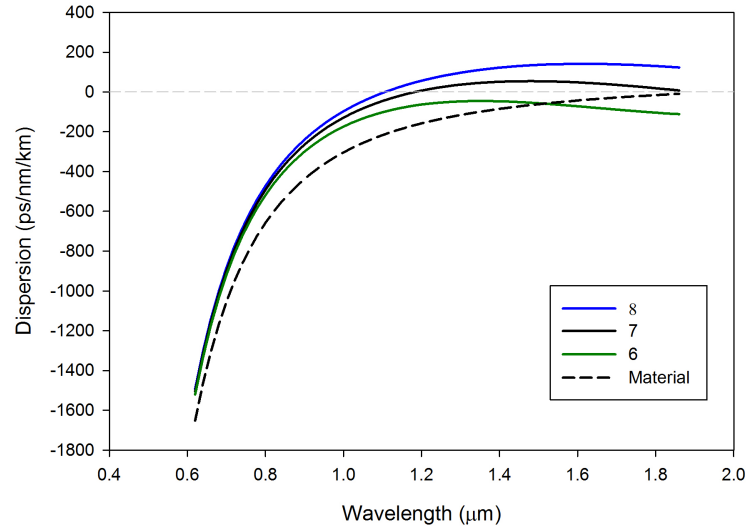


Fig. 4.8 Study the effect of varying  $N_{arms}$  on dispersion for ES-PCF design with  $\Lambda = 1\mu m$  and  $d/\Lambda = 0.4$  in soft glass SF57.

A wavelength close to the ZDW is typically chosen for the pump wavelength with which to excite non-linear effects. The pump sources are available only at specific wavelengths hence a shift of ZDW is important where a suitable pump is not available at the ZDW. The dispersion of the ES-PCF can be designed to have suitable slope and ZDWs by varying the structural parameters such as  $N_{arms}$ ,  $N_{rings}$ ,  $\Lambda$ ,  $d/\Lambda$  and  $\theta$ , whilst maintaining  $A_{eff}$  to be small enough to enhance non-linear interactions for SCG. The last thing to mention is the slope of the curve in the anomalous region. The curve is preferred to be flat so the value of the slope should be very small or zero.

The next parameter that is investigated is the pitch size which is very important due to the fact that at large values of  $\Lambda$  the dispersion does not change much with the variation of the other parameters. The dispersion of designs with core size larger than wavelength of operation (Figure (4.9) black and dark green lines ) have a similar curve shape to the material dispersion where curves are slight blue shifted when  $\Lambda$  is decreased. This trend in the dispersion curve changes at values when the core is comparable to operating wavelength or smaller, hence the light spreads into cladding region. Then the curve of dispersion differs from the material dispersion curve and the difference starts to increase as  $\Lambda$  is decreased. The behavior of such designs is shown in Figure (4.9) where  $\Lambda = 1\mu m$  (blue line). The behavior can be understood from the curves of the  $n_{eff}$  of the same structure, which is shown in Figure (4.6). The change in  $n_{eff}$  with smaller

$\Lambda$  is steep leading to significant change in dispersion. The best way to optimize the dispersion of a structure for any application is to find the right pitch size then play with the other parameters to smoothen the curve.

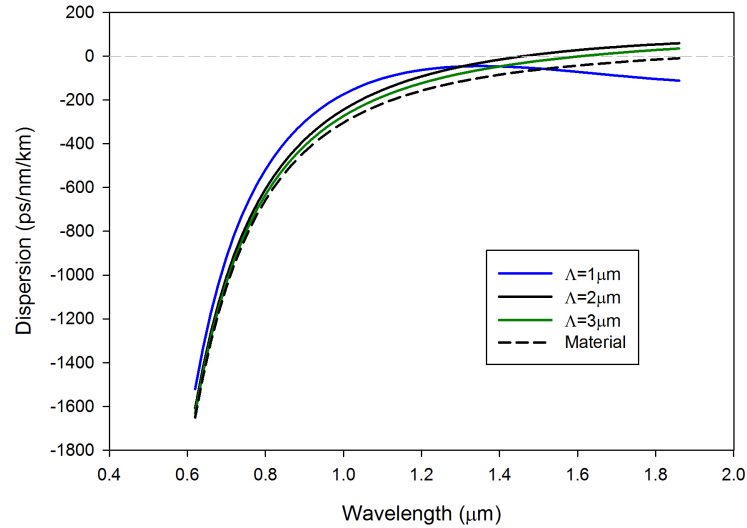


Fig. 4.9 Study the effect of varying  $\Lambda$  on dispersion for ES-PCF design with  $N_{arms} = 6$  and  $d/\Lambda = 0.4$  in soft glass SF57.

Another parameter which is important is the ratio  $d/\Lambda$  which is crucial in terms of defining the air filling fraction. The change in dispersion of a 7 arms structures with reference to  $d/\Lambda$  is shown in Figure (4.10).

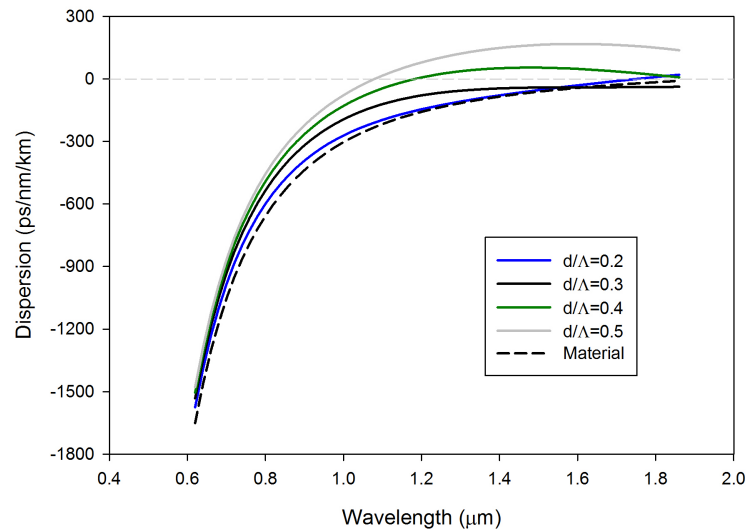


Fig. 4.10 Study the effect of varying  $d/\Lambda$  on dispersion for ES-PCF design with  $N_{arms} = 7$  and  $\Lambda = 1\mu m$  in soft glass SF57.

The change of dispersion increases as  $d/\Lambda$  is increased because the field is influenced by the air in the surrounding. The curves of  $d/\Lambda > 3$  have a convex shape which is of interest in terms of the flatness of the dispersion and in obtaining two ZDWs. The two ZDWs can possibly be shifted near the available pump wavelengths and two sources can be used to excite the non-linear effects. This improves the effect of SCG and also each pump can be used individually which gives the fiber three different SCG spectra. However, the shift of the ZDW to two specific wavelengths requires the adjustment of other parameters.

The change in  $n_{eff}$  is important because even a small change can manipulate dispersion significantly. Therefore, other parameters are varied in this section which are diameters of first ( $d_1$ ) and second ( $d_2$ ) rings. In this case only the hole sizes in one ring are varied at a time, either in the first or second ring. The hole size in the first ring is varied and results are shown in Figure (4.11a) and explained. Then the same steps are followed to study the effect of varying the diameter of second ring holes.

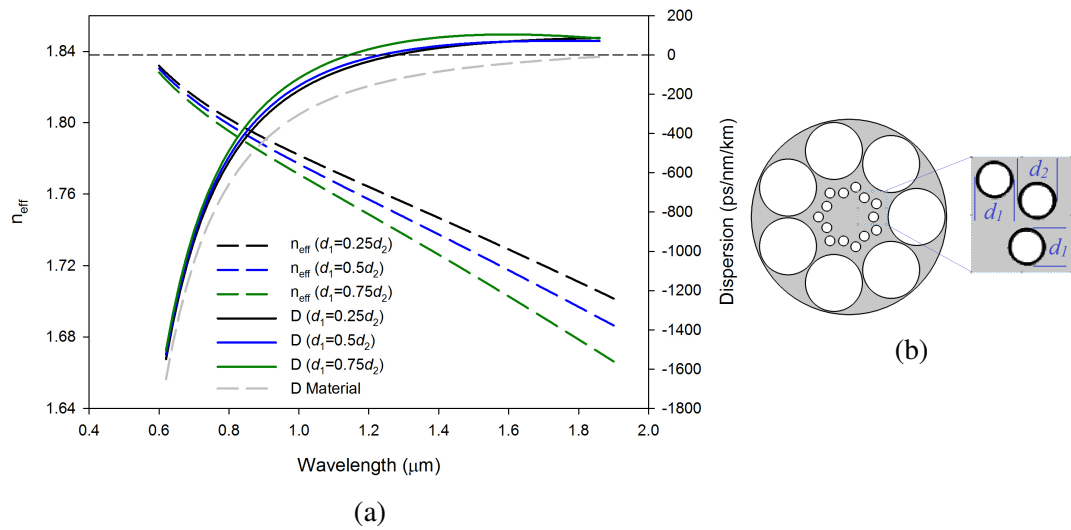


Fig. 4.11 (a) Study the effect of varying  $d_1$  on dispersion for ES-PCF design with  $N_{arms} = 7$ ,  $d/\Lambda = 0.5$  and  $\Lambda = 1\mu\text{m}$  in soft glass SF57, and (b) schematic of  $d_1$  and  $d_2$  the diameters of holes in first and second rings, respectively.

The dispersion does not change much by varying the size of holes in the first ring. The dispersion increases as the hole size increases and at larger wavelengths the curves are very similar with little difference between them. This may be as a result of the field expanding beyond the first ring and reaching other rings. The field in structures with smaller first ring holes expands more and hence interacts more with outer holes. The dispersion curve of structure with biggest holes (dark green solid line) tends to go

down towards zero at the higher wavelength end. On the other hand, the dispersion of the other curves (blue and black solid lines) are increasing thus would have a higher values beyond the higher wavelength end in the graph. The effective refractive index is shown in the same graph. Its behavior is similar to what is expected: as the hole size increases  $n_{eff}$  decreases and that is very clear from the graph (Figure (4.11a)).

The holes in the first ring have been investigated and the change in dispersion was small. In the study of varying hole size in the second ring the change in dispersion is small as well but the effect is more pronounced at the higher end of the wavelength range (Figure (4.12)).

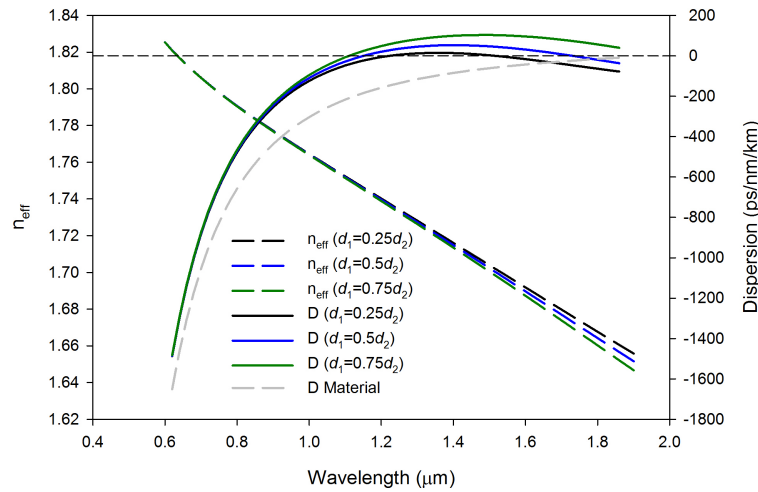


Fig. 4.12 Study the effect of varying  $d_2$  on dispersion for ES-PCF design with  $N_{arms} = 7$ ,  $d/\Lambda = 0.5$  and  $\Lambda = 1\mu m$  in soft glass SF57.

The various parameters have sufficient control of dispersion but some applications may require more flat dispersion. There is a parameter which has not been discussed in previous sections. This is  $d_c$  (diameter of central hole) so in this further study a hole is introduced in the center of the structure and its effect is examined. The hole in the center of the structure has been implemented in simulation of ES-PCF in soft glass SF57 to flatten the dispersion for SCG [184]. The hole size is related to the  $\Lambda$  in a similar way to the holes in the first and second rings. The first step is to chose a fixed ratio for the central hole and vary  $\Lambda$ . The ratio of  $d_c/\Lambda = 0.2$  is taken and the results of varying  $\Lambda$  are shown in Figure (4.13). The effect of varying  $\Lambda$  is similar to before where at large values of  $\Lambda$  the dispersion curve is very close to material dispersion. Furthermore, the  $n_{eff}$  is not changing much but at small pitch size the field interacts with hole and expands out of the core. The dispersion of the structure with small pitch is decreasing and diverting from the material dispersion at higher wavelengths.

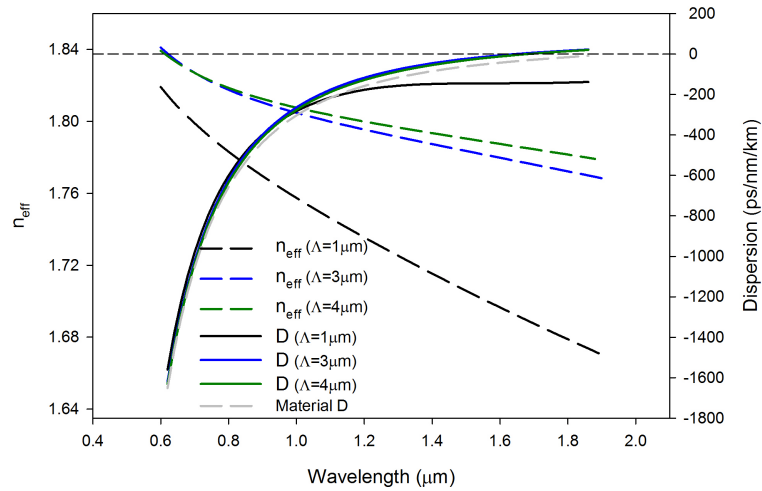


Fig. 4.13 Study the effect of varying  $\Lambda$  on dispersion for ES-PCF design with  $N_{arms} = 6$ ,  $d/\Lambda = 0.4$  and  $d_c/\Lambda = 0.2$  in soft glass SF57.

The second scenario is when  $\Lambda$  is a small value ( $1\mu m$ ) comparable with wavelength of operation. The study is concerned with varying size of the hole in the center to obtain the effect of this hole. The results of dispersion and  $n_{eff}$  are shown in Figure (4.14) for three different structures with  $d_c/\Lambda = 0.1, 0.2$  and  $0.3$ . The structure with the smallest hole in the center has the highest dispersion values at wavelengths longer than  $0.9\mu m$ . At the lower wavelength region the dispersion curves have similar values because the slopes in the curves are large and the other reason is that the values of dispersion are very large at lower wavelengths, therefore a small change can not be noticed. The dispersion decreases as the hole in the center increased with larger increase in the middle of the wavelength range shown and at higher wavelength the difference in the change is reduced due to the field expanding and the effect of the holes in the rings start to dominate on the dispersion and the hole in the center has less effect. The change in  $n_{eff}$  is smooth and agrees with the discussion given on dispersion and  $n_{eff}$  decreases with increase in the central hole. The central hole can be utilized to flatten dispersion further only if the curve is smooth and close to the desirable values because the central hole cannot be used to change dispersion significantly.

To sum up the dispersion is controlled flexibly at small  $\Lambda$  value. This parameter is the first to vary to find and fix a suitable value. The number of arms shifts the curve up which means increases the dispersion so for a dispersion curve below the zero can be shifted by increase number of arms to have anomalous dispersion (Figure (4.8)). The ratio  $d/\Lambda$  has similar effect to  $N_{arms}$  for  $d/\Lambda > 3$ . A good design procedure is to choose  $N_{arms}$  then use the ratio  $d/\Lambda$  to alter the dispersion. The holes in the first

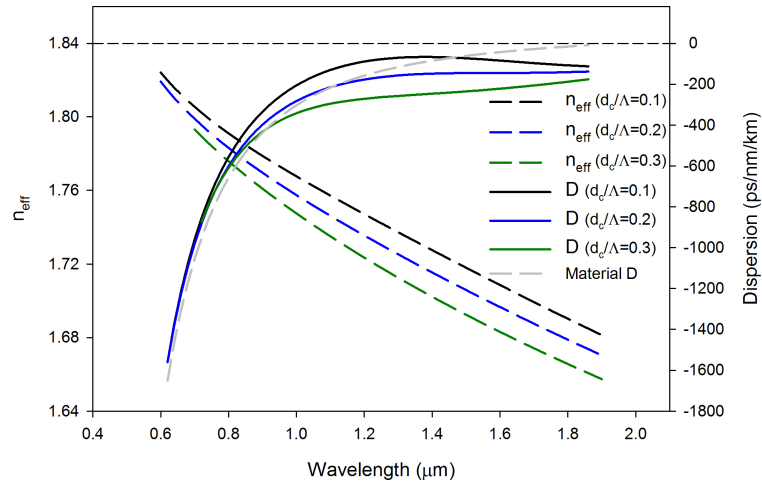


Fig. 4.14 Study the effect of varying  $d_c$  on dispersion for ES-PCF design with  $N_{arms} = 6$ ,  $d/\Lambda = 0.4$  and  $\Lambda = 1\mu m$  in soft glass SF57.

ring should be varied individually to flatten and shift the dispersion. The shift and flattening of the dispersion can be done by the varying of holes in first and/or second rings. Moreover, a hole in the center can be introduced to flatten the dispersion further if required. However, the change in dispersion by the variation of any parameter is mostly dependent on the field interaction with the parameter. The best way to optimize dispersion is to run simulations with various parameters and adjusting these to obtain the desired profile.

This study has clarified that each parameter has an impact on the dispersion if that parameter falls in the spatial range of the modal field to have interaction with it. All parameters have to be selected to control the dispersion to be flat and anomalous over a wide wavelength range with a ZDW near the pump. The first parameter to be fixed is  $\Lambda$  as it is the most important one and if it is chosen to be large the other parameters would not have a noticeable impact on the dispersion. After suitable values of  $\Lambda$  have been determined, the size of holes can be used to adjust the dispersion curves. Similar steps have been followed to obtain low and flat dispersion for a wide wavelength range with three ZDW in a tellurite based Steiner ES-PCF. The results of this design are discussed in Section (4.2).

### 4.1.3 Study of the non-linearity and effective area

In the previous sections the effect of varying the Steiner ES-PCF parameters on optical properties have been discussed. The dispersion and  $n_{eff}$  changes were explained

and linked to the interaction of the field profile with the micro structure of the fiber. A general view of the effect of the variation of the different parameters is given to understand the design process and reduce the simulation for optimizing structure for a required dispersion profile.

The other parameter to study is the effective area which is important to study the modal field and also used to calculate other properties such as the effective non-linearity ( $\gamma$ ). Non-linearity relies on  $A_{eff}$  for a given material at a specific wavelength as mentioned in Chapter 1. The formula to calculate  $\gamma$  is given in Equation (1.33). In this section the non-linearity is studied by varying the dimensional parameters of the structure to observe the effect of the different parameters and how to optimize these parameters to design the required structure with high  $\gamma$  and low flattened dispersion. The material used in this study is soft glass SF57 which has a non-linear coefficient of  $n_2 = 4.1 \times 10^{-19} m^2/W$  [184].

In general the effective non-linearity will always decrease in regard to wavelength increase. The reason is obvious from the formula used in calculating  $\gamma$ . However, the main concern is  $A_{eff}$  which is the only factor that can be enhanced for a given wavelength. The material parameter  $n_2$  is important but it cannot be varied or changed unless a different material is used.

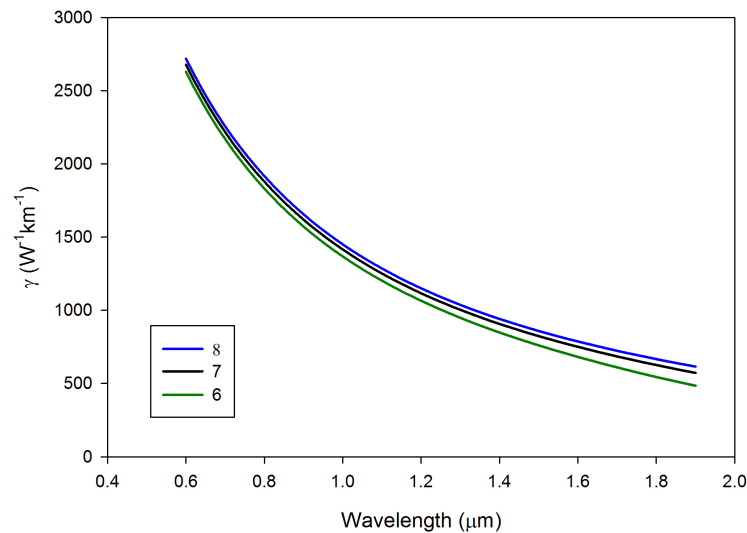


Fig. 4.15 Study the effect of varying  $N_{arms}$  on  $\gamma$  for ES-PCF design with  $d/\Lambda = 0.4$  and  $\Lambda = 1 \mu m$  in soft glass SF57.

The number of arms leads to increase in  $\gamma$  as  $N_{arms}$  increases and this can be explained in terms of  $A_{eff}$ . The effective area decreases with increase in  $N_{arms}$  due to better field confinement and the relation between  $\gamma$  and  $A_{eff}$  is inverse. The curves of  $\gamma$  vs wavelength for structures with different arms are shown in Figure (4.15). The variation

between the three structures is not large but still the effect of  $N_{arms}$  is noticeable especially at higher wavelengths where the difference is around one sixth of the value of  $\gamma$  at that wavelength when  $N_{arms}$  is incremented by 1.

The parameter  $\Lambda$  influences  $\gamma$  significantly similar to what is observed in other optical properties. The designs with small  $\Lambda$  have shown more variation in most properties discussed. These designs can be useful in exploring uniqueness of PCF where the interaction of the field with holes can be pronounced and the properties can be tailored to the desired level. In terms of non-linearity the situation is the same as the decrease in  $\Lambda$  leads to significant increase in  $\gamma$  as shown in Figure (4.16), where  $\gamma$  value is tripled when  $\Lambda$  reduces from 3 (dark-green line) to  $2\mu\text{m}$  (black line) and 2 (black line) to  $1\mu\text{m}$  (blue line), in the lower wavelength region. Even at higher wavelengths the  $\gamma$  value incremented by a factor of 2.5 for a reduction in  $\Lambda$  value by  $1\mu\text{m}$ . In the design process it is recommended to vary  $\Lambda$  and find the most appropriate value before changing other parameters. However, during the study of variation of  $\Lambda$ , other parameters should have reasonable values that are in the middle of the available ranges. An example is the hole size should not be set as maximum or minimum size possible as this would limit the possibilities of using the hole size to control the optical properties. This ideology should be followed with all parameters that can be varied.

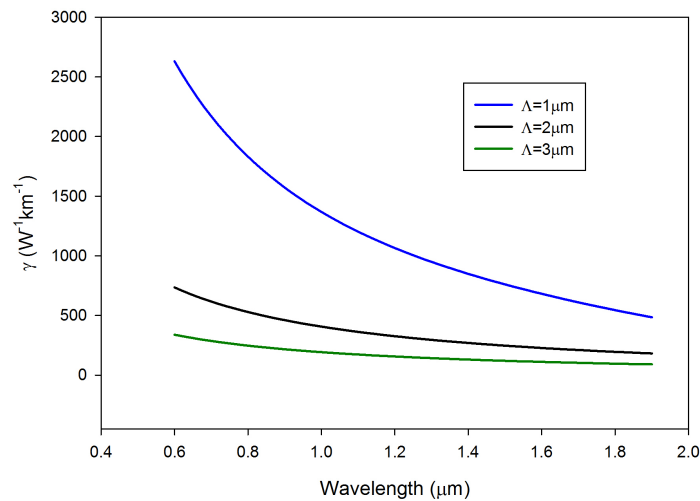


Fig. 4.16 Study the effect of varying  $\Lambda$  on  $\gamma$  for ES-PCF design with  $N_{arms} = 6$  and  $d/\Lambda = 0.4$  in soft glass SF57.

The variation of the ratio  $d/\Lambda$  is important as it controls the size of all holes and a small change would have more impact than changing just the size of holes in one ring. The change in  $\gamma$  is smooth and follows similar trend when varying  $d/\Lambda$  for a fixed  $\Lambda$  as shown in Figure (4.17). The relation is directly proportional between  $\gamma$

and  $d/\Lambda$ . However, higher values of  $\Lambda$  show very small change in  $\gamma$  with variation of  $d/\Lambda$  as shown in Figure (4.17) dotted lines. The change is more significant when  $\Lambda$  is sufficiently small. Even though the field is more confined in the core in the structures with large  $\Lambda$  than the one with small  $\Lambda$ , the value of  $\gamma$  is higher in the smaller design. The reason is that  $\gamma$  depends on  $A_{eff}$  which is smaller for designs with small  $\Lambda$  even with the field spreading in the cladding region because for large values of  $\Lambda$  the field expands freely in the core therefore the value of  $A_{eff}$  is large in comparison to designs with small  $\Lambda$ .

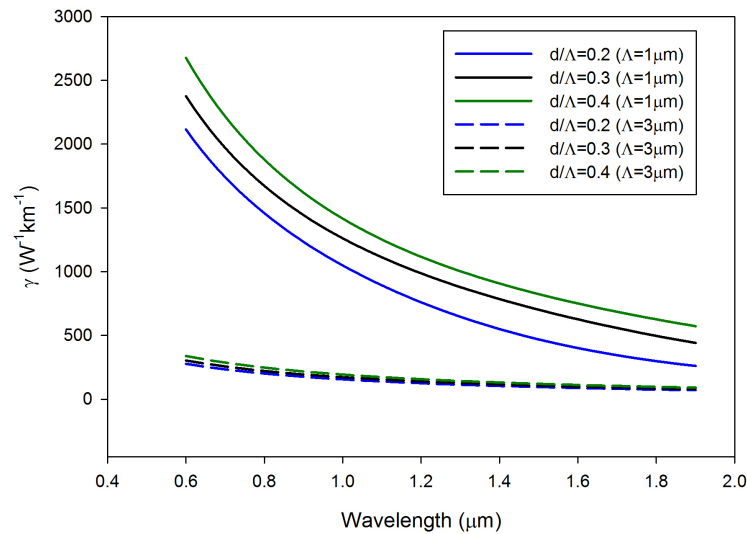


Fig. 4.17 Study the effect of varying  $d/\Lambda$  on  $\gamma$  for ES-PCF designs with  $\Lambda = 1\mu\text{m}$  (solid line) and  $3\mu\text{m}$  (dotted line), for  $N_{arms} = 6$  and  $7$ , respectively, in soft glass SF57.

The effect of varying size of the holes in the first two rings was discussed for two sets with different values of  $\Lambda$ . The case when  $\Lambda$  is small has shown better optical properties for non-linear applications. The next step is to vary the holes of each ring individually to tweak the properties of the design. The variation of the holes of the first ring is investigated and the results are shown in Figure (4.18). The curves of  $\gamma$  (solid lines) have similar shape which is an indication that the change is following a trend hence the parameter can be used to control the properties of the fiber sufficiently. However, when varying size of the holes in the first ring, the change in the non-linearity is not huge. The change in  $\gamma$  at lower wavelengths is more than at higher wavelengths and the maximum change is around 25% of its value when the radii of holes in the first ring are doubled in size. This fact is important in the optimization process where in optimization of the structure the dispersion property has superiority over  $\gamma$ . The reason is that dispersion being more sensitive to variation of the parameters and small change may shift the ZDW

and/or change the sign of the dispersion. Therefore, the non-linearity is considered when  $\Lambda$  is chosen and then the dispersion has to be optimized.

In Figure (4.18) the corresponding  $A_{eff}$  of each  $\gamma$  curve are plotted with similar color (dotted lines). The figure clearly shows that the smaller the effective area the higher is the non-linearity because as mentioned previously the relationship between effective area and non-linearity is inverse. In other words, the non-linearity depends on the field profile and how much it is spreading in the surroundings.

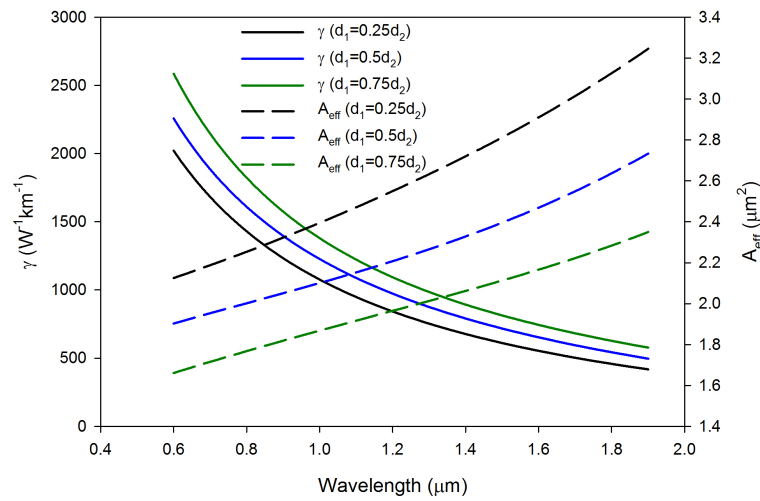


Fig. 4.18 Study the effect of varying  $d_1$  on  $\gamma$  for ES-PCF design with 7,  $d/\Lambda = 0.5$  arms and  $\Lambda = 1\mu m$  in soft glass SF57.

The other parameter to be investigated is the size of the holes in the second ring. The diameter of the holes in first ring are kept fixed to  $0.5\mu m$  and  $\Lambda = 1\mu m$ . The change in the size of the holes in the second ring does not lead to any noticeable difference in  $\gamma$  value and all the curves are almost superimposed on each other. The field does not expand by varying the size of the holes of the second ring and this can be satisfied by the variation in  $A_{eff}$  curves (dashed lines) which is very small as can be noticed from Figure (4.19). The field is stopped from expanding by the holes of the first ring. Therefore, the holes in the first ring have the major impact on the optical properties of the field where change in  $A_{eff}$  curves is large (see Figure(4.18) dotted lines).

However, the holes in the second ring play an important role in confining the light because they can be positioned in a way to block the gap between holes of the first ring. This is the distinguishing characteristic of ES-PCF from the H-PCF. The holes of the second ring in ES-PCF are positioned closer to the core and at an angle in the middle between two holes of the first ring. This distance is controlled by the spiral parameter ( $b$ ) which is fixed to the number of arms through the relation given by Equation (3.4).

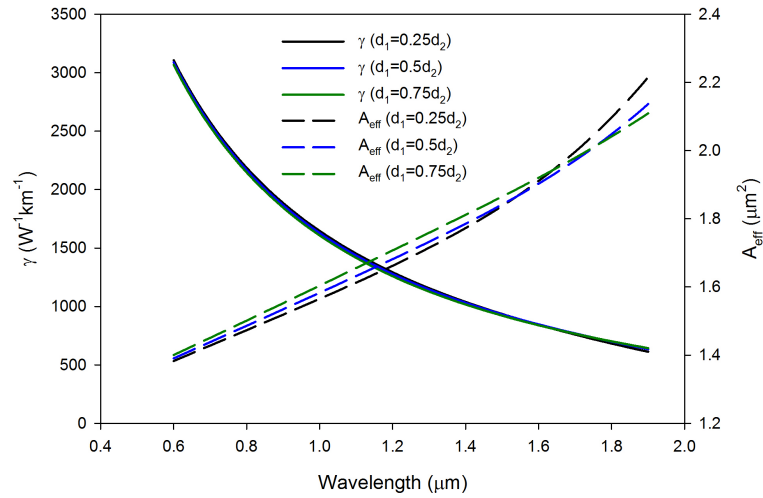


Fig. 4.19 Study the effect of varying  $d_2$  on  $\gamma$  for ES-PCF designs with 7,  $d/\Lambda = 0.5$  arms and  $\Lambda = 1\mu m$  in soft glass SF57.

In this discussion, the parameter  $b$  is varied to emphasize the effect of the position of the holes of the second ring. Figure (4.20) show the variation of  $b$  for a structure with  $N_{arms} = 6$ ,  $\Lambda = 1\mu m$  and  $d/\Lambda = 0.4$ , at the pump wavelength ( $1.064\mu m$ ). The field expands rapidly in the cladding as  $b$  is increased hence  $A_{eff}$  increases sharply. The distance of holes of second rings are shifted away from the core when  $b$  is increased, leading to more space between holes and the field can expand easily in the base material between the holes.

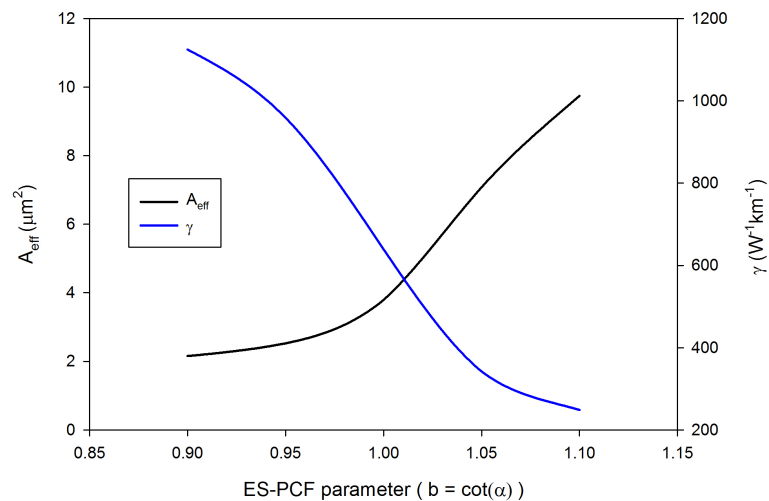


Fig. 4.20 Study the effect of varying spiral parameter  $b$  on  $\gamma$  and  $A_{eff}$  for ES-PCF designs with 6 arms,  $d/\Lambda = 0.4$  and  $\Lambda = 1\mu m$ , at wavelength  $1.064\mu m$  in soft glass SF57.

The non-linearity drops down at values of  $b$  above 1. The field expanding can be reduced by increasing the size of the holes in the first two rings but this explanation is given to point out the effect of the distance between the holes and position from the center.

Although it is preferable to have large holes in the first ring to increase the non-linearity, in the design proposed for SCG in Section (4.2.2) the holes in the first ring are made small to alter the dispersion.

The impact of a new parameter introduced in the last section on the optical properties is discussed here. The hole in the center can flatten the dispersion as noted but what effect does it have on  $A_{eff}$  and  $\gamma$ ? This is explored in this section. Figure (4.21) shows the result of varying  $\Lambda$  for structures with the hole in the center of a diameter to pitch ratio  $d_c/\Lambda = 0.2$ . The value of  $A_{eff}$  increased as the pitch increased which indicates the effect of the hole does not overcome or change the behavior obtained for other parameters. Similarly from the non-linearity the large  $\Lambda$  has small effect but when decreasing  $\Lambda$  to dimensions comparable with wavelength of operation the change in  $\gamma$  is large as can be seen from Figure (4.21) the value of  $\gamma$  is  $\approx 3800W^{-1}km^{-1}$  for structure with  $\Lambda = 1\mu m$  at wavelength  $0.6\mu m$  where at same wavelength with values of  $\Lambda = 3$  and  $4\mu m$  the value of  $\gamma < 600W^{-1}km^{-1}$ .

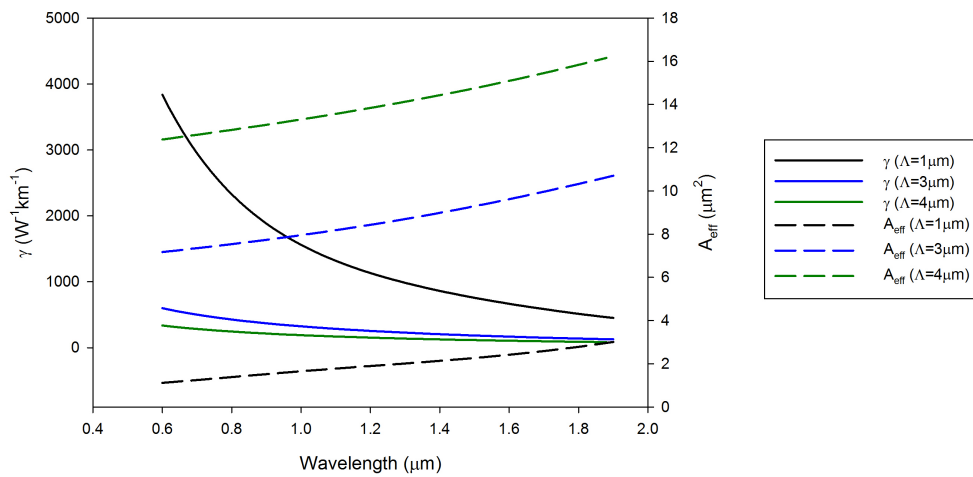


Fig. 4.21 Study the effect of varying  $d_c$  on  $\gamma$  for ES-PCF design with 6 arms,  $d/\Lambda = 0.4$ , and  $d_c/\Lambda = 0.2$  in soft glass SF57.

The effect of the defect hole at the center at small values of  $\Lambda$  is shown in Figure (4.22) where the defect hole is varied in size and all other parameters are kept fixed. The curves of  $A_{eff}$  at wavelengths lower than  $1.3\mu m$  show opposite behavior to the values above this wavelength. At higher wavelengths  $A_{eff}$  increases with increase in  $d_c$  and

the increase increases with wavelength (the difference between curves in the graph is higher at higher wavelengths). At lower wavelengths the opposite is true, where the structure with smallest  $d_c$ , ( $d_c/\Lambda = 0.1$ ), has highest  $A_{eff}$  values. The behavior is changing due to at lower wavelengths the field is concentrated in the core and the properties are mainly effected by the defect hole, if the hole size increases the  $A_{eff}$  decreases. However the difference is not large at values of  $A_{eff}$  when  $d_c/\Lambda$  is getting larger as in case of  $d_c/\Lambda = 0.2$  and  $0.3$  (blue and dark-green dashed lines). The field is not well confined at larger values of  $d_c/\Lambda$  as the effective refractive index of the core is reduced hence the refractive index difference between the core and the cladding is reduced.

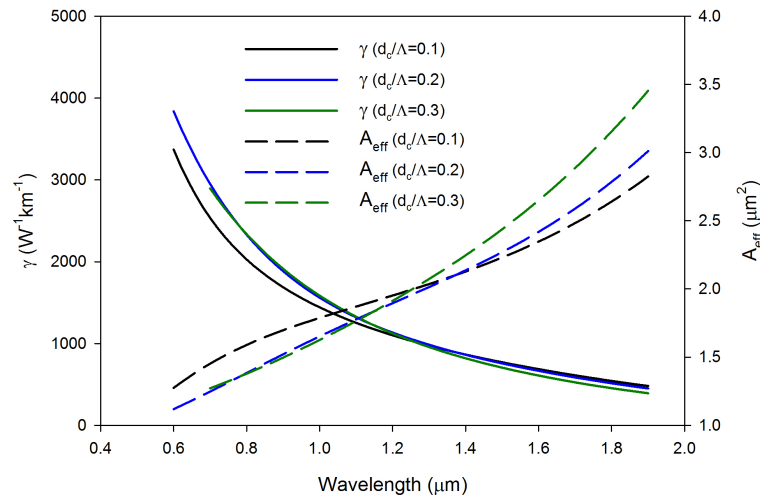


Fig. 4.22 Study the effect of varying  $d_c$  on  $\gamma$  for ES-PCF design with 6 arms,  $d/\Lambda = 0.4$ , and  $\Lambda = 1\mu m$  in soft glass SF57.

On the other hand, as the wavelength increases the field expands in the the cladding and the field gets more effected by the holes in the rings so the effect of the hole in the center has less effect on the over all properties.

The non-linearity is similar to the  $A_{eff}$  as it has different behavior at values above and under  $1.3\mu m$ . The non-linearity is lower for structure with smaller  $d_c/\Lambda$  at lower wavelength side, and at higher wavelengths the non-linearity is lower for structures with larger  $d_c/\Lambda$  for the same reason discussed in the  $A_{eff}$  discussion.

The study of the effect of varying the parameters of the Steiner structure on the optical properties of the interest in this thesis are discussed in the previous sections. The study is carried out with a base material of SF57 soft glass due to it is high non-linearity. The study included the effect of introducing a hole in the center of the core to flatten the dispersion further. The Steiner design in particular and ES-PCF in general are unique

structures for non-linear applications as they combine both characteristics that lead to increase in non-linear effects efficiency which are flat low dispersion and small  $A_{eff}$ . Therefore, the Steiner design is compared with H-PCF and ASC in the next section.

#### 4.1.4 Comparison of Steiner ES-PCF with other PCF

The properties of the Steiner design have been discussed and an explanation on how to control them was given. This section is to compare the ES-PCF with other PCF such as H-PCF and ASC which are widely studied and investigated. The advantages offered by the ES-PCF over the H-PCF arise due to the differences in the arrangement of holes and therefore, a comparison of the different structures of the two represents the starting point for the analysis. The position of the holes in the second ring of ES-PCF are positioned at a distance closer to the center and at angles that block the space between the holes of the first ring. This would lead to better field confinement in the core and a smaller  $A_{eff}$  (larger non-linearity or  $\gamma$ ) in the ES-PCF as discussed before. Table (4.2) shows the values of key parameters – non-linearity, dispersion and dispersion slope and Figures (4.23) and (4.24) present a synthesis of results for the two important factors ( $\gamma$  and dispersion) and allow a comparison of the ES-PCF, the conventional H-PCF and the ASC designs made from SF57 soft glass for pumping SCG at 1064nm.

Table 4.2 Comparison of the  $\gamma$ , dispersion and dispersion slope for H-PCF, ASC and ES-PCF structures at pump wavelength of 1064nm.

Design	ASC		ES-PCF		H-PCF		
					$\frac{d}{\Lambda} = 0.524$	$\frac{d}{\Lambda} = 0.8$	
$\Lambda(\mu m)$	0.5	0.6	0.5	0.6	0.5	0.5	0.6
$\gamma(W^{-1}km^{-1})$	5983	5455	5676	4555	2940	7238	2997
$D(ps/nm/km)$	409	248	6.7	2.1	-914	-701	-528
Slope ( $ps/nm^2/km$ )	1.11	1.12	1.16	0.026	0.21	3.79	0.83

Figure (4.23) shows the variation in the  $A_{eff}$  as a function of the core diameter as well the corresponding  $\gamma$  values for the three designs. To facilitate a comparison between the H-PCF and the ES-PCF, parameters such that the value of  $d/\Lambda$  are chosen to be the same. The smallest possible value of the effective area at the operating wavelength of 1064nm is the lowest for the ES-PCF ( $\approx 0.383\mu m^2$ ), while for the ASC fiber  $A_{eff} \approx 0.405\mu m^2$  and the H-PCF design,  $A_{eff} \approx 0.807\mu m^2$ . Usually increasing the value of  $d/\Lambda$  in a H-PCF leads to a smaller  $A_{eff}$  where an increase in  $d/\Lambda$  from 0.524 to 0.8 results in decrease in the value of  $A_{eff}$ , leading to an increase in  $\gamma$  from 2940

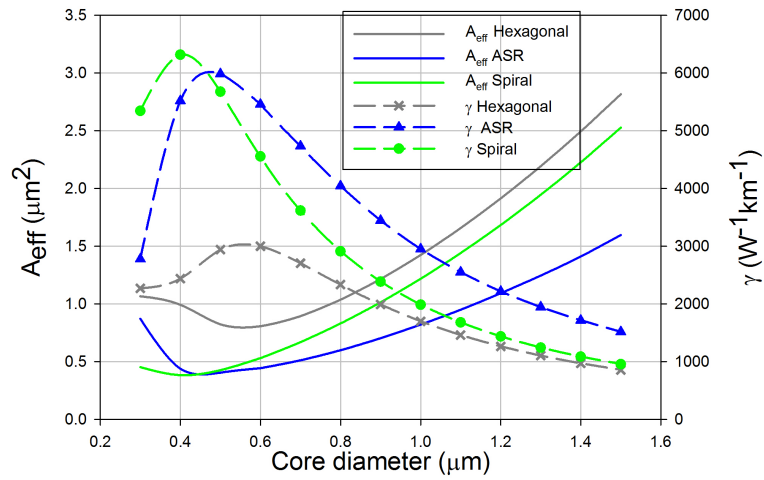


Fig. 4.23 A comparison of non-linearity and  $A_{eff}$  as a function of core diameter of ASC, H-PCF and ES-PCF designs in soft glass SF57.

to  $7238W^{-1}km^{-1}$ . However, this has an impact on the H-PCF dispersion (see Figure (4.24)), the change in the curve of H-PCF with  $d/\Lambda = 0.8$  (gray line with triangles) is steeper than H-PCF with  $d/\Lambda = 0.524$  (gray line). Therefore it is extremely important to choose a value of such that not only is the non-linearity enhanced but the dispersion is both small and flat at the same time.

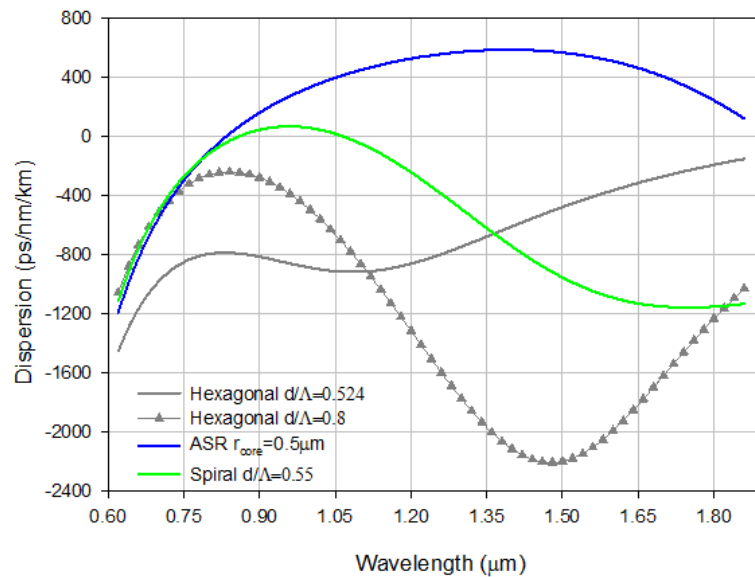


Fig. 4.24 A comparison of Dispersion of ASC, H-PCF and ES-PCF designs in soft glass SF57.

The non-linearity is reduced by reducing  $\Lambda$  but at a point the field gets cut-off beyond that dimension. Figure (4.25) shows the normalized  $A_{eff}$  of ES-PCF as  $\Lambda$  is decreased

where at values below  $\Lambda = 0.5\mu m$  the field is in the cut-off region as can be observed from the figure as the curve has a steep step when varying wavelength from  $0.5$  to  $0.4\mu m$  and then curve drops down below those values.

The dispersion associated with the fibers (for a core diameter of  $0.5\mu m$ ) is shown in Figure (4.24) A large value of  $d/\Lambda$  can lead to a large magnitude of dispersion: the absolute value of dispersion as well as the slope increase substantially when  $d/\Lambda$  changes from  $0.524$  to  $0.8$  for the H-PCF. Thus, it may be possible to find values of for the H-PCF to obtain either the dispersion or a value of  $\gamma$  that is comparable to the ES-PCF, but not to obtain superior performance with both characteristics at once. The ASC design has a larger dispersion at the pump wavelength of interest with a value of  $409ps/km/nm$  for a core of diameter of  $0.5\mu m$ , than does the ES-PCF with dispersion of  $6.7ps/km/nm$ . The associated  $\gamma$  values for the two PCF are  $5983$  and  $5676W^{-1}km^{-1}$ , respectively, as compared to  $2940W^{-1}km^{-1}$  for the H-PCF ( $d/\Lambda = 0.524$ ). Therefore, the ASC scores highly on the aspect of non-linearity but is not ideal with respect to dispersion. However, the ES-PCF has lower dispersion, a flat slope and a higher  $\gamma$  at  $1064nm$ . Hence, the ES-PCF offers advantages of both the ASC and H-PCF and can simultaneously be used to optimize the dispersion as well as the non-linearity.

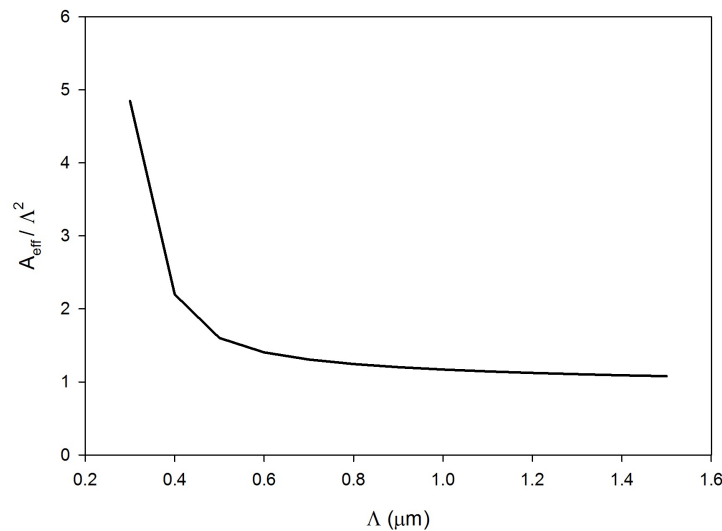


Fig. 4.25 Normalized  $A_{eff}$  for ES-PCF structure as a function of  $\Lambda$  in soft glass SF57.

The ES-PCF design offers excellent performance with respect to several key characteristics, especially control over the effective modal area and the dispersion, both essential for good SCG. It offers an alternative to the ASC/H-PCF designs and a means of obtaining optimal performance by offering superior properties over both characteristics

simultaneously [46]. In addition, the confinement and bending loss of ES-PCF are very low [243]. The drawback with the spiral design has been the lack of an effective fabrication method, which is addressed in Section (4.3).

The Steiner design has been investigated in more depth where systematic studies of the various parameters and their effect has been presented. The variation of the optical properties (effective refractive index, dispersion, effective area and non-linearity properties) has been presented. The relation between effective area and non-linearity is emphasized. The knowledge of the effect of each parameter would make it easier to optimize the optical properties of the design for the application of interest. The focus of this thesis is to optimize the properties of the design for the non-linear application, namely the SCG. The optimized design in tellurite glass is discussed in the next section and the results of the optical properties are given.

## 4.2 Supercontinuum Generation

The optical properties of modified Steiner ES-PCF have been studied in the previous section. The parameters of the structure have been varied and examined to understand their effect on the properties. The structure material in the previous section is SF57. In this section systematic studies similar to the one in the previous section are carried out to design Steiner ES-PCF for SCG. The structures studied in this section are based on tellurite material ( $76.5TeO_2 - 6Bi_2O_3 - 11.5Li_2O - 6ZnO(mol\%)$ ) [161, 244] as it has a transparency window approaching the mid-IR and it has a high Kerr non-linearity ( $n_2 = 5.9 \times 10^{-19} m^2/W^2$ ) [245, 246]. The refractive index is calculated by the Sellmeier equation (Equation (1.34)) with the use of Sellmeier coefficients from Table (4.3).

Table 4.3 Sellmeier coefficients of tellurite material [244]

Sellmeier Coefficient	1	2	3
$A_j$	1.67189	1.34862	0.62186
$B_j$	0.0004665	0.0574608	46.72542736

### 4.2.1 Parameters optimization

A study is carried out to optimize the dispersion to be low and flat in the anomalous region with ZDW near the pump wavelength of  $1.93 \mu m$  for SCG applications. The most important parameter is  $\Lambda$  in terms of variation of properties as discussed earlier.

Different designs have been simulated and their results are compared in this section. The best curve of each set is chosen to study the effect of the other parameters. The values of  $\Lambda$  ranged from  $0.75\mu\text{m}$  to  $4.5\mu\text{m}$  to see the influence on dispersion. The parameters were chosen as  $d/\Lambda = 0.6$  and  $N_{\text{arms}} = 6$  and results of some simulations are shown in Figure (4.26). The higher values of  $\Lambda$  are not of interest as the dispersion is not very different from the material dispersion and the variation of the other parameters would not have an adequate impact on the dispersion. The dispersion is large and has steep slope for structures with large  $\Lambda$ . The material dispersion (dashed line) has ZDW at  $1.84\mu\text{m}$  which is good for pump at  $1930\text{nm}$  but the higher  $\Lambda$  structures blue shift the ZDW, the structure with  $\Lambda = 4.5\mu\text{m}$  (red line) the ZDW is shifted to  $1.67\mu\text{m}$  and for smaller values the ZDW is shifted to lower wavelengths faraway from the pump wavelength of interest ( $1.93\mu\text{m}$ ). The change in dispersion at higher wavelengths occur at  $\Lambda = 2\mu\text{m}$  (gray line). By decreasing  $\Lambda$  further to  $1.5\mu\text{m}$  (dark-green line) the dispersion changes at wavelengths higher than  $3.5\mu\text{m}$ . The best curve obtained in terms of dispersion change is for  $\Lambda = 0.75\mu\text{m}$  (blue line) where dispersion is manipulated through all wavelengths and ZDW is  $1.78\mu\text{m}$  which can be shifted closer to the pump wavelength by controlling other parameters. This value of  $\Lambda$  is chosen for the simulations of altering the dispersion by the other parameters. The size can be decreased more but the field is near cut-off and further reduction in  $\Lambda$  has no advantages over the value of  $0.75\mu\text{m}$ .

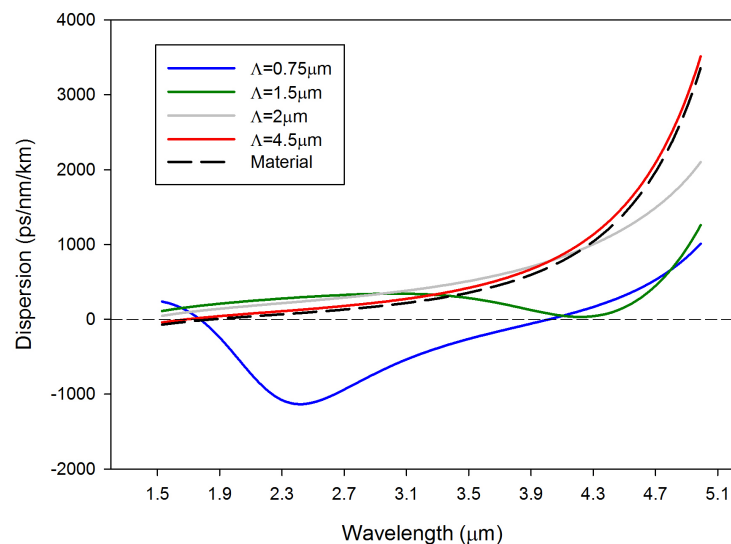


Fig. 4.26 Varying  $\Lambda$  to see effect on dispersion for Steiner ES-PCF design with 6 arms and  $d/\Lambda = 0.67$  in tellurite.

The pitch size and number of arms have been set according to the previous experiment of comparing  $\Lambda$ , for the design of interest. The parameter  $d/\Lambda$  is varied where three different sets of  $d/\Lambda$  with values of 0.55, 0.6 and 0.67 are simulated and the results are shown in Figure (4.27). The curve of the design with smallest ratio (dark-green line) is flatter and the curve is blue shifted with respect to the other dispersion as the lower ZDW has been shifted to below  $1.5\mu\text{m}$ . Therefore, the larger ratio of  $d/\Lambda$  is better in terms of ZDW position, but dispersion is higher which can be compensated. The variation of the ratio  $d/\Lambda$  would change the size of the hole in the first and second rings simultaneously. The final stage of the study is to vary the number of holes of each ring separately.

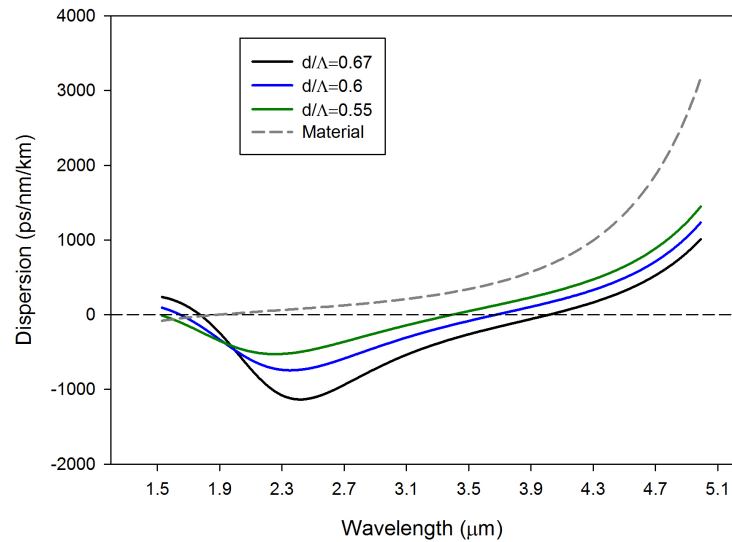


Fig. 4.27 Varying  $d/\Lambda$  to see effect on dispersion for Steiner ES-PCF design with 6 arms and  $\Lambda = 0.75\mu\text{m}$  in tellurite.

The parameters are kept fixed and the only parameter to be varied is the radius of holes in the first or second ring. Therefore, each set is tested and simulation results represent the best choice for the design. The effect of variation in the size of the holes in the first ring is shown in Figure (4.28). When hole size is reduced the dispersion is more flat and tends to zero at the lower half of the wavelength range shown. In the upper wavelength half, the curve is shifted up. The conclusion of this is that the variation of the holes in the first ring can be used to flatten the dispersion but not to shift its ZDW as shown in the graph.

The variation of the holes in the second ring impacts the dispersion where decreasing the radius of the holes leads to blue shift the dispersion at the lower wavelength region. The shift is significant as the ZDW is shifted from  $1.77$  to  $1.52\mu\text{m}$  for a reduction in

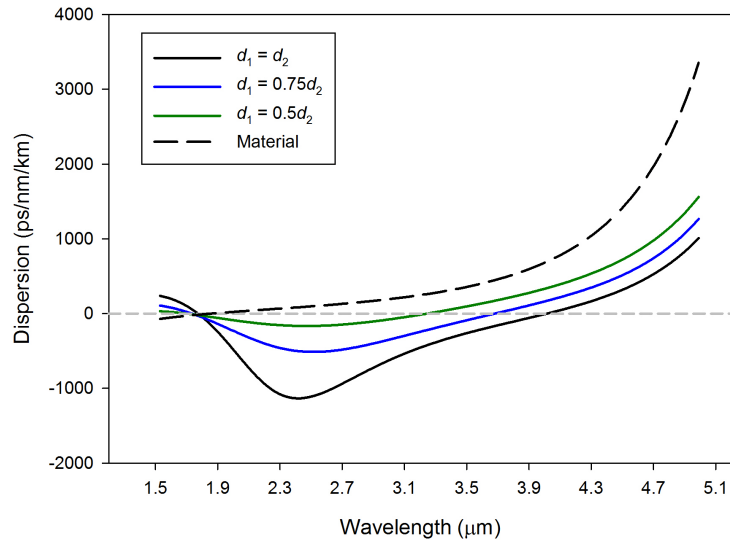


Fig. 4.28 Varying the holes diameter of the first ring to see effect on dispersion for Steiner ES-PCF design with 6 arms,  $d/\Lambda = 0.67$  and  $\Lambda = 0.75\mu\text{m}$  in tellurite.

size of 25% (see Figure (4.29)). However, the change in the dispersion curve at higher wavelengths follows the same trend of change when varying the other parameters. The reason is thought to be that the field expands to reach the holes in the third ring which are very large in comparison to the other holes. The change in air filling fraction of the area covered by the field profile is the same when changing either set of the holes in one of the two rings close to the core. The change in  $d_1$  and  $d_2$  at higher wavelength region has similar effect due to the field expanding through both rings. The field is not changing much at higher wavelengths as the field expands over both holes of the first and second rings and a change in one of them has similar effect. The holes influence the field independently at the lower side of the spectrum. The pitch size has an impact on dispersion at any wavelength window as can be noticed from Figure (4.26).

The study of the different parameters and their influence on the dispersion is concluded with choosing the parameters of the optimum structure for the study of SCG. The parameters are  $N_{arms} = 6$ ,  $\Lambda = 0.75\mu\text{m}$ , the radii of the first, second and third ring holes are  $0.1$ ,  $0.22$  and  $1.2134\mu\text{m}$ , respectively and  $d/\Lambda \approx 0.29$ , the ratio is taken in regards to holes in the second ring. The optical results and SCG are presented in the next section.

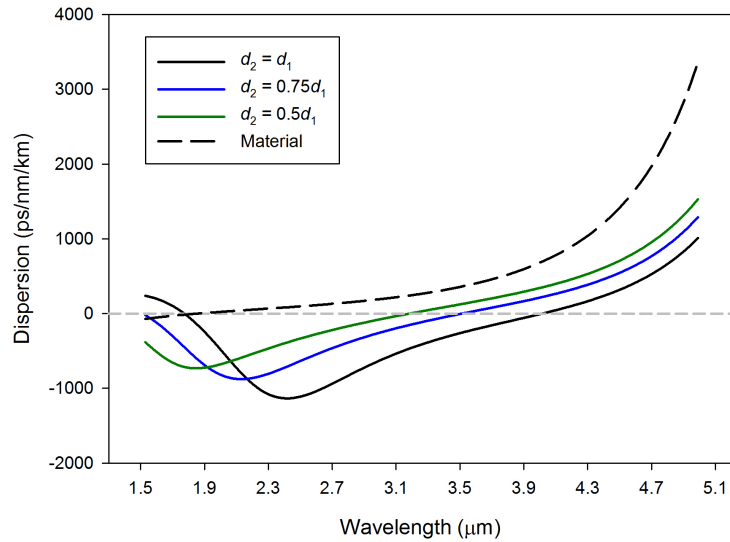


Fig. 4.29 Varying the holes diameter of the second ring to see effect on dispersion for Steiner ES-PCF design with 6 arms,  $d/\Lambda = 0.69$  and  $\Lambda = 0.75\mu m$  in tellurite.

#### 4.2.2 Results of optimum design

The design process requires several simulations and analysis of the results to understand the various factors that influence the outcome. The second task is to adjust some of the parameters and re-run the simulation to check the result whether they are of interest or not. The adjustment may require several stages similar to what has been done in this thesis. The final step is presenting the outcome of the work. A schematic of the optimum structure cross section is shown in Figure (4.30).

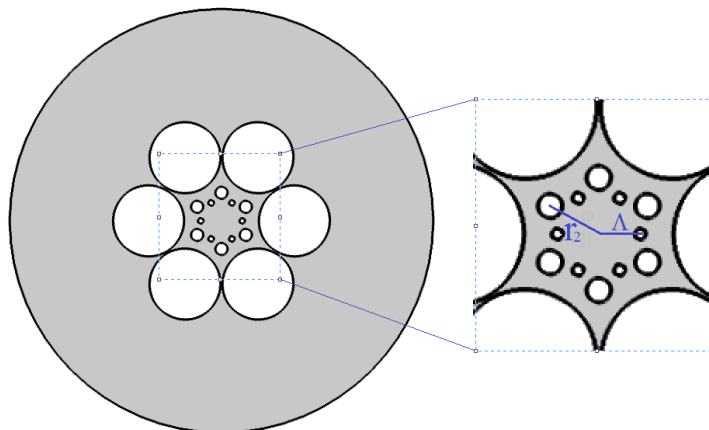


Fig. 4.30 Schematic of the cross section of the optimized Steiner ES-PCF structure.

The structure is perfect in dispersion management with excellent confinement of light. The larger holes impact the confinement of the light and the holes in the first and second

rings alter the dispersion as discussed in the last section. The variation of  $n_{eff}$  and  $A_{eff}$  with respect to wavelength are shown in Figure (4.31). The field at the lower end of the wavelength range is well confined in the core as can be extracted from  $A_{eff}$  data. At higher wavelengths the field expands all over the first and second rings of holes.

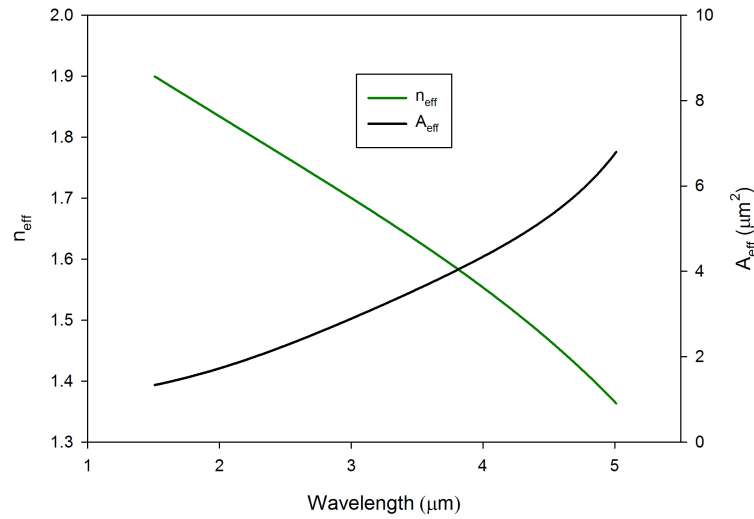


Fig. 4.31 Variation of  $n_{eff}$  and  $A_{eff}$  with regards to wavelength for the optimum design in tellurite with  $N_{arms} = 6$ ,  $\Lambda = 0.75\mu m$ , radius of the holes in 1<sup>st</sup>, 2<sup>nd</sup> and 3<sup>rd</sup> rings are 0.1, 0.22 and  $1.2134\mu m$ , respectively.

The dispersion of the structure is shown in Figure (4.32) along side with the bulk material dispersion. The curve is very flat and close to zero in the lower wavelength range. The dispersion value is  $\pm 4ps/nm/km$  in the range from 1.5 to  $2.3\mu m$  and  $\pm 2ps/nm/km$  at 1.8 to  $2\mu m$ . The design has three ZDWs at 1.5, 1.88 and  $2.22\mu m$ . The first two are suitable for using commercial lasers for pumping at 1557 and  $1930nm$  as the non-linear effects are more efficient when the pump wavelength is close to the ZDW. These result has been published in the CLEO2011 conference.

The dispersion flatness is the range of variation of dispersion with regards to wavelength, which is in simple words is the slope of the curve. The dispersion slope is calculated by using central difference technique as shown in Equation (4.1).

$$f' = \frac{f(x + \frac{1}{2}h) - f(x - \frac{1}{2}h)}{h} \quad (4.1)$$

The calculated slope is plotted in Figure (4.33). The slope is less than  $0.003ps/nm^2/km$  in the range 1.5 to  $2.3\mu m$ , which is ten order of magnitude lower than published results [247, 248].

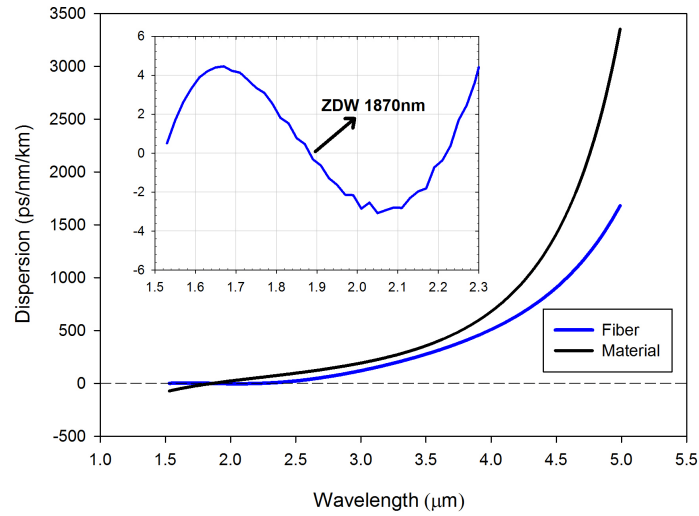


Fig. 4.32 Dispersion of Steiner ES-PCF in tellurite with  $N_{arms} = 6$ ,  $\Lambda = 0.75\mu m$ , radius of the holes in 1<sup>st</sup>, 2<sup>nd</sup> and 3<sup>rd</sup> rings are 0.1, 0.22 and  $1.2134\mu m$ , respectively.

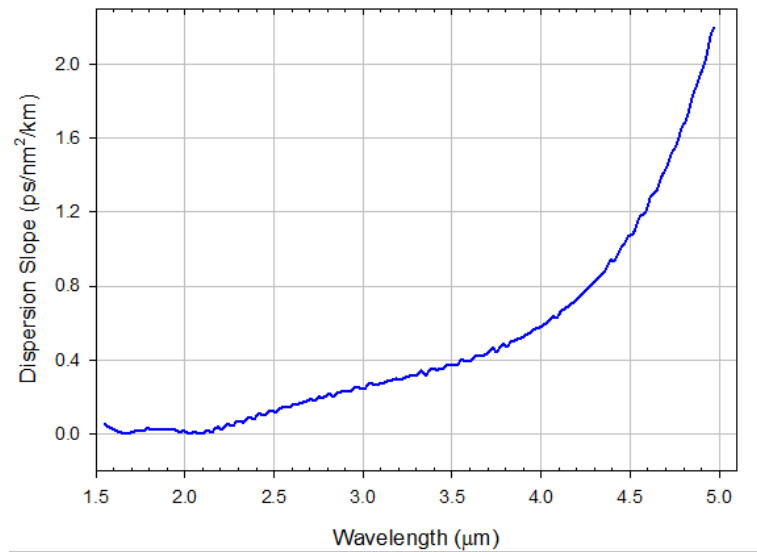


Fig. 4.33 Slope of dispersion of Steiner ES-PCF in tellurite with  $N_{arms} = 6$ ,  $\Lambda = 0.75\mu m$ , radius of the holes in 1<sup>st</sup>, 2<sup>nd</sup> and 3<sup>rd</sup> rings are 0.1, 0.22 and  $1.2134\mu m$ , respectively.

The other important property for SCG is the non-linearity which is calculated using Equation (1.33). The results are shown in Figure (4.34), the value of  $\gamma$  ranges from  $1800W^{-1}km^{-1}$  at wavelength  $1.5\mu m$  to  $800W^{-1}km^{-1}$  at  $2.3\mu m$ . The value of  $\gamma$  is equal to  $1155W^{-1}km^{-1}$  [239] at the pump wavelength of  $1.93\mu m$  which is much higher than published results of  $140W^{-1}km^{-1}$  at the same wavelength [249]. In other pub-

lished results the non-linearity reported is  $394W^{-1}km^{-1}$  [250] at wavelength  $1557nm$  which is a fraction of the value obtained by the Steiner design of  $1740W^{-1}km^{-1}$  [225]. In the latter experiment, the dispersion at the same wavelength is  $75ps/nm/km$  [250] compared to  $\approx 1ps/nm/km$  achieved with this design. Therefore, the Steiner ES-PCF design is well suited for non-linear application (SCG) where the non-linearity is high and dispersion is low.

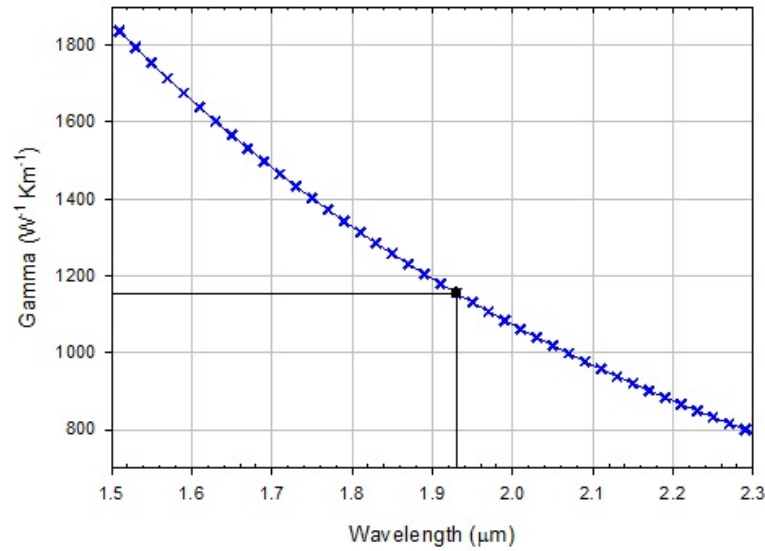


Fig. 4.34 Non-linearity of Steiner ES-PCF in tellurite with  $N_{arms} = 6$ ,  $\Lambda = 0.75\mu m$ , radius of the holes in  $1^{st}$ ,  $2^{nd}$  and  $3^{rd}$  rings are  $0.1$ ,  $0.22$  and  $1.2134\mu m$ , respectively.

There is an important property which was discussed in Chapter 1, which is the loss. The loss of Steiner ES-PCF structure with  $N_{arms} = 6$ ,  $\Lambda = 0.75\mu m$ , radius of the holes in  $1^{st}$ ,  $2^{nd}$  and  $3^{rd}$  rings are  $0.1$ ,  $0.22$  and  $1.2134\mu m$ , respectively, has been calculated and is shown in Figure (4.35). The total loss is almost identical to the material loss at wavelengths below  $3.8\mu m$  and at higher wavelengths the total loss increases sharply. The reason is that the field is well confined at lower wavelengths but at higher wavelengths the cut-off wavelength is reached and the field expands from the structure and the loss increases dramatically. It can be concluded from the loss results that when the field is confined the dominant loss is the material loss. The total loss is calculated by the two formulae shown:

$$\Im m(\beta) = \frac{2\pi}{\lambda} \Im m(n_{eff}) \quad (4.2)$$

$$L = \frac{20}{\ln(10)} \Im m(\beta) \quad (4.3)$$

where  $\Im m$  stands for imaginary part.

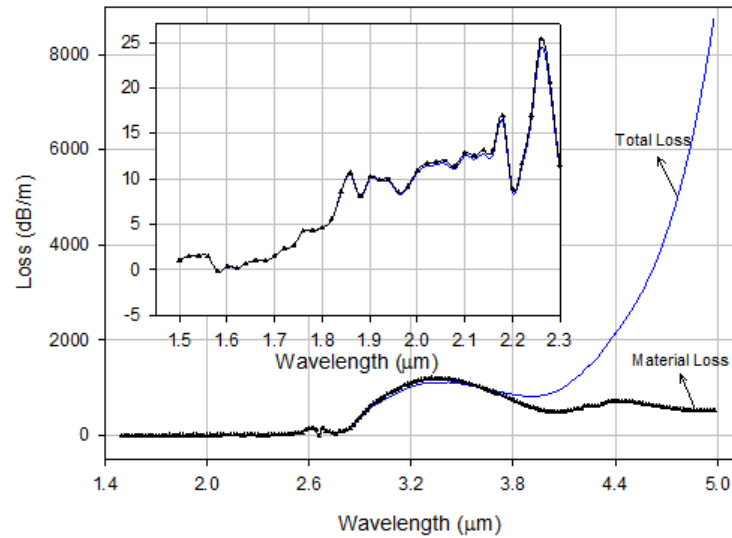


Fig. 4.35 Attenuation of tellurite material Steiner ES-PCF with  $N_{arms} = 6$ ,  $\Lambda = 0.75\mu m$ , radius of the holes in 1<sup>st</sup>, 2<sup>nd</sup> and 3<sup>rd</sup> rings are 0.1, 0.22 and  $1.2134\mu m$ , respectively. Inset is a scalable of the lower wavelength region from 1.5 – 2.3 $\mu m$ .

The results of modeling the structure have been discussed and compared to other published results. The proposed structure has shown better values for promising high SCG. The simulation results of SCG discussed in next section.

### 4.2.3 Result of supercontinuum generation

The simulation results of the basic optical properties of the structure have been presented and discussed. The simulation of the modal field provided all information in previous section which is either accessed directly from output such  $n_{eff}$ ,  $A_{eff}$  and loss, or that requires more processing of data to generate the output such as dispersion which is calculated from  $n_{eff}$  as function of wavelength, and  $\gamma$  which is calculated from  $A_{eff}$  and wavelength.

The non-linear effect, SCG, requires further simulation and input parameters to calculate the spectral broadening. The work to calculate SCG was done by a collaborator Dr. Manish Tiwari from Rajhani Engineering College, India. This work has been published in Journal of Modern Optics as a joint work, see list of publications.

In the simulation of SGC two pumping wavelengths were used at 1557nm and 1930nm. The former has an average power of 11.2mW and the SC bandwidth simulated for a 10m fiber expands more than two octaves from 970nm – 4100nm. The second pumping wavelength has an average power 12mW and SC bandwidth is 1300nm – 3700nm.

The combination of high non-linearity and wide range low flat dispersion in the anomalous region with ZDWs at pump has led to generation of broad and flat SC spectrum obtained. The bandwidth of SC achieved in this work is  $> 3000nm$  which is compared to results of  $1600nm$  [251] achieved with similar pump characteristics. However, very large bandwidth SC [252, 253] have been demonstrated but the pump power used is large compared to the power used in this work. The Steiner ES-PCF structure has superiority for non-linear application and the limitation is the fabrication process where in the conventional SaD only hexagonal packing is possible. This limitation is overcome by an algorithm proposed in the next section which adapts the SaD with some modifications. However, the fabrication of soft glass and polymer PCF can be done by several other methods like extrusion, drilling, casting and 3D printing.

### 4.3 Towards Steiner ES-PCF Fabrication

The simulation results of the ES-PCF have been presented in the previous chapters with discussion on the parameters that can be varied to manipulate the design to suit the desired application of interest. The simulations of ES-PCF have shown that the design has unique and superior characteristics such as control of both dispersion and non-linearity simultaneously for applications such as SCG. The obstacle in PCF designs with hole distribution in spiral or other complex patterns is the fabrication of these structures. Recently, the fabrication techniques have been improved significantly with new techniques that have emerged in the field as discussed in Chapter 1, this has made the fabrication of complex designs feasible with new techniques. However, the fabrication of complex structures using SaD procedure is still a challenging task, which limits the fabrication of these designs to certain materials. The fibers made of the most widely used material (silica) are fabricated by the SaD. Therefore, a procedure based on the SaD is proposed to fabricate ES-PCF. This procedure is implemented by stacking tubes and rods in a similar manner to the well know SaD technique. The procedure is explained in this chapter and it is coined as Adapted Stack and Draw (ASaD). The next section is an introduction to the Steiner chain rule which is implemented to calculate the position and the size of holes in the procedure proposed.

#### 4.3.1 Steiner chain

The procedure proposed to fabricate ES-PCF using the concept of SaD requires some modifications. The Steiner chain rule is implemented to adapt the SaD technique and make it feasible for the fabrication of ES-PCF designs. The Steiner chain concept

indicates that given two circles with one interior to the other the space between them can be filled with tangent circles such that the final one is tangent to the first leaving no space. In other words, the space between two tubes, when one is inside the other, can be filled with a number of rods and/or tubes such that tubes touch both outer and inner tubes, and there is no overlap between adjacent tubes. Therefore, all the tubes are supported and none are left free. The Steiner chain rule is explained in reference to Figure (4.36). The rule is general where any number of circles can be used.

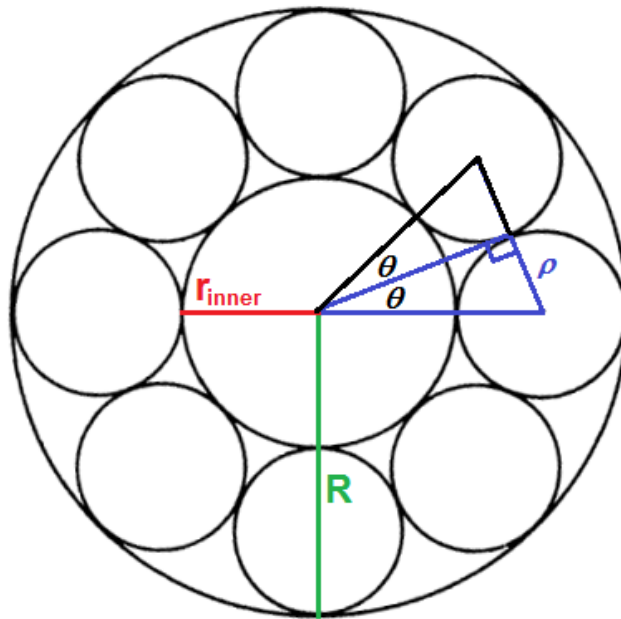


Fig. 4.36 Steiner Chains

The graphic representation of the Steiner chain rule is only useful to understand the derivation of the formula as it cannot be implemented in the simulations. However, the mathematical formula derived from the graph is used to code the structures in the simulations. The first relation derived is by implementing the trigonometric sine rule on  $\theta$  in the blue triangle (Figure (4.36)). The sine of the angle equals the opposite side over the hypotenuse and in this case the opposite is the radius of the circles filled in the annular region ( $\rho$ ) and hypotenuse is ( $r_{inner} + \rho$ ). Then the equation is written as

$$\sin(\theta) = \frac{\rho}{r_{inner} + \rho} \quad (4.4)$$

The ratio between outer and inner circles is used to define the relation between radii of inner circle and the circles in the middle space between the concentric circles. It is the factor that controls the number of circles. The ratio is defined as

$$x = \frac{R}{r_{inner}} \quad (4.5)$$

Substituting  $R = r_{inner} + 2\rho$  in the equation and rearranging then the radius of circles in the middle is defined as

$$\rho = r_{inner} \times \frac{x - 1}{2} \quad (4.6)$$

It is noticed that the circles in third ring,  $T_3$ , would have radius equal to the innermost circle for  $x = 3$ . If  $x > 3$  then the center circle is smaller and verse versa. There is another formula to calculate  $x$  which is more convenient for this thesis [233].

$$x = \frac{1 + \sin(180/N)}{1 - \sin(180/N)} \quad (4.7)$$

where  $N$  is the number of circles which fill the space between outer circle/tube and inner circle/tube which contains the inner structure of the fiber. In this work, the number of holes that are used in the Steiner rule is equal to number of arms, therefore  $N$  is referred to as  $N_{arms}$ . Also the value  $(180/N)$  is actually the same angle  $\theta$  shown in Figure (4.36) and the one used in the previous sections to accomplish results of ES-PCF designs. The utilization of Steiner chain rule is explained in the next section.

### 4.3.2 Algorithm of fabrication

The stack and draw technique is implemented by stacking equally sized tubes and rods in a hexagonal form inside a larger tube. The tubes are arranged in a hexagonal close packing which is the underlying mathematics of the SaD process. This arrangement results in the densest tube packing in two dimensions [240]. The tubes are stacked adjacent to each other in the same row and the following row of tubes are placed in the depressions formed between tubes in the previous row. These conditions limit the use of conventional SaD for quasi-crystal PCF structures. Therefore, an algorithm is proposed to modify the SaD technique to adapt to non-hexagonal structures. The concept is closely similar to SaD but the tubes and rods can be of different sizes and the stacking of tubes does not follow the same positioning as in SaD.

The first step is to calculate the centers of the 1<sup>st</sup> and 2<sup>nd</sup> holes of the same arm, where from the ES formula (Equation (3.2)) the  $r_i$  can be calculated, where  $r_i$  is the distance

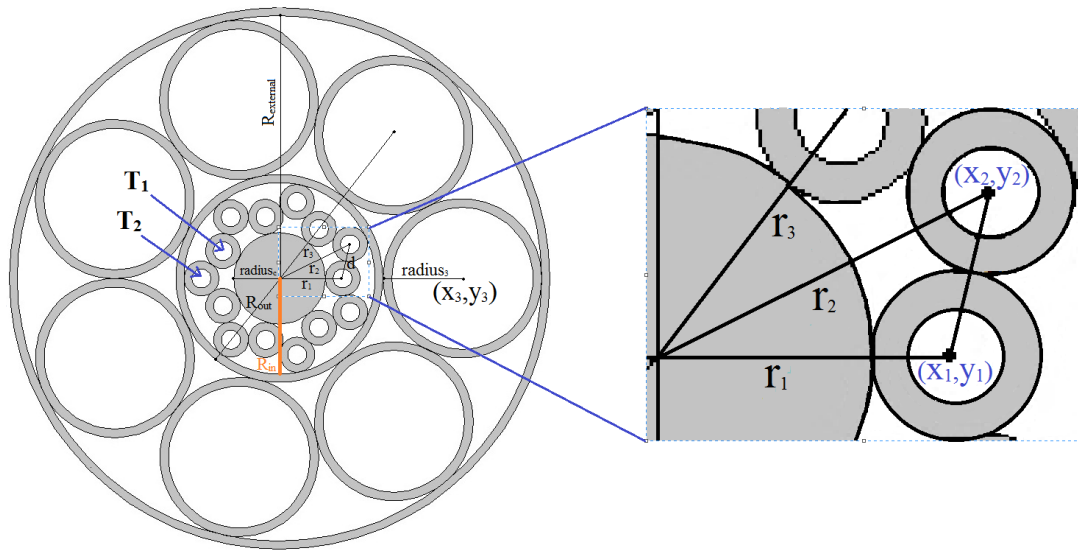


Fig. 4.37 Schematic of 7 arms Steiner ES-PCF preform

from center of structure to the center of the hole which has the  $i^{th}$  position. The holes of the first ring touch the rod in the center (see Figure (4.37) and holes of the second ring, where holes in the second ring touch the holes of first ring and the enclosing tube which has an inner radius  $R_{in}$  (orange line). The values are in polar coordinates so they are converted to their equivalent Cartesian coordinates using the two formulae  $x = r \cos(\theta)$  and  $y = r \sin(\theta)$ . The distance between the two centers ( $d$ ), is equal to the outer diameter of the tubes because the distance from the center of 1<sup>st</sup> hole to center of 2<sup>nd</sup> hole equals 2 times the radius of the tubes  $T_1$  and  $T_2$ . It is calculated by the formula

$$d = \sqrt{(x_1 - x_2)^2 + (y_1 - y_2)^2} \quad (4.8)$$

The outer diameter of the tubes of the first two rings are known. The outer diameter along side with the pitch, which is an input parameter in the simulations, are used to calculate the radius of the rod in the center. The rod radius ( $radius_c$ ) and the thickness of the first ring tubes form the core of the ES-PCF. The rod radius is

$$radius_c = \Lambda - \frac{d}{2} \quad (4.9)$$

where  $\Lambda$  is the distance from the center of the structure to the center of the tubes in the first ring and is equal to  $r_1$ .

The tubes of the first two rings and the rod are stacked in a larger tube which has inner ( $R_{in}$ ) and outer ( $R_{out}$ ) radii. The former is calculated by knowing distance of tubes of

$2^{nd}$  ring from the center and the outer radius of the same tube. It is the summation of both values as given by the equation below

$$R_{in} = r_2 + \frac{d}{2} \quad (4.10)$$

The concept of Steiner chain rule is used to calculate the outer radius of the tubes of  $3^{rd}$  ring. The Equation (4.6) is used to find the  $radius_3$  as

$$radius_3 = R_{out} \frac{x-1}{2} \quad (4.11)$$

where  $x$  is defined in Equation (4.7).

The distance from the center of the structure to the center of  $3^{rd}$  ring tubes is calculated as the distance to the outer surface ( $R_{out}$ ) of the enclosing tube of the inner structure plus the radius of the tube of the  $3^{rd}$  ring. The formula is

$$r_3 = radius_3 + R_{out} \quad (4.12)$$

The final step is to find the radius of the tube enclosing the entire structure that acts as the preform and which consists of the tube that contains the first two rings of tubes and central rod that acts as the core, and the tubes of the  $3^{rd}$  ring. Its thickness can be chosen independently of the structure as there are no other tubes involved. Therefore only the inner radius of the most outer tube is concerned in this procedure because the outer radius can be chosen large to form the outer PCF cladding. The radius of the outermost tube is equal to the distance from the center of the structure to the center of the tube in the third ring ( $r_3$ ) plus outer radius of tubes in the  $3^{rd}$  ring ( $radius_3$ ). This relation is written in a mathematical form as shown

$$R_{external} = radius_3 + r_3 \quad (4.13)$$

The tubes and rod of the structure are all known, the only missing ones are the inner radii of the holes which are the tubes in the three rings. These radii depend on the holes of the structure and their sizes. For identical spirals the values of  $N_{arms}$  and  $\Lambda$ , radii are calculated as above and are kept constant. By varying the inner radii of the tubes it is possible to change the radius of the holes in the different rings. The tubes are made when the inner radius is given and all tubes and rods are ready for the stacking.

By using the Steiner rule, it is possible to place holes at different angles and break away from the hexagonal structure. Furthermore, the tubes (rods) can be replaced by rods (tubes) to create designs with low index core and/or high index inclusions in the

cladding. This latter can be used to exploit band-gap guidance. The stacking process of tubes and the rod is shown in the next section.

### 4.3.3 Adapted stack and draw

The procedure used above is simple and straight forward but the various parameters may look complex. For this reason in the stacking process it is better to define each tube group with a unique name to make explanation easier to follow and understand. The tubes in each ring are referred to as  $T_1$ ,  $T_2$  and  $T_3$  for first, second and third ring tubes, respectively. The other two tubes are; one which encloses the first two rings and is referred to as  $T_{inner}$ , and the other which encloses the whole structure is referred to as  $T_{outer}$ . The convention is used for clarification and it does not have any impact on the procedure.

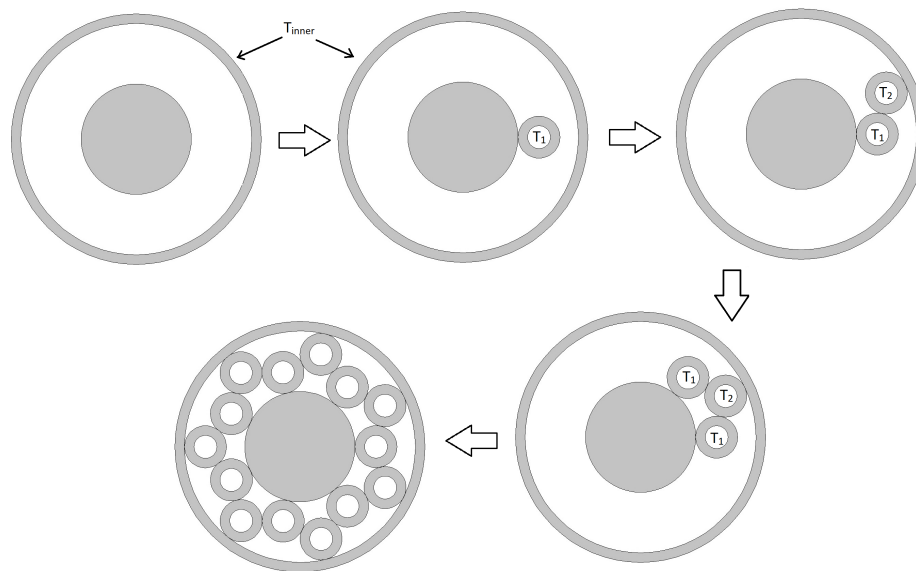


Fig. 4.38 Schematic of stacking inner tubes of 7 arm Steiner ES-PCF structure

The stacking process takes place after the tubes and rods are made and ready with the dimension specified for the required design. The first tube concerned is  $T_{inner}$  which is used to stack the central rod, and the tubes  $T_1$  and  $T_2$  inside it. The process is shown in Figure (4.38) where first the rod is inserted and the second step is insert tube  $T_1$  which touches the rod. The third step is to stack the tube  $T_2$  of the same arm in a way that it touches tube  $T_1$  of the same arm and the tube  $T_{inner}$ . Then the second and third steps are repeated with tube  $T_1$  touching preceding tube  $T_2$  of the neighboring arm. The last tube to be stacked in this stage is  $T_2$  which would touch tube  $T_1$  of same arm, tube  $T_1$  of the first arm which is stacked in second step, and tube  $T_{inner}$ . In this way all tubes are held

tight where each tube is fixed from three places so no tube is left free to move. By these arrangement the holes position (angle and distance from center) are exactly the same as predicated by the ES equation. There is not any manipulation in the position of the holes in the first and second rings which means the optical properties of the structure are not changing dramatically. There is a small change in the values of some optical properties which has unnoticeable effect. A comparison between the results of Steiner and the ideal spiral are given in the next section.

The final step is to stack the tube  $T_{inner}$ , which has the inner tubes and rod, into the middle of tube  $T_{outer}$  surrounded by tubes  $T_3$ . The tubes fill the space with each tube  $T_3$  touching tubes  $T_{inner}$ ,  $T_{outer}$  and two adjacent  $T_3$ . The final preform is stable and no tube is left free moving as shown in Figure (4.39).

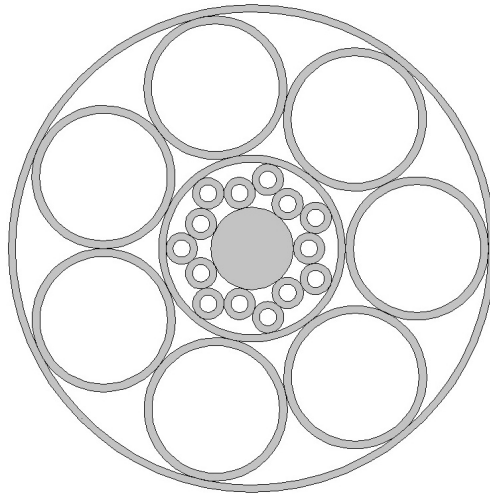


Fig. 4.39 Schematic of stacking outer tubes of 7 arm Steiner ES-PCF structure

## 4.4 Comparison between Ideal and Steiner ES-PCF

The proposed structure (Steiner ES-PCF) is simulated and results are compared to ideal ES-PCF results. The material used in the simulation is the soft glass SF57 and all result in this section are in the same material. The study comprises of different scenarios with different arms and  $\Lambda$ . The parameters are chosen to be same for every set of results for comparison reasons. The value of the ratio  $d/\Lambda$  is set equal to 0.4 for structures studied in the comparison. The comparison is in terms of the optical properties which are  $n_{eff}$ ,  $A_{eff}$  and dispersion.

#### 4.4.1 Comparison of ideal and Steiner ES-PCF ( $\Lambda = 3\mu m$ )

The speed and interaction of the light within a material is dependent on the most important optical property which is the effective refractive index. The results of  $n_{eff}$  for ideal and Steiner ES-PCF structures with  $N_{arms} = 6$  and  $\Lambda = 3\mu m$  are shown in Figure (4.40). It is noticeable that there is hardly any change between the two curves so the fields have identical value of  $n_{eff}$  through the entire wavelength window ( $0.6 - 1.9\mu m$ ). This is due to the fact that the holes in the first two rings are identical for both structures as they have exactly the same positions and size, and the field is not expanding away from the core as the size of the core is larger than the wavelength of operation.

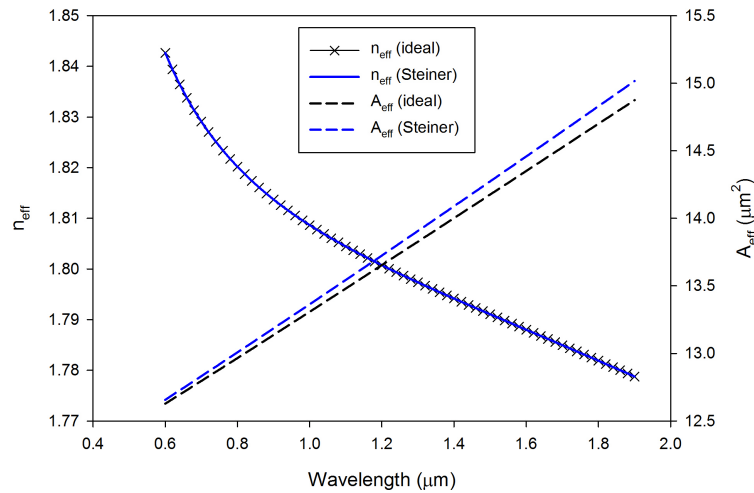


Fig. 4.40 Comparison of  $n_{eff}$  and  $A_{eff}$  for the ideal and Steiner ES-PCF in soft glass SF57 with  $N_{arms} = 6$ ,  $N_{rings} = 3$ ,  $d/\Lambda = 0.4$  and  $\Lambda = 3\mu m$

However, there is some difference in  $A_{eff}$  between the two structures as shown in the same figure. The ideal ES-PCF structure has a lower  $A_{eff}$  than Steiner ES-PCF which is as a result of the position of the holes in the third ring. The holes in ideal ES-PCF are closer to the center of the structure and hence have more effect on the  $A_{eff}$  and the field is more confined in this case. The difference in  $A_{eff}$  increases with increasing wavelength due to expansion of the field. The increase is believed to be as a result of the air filling fraction of ideal ES-PCF, in the area that the field interact with, is more than in the Steiner ES-PCF. The reason beyond this is the distance between second and third hole edges are larger in Steiner ES-PCF as shown in Figure (4.3).

A similar study was carried out on a design with  $N_{arms} = 7$  and  $\Lambda = 3\mu m$ . It is found that the results have similar trend in the change of  $A_{eff}$  and dispersion (see Figure(4.41)).

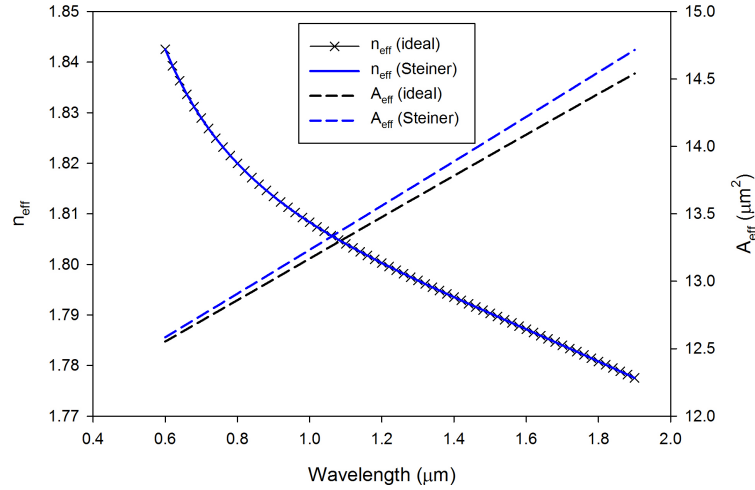


Fig. 4.41 Comparison of  $n_{eff}$  and  $A_{eff}$  for the ideal and Steiner ES-PCF in soft glass SF57 with  $N_{arms} = 7$ ,  $N_{rings} = 3$ ,  $d/\Lambda = 0.4$  and  $\Lambda = 3\mu m$ .

The change in  $n_{eff}$  with wavelength is an important property as this controls the dispersion. The dispersion of the 6 arms structure is shown in Figure (4.42). The dispersion of both structures is identical which is expected because  $n_{eff}$  is identical.

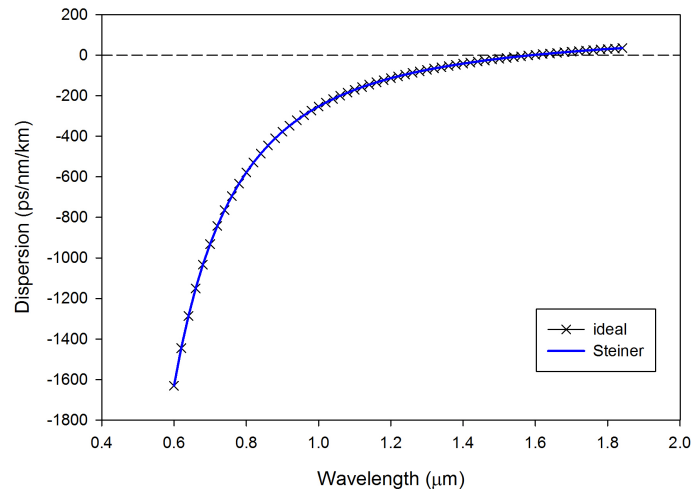


Fig. 4.42 Comparison of dispersion for the ideal and Steiner ES-PCF in soft glass SF57 with  $N_{arms} = 6$ ,  $N_{rings} = 3$ ,  $d/\Lambda = 0.4$  and  $\Lambda = 3\mu m$ .

To sum up, the Steiner ES-PCF concept does not change the optical properties of the ideal ES-PCF when  $\Lambda$  is larger than the operating wavelength, therefore the unique spiral characteristic is still observed. Although this section is mainly on the comparison between ideal and Steiner ES-PCF, it can still be emphasized the fact that for large pitch size the dispersion cannot be controlled with extreme freedom to generate a flat low dispersion with ZDW near pump wavelength. In the next section the study is concerned with small pitch size to influence the optical properties of the fiber.

#### 4.4.2 Comparison of ideal and Steiner ES-PCF ( $\Lambda = 1\mu m$ )

In the previous section the comparison of of ideal and Steiner ES-PCF structures with a pitch size larger than the operating wavelength has been discussed. The effective areas have small difference and the  $n_{eff}$  of both structures are identical. In this section the pitch is chosen to be comparable with the operating wavelength. The structure studied has 6 arms, 3 rings,  $d/\Lambda = 0.4$  and  $\Lambda = 1\mu m$ . The properties studied are the same ones investigated in the previous section to have a good understanding of both cases and what distinguishes them.

The first property to start with is the  $n_{eff}$  which is shown in Figure (4.43). The Steiner ES-PCF structure has lower  $n_{eff}$  values than ideal ES-PCF through the entire wavelength window. The field is expanding due to small core size and the field is influenced by the holes in the third ring. In the Steiner structure the holes are extremely large compared to holes in the ideal ES-PCF. Therefore, the field interacts with the holes in the Steiner design. The difference at higher wavelengths is slightly larger as the field interacts more with the holes of the third ring. The dispersion is not calculated but its clear from the  $n_{eff}$  data that both dispersion will be similar as the  $n_{eff}$  curves have similar change trend.

Similarly,  $A_{eff}$  is smaller for the Steiner structure as the field is well confined near the center of the structure. The air filling fraction is smaller in the ideal ES-PCF which leads to the expanding of the field out of the core and hence large effective area. The light is confined more tightly in the Steiner structure, which is an advantage in many applications especially in non-linear applications. The non-linearity depends on  $A_{eff}$  and this is explained in Section (4.1.3).

The differences of the optical properties for two different scenarios with  $\Lambda = 1$  and  $3\mu m$  have been presented in this section. The optical properties do not change at large value of pitch as the field is well confined in the core and the interaction with air of the holes is small so changing the outer holes does not effect the optical properties of the

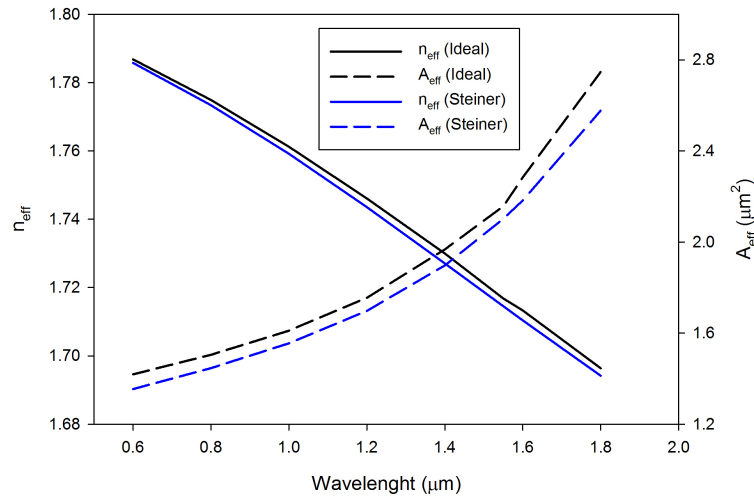


Fig. 4.43 Comparison of  $n_{eff}$  and  $A_{eff}$  for the ideal and Steiner ES-PCF in soft glass SF57 with  $N_{arms} = 6$ ,  $N_{rings} = 3$ ,  $d/\Lambda = 0.4$  and  $\Lambda = 1\mu m$ .

design. Therefore, at higher values of  $\Lambda$  the number of holes does not need to be large as shown in the case studied here.

In conclusion, the Steiner ES-PCF structure has been presented and compared to ideal ES-PCF. The comparison at values of  $\Lambda$  larger than the operating wavelength show almost identical results for both designs with similar structural parameter. In contrast, when  $\Lambda$  is comparable with the operating wavelength or smaller the optical properties differ slightly for both designs. The Steiner pattern shows better confinement of the field. Therefore, the holes in the third ring of the Steiner structure has a positive effect on the properties of the fiber.

A final remark on the outcome of this work is that the Steiner and ideal ES-PCF have proven very good control of dispersion and  $A_{eff}$  by varying the different parameters. The dispersion can be flattened, the ZDW can be either blue or red shifted and/or produce two or more ZDWs. This smooth control of the dispersion is only possible when the index difference is high between the refractive index of the base material and the refractive index of the material of the holes. In all simulations in this thesis the holes were considered to be filled with air which has refractive index of 1 and the base material used in these studies are silica, SF57 soft glass and tellurite, which have refractive index of 1.44, 1.7997 and 1.9354, respectively. In the case of using a material with small refractive index then the dispersion can not be controlled as before.

## 4.5 Summary

In conclusion, the modified ES-PCF which is the focus of this thesis has been explained and simulated to show the benefits of the work done in this project. The relation between dimensional parameters with optical properties has been mentioned in the first section and through out the chapter is emphasized. The variation of most parameters lead to change in the air filling fraction hence modification in the effective refractive index. The field profile depends on the refractive indices of the core and the cladding which is the refractive index profile of the PCF. Therefore any change induced by varying one of the parameters leads to change in the optical properties of the structure. The main optical properties studied in this work are  $n_{eff}$ ,  $A_{eff}$ , dispersion and non-linearity. The small structure size has two advantages; the dispersion is smoothly controlled because interaction of the field with holes is high. The second is that  $A_{eff}$  decreases as the core dimension is reduced but not reaching cut-off. Both of these advantages are in favor to the non-linear effects which requires small  $A_{eff}$  to have high non-linearity and low flat dispersion in the anomalous region with ZDW near the pump. These specification are desirable in SCG.

The results presented in this chapter on Steiner ES-PCF show how to control the various parameters and what is their effect on the optical properties. The most fundamental property is the pitch size which as mention has to be small enough for the field to interact with holes efficiently. Then the rest for parameters are adjusted to have the required optical properties. In this work a design has been optimized with small  $A_{eff}$  and a low flat dispersion in wide wavelength range, published in CLEO2011. This structure is used in a study of SCG and the results have been published in a joint paper in Journal of Modern Optics.

The point discussed after that is the ASaD algorithm. This algorithm is a modification of the conventional SaD which is limited to hexagonal stacking of tubes with similar diameter. These limitations have been overcome and now it is possible to fabricate the Steiner ES-PCF by stacking tubes and rods. The algorithm of fabrication has been published in conference IONs Southampton and IEEE Photonics Technology Letters. The optical properties of the Steiner design have been compared with the ideal spiral. The comparison proved that Steiner and ideal structures have similar results with small variation in some cases when using identical dimensional parameters. The only difference is the holes in the third ring of the Steiner design are shifted further from the center and made larger in size. This have a positive effect as the field is well confined even at small core size. The interest in this work is with small core size of dimensions comparable to the operating wavelength or smaller. The field spreads at

these dimensions and the interaction of the field with holes increases leading to efficient control of the optical properties.

The work done in this project has been introduced in this thesis and the future work to be carried is discussed in the next chapter.

# Chapter 5

## Conclusion and Suggestions for Future Work

In the previous two chapters the results are discussed and followed up by a summary on the results of the chapter. In this chapter, a general summary on the key findings of the entire thesis is presented, at the first part of the chapter, to high light the advantages and limitation of the structures proposed in this work. The second section of this chapter constrained on how the research can be extended for future work to further analyze, simulate and utilize the spiral PCF in other applications.

### 5.1 Conclusion

The work carried in this thesis is aimed to study the optical properties of spirals Photonic Crystal Fibers (PCF) and how they can be implemented in some applications. The study is based on modeling of the structures using numerical method to find the modal field and obtain the optical properties. The method used is the Finite Element Method (FEM) which was chosen because of its versatility in presenting an arbitrary boundaries. The spiral PCF has a complex boundary and requires an efficient mesh to present the structure accurately. Furthermore, the penalty function and the perfectly matched layers used in FEM to limit spurious solutions and absorb non-physical reflected radiations, respectively.

Spirals are natural occurring shapes in variety of creatures ranging from planets, insects, animal, galaxies, etc... These shapes are investigated and presented in mathematical formulae by mathematicians. In this work, the formulae are implemented in codes to simulate the spirals PCFs and study their optical properties. The study comprises of three spirals: Equiangular, Archimedean and Fermat's. In Chapter 3, a systematic

study of varying the parameters of each spiral is carried out to understand to effects of parameters and by analyzing the results the author proposed the best suitable application for each spiral. The three spirals have in common parameters which are pitch and hole size. The Fermat's spiral has the least parameters to vary because the angle between holes is fixed to the Golden Ratio ( $\theta = 222.5^\circ$ ). Therefore, only the previous two parameters and number of holes were varied. The Fermat's spiral have shown large values of birefringence due to a asymmetry of the core. The Archimedean spiral has two other parameters which are varied; the angle between holes and the  $b$  factor which controls the tightness of the spiral (distance between successive turns). The Archimedean spiral is very efficient in hole distribution when the number of holes is large. The Equiangular Spiral (ES) has two parameters which control the number of holes; the number of arms and rings. These can be controlled separately which have advantages and disadvantages. The bad side of this is that not any hole number can be presented efficiently such as prime number of holes is not efficient for ES. The good side of this combination is that the holes are positioned in a symmetric way and can be controlled more freely. The equiangular spiral is manipulated to facilitate the possibilities of fabrication of exotic designs with the traditional Stack and Draw (SaD) technique.

The modified equiangular spiral is studied further to optimize a design for SuperContinuum Generation (SCG). The structures are simulated and results are analyzed and simulation repeated with modification in the parameters to get to the desirable specifications. The requirements for SCG is high non-linearity and small anomalous dispersion. The former is obtained by small effective area. Both properties are controlled efficiently when the pitch size is comparable to the wavelength of operation. The Steiner chain rule is implemented in distribution of holes in the third ring in the proposed structure. The position of the holes in the first two rings has not changed from that in the ideal spiral. The only difference is the holes in the third ring are shifted farther from the center and made more larger in size to better confine the light in the core. A procedure to fabricate the Steiner ES-PCF using SaD is proposed. The procedure is similar to traditional SaD with small changes where tubes size in the proposed procedure are of different sizes and the stacking of tubes is not in a hexagonal packing form. The spirals PCF have shown various superiorities to other PCF in many applications and still much to be investigated and discovered in these unique designs. Some of these applications are the proposed in the next section.

## 5.2 Future Work

This thesis is dedicated to the study of the spiral photonic crystal fibers and to highlight their unique properties over fibers including other microstructured fibers. Photonic crystal fibers in general have many advantages over conventional optical fibers some of which are discussed in the thesis. The basics of fiber optics have been explained in Chapter 1 and the properties of photonic crystal fibers with reference to literature have been given. The methodology is included in Chapter 2 which contains the explanation of the numerical method employed in the simulation, FEM.

The knowledge of the theory and simulation tools has been implemented to study different structures. Some data from this work and predictions show promising results. These results requires more investigation and simulations but due to the huge amount of data and structures simulated the author has included only the relevant information and the complete sets of results which led to publications. The promising information obtained through the period of study of this work are proposed for future work to be carried to investigate the unique undiscovered properties of spiral PCF.

The spiral structures studied in this thesis have proved the diversity of spiral PCF in terms of their properties. Therefore, the spiral structure can be utilized in most of the applications due to different spirals curves that can be adapted and the large number of structural parameters which can be exploited to suit the required specifications.

The focus of this work is on ES-PCF structure which has been employed in non-linear applications. The simulation of ES-PCF to study some of the unique properties have been carried to study different properties. The property that is interesting to study is the single mode condition similar to the H-PCF. A set of results showed that the higher order modes either do not exist or have poor field profile shape. This property can be investigated further to find the parameter range at which the fiber supports single mode operation. It is found that the ratio  $d/\Lambda$  is not the parameter responsible for single mode operation. The angle  $\theta$  is believed to be the parameter that controls the single mode region. This is interesting as the cladding can have large holes and be single mode which is not possible in the H-PCF structure.

High index core guiding spiral PCFs have been investigated and simulation result are published by different groups, but the spiral HC-PCFs have not been studied so far to the best knowledge of the author. Therefore, the spiral can be studied to investigate band-gap guidance.

In normal pressure fiber sensors the orientation of the fiber affects the sensing. Therefore orientation independent fiber sensors would offer advantages in sensing. However,

one of the structured studied in the thesis (AS-PCF) has shown promising results for sensing applications. The results are in the initial stage and require more investigation. The advantage of PCF is the core can be ranged in size from sub micron to large of tens of microns. The large mode area is used for high power delivery and three spirals studied in this thesis are predicted to have LMA with lower losses than H-PCF. The ES-PCF have losses lower than H-PCF and as mentioned the single mode operation depends on angle and not  $d/\Lambda$ . Therefore, the design can have large core with large holes to reduce the losses. Another proposal is to design a structure with large core with high  $N_{arms}$  which is better than having large core with few large holes in the first ring. A large number of small rings would have a better circular shape than using large holes.

The simulations of spiral PCFs have demonstrated their advantages over other PCFs. The theoretical results are presented in the thesis and in published papers of this work but the requirement to validate the results and implement the spiral PCF in the real world requires the fabrication of these fibers. The fabrication of ES-PCF using adaptive stack and draw is presented in this thesis. The fabrication of these fibers will open the horizon for researchers to study the unique properties of spiral PCF and implement them in applications.

Furthermore, there are other spirals which can be studied and implemented in PCF. Each spiral has its unique characteristics and the new spirals may lead to enhancement in the outcome or new applications to be discovered.

# Author Publications

## Journal Papers

- M. R. Karim, B. M. A. Rahman, Y. O. Azabi, A. Agrawal, and G. P. Agrawal, "Ultrabroadband mid-infrared supercontinuum generation through dispersion engineering of chalcogenide microstructured fibers," *JOSA B*, vol. 32, Iss. 11, pp. 2343-2351, 2015.
- A. Agrawal, M. Tiwari, Y. O. Azabi, V. Janyani, B. M. A. Rahman, and K. T. V. Grattan, "Ultrabroad supercontinuum generation in tellurite equiangular spiral photonic crystal fiber," *Journal of Modern Optics*, vol. 60, Iss. 12, pp. 956-962, 2013.
- A. Agrawal, Y. O. Azabi, and B. M. A. Rahman, "Stacking the Equiangular Spiral," *IEEE Photonics Technology Letters*, vol. 25, Iss. 3, pp. 291-294, 2013.

## Conference Papers

- H. Karakuzu, M. Dubov, S. Boscolo, Y. O. Azabi, and A. Agrawal, "Equiangular spiral micro-structured waveguides in lithium niobate," *Proceedings of the XXIII International Workshop on Optical Wave & waveguide Theory and Numerical Modelling (OWTNM 2015)*. London (UK).
- Y. O. Azabi, A. Agrawal, B. M. A. Rahman, and K. T. V. Grattan, "Residual Dispersion Compensation with a Spiral PCF," *Specialty Optical Fibers, Advanced Photonics Congress*, 17-21 June, 2012, Colorado, USA, paper SW4F.
- Y. O. Azabi, A. Agrawal, N. Kejalakshmy, B. M. A. Rahman, and K. T. V. Grattan, "Equiangular spiral tellurite photonic crystal fiber for supercontinuum generation in Mid-Infrared," *CLEO:2011 - Laser Applications to Photonic Applications, OSA Technical Digest (CD) (Optical Society of America, 2011)*, Baltimore, USA, paper JThB72.

- Y. O. Azabi, and A. Agrawal, “Fabrication Technique for Equiangular Spiral PCF,” IONS-10 Southampton, 2011.
- A. Agrawal, N. Kejalakshmy, Y. Azabi, and B. M. A. Rahman, “Spiral photonics crystal fibers: special properties,” SPIE’s International Symposium, Photonics Europe (EPE10), 12-16 April, 2010, Brussels, Belgium.
- B. M. A. Rahman, A. Agrawal, N. Kejalakshmy, M. Uthman, Y. Azabi, and K. T. V. Grattan, “Progress in Finite Element Analysis of Photonic Crystal Fibres,” OWTNM 2010, The XVIIIth International Workshop on Optical Waveguide Theory and Numerical Modelling, 9-10 April, 2010, Cambridge, UK.

# References

- [1] H. A. Haus, "Optical fiber solitons, their properties and uses," *Proceedings of the IEEE*, vol. 81, no. 7, pp. 970–983, 1993.
- [2] E. A. Golovchenko, A. N. Pilipetskii, N. S. Bergano, C. R. Davidson, F. I. Khatri, R. M. Kimball, and V. J. Mazurczyk, "Modeling of transoceanic fiber-optic WDM communication systems," *IEEE Journal of Selected Topics in Quantum Electronics*, vol. 6, no. 2, pp. 337–347, 2000.
- [3] P. W. Shumate, "Fiber-to-the-Home: 1977–2007," *Journal of Lightwave Technology*, vol. 26, no. 9, pp. 1093–1103, 2008.
- [4] B. Lee, "Review of the present status of optical fiber sensors," *Optical Fiber Technology*, vol. 9, no. 2, pp. 57–79, 2003.
- [5] T. G. Giallorenzi, J. A. Bucaro, A. Dandridge, G. H. Sigel, J. J. H. Cole, S. C. Rkshleigh, and R. G. Priest, "Optical fiber sensor technology," *IEEE Journal of Quantum Electronics*, vol. QE-18, no. 4, pp. 626–665, 1982.
- [6] R. J. Mears, L. Reekie, I. M. Jauncey, and D. N. Payne, "Low-noise erbium-doped fiber amplifier operating at 1.54 $\mu\text{m}$ ," *Electronics Letters*, vol. 23, no. 19, pp. 1026–1028, 1987.
- [7] A. Mendez and T. Morse, *Specialty Optical Fibers Handbook*. Elsevier, 2007.
- [8] M. Bass, C. DeCusatis, J. Enoch, V. Lakshminarayanan, G. Li, C. MacDonald, V. Mahajan, and E. V. Stryland, *Handbook of Optics, Volume V: Atmospheric Optics, Modulators, Fiber Optics, X-Ray and Neutron Optics*. 3 ed., 2009.
- [9] S. A. Claypoole and D. C. Wilhelm, "Buffered optical waveguide fiber," Feb 1978.
- [10] R. P. Khare, *Fiber Optics and Optoelectronic*. Oxford University Press, 2004.
- [11] M. H. Weik, *Fiber Optics Standard Dictionary*. New York: Chapman & Hall, 1997.
- [12] I. H. Malitson, "Interspecimen comparison of the refractive index of fused silica," *Journal of the Optical Society of America*, vol. 55, no. 10, pp. 1205–1209, 1965.
- [13] J. K. Ranka, R. S. Windeler, and A. J. Stentz, "Visible continuum generation in air–silica microstructure optical fibers with anomalous dispersion at 800 nm," *Optics Letters*, vol. 25, no. 1, pp. 25–27, 2000.
- [14] F. Mitschke, *Fiber Optics Physics and Technology*. Springer-Verlag, 2009.

- [15] R. S. Quimby, *Photonics and Lasers: An Introduction*. John Wiley & Sons, 2006.
- [16] K. Thyagarajan and A. Ghatak, *Fiber Optic Essentials*. New Jersey: John Wiley & Sons, 2007.
- [17] A. Zheltikov, A. L'Huillier, and F. Krausz, *Springer Handbook of Lasers and Optics*, ch. 5, pp. 157–248. Springer, 2007. Nonlinear Optics.
- [18] R. Paschotta, “article on ‘silica fibers’ in the encyclopedia of laser physics and technology.” [http://www.rp-photonics.com/silica\\_fibers.html](http://www.rp-photonics.com/silica_fibers.html), 05 2015. Accessed: 2017-11-15.
- [19] J. B. MacChesney and P. B. O’Connor, “Optical fiber fabrication and resulting product,” Aug 1980.
- [20] S. R. Nagel, J. B. MacChesney, and K. L. Walker, “An overview of the Modified Chemical Vapor Deposition (MCVD) process and Performance,” *IEEE Journal of Quantum Electronics*, vol. QE-18, no. 4, pp. 459–476, 1982.
- [21] T. Izawa, T. Miyashita, and F. Hanawa, “Continuous optical fiber preform fabrication method,” Dec 1977.
- [22] D. Kuppers, J. Koenings, and H. Wilson, “Codeposition of glassy silica and germania inside a tube by plasma-activated CVD,” *Journal of Electrochemical Society*, vol. 123, no. 7, pp. 1079–1083, 1976.
- [23] R. Paschotta, “article on ‘V Number’ in the Encyclopedia of Laser Physics and Technology.” [https://www.rp-photonics.com/v\\_number.html](https://www.rp-photonics.com/v_number.html), (accessed 16/07/2017).
- [24] L. B. Jeunhomme, *Single-Mode Fiber Optics: Principles and Applications*. New York: Marcel Dekker Inc., 2nd ed., 1990.
- [25] D. Gloge, “Weakly guiding fibers,” *Applied Optics*, vol. 10, no. 10, pp. 2252–2258, 1971.
- [26] C.-L. Chen, *Foundations for Guided-Wave Optics*. John Wiley & Sons, 2007.
- [27] N. Shibata, K. Okamoto, K. Suzuki, and Y. Ishida, “Polarization-mode properties of elliptical-core fibers and stress-induced birefringent fibers,” *Journal of the Optical Society of America*, vol. 73, no. 12, pp. 1792–1798, 1983.
- [28] M. P. Varnham, D. D. Payne, R. D. Birch, and E. J. Tarbox, “Single-polarisation operation of highly birefringent bow-tie optical fibres,” *Electronics Letters*, vol. 19, pp. 246–247, 1983.
- [29] Y. Sasaki, K. Okamoto, T. Hosaka, and N. Shibata, “Polarization-maintaining and absorption-reducing fibers,” *Conference on Optical Fiber Communication (OFC)*, p. ThCC6, April 1982.
- [30] K. Okamoto, *Fundamentals of Optical Waveguides*. London: Academic Press, 2nd ed., 2006.
- [31] M. Azadeh, *Fiber Optics Engineering*. Springer, 2009.

- [32] G. P. Agrawal, *Nonlinear Fiber Optics*. New York: Academic Press, 4th ed., 2007.
- [33] R. Tricker, *Optoelectronics and Fiber Optic Technology*. Oxford: Newnes, 2002.
- [34] B. E. A. Saleh and M. C. Teich, *Fundamentals of Photonics*. New York: John Wiley & Sons, 1991.
- [35] J. M. Senior and M. Y. Jamro, *Optical Fiber Communications Principles and Practice*. London: Pearson Education Limited, 2009.
- [36] R. T. Schermer and J. H. Cole, "Improved bend loss formula verified for optical fiber by simulation and experiment," *IEEE Journal of Quantum Electronics*, vol. 43, no. 10, pp. 899–909, 2007.
- [37] T. M. Monro and H. Ebendorff-Heidepriem, "Progress in microstructured optical fibers," *Annual Review of Materials Research*, vol. 36, no. 1, pp. 467–495, 2006.
- [38] A. Argyros, R. Lwin, and M. C. Large, "Bend loss in highly multimode fibres," *Optics Express*, vol. 16, no. 23, pp. 18590–18598, 2008.
- [39] G. Agrawal, *Nonlinear Fiber Optics*. Oxford: Elsevier, 2013.
- [40] "Thorlabs." <https://www.google.co.uk/imghp?hl=en&tab=wi>. Accessed: 15/11/2017.
- [41] D. J. DiGiovanni, S. K. Das, L. L. Blyler, W. White, R. K. Boncek, and S. E. Golowich, "Chapter 2 - design of optical fibers for communications systems," in *Optical Fiber Telecommunications IV-A* (I. P. Kaminow, , and T. Li, eds.), Optics and Photonics, pp. 17 – 79, Burlington: Academic Press, 4 ed., 2002.
- [42] M. Brodsky, N. J. Frigo, M. Boroditsky, and M. Tur, "Polarization mode dispersion of installed fibers," *Journal of Lightwave Technology*, vol. 24, no. 12, pp. 4584–4599, 2006.
- [43] E. H. LeeK, H. Kim, and H. K. Lee, "Nonlinear effects in optical fiber: Advantages and disadvantages for high capacity all-optical communication application," *Optical and Quantum Electronics*, vol. 34, no. 12, pp. 1167–1174, 2002.
- [44] A. Barh, B. P. Pal, G. P. Agrawal, R. K. Varshney, and B. M. A. Rahman, "Specialty fibers for terahertz generation and transmission: A review," *IEEE Journal of Selected Topics in Quantum Electronics*, vol. 22, no. 2, pp. 365–379, 2016.
- [45] M. Ebrahimzadeh, "Parametric light generation," *Philosophical Transactions of the Royal Society of London A: Mathematical, Physical and Engineering Sciences*, vol. 361, no. 1813, pp. 2731–2750, 2003.
- [46] M. R. Karim, *Design and optimization of chalcogenide waveguides for supercontinuum generation*. PhD thesis, City University London, School of Mathematics, Computing Science & Engineering, 2015.
- [47] C. Thiel, "Four-wave mixing and its applications," *Faculty of Washington, Washington DC*, 2008.

- [48] J. M. Dudley, G. Genty, and S. Coen, "Supercontinuum generation in photonic crystal fiber," *Reviews of Modern Physics*, vol. 78, pp. 1135–1184, 2006.
- [49] F. Shimizu, "Frequency broadening in liquids by a short light pulse," *Physical Review Letters*, vol. 19, no. 19, pp. 1097–1100, 1967.
- [50] R. R. Alfano, *The supercontinuum laser source: fundamentals with updated references*. New York: Springer, 2006.
- [51] E. P. Ippen, C. V. Shank, and T. K. Gustafson, "Self-phase modulation of picosecond pulses in optical fibers," *Applied Physics Letters*, vol. 24, no. 4, pp. 190–192, 1974.
- [52] R. H. Stolen and C. Lin, "Self-phase-modulation in silica optical fibers," *Physical Review A*, vol. 17, no. 4, pp. 1448–1453, 1978.
- [53] Y. S. Kivshar and G. Agrawal, *Optical Solitons: From Fibers to Photonic Crystals*. New York: Academic Press, 2003.
- [54] "Soliton (optics)." [https://en.wikipedia.org/wiki/Soliton\\_\(optics\)](https://en.wikipedia.org/wiki/Soliton_(optics)). Accessed: 15/11/2017.
- [55] C. Lin, W. Reed, A. Pearson, H.-T. Shang, and P. Glodis, "Designing single-mode fibres for near-ir (1.1–1.7  $\mu\text{m}$ ) frequency generation by phase-matched four-photon mixing in the minimum chromatic dispersion region," *Electronics Letters*, vol. 18, no. 2, pp. 87–89, 1982.
- [56] N. Shibata, K. Nosu, K. Iwashita, and Y. Azuma, "Transmission limitations due to fiber nonlinearities in optical fdm systems," *IEEE Journal on Selected Areas in Communications*, vol. 8, no. 6, pp. 1068–1077, 1990.
- [57] K. O. Hill, B. S. Kawasaki, and D. C. Johnson, "cw Brillouin laser," *Applied Physics Letters*, vol. 28, no. 10, pp. 608–609, 1976.
- [58] R. K. Jain, C. Lin, R. H. Stolen, W. Pleibel, and P. Kaiser, "A high-efficiency tunable cw Raman oscillator," *Applied Physics Letters*, vol. 30, no. 3, pp. 162–164, 1977.
- [59] D. C. Johnson, K. O. Hill, B. S. Kawasaki, , and D. Kato, "Tunable Raman fibre-optic laser," *Electronics Letters*, vol. 13, no. 2, pp. 53–55, 1977.
- [60] C. Lin and R. H. Stolen, "Backward Raman amplification and pulse steepening in silica fibers," *Applied Physics Letters*, vol. 29, no. 7, pp. 428–431, 1976.
- [61] M. Ikeda, "Stimulated Raman amplification characteristics in long span single-mode silica fibers," *Optics Communications*, vol. 39, no. 3, pp. 148–152, 1981.
- [62] Y. Aoki, S. Kishida, H. Honmou, K. Washio, and M. Sugimoto, "Efficient backward and forward pumping CW Raman amplification for InGaAsP laser light in silica fibres," *Electronics Letters*, vol. 19, no. 16, pp. 620–622, 1983.
- [63] R. R. Alfano and S. L. Shapiro, "Emission in the region 4000 to 7000  $\text{\AA}$  via four-photon coupling in glass," *Physical Review Letters*, vol. 24, no. 11, pp. 584–587, 1970.

- [64] R. R. Alfano and S. L. Shapiro, "Observation of self-phase modulation and small-scale filaments in crystals and glasses," *Physical Review Letters*, vol. 24, no. 11, pp. 592–594, 1970.
- [65] N. G. Bondarenko, I. V. Eremina, and V. I. Talanov, "Broadening of spectrum in self-focusing of light in crystals," *Soviet Journal of Experimental and Theoretical Physics Letters*, vol. 12, pp. 85–87, 1970.
- [66] B. P. Stoicheff, "Characteristics of stimulated Raman radiation generated by coherent light," *Physics Letters*, vol. 7, no. 3, pp. 186–188, 1963.
- [67] W. J. Jones and B. P. Stoicheff, "Inverse Raman spectra: Induced absorption at optical frequencies," *Physical Review Letters*, vol. 13, no. 22, pp. 657–659, 1964.
- [68] R. G. Brewer, "Frequency shifts in self-focused light," *Physical Review Letters*, vol. 19, no. 1, pp. 8–10, 1967.
- [69] R. H. Stolen, C. Lee, and R. K. Jain, "Development of the stimulated raman spectrum in single-mode silica fibers," *Journal of the Optical Society of America B*, vol. 1, no. 4, p. 652–657, 1984.
- [70] I. Ilev, H. Kumagai, K. Toyoda, and I. Koprnikov, "Highly efficient wideband continuum generation in a singlemode optical fiber by powerful broadband laser pumping," *Applied Optics*, vol. 35, no. 15, p. 2548–2553, 1996.
- [71] P. L. Baldeck, , and R. R. Alfano, "Intensity effects on the stimulated four photon spectra generated by picosecond pulses in optical fibers," *Journal of Lightwave Technology*, vol. 5, no. 12, pp. 1712–1715, 1987.
- [72] D. Mogilevtsev, T. A. Birks, and P. S. J. Russell, "Group-velocity dispersion in photonic crystal fibers," *Optics Letters*, vol. 23, no. 21, pp. 1662–1664, 1998.
- [73] N. G. R. Broderick, T. M. Monro, P. J. Bennett, and D. J. Richardson, "Nonlinearity in holey optical fibers: Measurement and future opportunities," *Optics Letters*, vol. 24, no. 20, pp. 1395–1397, 1999.
- [74] P. S. J. Russell, "Photonic crystal fibers," *Journal of Lightwave Technology*, vol. 24, no. 12, pp. 4729–4749, 2006.
- [75] T. A. Birks, W. J. Wadsworth, and P. S. J. Russell, "Supercontinuum generation in tapered fibers," *Optics Letters*, vol. 25, no. 19, pp. 1415–1417, 2000.
- [76] S. Coen, A. H. L. Chau, R. Leonhardt, J. D. Harvey, J. C. Knight, W. J. Wadsworth, and P. S. J. Russell, "White-light supercontinuum generation with 60-ps pump pulses in a photonic crystal fiber," *Optics Letters*, vol. 26, no. 17, pp. 1356–1358, 2001.
- [77] C. Sibilia, T. Benson, M. Marciniak, and T. Szoplik, eds., *Nonlinear Optics with Photonic-Crystal Fibres*, vol. A. M. Zheltikov of *Photonic Crystals: Physics and Technology*. Springer-Verlag, 2008.
- [78] P. Russell, "Photonic crystal fibers," *Science*, vol. 299, pp. 358–362, 2003.

- [79] J. C. Knight, T. A. Birks, P. S. Russell, and D. M. Atkin, "All-silica single-mode optical fiber with photonic crystal cladding," *Optics Letters*, vol. 21, no. 19, p. 1547–1549, 1996.
- [80] T. A. Birks, J. C. Knight, and P. S. J. Russell, "Endlessly single-mode photonic crystal fiber," *Optics Letters*, vol. 22, no. 13, pp. 961–963, 1997.
- [81] J. C. Knight, J. Arriaga, T. A. Birks, A. Ortigosa-Blanch, W. J. Wadsworth, and P. S. J. Russell, "Anomalous dispersion in photonic crystal fiber," *IEEE Photonics Technology Letters*, vol. 12, no. 7, pp. 807–809, 2000.
- [82] J. C. Knight, T. A. Birks, R. F. Cregan, P. S. J. Russell, and P. D. de Sandro, "Large mode area photonic crystal fiber," *Electronics Letters*, vol. 34, no. 13, p. 1347–1348, 1998.
- [83] R. F. Cregan, B. J. Mangan, J. C. Knight, T. A. Birks, P. S. Russell, P. J. Roberts, and D. C. Allan, "Singlemode photonic band gap guidance of light in air," *Science*, vol. 285, no. 5433, p. 1537–1539, 1999.
- [84] B. J. Mangan, J. C. Knight, T. A. Birks, P. S. J. Russell, and A. H. Greenaway, "Experimental study of dualcore photonic crystal fibre," *Electronics Letters*, vol. 36, no. 16, p. 1358–1359, 2000.
- [85] A. Ortigosa-Blanch, A. Diez, M. Delgado-Pinar, J. L. Cruz, and M. V. Andres, "Ultrahigh birefringent nonlinear microstructured fiber," *IEEE Photonics Technology Letters*, vol. 16, no. 7, pp. 1667–1669, 2004.
- [86] F. Zolla, G. Renversez, A. Nicolet, B. Kuhlmeiy, S. Guenneau, and D. Felbacq, *Foundations of Photonic Crystal Fibres*. London: Imperial College Press, 2005.
- [87] J. Knight, T. Birks, P. Russell, and D. Atkin, "Pure silica singlemode fiber with hexagonal photonic crystal cladding," *Conference on Optical Fiber Communication (OFC)*, p. PD3, Mar. 1996.
- [88] J. C. Knight, "Photonic crystal fibers," *Nature*, vol. 424, pp. 847–851, 2003.
- [89] O. G. Okhotnikov, *Fiber Lasers*. Wiley-VCH Verlag GmbH & Co. KGaA, 2012.
- [90] G. Vienne, Y. Xu, C. Jakobsen, H.-J. Deyerl, J. B. Jensen, T. Sorensen, T. P. Hansen, Y. Huang, M. Terrel, R. K. Lee, N. A. Mortensen, J. Broeng, H. Simonsen, A. Bjarklev, and A. Yariv, "Ultra-large bandwidth hollow-core guiding in all-silica bragg fibers with nano-supports," *Optics Express*, vol. 12, no. 15, pp. 3500–3508, 2004.
- [91] S. John, "Strong localization of photons in certain disordered dielectric superlattices," *Physical Review Letters*, vol. 58, no. 23, pp. 2486–2489, 1987.
- [92] E. Yablonovitch, "Inhibited spontaneous emission in solid-state physics and electronics," *Physical Review Letters*, vol. 58, no. 20, pp. 2059–2062, 1987.
- [93] E. Yablonovitch and T. J. Gmitter, "Photonic band structure: The face-centered-cubic case," *Physical Review Letters*, vol. 63, no. 18, pp. 1950–1953, 1989.
- [94] E. Yablonovitch, "Photonic crystals: What's in a name?," *Optics and Photonics News*, vol. 18, pp. 12–13, 2007.

- [95] F. Poli, A. Cucinotta, and S. Selleri, *Photonic Crystal Fibers: Properties and Applications*. Springer, 2007.
- [96] W. Belardi and J. C. Knight, “Effect of core boundary curvature on the confinement losses of hollow antiresonant fibers,” *Optics Express*, vol. 21, no. 19, pp. 21912–21917, 2013.
- [97] M. A. Duguay, Y. Kokubun, T. L. Koch, and L. Pfeiffer, “Antiresonant reflecting optical waveguides in SiO<sub>2</sub>/Si multilayer structures,” *Applied Physics Letters*, vol. 49, no. 1, pp. 13–15, 1986.
- [98] F. Benabid, J. C. Knight, G. Antonopoulos, and P. S. J. Russell, “Stimulated raman scattering in hydrogen-filled hollow-core photonic crystal fiber,” *Science*, vol. 298, no. 5592, pp. 399–402, 2002.
- [99] Y. Wang, F. Couny, P. J. Roberts, and F. Benabid, “Low Loss Broadband Transmission In Optimized Core-shape Kagome Hollow-core PCF,” in *Conference on Lasers and Electro-Optics 2010*, p. CPDB4, Optical Society of America, 2010.
- [100] J. C. Knight, T. A. Birks, P. S. Russell, and J. P. de Sandro, “Properties of photonic crystal fiber and the effective index model,” *Journal of the Optical Society of America A*, vol. 15, no. 3, pp. 748–752, 1998.
- [101] F. Brechet, P. Roy, J. Marcou, and D. Pagnoux, “Single mode propagation in depressed-core-index photonic-bandgap fiber designed for zero-dispersion propagation at short wavelengths,” *Electronics Letters*, vol. 36, no. 6, pp. 514–515, 2000.
- [102] J. C. Knight, J. Broeng, T. A. Birks, and P. S. Russell, “Photonic band gap guidance in optical fibers,” *Science*, vol. 282, no. 5393, pp. 1476–1478, 1998.
- [103] P. J. Roberts, F. Couny, H. Sabert, B. J. Mangan, D. P. Williams, L. Farr, M. W. Mason, A. Tomlinson, T. A. Birks, J. C. Knight, and P. S. J. Russell, “Ultimate low loss of hollow-core photonic crystal fibers,” *Optics Express*, vol. 13, no. 1, pp. 236–244, 2005.
- [104] F. Benabid and P. J. Roberts, “Linear and nonlinear optical properties of hollow core photonic crystal fiber,” *Journal of Modern Optics*, vol. 58, no. 2, pp. 87–124, 2011.
- [105] F. Yu, *Hollow core negative curvature optical fibers*. PhD thesis, University of Bath, Department of Physics, 2013.
- [106] NTK Photonics, “article on ‘Photonic crystal fibers’ in NTK Photonics.” <https://www.nktphotonics.com/lasers-fibers/technology/photonic-crystal-fibers/>, (accessed 16/07/2015).
- [107] V. N. Melekin and A. B. Manenkov, “Dielectric tube as low-loss waveguide,” *Soviet physics*, vol. 13, no. 12, pp. 1698–1699, 1968.
- [108] S. G. Johnson, M. Ibanescu, M. Skorobogatiy, O. Weisberg, T. D. Engeness, M. Soljacic, S. A. Jacobs, J. D. Joannopoulos, and Y. Fink, “Low-loss asymptotically single-mode propagation in large-core omniguide fiber,” *Optics Express*, vol. 19, no. 13, pp. 748–779, 2001.

- [109] F. Couny, F. Benabid, and P. S. Light, "Large-pitch kagome-structured hollow-core photonic crystal fiber," *Optics Letters*, vol. 31, no. 24, pp. 3574–3576, 2006.
- [110] F. Gerome, R. Jamier, J. Auguste, G. Humbert, and J. Blondy, "Simplified hollow-core photonic crystal fiber," *Optics Letters*, vol. 35, no. 8, pp. 1157–1159, 2010.
- [111] F. Benabid, P. J. Roberts, F. Couny, and P. S. Light, "Light and gas confinement in hollow-core photonic crystal fibre based photonic microcells,"
- [112] J. Anthony, R. Leonhardt, S. G. Leon-Saval, and A. Argyros, "THz propagation in kagome hollow-core microstructured fibers," *Optics Express*, vol. 19, no. 19, p. 18470–18478, 2011.
- [113] R. Kitamura, L. Pilon, and M. Jonasz, "Optical constants of silica glass from extreme ultraviolet to far infrared at near room temperature," *Applied Optics*, vol. 46, no. 33, pp. 8118–8133, 2007.
- [114] W. Belardi and J. C. Knight, "Hollow antiresonant fibers with reduced attenuation," *Optics Letters*, vol. 39, no. 7, p. 1853–1856, 2014.
- [115] A. Urich, R. Maier, F. Yu, J. Knight, D. Hand, and J. Shephard, "Silica hollow core microstructured fibres for mid-infrared surgical applications," *Journal of Non-Crystalline Solids*, vol. 377, p. 236–239, 2013.
- [116] J. D. Shephard, A. Urich, R. M. Carter, P. Jaworski, R. R. J. Maier, W. Belardi, F. Yu, W. J. Wadsworth, J. C. Knight, and D. P. Hand, "Silica hollow core microstructured fibers for beam delivery in industrial and medical applications," *Frontiers in Physics*, vol. 3, p. article 10, 2015.
- [117] P. Jaworski, F. Yu, R. M. Carter, J. C. Knight, J. D. Shephard, , and D. P. Hand, "High energy green nanosecond and picosecond pulse delivery through a negative curvature fiber for precision micromachining," *Optics Express*, vol. 23, no. 7, p. 8498–8506, 2015.
- [118] F. Yu and J. C. Knight, "Negative curvature hollow-core optical fiber," *IEEE Journal of Selected Topics in Quantum Electronics*, vol. 22, no. 2, pp. 146–155, 2016.
- [119] F. Poli, M. Foroni, M. Bottacini, M. Fuochi, N. Burani, L. Rosa, A. Cucinotta, and S. Selleri, "Single-mode regime of square-lattice photonic crystal fibers," *Journal of the Optical Society of America A*, vol. 22, no. 8, pp. 1655–1661, 2005.
- [120] K. Saitoh, M. Koshiba, T. Hasegawa, and E. Sasaoka, "Chromatic dispersion control in photonic crystal fibers: application to ultra-flattened dispersion," *Optics Express*, vol. 11, no. 8, p. 843–851, 2003.
- [121] J. Y. Y. Leong, P. Petropoulos, J. H. V. Price, H. Ebendorff-Heidepriem, S. Asimakis, R. C. Moore, K. E. Frampton, V. Finazzi, X. Feng, T. M. Monro, and D. J. Richardson, "High-nonlinearity dispersion-shifted lead-silicate holey fibers for efficient  $1 - \mu\text{m}$  pumped supercontinuum generation," *Journal of Lightwave Technology*, vol. 24, no. 1, pp. 183–190, 2006.

- [122] K. Suzuki, H. Kubota, S. Kawanishi, M. Tanaka, and M. Fujita, "Optical properties of a low-loss polarization-maintaining photonic crystal fiber," *Optics Express*, vol. 9, no. 13, pp. 676–680, 2001.
- [123] M. J. Steel and R. M. Osgood, "Elliptical-hole photonic crystal fibers," *Optics Letters*, vol. 26, no. 4, pp. 229–231, 2001.
- [124] A. Ortigosa-Blanch, J. C. Knight, W. J. Wadsworth, J. Arriaga, B. J. Mangan, T. A. Birks, and P. S. J. Russell, "Highly birefringent photonic crystal fibers," *Optics Letters*, vol. 25, no. 18, pp. 1325–1327, 2000.
- [125] T. P. Hansen, J. Broeng, S. E. B. Libori, E. Knudsen, A. Bjarklev, J. R. Jensen, and H. Simonsen, "Highly birefringent index-guiding photonic crystal fibers," *IEEE Photonics Technology Letters*, vol. 13, no. 6, pp. 588–590, 2001.
- [126] W. S. Wong, X. Peng, J. M. McLaughlin, and L. Dong, "Breaking the limit of maximum effective area for robust single-mode propagation in optical fibers," *Optics Letters*, vol. 30, no. 21, pp. 2855–2857, 2005.
- [127] S. Kabir, M. R. H. Khandokar, and M. A. G. Khan, "Design of triangular core LMA-PCF with low-bending loss and low non-linearity for laser application," *Optics & Laser Technology*, vol. 81, pp. 84–89, 2016.
- [128] T. Sorensen, J. Broeng, A. Bjarklev, E. Knudsen, S. E. B. Libori, H. R. Simonsen, and J. R. Jensen, "Macrobending loss properties of photonic crystal fibres with different air filling fractions," in *Proceedings 27th European Conference on Optical Communication (Cat. No.01TH8551)*, vol. 3, pp. 380–381, 2001.
- [129] M. J. Gander, R. McBride, J. D. C. Jones, D. Mogilevtsev, T. A. Birks, J. C. Knight, and P. S. J. Russell, "Experimental measurement of group velocity dispersion in photonic crystal fiber," *Electronics Letters*, vol. 35, no. 1, pp. 63–64, 1999.
- [130] T. A. Birks, D. Mogilevtsev, J. C. Knight, and P. S. J. Russell, "Dispersion compensation using single-material fibers," *IEEE Photonics Technology Letters*, vol. 11, no. 6, pp. 674–676, 1999.
- [131] W. J. Wadsworth, J. C. Knight, A. Ortigosa-Blanch, J. Arriaga, E. Silvestre, and P. S. J. Russell, "Soliton effects in photonic crystal fibers at 850 nm," *Electronics Letters*, vol. 36, no. 1, pp. 53–55, 2000.
- [132] R. Sinha and S. Varshney, "Dispersion properties of photonic crystal fibers," *Microwave and Optical Technology Letters*, vol. 37, no. 2, pp. 129–132, 2003.
- [133] Y. Ni, L. Zhang, L. An, J. Peng, and C. Fan, "Dual-core photonic crystal fiber for dispersion compensation," *IEEE Photonics Technology Letters*, vol. 16, no. 6, pp. 1516–1518, 2004.
- [134] F. Gerome, J. Auguste, and J. Blondy, "Design of dispersion-compensating fibers based on a dual-concentric-core photonic crystal fiber," *Optics Letters*, vol. 29, no. 23, p. 2725–2727, 2004.

- [135] J. M. Hsu, C. W. Yao, and J. Z. Chen, "Wavelength-tunable dispersion compensating photonic crystal fibers suitable for conventional/coarse wavelength division multiplexing systems," *Journal of Lightwave Technology*, vol. 33, no. 11, pp. 2240–2245, 2015.
- [136] B. L. Wang and J. M. Hsu, "Broadband dispersion compensating photonic crystal fiber with a high compensation ratio," in *2016 International Conference on Advanced Materials for Science and Engineering (ICAMSE)*, pp. 479–481, Nov 2016.
- [137] A. Ferrando, E. Silvestre, and P. Andres, "Designing the properties of dispersion flattened photonic crystal fibers," *Optics Express*, vol. 9, no. 13, p. 687–697, 2001.
- [138] W. H. Reeves, J. C. Knight, and P. S. J. Russell, "Demonstration of ultra-flattened dispersion in photonic crystal fibers," *Optics Express*, vol. 10, no. 14, pp. 609–613, 2002.
- [139] J. H. V. Price, K. Furusawa, T. M. Monroe, L. Lefort, and D. J. Richardson, "Tunable, femtosecond pulse source operating in the range 1.06 – 1.33 $\mu\text{m}$  based on an Yb<sup>3+</sup>-doped holey fiber amplifier," *Journal of the Optical Society of America B*, vol. 19, no. 6, pp. 1286–1294, 2002.
- [140] W. Belardi, J. H. Lee, K. Furusawa, Z. Yusoff, P. Petropoulos, M. Ibsen, T. M. Monroe, and D. J. Richardson, "A 10GBIT/S Tuneable Wavelength Converter Based on Four-Wave MIXING in Highly Nonlinear Holey Fibre," in *2002 28th European Conference on Optical Communication*, vol. 5, pp. 1–2, 2002.
- [141] J. Y. Leong, P. Petropoulos, S. Asimakis, H. Ebendorff-Heidepriem, R. C. Moore, K. Frampton, V. Finazzi, X. Feng, J. H. Price, T. M. Monroe, and D. J. Richardson, "A Lead Silicate Holey Fiber with  $\gamma = 1820\text{W}^{-1}\text{km}^{-1}$  at 1550 nm," in *Optical Fiber Communication Conference and Exposition and The National Fiber Optic Engineers Conference*, p. PDP22, 2005.
- [142] D. G. Ouzounov, F. R. Ahmad, D. Müller, N. Venkataraman, M. T. Gallagher, M. G. Thomas, J. Silcox, K. W. Koch, and A. L. Gaeta, "Generation of Megawatt optical solitons in hollow-core photonic band-gap fibers," *Science*, vol. 301, no. 5640, pp. 1702–1704, 2003.
- [143] O. Frazao, J. M. Baptista, and J. L. Santos, "Temperature-independent strain sensor based on a Hi-Bi photonic crystal fiber loop mirror," *IEEE Sensors Journal*, vol. 7, no. 10, pp. 1453–1455, 2007.
- [144] C. feng Fan, C. lun Chiang, and C. ping Yu, "Birefringent photonic crystal fiber coils and their application to transverse displacement sensing," *Optics Express*, vol. 19, no. 21, pp. 19948–19954, 2011.
- [145] C. Caillaud, C. Gilles, L. Provino, L. Brilland, T. Jouan, S. Ferre, M. Carras, M. Brun, D. Mechin, J.-L. Adam, and J. Troles, "Highly birefringent chalcogenide optical fiber for polarization-maintaining in the 3 – 8.5 $\mu\text{m}$  mid-IR window," *Optics Express*, vol. 24, no. 8, pp. 7977–7986, 2016.
- [146] A. Yin and L. Xiong, "Novel single-mode and polarization maintaining photonic crystal fiber," *Infrared Physics & Technology*, vol. 67, pp. 148–154, 2014.

- [147] D. Kim and J. U. Kang, "Sagnac loop interferometer based on polarization maintaining photonic crystal fiber with reduced temperature sensitivity," *Optics Express*, vol. 12, no. 19, pp. 4490–4495, 2004.
- [148] M. Fuochi, J. Hayes, K. Furusawa, W. Belardi, J. Baggett, T. Monro, and D. Richardson, "Polarization mode dispersion reduction in spun large mode area silica holey fibres," *Optics Express*, vol. 12, no. 9, pp. 1972–1977, 2004.
- [149] S. Gowre, S. Mahapatra, S. Varshney, and P. Sahu, "Dispersion characteristics of all-glass photonic crystal fibers," *Optik - International Journal for Light and Electron Optics*, vol. 124, no. 18, pp. 3730–3733, 2013.
- [150] V. V. R. K. Kumar, A. K. George, W. H. Reeves, J. C. Knight, P. S. J. Russell, F. Omenetto, and A. J. Taylor, "Extruded soft glass photonic crystal fiber for ultrabroad supercontinuum generation," *Optics Express*, vol. 10, no. 25, pp. 1520–1525, 2002.
- [151] K. M. Kiang, K. Frampton, T. M. Monro, R. Moore, J. Tucknott, D. W. Hewak, D. J. Richardson, and H. N. Rutt, "Extruded singlemode non-silica glass holey optical fibres," *Electronics Letters*, vol. 38, no. 12, pp. 546–547, 2002.
- [152] T. M. Monro, K. M. Kiang, J. H. Lee, K. Frampton, Z. Yusoff, R. Moore, J. Tucknott, D. W. Hewak, H. N. Rutt, and D. J. Richardson, "High nonlinearity extruded single-mode holey optical fibers," in *Optical Fiber Communication Conference and Exhibit*, pp. FA1–1–FA1–3, Mar 2002.
- [153] T. M. Monro, Y. D. West, D. W. Hewak, N. G. R. Broderick, and D. J. Richardson, "Chalcogenide holey fibres," *Electronics Letters*, vol. 36, no. 24, pp. 1998–2000, 2000.
- [154] M. A. van Eijkelenborg, M. C. J. Large, A. Argyros, J. Zagari, S. Manos, N. A. Issa, I. Bassett, S. Fleming, R. C. McPhedran, C. M. de Sterke, and N. A. Nicorovici, "Microstructured polymer optical fibre," *Optics Express*, vol. 9, no. 7, pp. 319–327, 2001.
- [155] V. V. R. K. Kumar, A. K. George, J. C. Knight, and P. S. J. Russell, "Tellurite photonic crystal fiber," *Optics Express*, vol. 11, no. 20, pp. 2641–2645, 2003.
- [156] P. Kaiser and H. W. Astle, "Low loss single material fibers made from pure fused silica," *The Bell System Technical Journal*, vol. 53, no. 6, p. 1021–1039, 1974.
- [157] B. Temelkuran, S. D. Harts, G. Benoit, J. D. Joannopoulos, and Y. Fink, "Wavelength-scalable hollow optical fibres with large photonic bandgaps for CO<sub>2</sub> laser transmission," *Nature*, vol. 420, pp. 650–653, 2002.
- [158] H. E. Hamzaoui, L. Bigot, G. Bouwmans, I. Razdobreev, M. Bouzaoui, and B. Capoen, "From molecular precursors in solution to microstructured optical fiber: a sol-gel polymeric route," *Optical Materials Express*, vol. 1, no. 2, pp. 234–242, 2011.
- [159] K. Cook, G. Balle, J. Canning, L. Chartier, T. Athanaze, M. A. Hossain, C. Han, J.-E. Comatti, Y. Luo, and G.-D. Peng, "Step-index optical fiber drawn from 3D printed preforms," *Optics Letters*, vol. 41, no. 19, pp. 4554–4557, 2016.

- [160] P. Pureza, V. Q. Nguyen, F. Kung, and I. D. Aggarwal, "Nonlinear properties of chalcogenide glass fibers," *Journal of Optoelectronics and Advanced Materials*, vol. 8, no. 6, pp. 2148–2155, 2006.
- [161] M. Liao, C. Chaudhari, G. Qin, X. Yan, C. Kito, T. Suzuki, Y. Ohishi, M. Matsumoto, and T. Misumi, "Fabrication and characterization of a chalcogenide-tellurite composite microstructure fiber with high nonlinearity," *Optics Express*, vol. 17, no. 24, pp. 21608–21614, 2009.
- [162] J. Chenč, "Novel optical properties of photonic quasi crystal fibers," Master's thesis, City University London, 2008.
- [163] C. J. Voyce, A. D. Fitt, and T. M. Monro, "Mathematical model of the spinning of microstructured fibres," *Optics Express*, vol. 12, no. 23, pp. 5810–5820, 2004.
- [164] X. Feng, A. K. Mairaj, D. W. Hewak, and T. M. Monro, "Nonsilica glasses for holey fibers," *Journal of Lightwave Technology*, vol. 23, no. 6, p. 2046, 2005.
- [165] P. Zhang, J. Zhang, P. Yang, S. Dai, X. Wang, and W. Zhang, "Fabrication of chalcogenide glass photonic crystal fibers with mechanical drilling," *Optical Fiber Technology*, vol. 26, no. Part B, pp. 176–179, 2015.
- [166] S. Bhandarkar, "Sol-gel processing for optical communication technology," *Journal of the American Ceramic Society*, vol. 87, no. 7, pp. 1180–1199, 2004.
- [167] B. MacChesney, D. W. Johnson, S. Bhandarkar, M. P. Bohrer, J. W. Fleming, E. M. Monberg, and D. J. Trevor, "Optical fibers using sol-gel silica overcladding tubes," *Electronics Letters*, vol. 33, no. 18, p. 1573–1574, 1997.
- [168] J. B. MacChesney, D. W. Johnson, S. Bhandarkar, M. P. Bohrer, J. W. Fleming, E. M. Monberg, and D. J. Trevor, "Optical fiber by a hybrid process using sol-gel silica overcladding tubes," *Journal of Non-Crystalline Solids*, vol. 226, no. 3, p. 232–238, 1998.
- [169] Z. G. Lian, J. A. Tucknott, N. White, L. Xiao, X. Feng, D. N. Payne, and W. H. Loh, "Technique for fabricating complex structured fibers by rolling of glass preforms," in *2011 37th European Conference and Exhibition on Optical Communication*, pp. 1–3, Sept 2011.
- [170] Q. Coulombier, L. Brilland, P. Houizot, T. Chartier, T. N. N'Guyen, F. Smektala, G. Renversez, A. Monteville, D. Méchin, T. Pain, H. Orain, J.-C. Sangleboeuf, and J. Trolès, "Casting method for producing low-loss chalcogenide microstructured optical fibers," *Optics Express*, vol. 18, no. 9, pp. 9107–9112, 2010.
- [171] Y. Zhang, K. Li, L. Wang, L. Ren, W. Zhao, R. Miao, M. C. J. Large, and M. A. van Eijkelenborg, "Casting preforms for microstructured polymer optical fibre fabrication," *Optics Express*, vol. 14, no. 12, pp. 5541–5547, 2006.
- [172] Z. Guiyao, H. Zhiyun, L. Shuguang, and H. Lantian, "Fabrication of glass photonic crystal fibers with a die-cast process," *Applied Optics*, vol. 45, no. 18, pp. 4433–4436, 2006.

- [173] Q. Zhao, F. Tian, X. Yang, S. Li, J. Zhang, X. Zhu, J. Yang, Z. Liu, Y. Zhang, T. Yuan, and L. Yuan, "Optical fibers with special shaped cores drawn from 3D printed preforms," *Optik - International Journal for Light and Electron Optics*, vol. 133, pp. 60–65, 2017.
- [174] M. Cassataro, D. Novoa, M. C. Günendi, N. N. Edavalath, M. H. Frosz, J. C. Travers, and P. S. Russell, "Generation of broadband mid-IR and UV light in gas-filled single-ring hollow-core PCF," *Optics Express*, vol. 25, no. 7, pp. 7637–7644, 2017.
- [175] F. Yu, W. J. Wadsworth, and J. C. Knight, "Low loss silica hollow core fibers for 3-4  $\mu\text{m}$  spectral region," *Optics Express*, vol. 20, no. 10, p. 11153–11158, 2012.
- [176] A. Husakou and J. Herrmann, "Supercontinuum generation in photonic crystal fibers made from highly nonlinear glasses," *Applied Physics B*, vol. 77, no. 2, pp. 227–234, 2003.
- [177] X. Jiang, N. Y. Joly, R. Sopalla, F. Babic, J. Huang, and P. Russell, "Soft glass microstructured fibers and their applications," in *Advanced Photonics 2016 (IPR, NOMA, Sensors, Networks, SPPCom, SOF)*, p. SoW3G.1, Optical Society of America, 2016.
- [178] X. Jiang, N. Y. Joly, M. A. Finger, F. Babic, G. K. L. Wong, J. C. Travers, and P. S. J. Russell, "Deep-ultraviolet to mid-infrared supercontinuum generated in solid-core ZBLAN photonic crystal fibre," *Nature Photonics*, vol. 9, pp. 133–139, 2015.
- [179] A. Zakery and S. Elliott, "Optical properties and applications of chalcogenide glasses: a review," *Journal of Non-Crystalline Solids*, vol. 330, no. 1, pp. 1–12, 2003.
- [180] K. Cerqua-Richardson, J. McKinley, B. Lawrence, S. Joshi, and A. Villeneuve, "Comparison of nonlinear optical properties of sulfide glasses in bulk and thin film form," *Optical Materials*, vol. 10, no. 2, pp. 155–159, 1998.
- [181] M. El-Amraoui, G. Gadret, J. C. Jules, J. Fatome, C. Fortier, F. Désévéday, I. Skripatchev, Y. Messaddeq, J. Troles, L. Brilland, W. Gao, T. Suzuki, Y. Ohishi, and F. Smektala, "Microstructured chalcogenide optical fibers from  $\text{As}_2\text{S}_3$  glass: towards new IR broadband sources," *Optics Express*, vol. 18, no. 25, pp. 26655–26665, 2010.
- [182] X. Feng, J. Shi, M. Segura, N. M. White, P. Kannan, L. Calvez, X. Zhang, L. Brilland, and W. H. Loh, "Towards water-free tellurite glass fiber for 2 – 5  $\mu\text{m}$  nonlinear applications," *Fibers*, vol. 1, no. 3, pp. 70–81, 2013.
- [183] A. Bjarklev, J. Broeng, and A. S. Bjarklev, *Photonic Crystal Fibres*. New York: Springer, 2003.
- [184] A. Agrawal, N. Kejalakshmy, B. M. A. Rahman, and K. T. V. Grattan, "Soft glass equiangular spiral photonic crystal fiber for supercontinuum generation," *IEEE Photonics Technology Letters*, vol. 21, no. 22, pp. 1722–1724, 2009.

- [185] Y. Koike, T. Ishigure, and E. Nihei, "High-bandwidth graded-index polymer optical fiber," *Journal of Lightwave Technology*, vol. 13, no. 7, pp. 1475–1489, 1995.
- [186] A. Barh, R. K. Varshney, B. P. Pal, G. P. Agrawal, and B. M. A. Rahman, "Design of a polymer-based hollow-core bandgap fiber for low-loss terahertz transmission," *IEEE Photonics Technology Letters*, vol. 28, no. 15, pp. 1703–1706, 2016.
- [187] I. P. Johnson, D. J. Webb, K. Kalli, W. Yuan, A. Stefani, K. Nielsen, H. K. Rasmussen, and O. Bang, "Polymer PCF Bragg grating sensors based on poly(methyl methacrylate) and topas cyclic olefin copolymer," *Proc.SPIE*, pp. 8073 – 8073 – 8, 2011.
- [188] D. J. Webb, "Polymer photonic crystal fibre for sensor applications," *Proc.SPIE*, vol. 7726, pp. 7726 – 7726 – 8, 2010.
- [189] M. J. Weber, *Handbook of Optical Materials*. New York: CRC Press, 2003.
- [190] Y. S. Jin, G. J. Kim, and S. G. Jeon, "Terahertz dielectric properties of polymers," *Journal of the Korean Physical Society*, vol. 49, no. 2, pp. 513–517, 2006.
- [191] M. Goto, A. Quema, S. O. H. Takahashi, and N. Sarukura, "Teflon photonic crystal fiber as terahertz waveguide," *Japanese Journal of Applied Physics*, vol. 43, no. 2B, pp. L317–L319, 2004.
- [192] K. Nielsen, H. K. Rasmussen, A. J. Adam, P. C. Planken, O. Bang, and P. U. Jepsen, "Bendable, low-loss topas fibers for the terahertz frequency range," *Optics Express*, vol. 17, no. 10, pp. 8592–8601, 2009.
- [193] W. MacPherson, M. Gander, R. McBride, J. Jones, P. Blanchard, J. Burnett, A. Greenaway, B. Mangan, T. Birks, J. Knight, and P. Russell, "Remotely addressed optical fibre curvature sensor using multicore photonic crystal fibre," *Optics Communications*, vol. 193, no. 1, p. 97–104, 2001.
- [194] M. T. Myaing, J. Y. Ye, T. B. Norris, T. Thomas, J. J. R. Baker, W. J. Wadsworth, G. Bouwmans, J. C. Knight, and P. S. J. Russell, "Enhanced two-photon biosensing with dual-core photonic crystal fibers," *Optics Letters*, vol. 28, no. 14, p. 1224–1226, 2003.
- [195] T. Udem, R. Holzwarth, and T. Hansch, "Optical frequency metrology," *Nature*, vol. 416, p. 233–237, 2002.
- [196] B. Povazay, K. Bizheva, A. Unterhuber, B. Hermann, H. Sattmann, A. F. Fercher, W. Drexler, A. Apolonski, W. J. Wadsworth, J. C. Knight, P. S. J. Russell, M. Vetterlein, and E. Scherzer, "Submicrometer axial resolution optical coherence tomography," *Optics Letters*, vol. 27, no. 20, p. 1800–1802, 2002.
- [197] J. Limpert, T. Schreiber, S. Nolte, H. Zellmer, A. Tünnermann, R. Iliew, F. Lederer, J. Broeng, G. Vienne, A. Petersson, and C. Jakobsen, "High-power air-clad large-mode-area photonic crystal fiber laser," *Optics Express*, vol. 11, no. 7, pp. 818–823, 2003.

- [198] M. N. Sadiku, *Numerical Techniques in Electromagnetics*. New York: CRC Press, 2 ed., 2001.
- [199] T. Rylander, P. Ingelström, and A. Bondeson, *Computational Electromagnetics*. New York: Springer, 2013.
- [200] B. M. A. Rahman and A. Agrawal, *Finite Element Modeling Methods for Photonics*. London: Artech House, 2013.
- [201] R. Garg, *Analytical and Computational Methods in Electromagnetics*. Norwood: Artech House, 2008.
- [202] Y. M. Desai, T. I. Eldho, and A. H. Shah, *Finite Element Method with Applications in Engineering*. India: Dorling Kindersley, 2011.
- [203] R. C. Booton, *Computational Methods for Electromagnetics and Microwaves*. New York: John Wiley & Sons, 1992.
- [204] G. Meunier, ed., *The Finite Element Method for Electromagnetic Modeling*. London: ISTE, 2008.
- [205] A. K. Ghatak and K. Thyagarajan, *Optical Electronics*. Cambridge: Cambridge University Press, 1989.
- [206] D. Poljak, *Advanced Modeling in Computational Electromagnetic Compatibility*. New Jersey: John Wiley & Sons, Ltd, 2007.
- [207] G. B. Hocker and W. K. Burns, "Mode dispersion in diffused channel waveguides by the effective index method," *Applied Optics*, vol. 16, no. 1, pp. 113–118, 1977.
- [208] E. A. Marcatili, "Dielectric rectangular waveguide and directional coupler for integrated optics," *The Bell System Technical Journal*, vol. 48, no. 7, pp. 2071–2102, 1969.
- [209] D. B. Davidson, *Computational Electromagnetics for RF and Microwave Engineering*. Cambridge: Cambridge University Press, 2010.
- [210] X. Q. Sheng and W. Song, *Essentials of Computational Electromagnetics*. Singapore: John Wiley & Sons, 2012.
- [211] C. Christopoulos, *The Transmission-line Modeling (TLM) Method in Electromagnetics*. USA: Morgan & Claypool, 2006.
- [212] R. Pregla, *Analysis of Electromagnetic Fields and Waves: The Method of Lines*. Chichester: John Wiley & Sons, Ltd, 2008.
- [213] J. Jin, *The Finite Element Method in Electromagnetics*. New York: John Wiley & Sons, 2 ed., 2002.
- [214] T. Itoh, *Numerical Techniques For Microwave And Millimeter-Wave Passive Structures*. New York: John Wiley & Sons, 1989.
- [215] S. Humphries, *Field Solutions on Computers*. Florida: CRC Press LLC, 1998.

- [216] B. A. Rahman, F. A. Fernandez, and J. B. Davies, "Review of finite element methods for microwave and optical waveguides," *Proceedings of the IEEE*, vol. 79, no. 10, pp. 1442–1448, 1991.
- [217] B. A. Finlayson, *Method of Weighted Residuals and Variational Principles*. New York: Academic Press, 1972.
- [218] B. A. Rahman and J. B. Davies, "Penalty function improvement of waveguide solution by finite elements," *IEEE Transactions on Microwave Theory and Techniques*, vol. 32, no. 8, pp. 922–928, 1984.
- [219] A. C. Polycarpou, *Introduction to the Finite Element Method in Electromagnetics*. USA: Morgan & Claypool, 1 ed., 2006.
- [220] K. Ise, K. Inoue, and M. Koshiba, "Three-dimensional finite-element solution of dielectric scattering obstacles in a rectangular waveguide," *IEEE Transactions on Microwave Theory and Techniques*, vol. 38, no. 9, pp. 1352–1359, 1990.
- [221] K. K. Mei, M. A. Morgan, and S. K. Chang, *Finite methods in electromagnetic scattering*. New York: Academic Press, 1978.
- [222] B. Engquist and A. Majda, "Absorbing boundary conditions for the numerical simulation of waves," *Mathematics of Computation*, vol. 31, no. 139, pp. 629–651, 1977.
- [223] J.-P. Berenger, "A perfectly matched layer for the absorption of electromagnetic waves," *Journal of Computational Physics*, vol. 114, no. 2, pp. 185–200, 1994.
- [224] K. Kawano and T. Kitoh, *Introduction to Optical Waveguide Analysis: Solving Maxwell's Equations and the Schrödinger Equation*. New York: John Wiley & Sons, 2001.
- [225] A. Agrawal, M. Tiwari, Y. O. Azabi, V. Janyani, B. Rahman, and K. Grattan, "Ultrabroad supercontinuum generation in tellurite equiangular spiral photonic crystal fiber," *Journal of Modern Optics*, vol. 60, no. 12, pp. 956–962, 2013.
- [226] "Succulent Inspirations." <http://wmevents.com/2013/01/succulent-inspirations/>. Accessed: 2017-11-16.
- [227] "The Anatomy of Galaxies." <https://blog.galaxyzoo.org/2010/06/09/the-anatomy-of-galaxies/>. Accessed: 2017-11-16.
- [228] "Nanotechnology inspired by mussels and seashells." <https://www.nanowerk.com/spotlight/spotid=1723.php>. Accessed: 2017-11-16.
- [229] "Explore Flower Petals, Flower Art and more!" <https://www.pinterest.com.au/pin/56576539042201868/>. Accessed: 2017-11-16.
- [230] "Peonies Flower Wallpaper 7362." <https://wallpaperlayer.com/peonies-flower-wallpaper-7362.html>. Accessed: 2017-11-16.
- [231] "Chameleon tail." [https://travel.mongabay.com/madagascar/images/madagascar\\_1577.html](https://travel.mongabay.com/madagascar/images/madagascar_1577.html). Accessed: 2017-11-16.

- [232] R. C. Yates, *A Handbook on Curves and Their Properties*. New York: J. W. Edwards, 1952.
- [233] E. W. Weisstein, *CRC Concise Encyclopedia of Mathematics, Second Edition*. New York: CRC Press, 2003.
- [234] H. Karakuzu, M. Dubov, S. Boscolo, Y. O. Azabi, and A. Agrawal, "Equiangular spiral micro-structured waveguides in lithium niobate," in *XXIII International Workshop on Optical Wave & waveguide Theory and Numerical Modelling (OWTNM 2015)*, 2015.
- [235] J. W. Rutter, *Geometry of Curves*. New York: CRC Press, 2000.
- [236] R. Dixon, "The mathematics and computer graphics of spirals in plants," *Leonardo*, vol. 16, pp. 86–90, 1983.
- [237] M. Naylor, "Golden,  $\sqrt{2}$ , and  $\pi$  flowers: A spiral story," *Mathematics Magazine*, vol. 75, pp. 163–172, 2002.
- [238] A. Agrawal, N. Kejalakshmy, J. Chen, B. M. A. Rahman, and K. T. V. Grattan, "Golden spiral photonic crystal fiber: polarization and dispersion properties," *Optics Letters*, vol. 33, no. 22, pp. 2716–2718, 2008.
- [239] Y. O. Azabi, A. Agrawal, B. M. Rahman, K. T. Grattan, and J. Kejalakshmy, "Equiangular spiral tellurite photonic crystal fiber for supercontinuum generation in mid-infrared," in *CLEO:2011 - Laser Applications to Photonic Applications*, p. JThB72, Optical Society of America, 2011.
- [240] A. Agrawal, Y. O. Azabi, and B. M. A. Rahman, "Stacking the equiangular spiral," *IEEE Photonics Technology Letters*, vol. 25, no. 3, pp. 291–294, 2013.
- [241] C. Li, *Nonlinear Optics Principles and Applications*. China: Springer, 2017.
- [242] L. Shuo, L. Shu-Guang, and D. Ying, "Analysis of the characteristics of the polarization splitter based on tellurite glass dual-core photonic crystal fiber," *Optics & Laser Technology*, vol. 44, no. 6, pp. 1813 – 1817, 2012.
- [243] A. Agrawal, N. Kejalakshmy, M. Uthman, B. M. A. Rahman, A. Kumar, and K. T. V. Grattan, "Ultra low bending loss equiangular spiral photonic crystal fibers in the terahertz regime," *AIP Advances*, vol. 2, no. 2, p. 022140, 2012.
- [244] T. Cheng, X. Xue, D. Deng, M. Matsumoto, H. Tezuka, T. Suzuki, and Y. Ohishi, "Fabrication and characterization of a three-core chalcogenide–tellurite hybrid optical fiber," *Optics Communications*, vol. 341, no. Supplement C, pp. 252 – 256, 2015.
- [245] G. Qin, M. Liao, C. Chaudhari, X. Yan, C. Kito, T. Suzuki, and Y. Ohishi, "Second and third harmonics and flattened supercontinuum generation in tellurite microstructured fibers," *Optics Letters*, vol. 35, no. 1, pp. 58–60, 2010.
- [246] G. Qin, X. Yan, C. Kito, M. Liao, T. Suzuki, A. Mori, and Y. Ohishi, "Zero-dispersion-wavelength-decreasing tellurite microstructured fiber for wide and flattened supercontinuum generation," *Optics Letters*, vol. 35, no. 2, pp. 136–138, 2010.

- [247] E. S. Hu, Y.-L. Hsueh, M. E. Marhic, and L. G. Kazovsky, "Design of highly-nonlinear tellurite fibers with zero dispersion near 1550nm," in *2002 28th European Conference on Optical Communication*, vol. 2, pp. 1–2, 2002.
- [248] C. Chaudhari, M. Liao, T. Suzuki, and Y. Ohishi, "Chalcogenide core tellurite cladding composite microstructured fiber for nonlinear applications," *Journal of Lightwave Technology*, vol. 30, no. 13, pp. 2069–2076, 2012.
- [249] D. Buccoliero, H. Steffensen, O. Bang, H. Ebendorff-Heidepriem, and T. M. Monro, "Thulium pumped high power supercontinuum in loss-determined optimum lengths of tellurite photonic crystal fiber," *Applied Physics Letters*, vol. 97, no. 6, p. 061106, 2010.
- [250] C. Chaudhari, T. Suzuki, and Y. Ohishi, "Design of zero chromatic dispersion chalcogenide  $\text{As}_2\text{S}_3$  glass nanofibers," *Journal of Lightwave Technology*, vol. 27, no. 12, pp. 2095–2099, 2009.
- [251] M. Liao, X. Yan, G. Qin, C. Chaudhari, T. Suzuki, and Yasutake Ohishi, "A highly non-linear tellurite microstructure fiber with multi-ring holes for supercontinuum generation," *Optics Express*, vol. 17, no. 18, pp. 15481–15490, 2009.
- [252] G. Qin, X. Yan, C. Kito, M. Liao, C. Chaudhari, T. Suzuki, and Y. Ohishi, "Ultra-broadband supercontinuum generation from ultraviolet to  $6.28\mu\text{m}$  in a fluoride fiber," *Applied Physical Letters*, vol. 95, no. 16, p. 161103, 2009.
- [253] P. Domachuk, N. A. Wolchover, M. Cronin-Golomb, A. Wang, A. K. George, C. Cordeiro, J. Knight, and F. G. Omenetto, "Over 4000 nm bandwidth of mid-IR supercontinuum generation in sub-centimeter segments of highly nonlinear tellurite PCFs," *Optics Express*, vol. 16, no. 10, pp. 7161–7168, 2008.